SAND2018-10149J

Radiation damage in nanostructured materials

Xinghang Zhang[1], Khalid Hattar[2], Youxing Chen[3], Lin Shao[4], Jin Li[1], Cheng Sun[5], Kaiyuan Yu[6], Nan Li[3], Mitra L. Taheri[7], Haiyan Wang[1,8], Jian Wang[9], and Michael Nastasi[9,10].

[1] School of Materials Engineering, Purdue University, *West Lafayette, IN 47907, USA*

[2] Department of Radiation-Solid Interactions, Sandia National Laboratories, Albuquerque, NM 87185

[3] MPA-CINT, Los Alamos National Laboratory, Los Alamos, NM 87545, USA

[4] Department of Nuclear Engineering, Texas A&M University, College Station, TX 77843-3128, USA

[5] Materials and Fuels Complex, Idaho National Laboratory, Idaho Falls, ID 83415

[6] Department of Materials Science and Engineering, China University of Petroleum-Beijing, Beijing, 102246, China

[7] Materials Science and Engineering, Drexel University, Philadelphia, PA 19104

[8] School of Electrical and Computer Engineering, Purdue University, *West Lafayette, IN 47907, USA*

[9] Materials Science and Engineering, Drexel University, Philadelphia, PA 19104

[10] Nebraska Center for Energy Sciences Research, University of Nebraska-Lincoln, Lincoln, NE 68583-0857, USA

Corresponding author: Xinghang Zhang, xzhang98@purdue.edu;

Contents

Abstract

There is a significant demand for the discovery of advanced materials that can survive high temperature and high dose radiations for the next generation nuclear reactors. Materials subjected to high dose and high energy particle radiation often experience severe damage in form of drastic increase of density of defects, and significant degradation of their mechanical and physical properties. Extensive studies on radiation effects in materials in the past few decades show that, although nearly no materials are immune to radiation damage, the approach of deliberate introduction of certain types of defects in materials before radiation, though somewhat counterintuitive, has been proven effective for mitigation of radiation damage for a variety of materials. Nanomaterials with abundant internal defects have been intensely investigated for various applications. However, their impact on the alleviation of radiation damage remains less well understood. In this review article, we summarize and analyze the current understandings on the influence of various types of internal defect sinks on reduction of radiation damage in primarily nanostructured metallic materials, and partially on some nanoceramic materials (nitrides and oxides). We also point out open questions and future directions that may significantly improve our understanding on fundamental radiation damage mechanisms in nanomaterials. The field of radiation damage in nanostructured materials is an exciting and rapidly evolving new arena, enriched with challenges and opportunities. The integration of extensive research effort, resources and expertise in the field materials science, nuclear science and technology, advanced microscopy, physics, mechanics, chemistry, and modeling and simulations may eventually lead to the design of a family of nanomaterials with unprecedented radiation tolerance.

Chapter 1. Introduction

1.1. Motivation, scope and architecture

Motivation

Nuclear energy accounts for more than 13% of electricity generated worldwide [1]. The design of advanced (next generation) nuclear reactors calls for materials that can survive a much greater radiation dose, 400-600 (displacements-per-atom) dpa, equivalent to the service lifetime of ~ 80 plus years in advanced nuclear reactors. However, most materials adopted in the current nuclear reactors have not been tested to a dose of more than 200 dpa. Fundamental studies show that radiation by high-energy particles, including electrons, protons, neutrons, light and heavy ions, can introduce significant microstructural damage in a variety of metallic materials. Extensive national and international nuclear materials research studies in the past few decades show that although the magnitude of microstructural damage varies drastically for various materials, the nature of the damage in crystalline materials is mostly associated with the formation, distribution and interaction of point defects (vacancies and interstitials), and their clusters, such as Frenkel pair (vacancy-interstitial pair), vacancy clusters, interstitial loops, radiation induced dislocation segment and networks, inert gas bubbles and voids [1-3]. To a large extent, there are nearly no existing materials that are immune to radiation damage. Understanding the mechanisms of radiation damage clearly has a significant impact on the design of radiation tolerant materials for advanced nuclear energy applications.

Scope

Radiation involves extensive ion-solid interactions, which may have beneficial or deleterious impacts on the properties of materials [1, 4]. For materials used in nuclear reactors, radiation damage can pose a serious challenge to the stability and reliability of these materials over

a long period of time, which is relevant to the safe operation of nuclear reactors [5]. In this review article, we summarize recent progress in the investigation of radiation damage in nanostructured materials, focusing on metallic materials and/or metal-ceramic compounds. The radiation damage in nanostructured ferritic alloys and oxide dispersion strengthened (ODS) steels is another subject that is intensely studied but will not be covered here as there are several recent reviews and numerous highlights on this subject [6-16].

Meanwhile, ion implantation has been routinely adopted by the semiconductor industry to tune electrical conductivity or engineering seminar conductor device [17-22], and increasingly applied to introduce various unique nanofeatures that may drastically change the chemical and physical properties via surface engineering [23, 24]. The subject on nanopatterning using ion irradiation technique is not the focus of the current review and is not included for further discussions.

Architecture

The architecture of the current review article is organized as follows. The Introduction (Chapter 1) briefly summarizes some of the major findings on the nature, formation of defects and their interactions. Introducing these concepts may be beneficial for graduate students and junior researchers to understand radiation damage related to microstructure evolution at a fundamental level. The significance of various types of defect sinks is briefly touched on in this chapter. At the end of the Introduction chapter, an overview is provided to summarize various types of defect sinks that will be discussed in various nanostructured materials in this review. There are several succeeding chapters that describe mitigation of radiation damage using various strategies and defect sinks. Chapter 2 targets the application of grain boundaries on the alleviation of radiation damage. Chapter 3 focuses on the reduction of radiation damage by using various layer interfaces

in metallic and metal/ceramics nanolayer composites. Chapter 4 eyes on the strategy of using twin boundaries in nanotwinned metals to transport and eliminate radiation induced defects. This chapter also describes the combination of nanotwins and nanovoids to design radiation tolerant materials. Chapter 5 explore the influence of free surface on tailoring radiation tolerance of nanoporous, 0D and 1D metallic materials.

Each chapter has its own outlook that is more specific for a particular type of nanomaterials. At the end of the review, a broader picture is presented to engage and stimulate collaborations among nuclear materials, nanomaterials, physics, chemistry, mechanics and modeling community. Intimate collaborations among scientists in these communities may be the key to move the forefront of science forward rapidly and to accelerate the design of radiation tolerant, and ultimately "radiation immune" materials for the future generation nuclear reactors.

1.2. Radiation induced defects in metals with various crystal structures

Radiation induces various types of defects that may degrade the mechanical and structural stability of irradiated metallic materials. Hence it is critical to understand the nature of these defects before we move forward with effective approaches to eliminate these defects. In what follows we briefly describe different types of defects based on the crystal structure of irradiated metallic materials.

Radiation induced defects in metals with face-centered-cubic (FCC) structures

Metallic materials with FCC like structures are widely used as structural materials in nuclear reactors, including austenitic stainless steels, Ni alloys and certain Cu conducting cables [1-3, 5, 25]. Very often monolithic metals are irradiated as model systems, where the influence of chemistry from a second phase can be ignored. Yet, the nature of defects induced in these monolithic metals is often a good ensemble of what has been identified in austenitic stainless steels.

Also these monolithic FCC metals have drastically different stacking fault energy (SFE), which is critical to tailor radiation induced defects [26].

The vacancy migration energy for FCC metals typically varies from 0.7 to 1.7 eV, and the vacancy migration energy is typically less, 50-70% of the vacancy formation energy. Several types of interstitials may exist, including 3 types of dumbbells, <111>, <110>, and <100> dumbbell, crowdion (shown in Fig. 1.1a) and the classical tetrahedral and octahedral position (not shown here). As the interstitial formation energy is often the lowest for the <100> split dumbbell, most studies use the <100> dumbbell site to calculate the interstitial formation energy. The interstitial migration energy is typically 0.05-0.1 eV, significantly less than the vacancy migration energy. Hence it is widely adopted that interstitials (and interstitial loops) are highly mobile even at room temperature, whereas vacancies are mobile at elevated temperature. Such a drastic difference between the migration energy of vacancy and interstitial has a profound impact on the accumulation of radiation damage and void swelling in FCC metals and alloys. To some extent, the rapid migration of interstitials (which evolve quickly into interstitial loops) leave vacancies behind, and hence accelerate the accumulation of radiation induced damage in form of undesirable large vacancies and interstitial clusters.

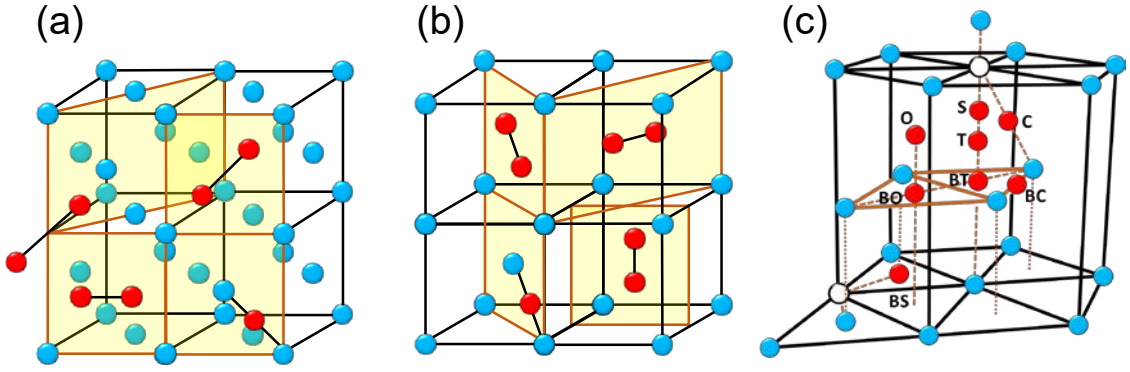

Fig. 1.1. Various types of interstitials in monolithic metals with FCC, BCC and HCP crystal structures. (a) FCC: <111>, <110> and <100> dumbbells, and crowdion; (b) BCC: <111>, <110> and <100> dumbbells and crowdion; (c) Eight available interstitial sites in HCP metals: octahedron

(O), tetrahedron (T), BO and BT – on the basal plane below O and T sites, BC and C - crowdions halfway between two nearest neighbor atoms along <11 $\bar{2}$ 0> (on the basal plane) and 1/6 < 20 $\bar{2}$ 3> direction (out of the basal plane), BS and S - split dumbbells within or orthogonal to the basal plane (replotted following [27]).

The volume of a vacancy, V_V^F, is known to be less than the volume of the individual atom, typically 0.75Ω (Ω is the atomic volume), due to the relaxation of atoms surrounding the vacancy. Such a relaxation volume due to the formation of a vacancy, V_V^{rel}, can be written as:

$$V_V^{rel} = \Omega - V_V^F \quad (1.1),$$

and is typically ~ 0.25Ω for a suite of FCC metals [28]. The activation volume for self-diffusion (V_V^{SD}) of FCC metals is described by

$$V_V^{SD} = V_V^F + V_V^M \quad (1.2),$$

where V_V^F, V_V^M are respective activation volume for formation and migration of vacancies. As the vacancy migration volume is typically 0.1Ω, the activation volume for self-diffusion of FCC metals is ~ 0.85 Ω. The dilatational volume expansion associated with the insertion of an interstitial atom in FCC metal, V_{SIA}^F, is ~ 1.1 Ω. Considering the volume expansion arising from non-linear elastic strain, δV, the relaxation volume for self-interstitials ($\mathbf{V_{SIA}^{rel}}$), estimated by

$$V_{SIA}^{rel} = V_{SIA}^F + \delta V \quad (1.3),$$

is typically ~ 2 Ω. As will be shown later, the V_{SIA}^{rel} for SIA in BCC metal is much smaller. Such a difference has an important consequence on the radiation tolerance (such as void swelling resistance) of BCC metals.

The clustering of these point defects leads to defect clusters. Among the known defect clusters in FCC metals, interstitial loops and vacancy loops are widely observed. Furthermore

vacancy clusters can form stacking fault tetrahedrons (SFTs), which is a type of 3D defect and difficult to be eliminated. As a variety of FCC metals typically have low-to-intermediate SFE, faulted dislocation (both vacancy and interstitial) loops are frequently observed. Many of these faulted loops have Burgers vector of 1/3 <111>, making them sessile (immobile) loops. However, abundant Shockley partials (an inherent nature of FCC metals) can migrate and interact with these faulted loops and consequently change interstitial loops into mobile perfect loops, with Burgers vector of ½ <110>. The glide plane of these perfect interstitial loops is either {111} or {110} [2].

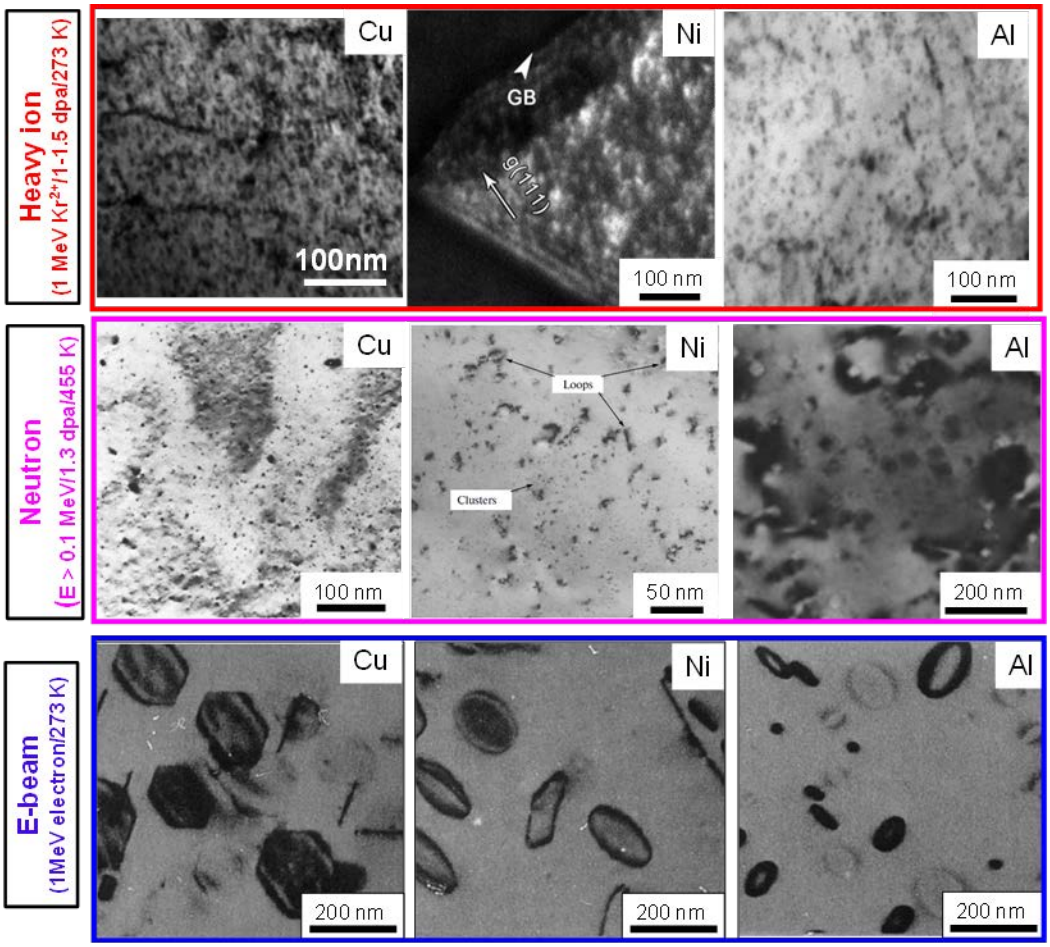

Fig. 1.2. Compilation of TEM micrographs showing neutron, heavy ion, and electron beam induced damage in irradiated FCC metals. The radiation condition in terms of dpa or fluence is also provided. Under heavy Kr ion irradiation at 273 K, a large number of small interstitial dislocation loops are generated in Cu, Ni and Al [29, 30]. Neutron radiation at 455 K to a similar level of the dose generates defects with similar morphology (small loops) but with somewhat lower

defect density [31-33]. Room temperature e-beam (1 MeV) radiation introduces large interstitial loops, which are mostly faulted loops on {111} planes [34].

Fig. 1.2 compiles selected examples of radiation damage in Cu, Ni and Al to a similar dose level by using heavy ions (such as Kr), neutrons and electron beam (e-beam). Under heavy Kr ion irradiation at 273 K to 1-1.5 dpa, a large number of small interstitial dislocation loops are observed in all 3 FCC metals [29, 30]. Defect density appears to be greater in Cu than in Al. Neutron radiation at a higher temperature (455 K) to a similar dose level of dose (1.3 dpa) generates defects with similar morphology (small loops) but with somewhat lower defect density [31-33]. Meanwhile, e-beam (1 MeV) radiations at room temperature introduce rather large isolated interstitial loops in all FCC metals, which are mostly faulted loops on {111} planes [34]. The differences between e-beam and neutron induced defects are mostly due to the fact that e-beam radiation typically induces low energy recoil atoms (0.1-1 kev), whereas neutrons produce much more energetic recoil atoms (> 10 kev). Consequently e-beam radiation induces isolated SIAs and vacancies that nucleate and coarsen via diffusional process [2]. In contrast, high-energy neutron radiation induces small defect clusters directly within the cascade, and these small defect clusters act as defect sinks and curtail the coarsening of defect clusters [35-37]. Comparison of weighted average recoil spectra (a measure of fraction of defects with recoil energy) of neutrons, proton and heavy ions shows that Kr provides a much better approximation to the neutron irradiation than light ions [38].

SFTs are intriguing defects in irradiated FCC metals and they often appear triangular in geometry examined under TEM. Some examples of SFTs are shown by dark field TEM and HRTEM in Fig. 1.3a-b for Ag [39] and Fig. 1.3c-d for Au, irradiated by 1 MeV Kr ions to 1 dpa at room temperature [40]. The formation of SFTs has also been investigated by MD simulations.

In general, SFTs can evolve from vacancy clusters via the classical Silcox and Hirsch [41] mechanism and validated by MD simulations [42]. MD simulations of a large number collision cascade show that a regular SFT or conjoint SFTs can form (Fig. 1.3e) [43]. SFT-like vacancy clusters are also typical in irradiated FCC Cu. SIA loops can be either glissile, in the case of perfect interstitial loops with Burgers vector of ½ <110>, or sessile, in the case of faulted loops with Burgers vector of 1/3 <111>. Furthermore, the MD simulations also show that SFTs can stem from a void, instead of Frank loops, as shown in Fig. 1.3f. The transformation is driven by large increase in entropy, in spite of a high potential energy barrier. Such a mechanism may be applicable to a variety of FCC metals [44].

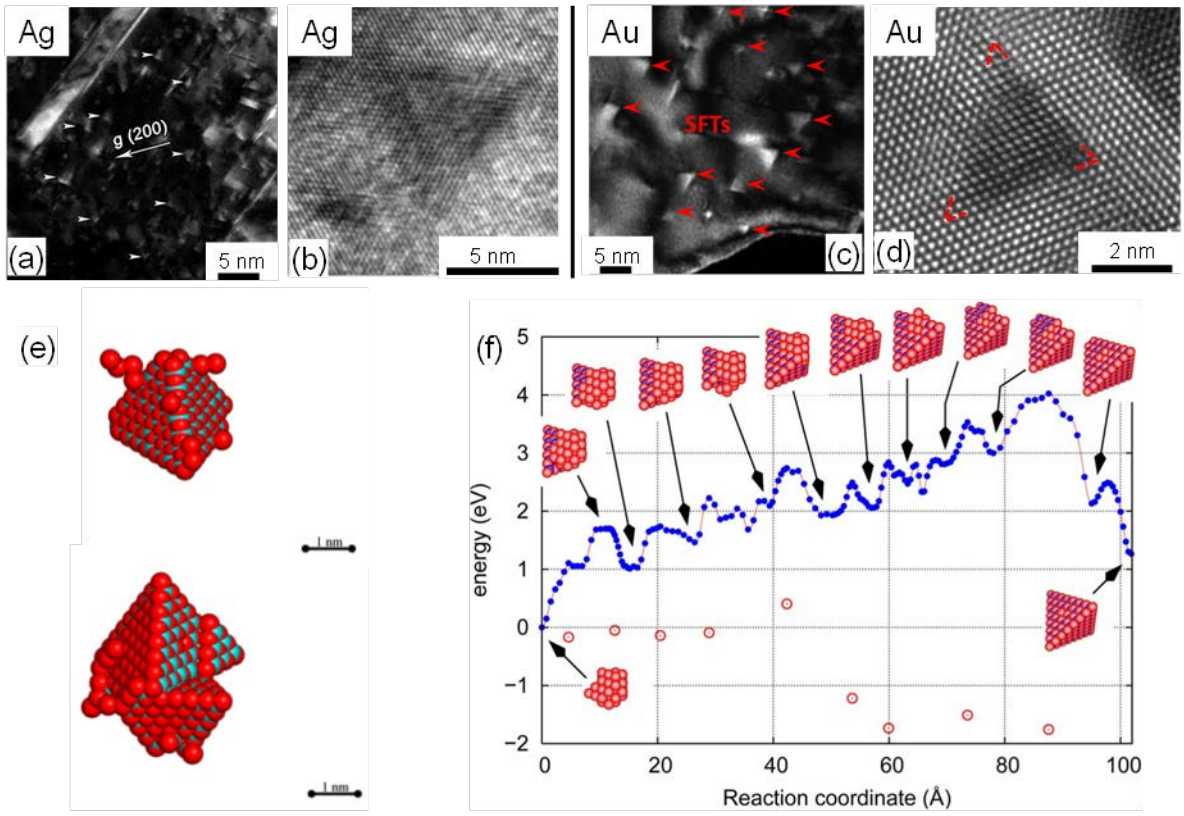

Fig. 1.3. SFTs in irradiated FCC metals. (a-b) Dark field TEM and HRTEM micrographs of SFTs in irradiated Ag films (1 MeV Kr ions/1 dpa/RT) [39]. (c-d) Dark field TEM and atomic resolution TEM micrographs of SFTs in irradiated Au films (1 MeV Kr ions/1 dpa/RT) [40]. (e) MD simulations on the formation and evolution of regular SFT and two adjunct SFTs in Cu [43]. (f) MD simulations showing the evolution of a void into an SFT [44].

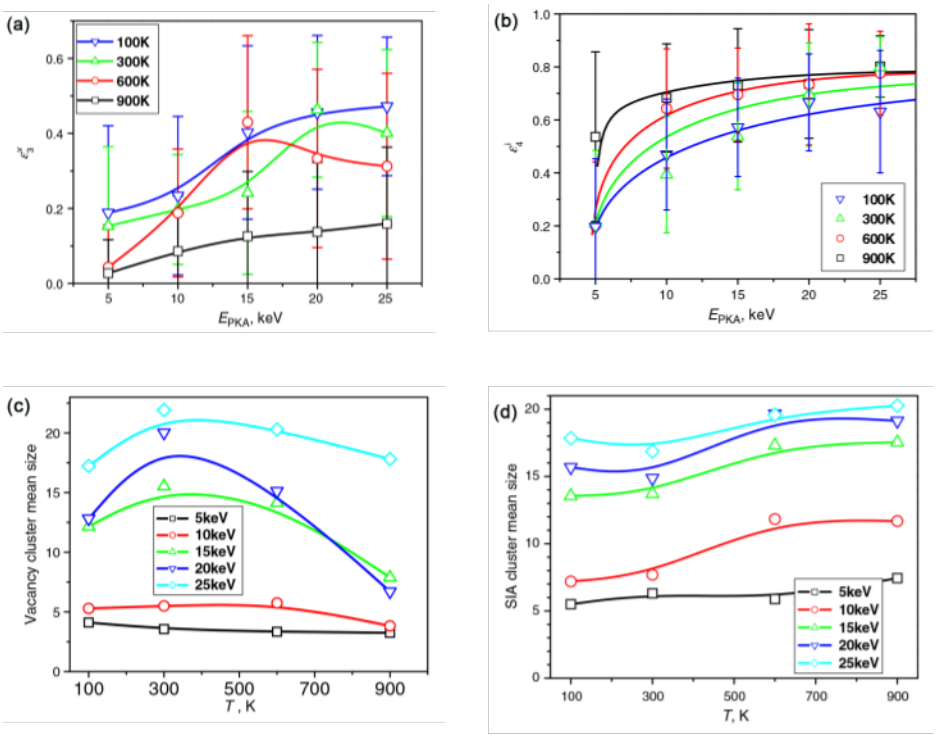

Fig. 1.4. MD simulations studies on self-ion irradiated Cu [43]. (a-b) Evolution of the fraction of vacancy and interstitial clusters under different temperatures in self-ion irradiated Cu. (c-d) Evolution of the mean size of vacancy and SIA clusters as a function of irradiation temperature.

Large scale MD simulations (Fig. 1.4) also show that at room to intermediate (< 600 K) temperature, 40% of the vacancy clusters have more than 3 vacancies; whereas 80% of the interstitial clusters have more than 4 interstitials [43]. The fraction of vacancy clusters decreases with radiation temperature. In contrast, the fraction of interstitial clusters continues to increase at higher irradiation temperature. The vacancy cluster size in irradiated Cu appears to reach a maximum at 300K in certain cases, due to a transition from compact cascade below 300K (yielding large vacancy clusters) to thermal spike promoted destabilization of large vacancy clusters (due to interstitial-vacancy recombination) at elevated temperature. In comparison, the SIA cluster size increases monotonically with temperature due to their higher binding energy [43].

Radiation induced defects in metals with body-centered-cubic (BCC) structures

Radiation damage in BCC metals, such as Fe and refractory metals, has also been extensively investigated as a variety of reactor steels, such as ferritic/martensitic steels and W alloys, have similar crystal structures [1, 8, 45, 46]. Similar to FCC metals, a suite of point defects and their clusters will be generated in irradiated BCC metals. The vacancy formation energy for BCC metals is typically 1.6-3 eV, and vacancy migration energy is 0.5-2 eV. Various types of interstitial can be generated in BCC metals, including crowdions, <111>, <110> and <100> dumbbells (as shown in Fig. 1.1b) and octahedral and tetrahedral SIAs. The activation volume for self-diffusion of BCC metals is ~ 0.4-0.6 Ω, smaller than that in FCC metals, ~ 0.85 Ω. In comparison to FCC metal, the volume expansion associated with the insertion of an interstitial atom in BCC metal is much smaller, ~ 0.64 Ω (versus 1.1 Ω for FCC) presumably due to the lower packing density of BCC metals. The relaxation volume for self-interstitials in BCC metal is ~ 1.0-1.5 Ω, also much smaller than that in FCC metals, ~ 2 Ω. These differences between FCC and BCC metals may be correlated to the enhanced radiation tolerance of BCC metals vs. FCC metals to some extent.

In general the high SFE of BCC metals prohibits the formation of large faulted dislocation loops [47]. The perfect glissile loops in BCC metals have {110} habit planes with b = a/2 <111>, whereas the perfect sessile loops are often on {100} habit planes with *b* = a <100> [34, 48]. Fig. 1.5 shows various types of dislocation loops in BCC Fe, Mo and W irradiated by heavy ions, neutrons or e-beam [25, 34, 49-56]. In general, the defect clusters induced by heavy ions and neutrons are similar, in form of dislocation loops with dimensions of several to 10 nm, in these irradiated BCC metals. Heavy ion irradiation of Fe induces abundant dislocation loops (string of loops) [49], whereas neutron radiation induces rafts in Fe [25]. In comparison, e-beam introduces much fewer loops with greater loop diameter. For instance e-beam radiation induces perfect {100}

loops in Fe [34]. In comparison to e-beam radiation of FCC metals, Kiritani reported that no vacancy clusters were observed in e-beam irradiated Fe [34].

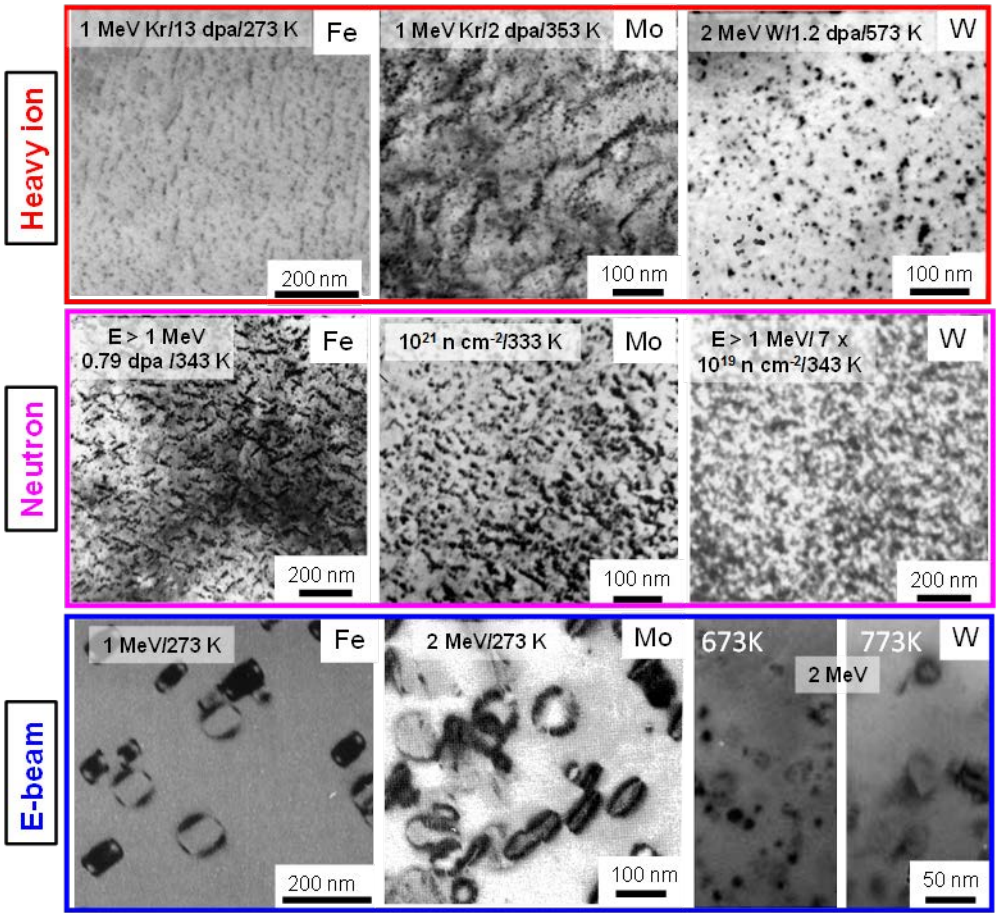

Fig. 1.5. Compilation of TEM micrographs showing radiation damage in Fe, Mo and W induced by heavy ions, neutrons and e-beam. The ion energy, dose/fluence and radiation temperature are also provided [25, 34, 49-56]. In general heavy ion and neutron radiation induce small dislocation loops, string or rafts of loops, whereas e-beam generates large isolated dislocation loops.

Radiation induced loops in Fe have also been extensively investigated by simulations. A recent MD simulation shows (Fig. 1.6a-c) the interaction between two ½ <111> loop may lead to 3 scenarios (path A, B and C), one of these leading to the formation of <100> loops [57]. The mobility of ½ <111> loops is important as such will ensure the probability of interaction among these loops [57]. Furthermore MD simulations have predicted the formation of nanoclusters with

C15 structure in Fe (Fig. 1.6d). These C15 nanoclusters are of interstitial types but are immobile and have a low formation energy (Fig. 1.6e) [58].

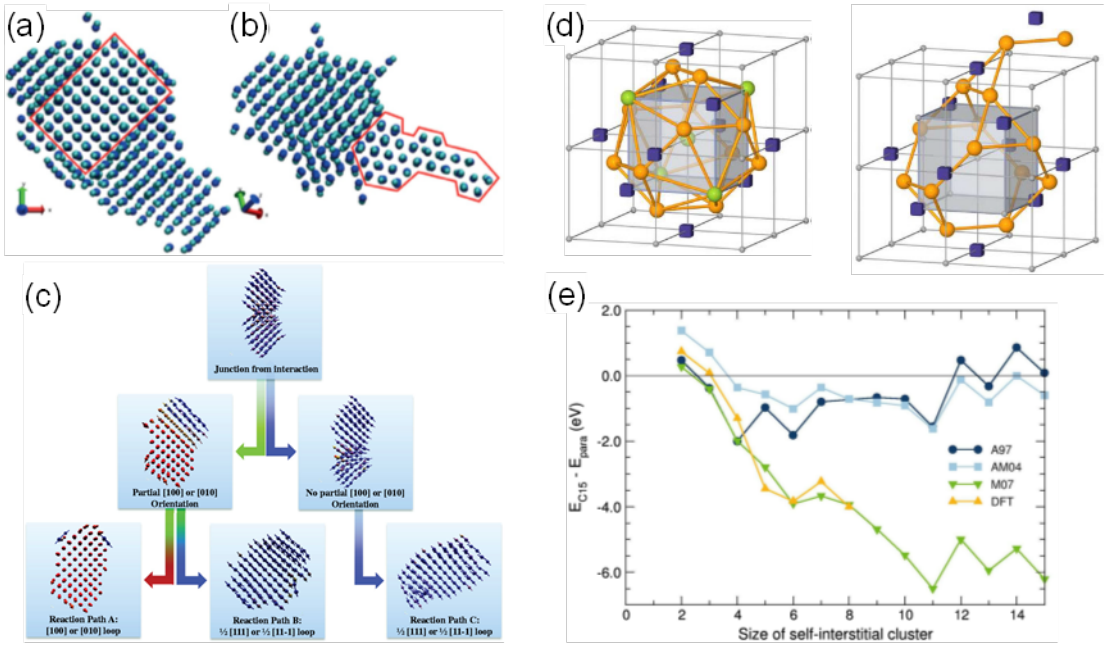

Fig. 1.6. (a-c) MD simulations showing the formation of <100> dislocation loops in BCC Fe [57]. (d-e) The formation of C15 clusters in irradiated Fe and the energy of the defect cluster [58].

Radiation induced defects in metals with HCP structures.

The investigations on the nature of defects in HCP metals are largely driven by the application of HCP Zr based alloys as fuel cladding tubes in light water reactors. Vacancies and interstitials have much more completed configurations in HCP metals than in cubic systems. Both individual and divacancies have been investigated in HCP metals. The formation and migration energy for monovacancies are typically 0.6-2 eV and 0.3-1 eV respectively. Formation volume of monovacancies typically varies from 0.78 to 0.97 Ω [27, 59, 60]. Monovacancies can diffuse within or out of the basal planes. Calculations, though somewhat controversial in certain cases, suggest that the activation energy for self-diffusion (summation of vacancy formation and

migration energy) is smaller for the non-basal plane for Zr with c/a less than ideal value [27, 59, 60]; whereas the vacancy migration is more isotropic for Mg and Co with near ideal c/a ratios.

Two types of divacancies appear stable, including divacancies between the first nearest (FN) neighbors and second nearest (SN) neighbors. When c/a < 1.633, the FN divacancies are out of the basal plane, whereas the SN divacancies are within the basal plane [27]. The divacancies have formation energy of 1.1-3.5 eV, and formation volume of 1.5-1.9 Ω [27]. Among numerous types of migration path, two paths (within or out-of-basal planes) have low energy of migration, 0.45 - 0.75 eV [27]. There are 8 different sites for SIAs in HCP metals, as shown in Fig. 1.1c, including octahedron (O), tetrahedron (T), BO and BT in the basal plane underneath the O and T sites. BC and C are crowdions located halfway between the two nearest neighbor atoms along <11 $\bar{2}$ 0> (on the basal plane) and 1/6 < 20 $\bar{2}$ 3> direction (out of basal plane). BS and S are respective split dumbbells within or orthogonal to the basal plane [27, 59, 60]. In general, the basal split or crowdion is the most stable configuration for HCP metals with a rather large deviation from the ideal *c/a* value, and the non-basal dumbbell (C or S) is the most stable configuration for metals with *c/a* near ideal ratio [27]. The interstitial formation energy in HCP metals is also high, typically 2-6 eV, whereas their migration energy is very low, 0.05-1 eV. The formation volume of interstitials is typically 0.6-1.2 Ω [27].

The major types of defect clusters generated by radiation in HCP metals include vacancy clusters and interstitial loops. A perfect vacancy loop resides on $\{10\bar{1}0\}$ prismatic plane with Burgers vector of 1/3 <11 $\bar{2}$ 0>; and a faulted vacancy loop on (0001) basal plane has Burgers vector of 1/6 <20 $\bar{2}$ 3>. A perfect interstitial loop on $\{10\bar{1}0\}$ plane also has the Burgers vector of

1/3 <11 $\bar{2}$ 0>; and faulted interstitial loops are typically observed on (0001) plane with Burgers vector of 1/6 <20 $\bar{2}$ 3> or 1/2 [0001] [48, 59, 61].

Fig. 1.7 shows selected examples of radiation induced damage in Zr and Mg induced by heavy ions, neutron and e-beams. Heavy ion irradiation induced c-component loops in Zr have been observed (Fig. 1.7a)[62]. The density of c-loops in Zr decreases rapidly when T < 600K. Neutron (Fig. 1.7b) and e-beam (Fig. 1.7c) radiation induce both a-loops and c-loops in Zr [63]. In heavy ion (1 MeV Kr^{2+}) irradiated Mg [64], nearly all basal loops have Burgers vector of 1/6 <20 $\bar{2}$ 3>, and are interstitial loops in nature, whereas prism loops (interstitial and vacancy) have Burgers vector of 1/3 <11 $\bar{2}$ 0> (Fig. 1.7d). Meanwhile neutron irradiation of Mg induces dislocation networks (Fig. 1.7e) [65]. Griffiths [61] showed that e-beam irradiation of Mg (300 K/5 dpa) led to a-type vacancy (A_v,) and interstitial (A_i) loops with Burgers vectors 1/3 <11 $\bar{2}$ 0>, and c-component interstitial loop (C_i) with Burgers vector of 1/6 <20 $\bar{2}$ 3> (Fig. 1.7f).

The relative stability of the dislocation loops in HCP metals generally depends on the c/a ratio (as described below) as well as purity. When c/a < 1.633, {10 $\bar{1}$ 0} prismatic plane is the most closely packed plane, and dislocation loops (prism loop) typically have Burgers vector of 1/3 <11 $\bar{2}$ 0>. When c/a > 1.633, the basal planes are the most closely packed, and dislocation loops (Basal loops) have Burgers vector of 1/6 <20 $\bar{2}$ 3> (or ½ [0001]). In reality, however, the situation under irradiation damage is more complex than that dictated by this simple rule. Exceptions have been reported via both experiment and simulations. For instance, basal plane loops have been observed in Mg [66], Zr [67], Ti [68], in which the c/a ratio is less than the ideal value (1.633). In Zr and Ti, the situation is further complicated by the co-existence of prismatic loops with both vacancy and

interstitial character [63]. When c/a < 1.633. The probability of basal loop nucleation increases with increasing impurity concentration. In Mg, for instance, prism loops with Burgers vector of 1/3<1120> is dominant; whereas in Mg with low purity, basal loops with Burgers vector of 1/6<20 $\bar{2}$ 3> have been observed.

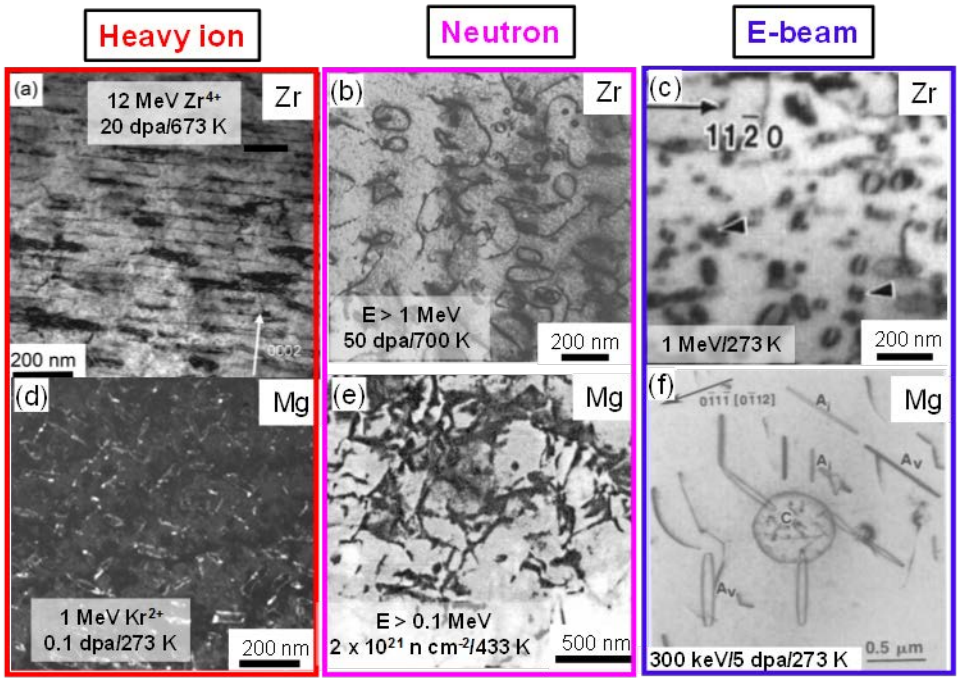

Fig. 1.7. Compilation of TEM micrographs showing radiation damage in HCP Zr and Mg irradiated by heavy ions, neutrons and e-beam. (a) Heavy self-ion irradiation of Zr showing c-component loops [62]. (b) Neutron radiation of Zr introduces a loop and c-loops [63]. (c) E-beam radiation of Zr induces a and c loops [63]. (d) 1 MeV Kr ion (273K/0.1 dpa) radiation of basal Mg foil showing abundant prism loop with Burgers vector of 1/3 <11 $\bar{2}$ 0>[64]. (e) Neutron radiation of Mg induces dislocation networks [65]. (f) E-beam radiation of Mg (300 K/5 dpa) [61]. The a-type loops are vacancy (A_v,) and interstitial (A_i) in character, have Burgers vectors 1/3 <11 $\bar{2}$ 0>, c-component interstitial loop (C_i), has Burgers vector of 1/6 <20 $\bar{2}$ 3>.

1.3. Radiation induced cavities: voids and gas bubbles

Voids and void swelling

Void swelling is a widely observed phenomenon in most neutron and heavy ion irradiated metallic materials [69-73]. Voids can have various geometry, including faceted, rectangles, or spherical shapes. As voids are typically weak mechanically and jeopardize the fracture toughness of irradiated materials, void swelling can post a serious threat to the mechanical and structural integrity of reactor structural materials [69, 71, 74]. The battle against void swelling is manifested by an extensive investigation of void swelling in metals with FCC, BCC and HCP crystal structures and constantly evolving the design of advanced void swelling resistant materials. In this review, we will briefly summarize several instances where void swelling can be significantly reduced or suppressed as shown in Chapter 2 in nanocrystalline materials. Furthermore there are numerous cases where voids are shown to shrink, instead of continuous growth, in irradiated nanotwinned (Chapter 4) or nanoporous (Chapter 5) materials.

Void swelling typically refers to the phenomenon where a prominent volume increase occurs in neutron or heavy ion irradiated materials accompanied with the formation of voids within the microstructure of materials. In certain case, high dose neutron radiation can introduce volume expansion as large as several tens of percent [71, 75, 76]. Void swelling consists of the continuous formation and growth of voids and high concentration of interstitials and their clusters. Fig. 1.8 lists several examples of void swelling in neutron irradiated metals with FCC [3, 77, 78] and BCC [79-81] crystal structures. Voids typically have spherical geometry. Faceted (rectangular) voids have also been observed. It should be noted that heavy ion irradiation typically generates a depth dependent variation of dose, and correspondingly the size and density of voids also vary as a function of radiation depth [82, 83].

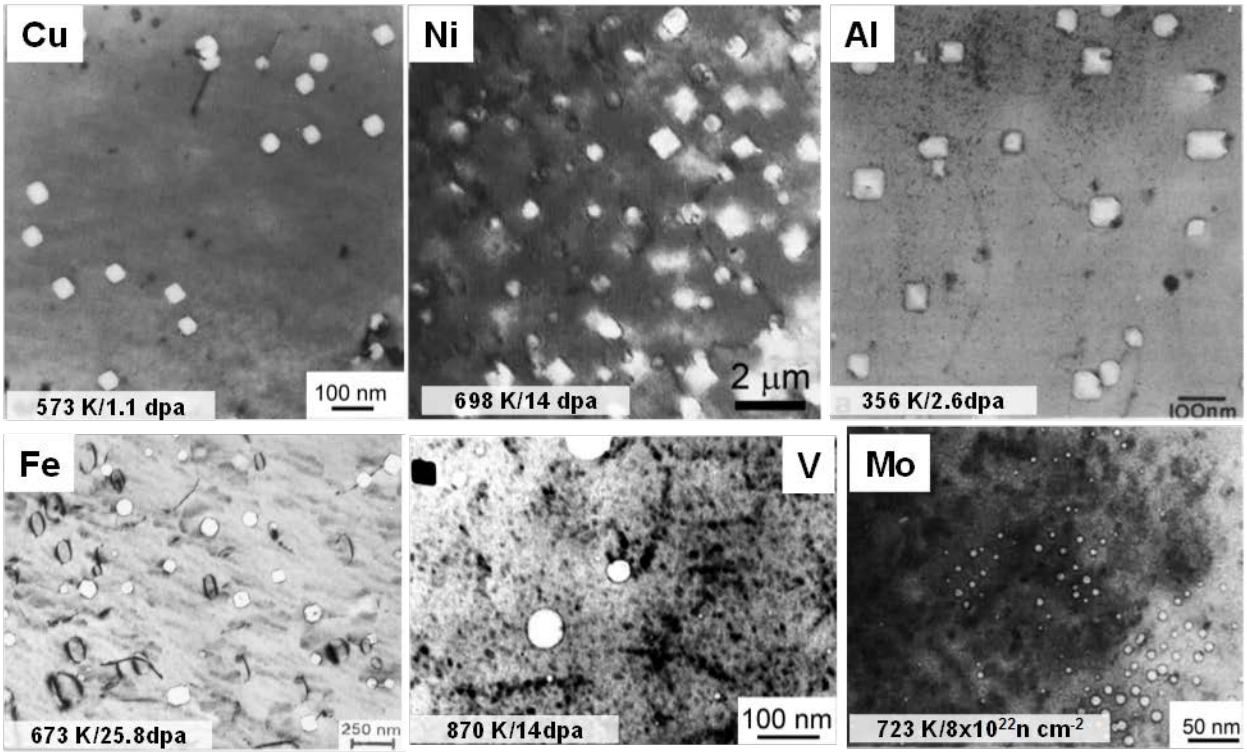

Fig. 1.8. Neutron irradiation induced void swelling in a variety of monolithic metals with FCC [3, 77, 78] and BCC [79-81] crystal structure. Voids with different geometry, spherical or rectangular, are observed.

Void swelling is sensitive to radiation temperature. As shown in Fig. 1.9a where Cu specimens were irradiated at different temperatures, swelling percentage, indicated by density change, can be divided into three phases [3, 84]. Void growth is difficult at temperatures lower than 200℃ (phase 1) due to the poor mobility of point defects. When the temperature is higher than 500℃ (phase 3), defects of opposite types are effectively recombined or trapped by sinks rather than contributing to void growth. Therefore, swelling often occurs at intermediate temperature (phase 2) when the defects are mobile enough, and their density is sufficient to agglomerate into voids, and less likely to be annihilated. Table 1.1 and 1.2 summarize vacancy migration temperature (T_V^M) and peak void swelling temperature (T_S^P) for various metallic

materials with FCC, BCC and HCP crystal structures. Void swelling is usually observed in metals and alloys at the temperatures of 0.3 – 0.5 T_m (where T_m is the melting temperature).

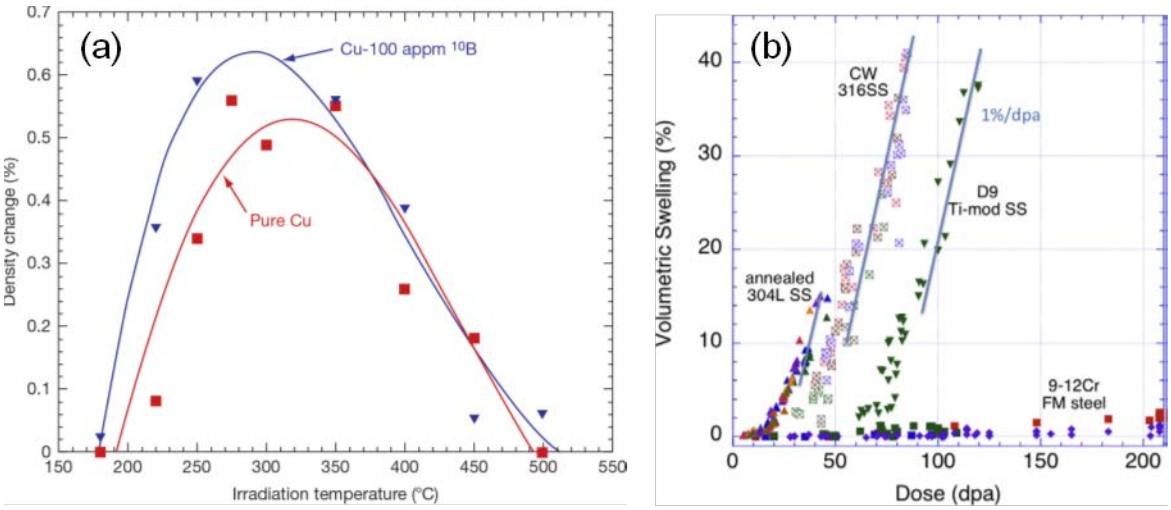

Fig. 1.9. (a) Density change in Cu as a function of irradiation temperature showing temperature dependent void swelling [3, 84]. (b) Swelling curves for numerous austenitic and ferritic/martensitic steels [1, 76, 85-87].

Table 1.1. Peak void swelling temperature T_S^P in FCC metals.

FCC	T_V^M (K) [2]	T_S^P (K)	T_M (K)	T_S^P/T_M	Radiation source
Al	220	423	933	0.45 [88]	Al^+ ions 1100 grade Al
Al	220	No void	933	[89]	Al^+ ions Pure Al (< 0.1 appm impurity)
Al	220	300	933	0.32 [89]	Al^+ ions pre-injected with 10 ppm He
Ag	240	-	1235	-	-
Au	290	-	1337	-	-
Cu	270	600	1358	0.44 [3, 90]	Neutron
Ni	350	780	1728	0.45 [91]	Neutron
		873	1728	0.51 [92]	Ni^+ ions
Pd	350	-	1828	-	-
Pt	350	-	2041	-	-

Note: T_V^M - The temperature at which vacancies are mobile.

Table 1.2. Peak void swelling temperature (T_S^P) in BCC and HCP metals.

BCC	T_S^P (K)	T_M (K)	T_S^P/T$_M$ ref	Source
Fe	630 – 780	1811	0.35 – 0.43 [71, 91]	Neutron
Mo	740 – 870	2896	0.26 – 0.3 [81, 93, 94]	Neutron
Mo	1173	2896	0.41 [95]	Ni^+ ions
Nb	1073 – 1273	2750	0.4 – 0.46 [95, 96]	Ni^+ ions
Ta	900	3290	0.27 [97]	Neutron
Ta	1400	3290	0.43 [98]	Cu^{2+} ions
V	630	2183	0.41 [94]	Neutron
V	973	2183	0.45 [99]	Cu^+ ions
W	1000	3695	0.27 [100]	Neutron
Zr (HCP)	750	2128	0.35 [101]	Electron, pre-injected with 100 appm helium
Zr (HCP)	700 - 740	2128	0.33 – 0.35 [102, 103]	Neutron

Swelling is also dose dependent. As radiation dose increases, swelling curve shows three regimes which are transient swelling, steady state swelling and saturation swelling respectively. Steady state undergoes the largest swelling rate before saturated. It has been reported that the eventual swelling rate of 316SS at all reactor-relevant temperatures is ~1%/dpa [104]. In comparison, the swelling rate of numerous ferritic/martensitic steels is merely 0.2%/dpa as shown in Fig. 1.9b [1, 76, 85-87]. Saturation regime may be applicable to only few materials, and is often not observed in practice because it requires very high dose and most materials usually fail mechanically long before saturation dose.

Void swelling has also been modeled extensively. Phase field modeling tools have been increasingly used to simulate the formation voids. Fig. 1.10a1-a4 shows the simultaneous nucleation and growth of voids in irradiated system supersaturated with vacancies [105]. When the temperature gradient is superimposed in the cascade core, the interstitial concentration gradient is established. Consequently voids may grow and migrate towards the interstitial rich region (Fig.

1.10b) [106]. At a much smaller length scale, MD simulations have been applied to show the influence of dislocation on the formation of voids in irradiated Zr. The dislocations were formed as a consequence of tensile strain (applied concurrently with radiation) [107].

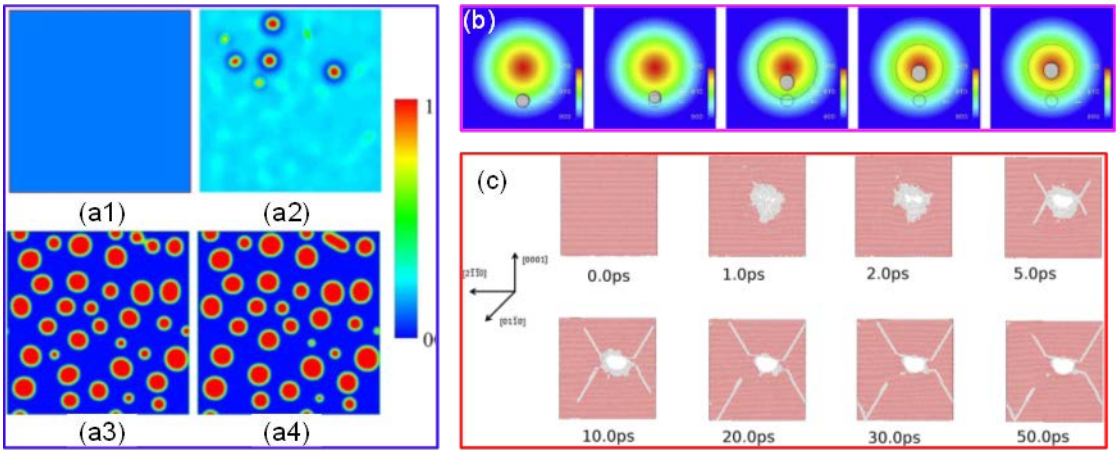

Fig. 1.10. (a) Phase field modeling of void swelling showing the concurrent nucleation and growth of voids with time in a system supersaturated with vacancies [105]. (b) Phase field model studies showing the migration and growth of a void to the interstitial enriched center region [106]. (c) MD simulations showing the formation of voids adjacent to dislocation in Zr subjected to radiation and tension [107].

Helium (He) also plays an important role on void swelling. In general, He bubbles are preferential nucleation sites for voids. The evolution of void diameter with time, *dr/dt*, can be expressed by [108]:

$$\frac{dr}{dt} = -\frac{D_V X_V^e}{r}\exp\left(\frac{2\gamma\Omega}{(r-p)kT}\right) \qquad (1.4),$$

where D_v is the diffusivity of vacancies, X_V^e is the concentration of vacancy at equilibrium, γ is surface energy, p is the He pressure inside cavities, and can be written as [108]

$$p = \frac{3\kappa mkT}{4\pi r^3} \qquad (1.5),$$

where κ is real gas compressibility factor. The solution of dr/dt shows that He bubbles will grow (evolve) into voids when reaches a critical radius (typically several nm), or a critical He concentration.

The influence of He on swelling is complicated. In general, there is an optimum He/dpa ratio for maximum void swelling in metallic materials, depending on the nature of nuclear reactor [109]. Meanwhile although He is attributed to the void swelling in many cases, a higher density of small He bubbles appear to suppress the magnitude of swelling [110]. To some extent, pressurized small He bubbles act as defect sinks for vacancies and interstitials and alleviate void swelling [110]. However, the usage of He bubbles to suppress void swelling may not be a straightforward strategy as He bubbles are known to be nucleation sites for voids; and once He bubbles reach critical radius, they may grow continuously, and lead to significant void swelling. Furthermore, He bubbles may segregate to grain boundaries and lead to He embrittlement and reduction of creep resistance.

Void formation has been observed in most HCP metals, such as neutron irradiated Mg [111], both neutron and electron irradiated Zr [101-103], neutron irradiated Ti [111] and Re [112]. Voids in HCP metals are normally faceted along $\{10\bar{1}1\}$ and (0001) planes and often align in layers parallel to the basal plane, and in many cases, voids are reported to be faceted. For instance, voids formed in Marz-grade Zr during neutron irradiation in DFR at temperatures between 725 and 740 K were faceted along basal, prism, and pyramidal planes [113], and were mostly near grain boundaries.

Radiation induced He bubbles

Radiation damage induced by He ions has been widely investigated in a variety of metallic materials [114]. He is produced in neutron irradiated metallic materials due to the transmutation

during neutron radiation. In numerous reactors, the concentration of He in irradiated metallic materials can achieve a few hundred to thousands of PPM level [108]. Fig. 1.11 compares the formation of He bubbles in a variety of irradiated monolithic metals with FCC [115-117] and BCC [118-120] crystal structures. He bubbles typically appear spherical in these metallic materials. However faceted (hexagonal) He bubbles emerge near grain boundaries in Al (Al matrix composites). The faceted He bubbles may form to minimize surface energy of the cavities [116]. Furthermore, He bubbles form superlattices in He ion irradiated Mo.

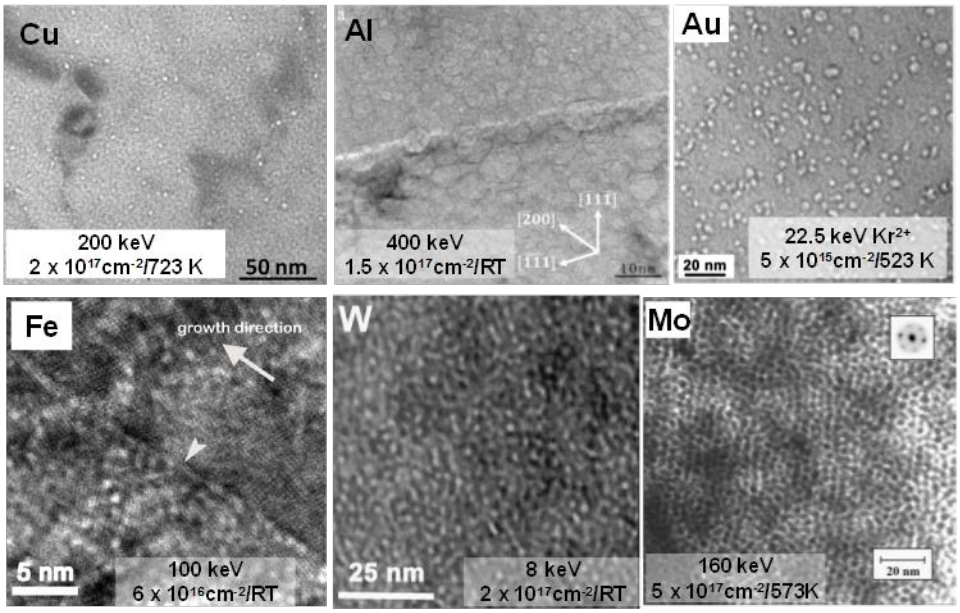

Fig. 1.11. The formation of He bubbles in He ion irradiated FCC [115-117] and BCC [118-120] metals. Note the formation of faceted He bubbles in Al, and superlattice of He bubbles in Mo.

When He/vacancy ratio is high, the pressured He bubbles may lead to lattice expansion as shown in Fig. 1.12a [121]. Interestingly the both lattice expansion (measured from selected area diffraction pattern in cross-sectional TEM studies) and He bubble density reach a peak value at ~ 200-300 nm. The equation of state (EOS) for He has been described by models [52, 122-125]. Mills et al provided a reliable empirical relation (MLB model) (based on experimental results) as follows [126]:

$$V = (22.575 + 0.00646557T - 7.26457T^{-1/2})\, P^{-1/3} + (-12.483 - 0.024549\, T)\, P^{-2/3} + (1.0596 + 0.10604T - 19.641\, T^{-1/2} + 189.84\, T^{-1})\, P^{-1} \quad (1.6),$$

where the molar volume V has the unit of cm^3, the pressure P is in kbar, T is absolute temperature.

The pressurized He bubbles could lead to lattice expansion based on the point source dilatation mechanism [127]. The pressure due to He bubbles is written as:

$$P = \frac{\mu \delta v}{\pi r_0^3} \quad (1.7),$$

where μ is the shear modulus of the metal matrix, and δv is the volume expansion induced by internal pressure, and r_0 is the radius of bubbles. Based on the measured peak lattice expansion in Cu/V 50 nm nanolayers, the pressure inside He bubbles is estimated to be ~ 3.8 GPa. By using the EOS of He, the molar volume of He is estimated to be 6.29 cm^3/mol, or approximately 1.3 He/vacancy in V, and 1.1 He/vacancy in Cu are obtained, in agreement with literature values (1.4 He/vacancy in He bubbles of 4 GPa pressure in V, and 1.0 He/vacancy in He bubbles of 2.8 GPa pressure in Cu [114]). Wolfer has also described the mechanism of tensile stress induced lattice expansion arising from pressurized He bubbles [128]. He bubble induced lattice expansions have been observed in numerous other systems, where the magnitude of lattice expansion is proportional to the He concentration [128, 129]. It is well known that the diameter of measured He bubbles varies as a function of under-focus distance in TEM studies. An example of such study is shown in Fig. 1.12b for He bubbles observed in He ion irradiated Cu/V 50 nm multilayers [130].

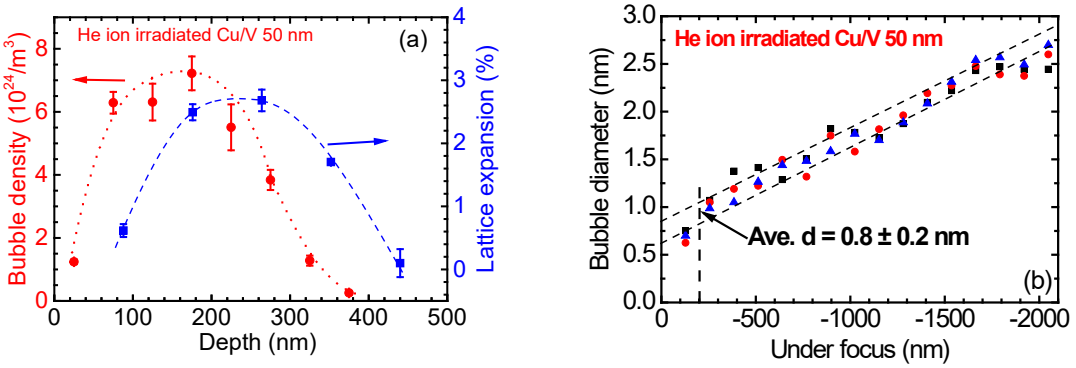

Fig. 1.12. (a) The density of He bubbles in He irradiated (50 keV/6 × 10^{20}/m^2 at room temperature) Cu/V 50 nm multilayers evolves with depth and reaches a maximum at 180 nm from film surface. In parallel, the lattice expansion measured by using selected area diffraction (SAD) pattern from cross-section TEM studies shows a similar trend and reaches a maximum at ~ 280 nm [121]. (b) The determination of He bubble diameter by varying underfocus distance in TEM studies. The average diameter of He bubbles in He ion irradiated Cu/V 50 nm multilayers is ~ 0.8 nm, as determined from the underfocus distance of -200 nm [130].

There are numerous studies that show He can be managed by using a variety of defect sinks, such as phase boundaries (layer interfaces of metal/oxide interfaces as shown in ODS alloys), grain boundaries etc, and He can also be stored in He bubbles [6, 9]. The discussion on the influence of defect sinks on He management is distributed in several succeeding chapters in this review. Furthermore He tends to combine with vacancy and vacancy clusters to form pressurized He bubbles. Additionally He may segregate to the grain boundaries and lead to grain boundary embrittlement, often referred to as He embrittlement [131-133].

1.4. Classical models on sink strength of various types of defect sinks

Forgoing sections describe the nature and types of defects that are generated by irradiations. Extensive studies have been carried out in the past few decades to improve the radiation tolerance of materials. An effective approach is to apply various types of defect sinks.

In general a material is designed by introducing various types of defects, such as grain boundaries, phase boundaries and dislocations. These defects engage and eliminate, to a greater extent, the irradiation induced point defects and defect clusters.

The interaction of various types of defects with defect sinks has been described by using kinetic rate theory. In general the defect-sink reaction rate is estimated, followed by derivation of a sink strength formula.

For vacancy and interstitials, the following equations sustain [134, 135]

$$\frac{\partial C_V}{\partial t} = K_0 - K_{iV} C_i C_V - K_{VS} C_V C_S + \nabla \bullet D_V \nabla C_V \qquad (1.8)$$

$$\frac{\partial C_i}{\partial t} = K_0 - K_{iV} C_i C_V - K_{iS} C_i C_S + \nabla \bullet D_i \nabla C_i \qquad (1.9)$$

Where C_v, C_i are vacancy and interstitial concentration; K_0 is defect production rate; K_{iV} is the vacancy-interstitial recombination rate coefficient; K_{VS} and K_{iS} are the vacancy-sink and interstitial-sink reaction rate coefficient. The reaction rate constants are estimated as follows:

$$K_{iV} = 4\pi r_{iv}(D_i + D_V) \approx 4\pi r_{iv} D_i \qquad (1.10)$$

$$K_{iS} = 4\pi r_{iS} D_i \qquad (1.11)$$

$$K_{VS} = 4\pi r_{VS} D_V \qquad (1.12)$$

Note that the defect absorption rate can be rewritten with the concept of defect sink strength, k^2:

$$K_{jx} C_j C_X = k^2 C_j D_j \,, \qquad (1.13)$$

Where K_{jx} the reaction rate between defect sink (X) and a mobile point defect (j). The sink strength k^2 has a unit of cm^{-2}. The inverse of k represents the average distance (or mean free path, λ) a mobile point defect can travel before being captured by a defect sink. It follows that in

nanostructured materials, λ is limited by the density of defect sinks, and physically could be similar to the value of grain size (d), twin spacing (t) or individual layer thickness (h) as illustrate in the following formula

$$k^{-1} = \lambda = d \text{ or } t \text{ or } h \text{ (distance between defect sinks)} \quad (1.14)$$

Hence to enhance the sink strength, it is critical to scale down the dimension of nanofeatures or increase the density of defect sinks. When considering the defect-GB reaction rate, the steady-state atomic concentration of point defect is given by:

$$D[\frac{d^2c}{dr^2} + \frac{2}{r}\frac{dc}{dr}] + K - Dk_{sc}^2 c = 0 \quad (1.15),$$

and the solution to the formula (assuming that GB is an ideal sink) is written as

$$k_{gb}^2 = \frac{k_{sc}^2[k_{sc}R\coth k_{sc}R - 1]}{[1 + \frac{k_{sc}^2R^2}{3} - k_{sc}R\coth k_{sc}R]} \quad (1.16),$$

When the point defects are lost mostly to GB sinks, then it can be shown that [134, 135]

$$k_{gb}^2 = 15/R^2 \quad (1.17)$$

Note the derivation is based on the cellular model using the average point defect concentration within a grain. When an embedding model is used, the GB sink strength becomes $14.4/R^2$, very close to the value derived using the cellular model. Clearly the smaller the grain size, the greater the sink strength.

Similarly using the cellular model, the sink strength for a void, k_V^2, is described by:

$$k_V^2 = 4\pi a C_V^0 f_c \quad (1.18),$$

$$C_V^0 = \frac{3}{4\pi R_0^3} \quad (1.19),$$

$$f_c = \frac{5(R_c^3 - a^3)^2}{[5R_c^6 - 9aR_c^5 + 5a^3R_c^3 - a^6]} \qquad (1.20).$$

Where a is void radius, R_c is the radius at zero flow condition, that is dc/dr = 0, when r = R_c. To a first approximation, R_c may be estimated as the void-to-void separation distance. $R_0 = R_c - a$; and C_V^0 is the initial volume distribution of voids. Note the sink strength formulas for twin boundaries or layer interfaces have not been derived to date.

1.5. Defect sinks and some general philosophies for alleviation of radiation damage

To date, there is literally no material that is known to be immune to radiation damage beyond several hundreds of dpa level. As stated in the previous sections, all crystalline materials, regardless of their crystal structures (FCC, BCC or HCP), are vulnerable to radiation damage. Although a large number of point defects may recombine immediately after damage cascade, the residual defects that are left uncombined can lead to gradual and substantial accumulation of radiation damage in terms of microstructure evolution. It remains a major challenge to design materials that have significantly enhanced radiation tolerance at high doses.

Zinkle and Snead [136] reviewed several strategies to alleviate radiation damage in irradiated materials. First, metallic materials with BCC structures appear to be more resistant to radiation damage, presumably due to the higher number density, smaller defect clusters generated during cascade in irradiated BCC metals and sessile point defects [48, 136-139]. Second, when either vacancies or interstitials are immobile at the operation temperature, the immobile point defects may facilitate recombination [136]. Third, high sink strength or greater number density of defect sinks.

The adoption of predesigned defects (sinks) to eliminate radiation induced defects, though appears counterintuitive at the beginning, is in fact a very effective approach. Defects in crystalline materials can be characterized by their dimensions, including 0D – point defects, 1D – dislocations, 2D – grain boundaries, phase boundaries and surfaces, and 3D – voids, pores, precipitates and 2nd phase etc. The applications of point defects to alleviate radiation have been mostly implemented through the design of solid solutions or alloys, where solid solution can assist the recombination of defects and reduce radiation damage [6, 140-143]. Dislocation networks have also been used to reduce radiation damage, although dislocations are often considered as biased defect sinks, which may accelerate the formation of voids in certain cases [107]. There are numerous examples that show dislocations, including mobile dislocations, can interact with SFTs and lead to their destruction [144-147]. Other widely used defect sinks include grain boundaries, phase boundaries, voids and He bubbles. Literature data show that a sink strength of $10^{16}/m^2$ may be necessary to curtail void swelling in steels to less than 5% [136]. Such a high sink strength is difficult to achieve in conventional materials. We will show in numerous succeeding chapters that various types of nanomaterials may reach such a high sink strength depending on the prominent size effect.

The influence of point defects and dislocations on radiation induced damage will not be covered in this review. Instead we will focus on the following nanostructured materials (with abundant defect sinks): nanocrystalline materials with fine grains, nanotwinned metals with high density nanotwins, nanolayer composites with small layer thickness, nanoporous materials, nanoparticles (0D) and nanowires (1D) – all with abundant free surfaces. Fig. 1.13 illustrates the application of these defect sinks in various nanostructured materials to alleviate radiation damage.

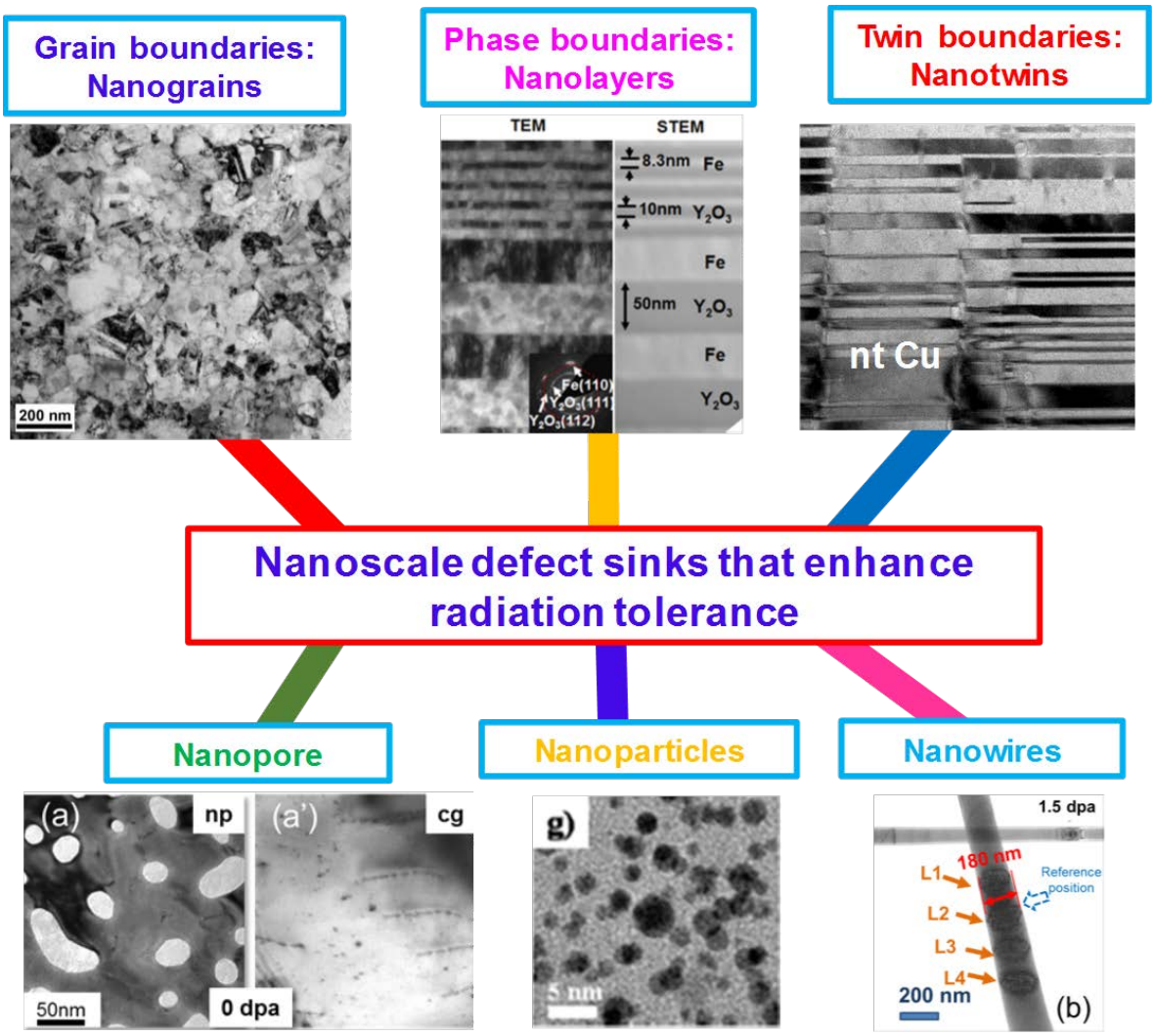

Fig. 1.13. The application of various types of defect sinks to alleviate radiation damage. Defect sinks include dislocations, grain boundaries, twin boundaries, layer interfaces, nanopores, nanoparticle, nanowires and amorphous materials. This review will cover radiation damage in various nanostructured materials, including nanocrystalline materials, nanotwinned metals, nanolayers, nanoporous metals, nanoparticles and nanowires, and amorphous materials.

The review article covers the emerging field (nanomaterials under extreme radiation environments) and emergent needs for the design of superior radiation tolerant nanomaterials. This article highlights what the community has learned to date on the radiation response of various nanomaterials, and points out future directions to move forward. We hope the article can stimulate

broad interest in the field of “nano under radiation” with the ultimate goal to discover new strategies (including nanoengineering) and design novel materials that may enable unprecedented radiation tolerance.

Chapter 2 Radiation Damage in Nanocrystalline Metals and Ceramics

This chapter will examine the methods, observations, and mechanisms associated with radiation response in nanocrystalline (NC) systems. The majority of the work to date is focused on model metal systems, but the limited work in NC metallic alloys and ceramic systems will also be highlighted. This chapter will not cover NC metals or ceramics in which the internal structure is dominated by heterogeneous interfaces such as nanolayered films (Chapter 3), in nanotwinned metals dominated with twin boundaries (Chapter 4), or nanoporous metals with abundant free surface (Chapter 5). In addition, a few previous reviews of note in radiation tolerant materials have included, in part, the studies of radiation tolerance of NC materials. These include the wide sweeping review of irradiation effects on nanomaterials [148], formation of nanostructures by irradiation techniques [149], radiation tolerance of ODS steels [6], radiation and creep response on metals with embedded nanoscale second phases [150], the recent development of accelerator technologies for investigating these systems [151], or the potential for processing radiation tolerant nanomaterials [152].

2.1. Sink strength of grain boundaries

When considering the defect-GB reaction rate, the steady-state atomic concentration of point defect is given by:

$$D[\frac{d^2c}{dr^2}+\frac{2}{r}\frac{dc}{dr}]+K-Dk_{sc}^2c=0 \tag{2.1}$$

and the solution to the formula (assuming that GB is an ideal sink) is written as [135]

$$k_{gb}^2=\frac{k_{sc}^2[k_{sc}R\coth k_{sc}R-1]}{[1+\frac{k_{sc}^2R^2}{3}-k_{sc}R\coth k_{sc}R]} \tag{2.2}$$

When the point defects are lost mostly to GB sinks, and in particular when $k_{sc}R$ is $\rightarrow 0$,

$$k_{gb}^2 = 15 / R^2 \tag{2.3}$$

This scenario works well for nanostructured materials, where a majority of irradiation induced defects are lost to defect sinks, mostly GBs. Note the derivation is based on the cellular model using the average point defect concentration within a grain. When an embedding model is used, the GB sink strength becomes $14.4/R^2$ [135],very close to the value derived using the cellular model. Clearly the smaller the grain size, the greater the sink strength.

We shall see that there is increasing evidence showing prominent size effects through a combination of experiment and MD simulations [26, 148, 152-179]. *In situ* experiments and MD simulations permit direct characterization of the interaction of radiation induced defect clusters with GBs (*i.e.* point defect-sink interactions). However, there are some limitations on the current formula, which will be discussed in the following sections.

2.2. Defect-GB interactions

2.2.1. Experimental observations of defect-GB interactions in NC metals

Recently, there has been a marked increase in research on radiation damage in monolithic NC metals, including Ni [30], Mo[179], W [180] and Fe [118, 181]. Fig. 2.1 shows an example for the absorption of defect cluster by GBs under *in situ* Kr ion irradiation at room temperature [9]. At least two types of absorption events have been identified in this study. First, a mobile dislocation loop in close proximity to high angle GB in NC Ni reduced its diameter gradually from 4.5 to 3.8 nm over 49s, and then migrated towards the GB within 0.1 s over ~ 10 nm (Fig. 2.1a-d)

and was eliminated by the GB. In a second case, a dislocation segment consisted a string of dislocation loops was gradually absorbed by GBs (Fig. 2.1a'-d') over 78 s.

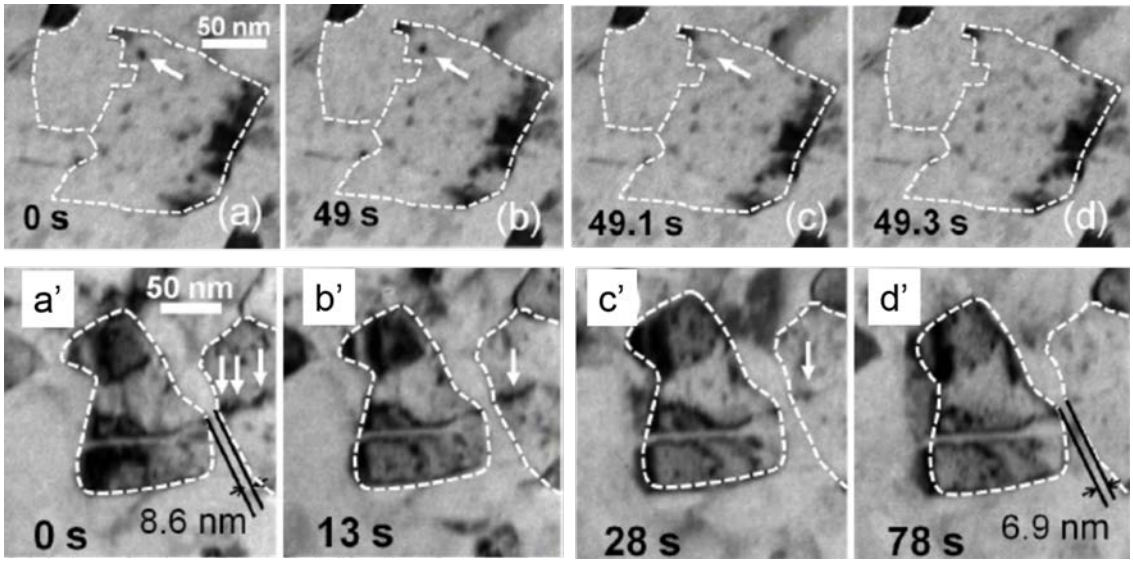

Fig. 2.1. (a-c) *In situ* evidence of absorption of individual loop by grain boundaries (GBs) of NC Ni. The radiation dose increased from 1.67 to 1.72 dpa within 49.3 s. (a) The loop, pointed by an arrow, was revealed near a grain boundary. (b) In 49 s, the loop diffused towards the grain boundary accompanied by the continuous reduction of diameter. (c) By 49.1 s, the loop rapidly migrated toward the GB. (d) By 49.3 s, the loop was fully absorbed and annihilated by the GB. (a'-c') Absorption of dislocation segment by GB. (a') Three discernible dislocation loops were formed near the GB. (b') by 13s, the individual loops form one dislocation segment. (c') By 28 s, the dislocation segment was absorbed continuously by the adjacent GB. (d') By 78 s, a majority of the dislocation segment was absorbed by GB. [30].

2.2.2. MD simulations showing defect absorption/capture by GBs.

The role of GBs in alleviation of radiation damage becomes significant when the distance between GBs with adequate and enduring sink strength approaches the mean free path of the SIAs and vacancies created during the cascade events. MD simulations can be utilized to examine the effect of GB character and structure on radiation tolerance at atomistic levels that are extremely difficult to accomplish if not impossible during radiation experiments. An MD in Fig. 2.2 on self-ion irradiated NC Ni shows that GBs act as effective defect sinks for interstitials [182]. One of the

major advantages of utilizing MD simulations is to determine the underlying physical mechanisms with ps resolution or better. Another mechanism showing the role of GBs on the absorption of defects is the interstitial emission model presented by Bai *et al.* in Fig. 2.3 and Fig. 2.4 [183]. Interstitials migrate towards GBs faster than vacancies, leaving behind vacancies, which can subsequently form cluster and thus modify the formation and migration options for subsequent defects in the same vicinity (Fig. 2.3). As shown in Fig. 2.4, point defects including interstitials and vacancies clusters tend to form in or near the GBs compared to the grain interior. Interestingly, this MD study predicted diffusion becomes easier in the interstitial-loaded GB when compared to a pristine boundary with no initial defects [183]. Self-healing has also observed by simulations near GBs in irradiated Cu[164]. With this concept in mind, one can imagine the potential for designing enhanced radiation tolerant materials utilizing a range of nanostructured metals in general. A nice review of the potential for the fabrication of radiation tolerant nanomaterials was presented previously by Beyerlein *et al.* [152] and will not be reviewed further here.

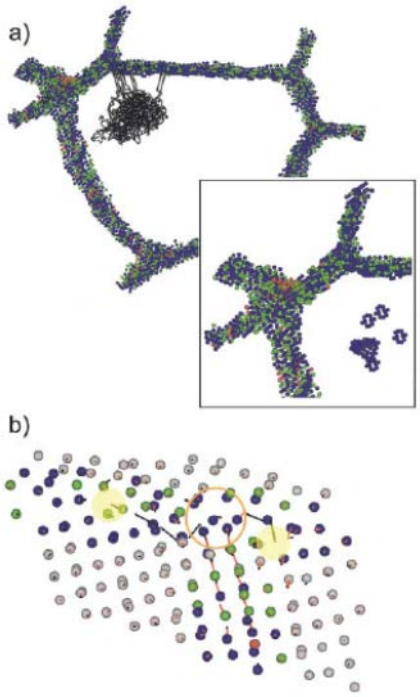

Fig. 2.2. (a) Selected area of the 12 nm NC Ni grain, the GB atoms and the displacement vector (> 1.5 Å) between the atoms due to a 5 keV primary knock on (PKA). The insert shows a magnified view of the defect region after cooling down. (b) An example of the GB acting as an interstitial sink, by the annihilation of interstitials with free volume in the GB [182].

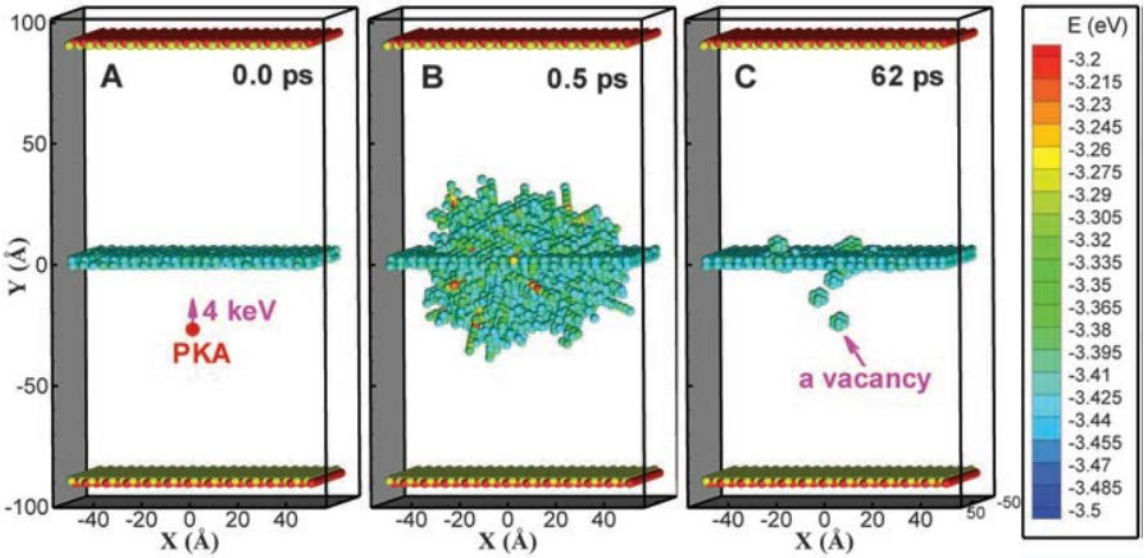

Fig. 2.3. Representative snapshots of a MD simulation of a collision cascade near a Σ11 symmetric tilt GB at 300 K in Cu. The atoms are colored by their potential energy; atoms with energies less

than 3.43 eV are treated as nondefective and are not shown. The top and bottom layers are fixed surfaces. (A) Initially, a 4-keV PKA is initiated at 25 Å below the GB with its velocity directed perpendicularly toward the GB. (B) After 0.5 ps, the cascade reaches its maximum size. (C) After 62 ps, the cascade cools down with some vacancies remaining below and above the GB. In this display scheme, a vacancy is characterized as a 12-atom cluster, as indicated in (C), because of the increase in energy of the 12 nearest neighboring atoms of the vacancy [183].

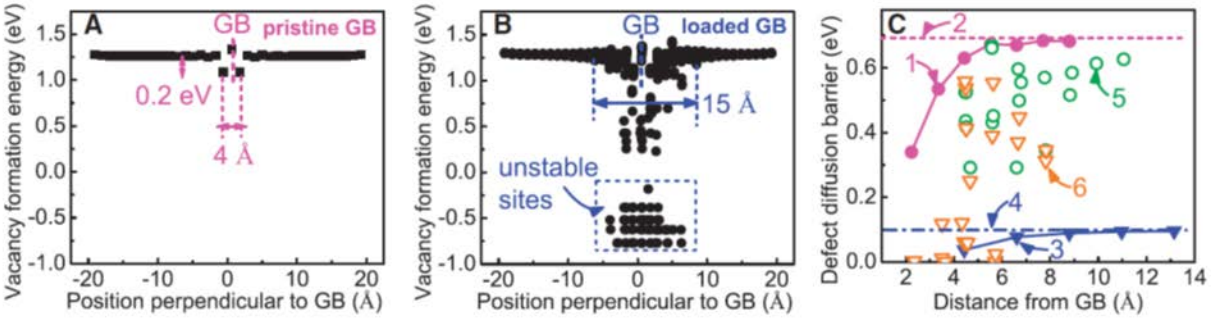

Fig. 2.4. Influence of interstitial loading on defect properties near the symmetric ∑11 GB in Cu. (A) Vacancy formation energy profile of a pristine GB. (B) Vacancy formation energy profile of a GB loaded with 10 interstitials, representing the situation occurring after a collision cascade. (C) Defect diffusion barriers as a function of distance from a pristine and an interstitial-loaded GB. Number 1-6 represents vacancy diffusion barriers near the pristine GB, vacancy diffusion barrier in the bulk, interstitial diffusion barriers near the pristine GB, interstitial diffusion barrier in the bulk, vacancy diffusion barriers near the interstitial-loaded GB and interstitial emission barriers near the interstitial-loaded GB, respectively [183].

Similarly, it was shown in the MD simulation of Chen *et al.*, Fig. 2.5, that the mechanism by which the cascade damage is absorbed by the boundary depends on the local GB structure [184]. In this work, two mechanisms, bulk chain-like (BC) absorption or GB chain-like (GBC) absorption are shown to work independently or simultaneously to eliminate the radiation induced damage. It is shown in this model that the mechanism of defect annihilation is dependent on the local structure of the GB present in the model alpha-Fe system [184].

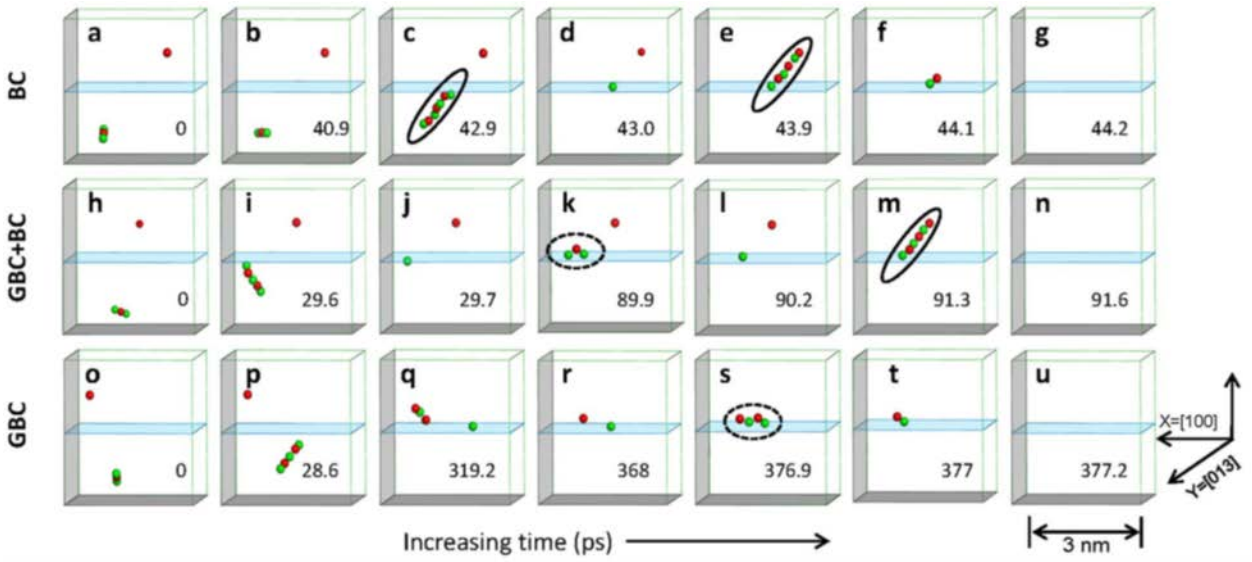

Fig. 2.5. Representative snapshots of an MD simulation of three different defect annihilation processes for (013) [100]S Σ=5 symmetric title GB in BCC Fe. All simulations start with one bulk vacancy and one bulk dumbbell defect close to a GB. (a–g) The process involving BC defect for annihilation: A BC defect is created at time t=5 42.9 ps to transport an interstitial to the boundary and then another BC defect is created t=543.9 ps to annihilate a bulk vacancy. (h–n) The process involving GBC defect for boundary migration and BC defect for annihilation: A GBC defect is created at t=589.9 ps to move a boundary trapped interstitial, and then a BC defect is created at t=591.3 ps to annihilate a bulk vacancy. (o–u) The process involving GBC defect for annihilation on the boundary: A GBC defect is created at t=5 376.9 ps to annihilate a defect pair separated and trapped on the boundary. The boundary is represented with a blue shadowed plane. The green balls refer to interstitial and red balls refer to vacancy. The solid circles refer to BC defects and dash circles refer to GC defects [184].

2.3. Size effect on radiation tolerance

The concept that decreasing grain size to enhance radiation tolerance has been around for several decades, as is highlighted in the early work by B.N Singh looking at the role of grain GBs on the effect of void formation [185]. Ever since then there have been increasing studies on the irradiation tolerance of fine grained materials [135, 170, 186-193].Rose *et al.* evaluated the role of grain size on Kr ion irradiated Pd [194] and show decreasing defect cluster density at smaller grain sizes (Fig. 2.6a). Similarly, an *in situ* Kr ion irradiation study shows a lower density of defect clusters in NC Ni than that in coarse-grained (CG) Ni (Fig. 2.6b). In another study, the evolution

of microstructure in He ion irradiated (100 keV/RT/6×10^{20} ions/m^2) CG Fe-14Cr-16Ni is compared to that of ultra-fine grained (UFG) specimens processed by severe plastic deformation [195]. Under-focused XTEM micrographs (Fig. 2.7a1-a3) of as-received, CG Fe-Cr-Ni alloy show abundant He bubbles, some of which decorate the GBs, and evidence of dislocation loops induced by displacement damage. In comparison, the irradiated UFG Fe-Cr-Ni alloy has a lower He bubble density and no clear evidence of dislocation loops (Fig. 2.7b1-b3). Both peak and average bubble density of UFG alloy are lower than those in CG counterpart (Fig. 2.7c). The magnitude of hardening in UFG alloy, probed by nanoindentation (Fig. 2.7d), is much lower than those in CG specimen at various depth.

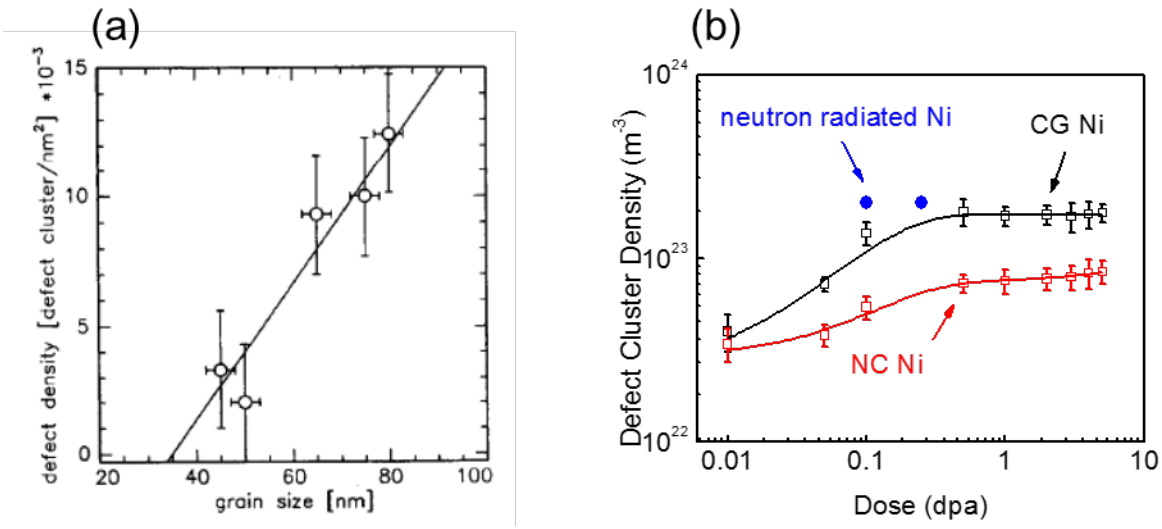

Fig. 2.6 (a) Defect densities vs. grain size on the irradiated Pd under Kr ion irradiation with energy of 240 keV to a fluence of 2×10^{16} ions/cm^2 [194]. (b) The density of dislocation loops of CG Ni increased rapidly within 0.1 dpa and appeared to reach saturation at ~ 0.5 dpa. Meanwhile the density of loops in NC Ni increased slowly and gradually throughout the radiation up to 5 dpa. At 5 dpa, the average loop density of CG Ni is 2 times greater than that of NC Ni[30].

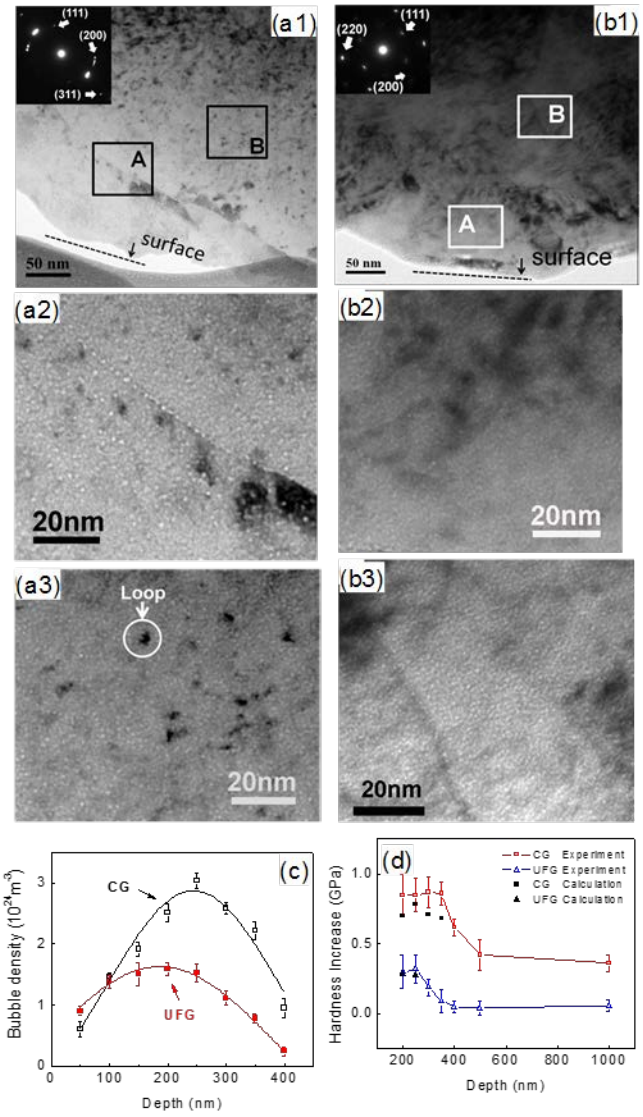

Fig. 2.7. Comparison of microstructure and radiation hardening in He ion irradiated UFG Fe-14Cr-16Ni alloys (100 keV He ions/RT/6×10^{20} ions/m^2)) [195]. (a1) Under focused XTEM micrograph of He ion irradiated CG Fe-Cr-Ni alloy. (a2) The magnified image of region A shows bubbles align along grain boundaries. (a3) The magnified image of region B shows dislocation loops and high density of He bubbles. (b1-b3) Under focused XTEM micrograph of He ion irradiated UFG Fe-Cr-Ni alloy. Magnified image of region B shows bubbles, but dislocation loops are not detected. (c) Depth dependent He bubble density in He irradiated CG and UFG Fe-Cr-Ni alloy. Both the peak and average He bubble density are reduced in the UFG alloy. (d) Hardness increase ($H_{\text{after irradiation}}$-$H_{\text{before irradiation}}$) of CG and UFG Fe-Cr-Ni alloy after He ion irradiation as a function of indentation depth. The measured radiation hardening in CG and UFG Fe-Cr-Ni alloy is indicated by open squares and triangles, respectively. The calculated radiation hardening in the peak damage region is shown by solid squares and triangles. In the CG alloy, both He bubbles and dislocation loops result in hardening, whereas hardening in the UFG alloy arises mainly from He bubbles[195].

In addition to monolithic NC metals, the role of grain size has also been investigated to a limited extent for NC and UFG commercially relevant alloys, including low carbon steel [192] and 304L stainless steel (SS) [83]. In the 304L SS study, GB engineering via equal channel angular pressing (ECAP) was used to refine the grain size of the alloy without significant change in the phase distribution. The resulting fine grained microstructure significantly decreases void density compared to CG counterparts when irradiated by 3.5 MeV Fe to tens of dpa, as shown in Fig. 2.8 [83].

A similar study by Song *et al.* looked at reactor relevant T91 alloy under Fe irradiation and found that the swelling rate was three times lower in an UFG microstructure (320 nm average grain size) produced by ECAP than a CG microstructure (2 μm average grain size) [82]. It is a bit surprising that the relatively small change in average grain size well above the interaction volume of the cascade event dimensions would decrease the swelling of the sample by a factor of three. Another interesting topic brought up in this study is the comparison of ion irradiation damage to neutron damage [82]. A full comparison of these radiation environments and the microstructural evolution resulting from each ion source is beyond the scope of this review, but greater information on this important topic can be found in references [196-198].

Fe ion irradiation experiments were also performed on NC 316 SS with an average grain size of 40 nm achieved by high pressure torsion (HPT) experiment. Annealing at 350 ºC for 24 hours has no influence on the grain size whereas the average grain size increased to 60 nm under irradiation with 160 keV iron ions at 350 ºC, suggesting radiation enhanced grain growth (discussed in detail in Section 2.5). Atom probe tomography shows the GBs are enriched in nickel and silicon and depleted in chromium, no intragranular extended defects or precipitates were formed under irradiation in NC 316 SS [191].

Fig. 2.9a-c show one of the limited studies that not only compares the dislocation loop diameter and bubble diameter as a function of grain size, but also the hardness of the irradiated BCC Mo with average grain sizes varying from several nm to microns [179]. The density and size of the radiation induced defects, as well as radiation induced hardening decrease with the reduction of average grain size. Fig. 2.10 compared the void swelling between CG and UFG 304L SS under Fe ion irradiation. The transient swelling period of swelling curve was delayed in UFG 304L SS, and the UFG grains clearly suppress the magnitude of void swelling significantly [199].

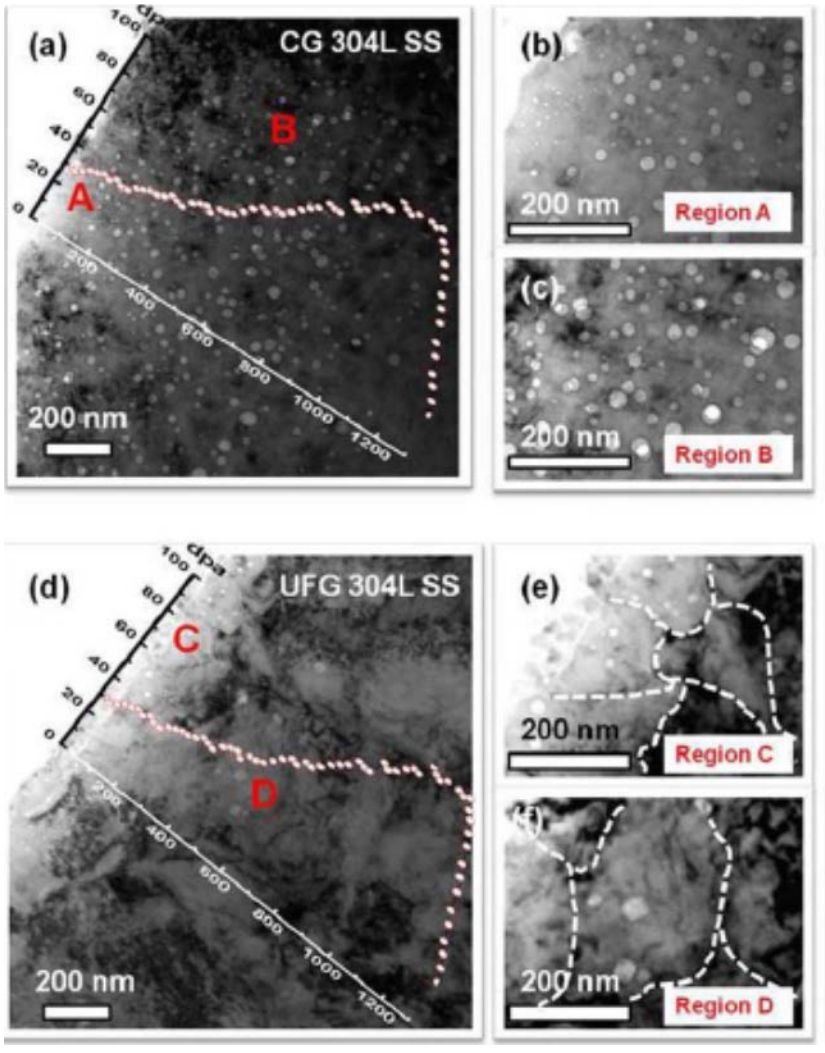

Fig. 2.8. Extraordinary void swelling resistance of UFG 304L SS subjected to Fe ion irradiation at ion energy of 3.5 MeV and a total fluence of 6 $\times 10^{20}$ ions/m^2 at 500ºC by defocusing the ion beam. (a) Panoramic cross-section TEM micrograph of Fe ion irradiated CG 304L SS showing

a large number of voids. (b) The magnified TEM image of region A in (a) shows high-density small voids near the surface of irradiated CG 304L SS. (c) In region B of the same specimen, at a depth of 500 nm from surface, high-density large voids were observed. (d) Cross-section TEM overview of irradiated UFG 304L SS showing much less voids. (e) The magnified TEM image of surface region E in irradiated UFG 304L SS shows numerous faceted voids distributed primarily along GBs. (f) Magnified TEM micrograph of region D in (d),~ 500 nm from surface shows much lower void density compared to that in irradiated CG counterpart [83].

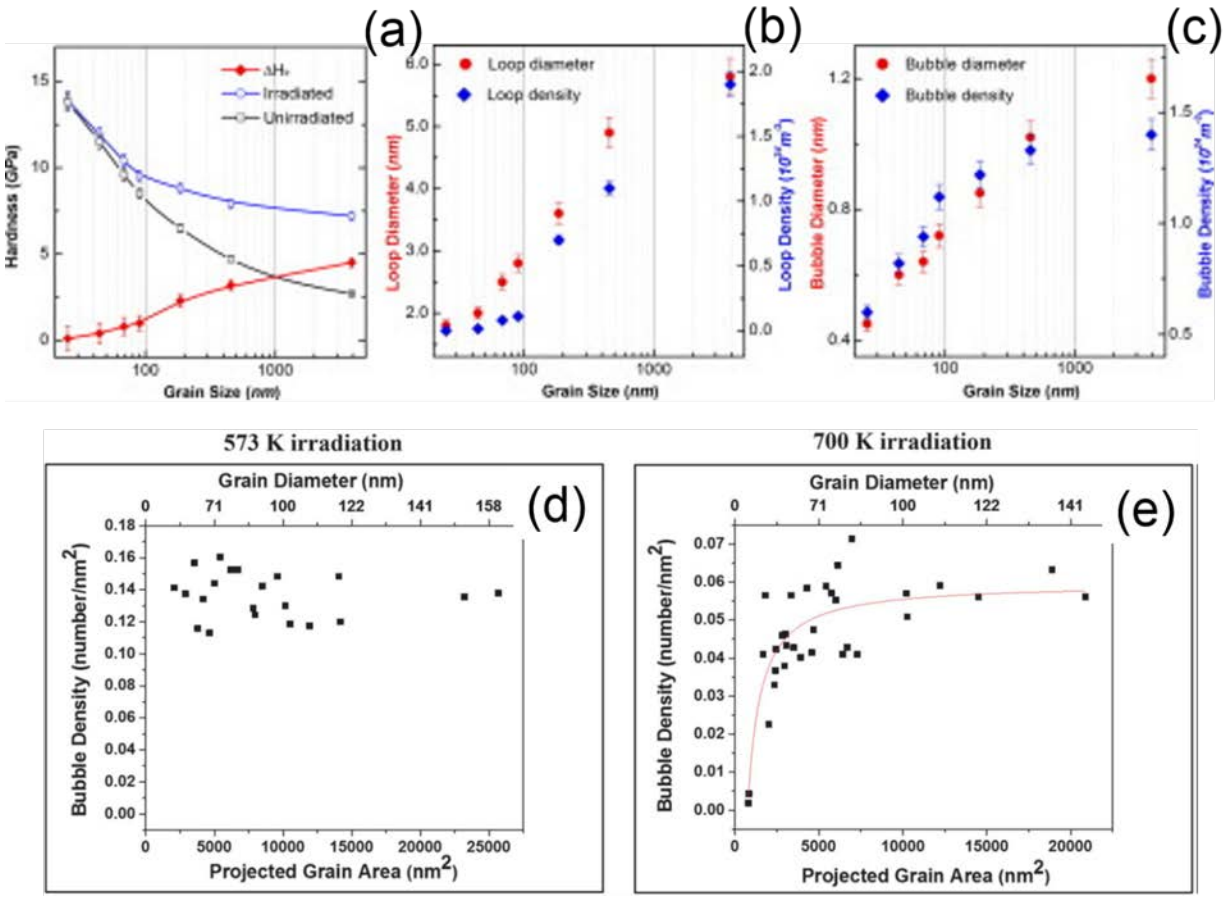

Fig. 2.9 (a-c) He ion irradiation of BCC Mo. (a) Grain size effect on the hardening behavior of BCC Mo before and after He ion irradiation. (b, c) Distribution of size and density of irradiation-induced He bubbles and dislocation loops in BCC Mo samples after irradiation, respectively [179]. (d-e) Areal bubble density (number/nm^2) vs. grain size (area) for 10 keV helium irradiation on nanocrystalline iron at (d) 573 and (e) 700 K. Red fitting in (e) demonstrates the trend in density change[181].

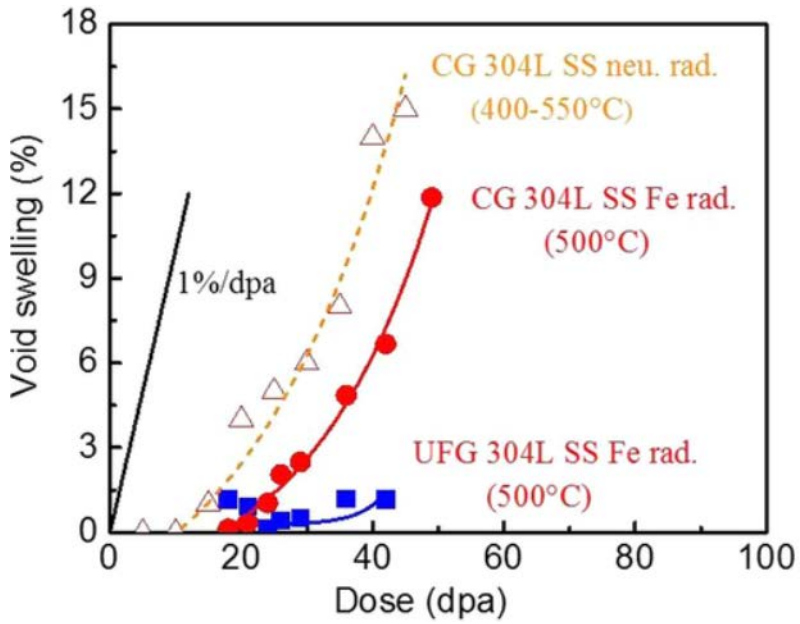

Fig. 2.10 Comparison of void swelling of Fe ion irradiated coarse-grained and ultrafine grained 304L SS with data on neutron irradiated 304L SS. In this Fig. all data for each variant were derived from one irradiation and each individual data point is derived from a ~100 nm depth increment plotted vs. the SRIM-calculated average dpa level for that increment with displacement energy of 40 eV[199].

Temperature plays an important role on radiation resistance of metallic materials. However the influence of irradiation temperature on irradiation tolerance of NC metals is a subject that is less well understood. As shown in Fig. 2.9d-e, the He bubble density in NC Fe is lower at 700K than that at 500K. Also grain size appears to have little influence on He bubble density in NC Fe irradiated at 500K, whereas smaller grains lead to lower He bubble density at 700K. The magnitude of swelling in NC Fe was estimated to be 0.63% (independent of grain sizes) at 500K, vs. 0.0096 to 0.98% (grain size dependent) for NC Fe irradiated at 700K. It is likely that small He-vacancy clusters are mobile at 700K, promoting their coalescence and or elimination of defect clusters at GBs [181]. It remains unclear why there is a lack of size effect on defect density in NC Fe irradiated at 500K.

The range of radiation conditions (ion species, energy, fluence, and flux) for a majority of investigated NC alloys are listed in Table 2.1. These studies have generally shown that the radiation induced defect size and density decrease with decreasing grain sizes to the UFG and NC regime. These studies consider a range of radiation environments produced by linear accelerators ranging from He ion implantation [180, 181] to heavy ion irradiation [30, 180]. Even within the heavy ion irradiation experiments, the choice of ion mass and energy was found to be important in the kinetics of the defect formation [180]. An important note regarding these scientific studies reviewed here is that the radiation tolerance is rarely measured from the subsequent effects on the variations of structural dimension (swelling), mechanical properties (yield strength), corrosion properties (corrosion rate), or other material properties of interest to nuclear industry. In contrast, a majority of these studies presented have investigated the size, density, and type of nanoscale radiation defects as a function of radiation condition. Although these microstructural investigations permit a fundamental understanding on the irradiation response of NC materials and are important for accurate model development, more studies are necessary to investigate the influence of radiation on the evolution of material properties needed for industrial implementation. Furthermore there is a need to perform systematic studies on irradiation response of NC metals and alloys under various radiation conditions. Neutron radiation studies on NC metals and alloys remain a wide empty area.

Table 2.1 Selected published results of radiation damage in NC and UFG metals.

Material	Sample crystallography	Initial Grain Size (nm)	Radiated Particle	Particle Energy (MeV)	Fluence (ion/cm^2 or dpa when noted)	Flux (ion/cm^2/s or dpa/s when noted)	Final grain size (nm)	Ref.

Au	FCC	10-15	Ar	0.5	5E14, 2E15	0.012 dpa/s	NA	[200]
Au	FCC	10-200	Si	10	2.70E+15	6.60E+11	10-275	[201]
Pt	FCC	10-15	Ar	0.5	5E14, 2E15	0.013 dpa/s	NA	[200]
Pt	FCC	10-15	Kr	1	5E14, 2E15	0.018 dpa/s	no change	[200]
Pd	FCC	10-300	Kr	4	NA	9.00E+12	40-80	[194]
Pd	FCC	10	Kr^+	4	1E17 to 6E17	NR	NA	[194]
Porous Pd (20%)	FCC	10-80	Kr	0.24	170-210 dpa	NR	NA	[148]
Mo	BCC	25-455	He	0.2	1.40E+17	NR	NA	[179]
Zr	HCP	10-15	Kr	0.5	5E14, 2E15	0.021 dpa/s	NA	[200]
Cu	FCC	10-15	Kr	0.5	5E14, 2E15	0.023 dpa/s	NA	[200]
Cu-0.5Al2O3	FCC	180	H	0.59	0.91 dpa	NR	495	[148]
Cu-0.5A2O3	FCC	178	H^+	590	0.91 dpa	1.5E-06 dpa/s	493	[190]
Ti49.4Ni50.6	metal alloy	23	Ar^+	1.5	5.6 dpa	6.40E+12	NA	[193]
Fe	BCC	49	He	0.1	6E20	NR	96	[181]
304L SS	FCC	100	Fe	3.5	6E20	0.003 dpa/s	200	[83]
Austenitic Steel (316 SS)	FCC	40	Fe	0.16	10 dpa	NR	NA	[148]

Fe-14Cr-16Ni	metal alloy	400	He	0.1	6E16	NR	400	[195]
T91	Metal alloy	320	Fe	3.5	9E16	NR	NA	[82]
Ferritic Steels 14YWT	BCC	500, 1,000	n	>0.1	1.2 - 1.6 dpa	NR	NA	[148]
Low-C Steel	BCC	350	n	NA	1.15E-3 dpa	1.6E-9 dpa/s	360	[192]
CrN Steel SUS316L + 1%TiC	FCC	100 to 50,000	n	>1	1.14E19 - 1.14E20	NR	NA	[148]
Ni	FCC	55	Kr+	1	5	0.003 dpa/s	62	[30]
Ni	FCC	115	H^+	590	0.56 dpa	1.5E-06 dpa/s	38	[190]
Ni	FCC	15-150	He^+	0.01	2E16, 8E16	10^13	no change	[202]
Ni	FCC	6 to 20,000	n	>1	1.14E19 - 1.14E20	NR	NA	[148]
ED Ni	FCC	20-30	Ni	0.84	5 dpa	NR	no change	[148]
SPD Ni	FCC	115	H	0.59	0.56 dpa	NR	38	[148]
Ni	FCC	15-150	Ni^{3+}	3	5.4E14, 2.7E14	1.50E+11	no change	[202]
PLD Ni	FCC and HCP phases	FCC: 13.9 (HCP: 8)	Ni^{6+}	35	3.00E+14	NR	HCP: 14, FCC: 17.4	[156]
Ni-W	metal alloy	6 to 20,000	n	>1	1.14E19 - 1.14E20	NR	NA	[148]

W	BCC	60-400	Si^{2+}	3	6.20E+14	3.40E+11	NA	[180]
W	BCC	60-400	W^{4+}	3	3.30E+14	1.80E+11	NA	[180]
W	BCC	60-400	Cu^{3+}	3	5.80E+14	1.40E+11	NA	[180]
W with (0.25-0.8)% TiC	BCC	50-200	He	3	2.00E+23	NR	NA	[148]

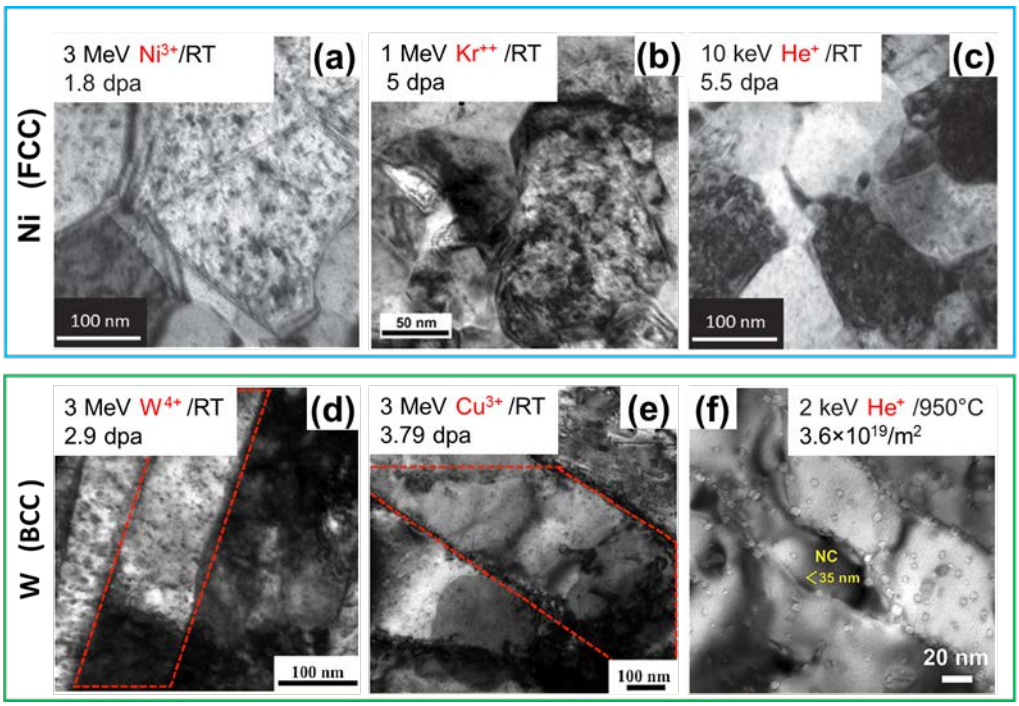

Fig. 2.11. The microstructure evolution of NC Ni irradiated by (a) Ni ions [202] (b) Kr ions [30], are similar in term of defect size and density even though the maximum irradiation doses are different, 1.8 dpa for Ni ions and 5 dpa for Kr ions. (c) He ion irradiation of NC Ni [202]. (d-e) NC W subjected to self-ion irradiation (2.9 dpa) and Cu ion irradiation (3.79 dpa) showing small dislocation loops with but with somewhat lower defect density as compared to heavy ion irradiation [180]. (f) He ion irradiation led to the formation of He bubles [165].

In comparison to radiation studies on NC metallic materials, there are limited research studies on irradiation response of nonmetallic NC systems. This can be seen in the visual comparison between Table 2.1 (review of nanocrystalline metals) and Table 2.2 (review of nanocrystalline ceramics). As shown in Table 2.2, a wide range of irradiation conditions and ceramic chemistry and crystallography have been investigated in NC ceramics. Although it is difficult to draw conclusions on the role of ceramic chemistry and crystallography on the irradiation tolerance of NC ceramics, many interesting observations have been made from the limited studies.

Table 2.2 A summary of studies on irradiation damage in nanocrystalline ceramic.

Material	Initial Grain Size (nm)	Radiated Particle	Particle Energy (MeV)	Fluence (ion/cm2 or dpa when noted)	Ref.
Zirconia	7.7	Au	2	1.00E+16	[203]
Ceria	6	Au	3	<=2E16	[204]
Ceria	NA	Au	3	0.3 dpa	[205]
ZrN	9, 31	Fe^{2+}	0.9	6.00E+15	[206]
TiN	8-100	He	0.012, 0.035	4E8, 1E9	[207]
Porous VN_x	5-50	He	0.02	1.20E+09	[208]
Porous CrN_x	5-50	He	0.02	1.00E+13	[208]

$MgGa_2O_4$	4-12	Kr	0.3	12-96 dpa	[209]
Porous ZrO_2	10-300	Kr	4	3-8 dpa	[194, 210]
ZrO_2	10-300	Kr	4	NA	[194, 210]
Pyrochlore	17	Kr^+	1	1.875E14, 7.5E14, 2.5E15, 6.25E14	[211]
Porous α-SiC	36	Xe	95	8 dpa	[212]
ZrO_2 in a-SiO_2	3	Xe	1	0.3-0.9 dpa	[213]

An earlier study by Wang *et al* has shown that NC TiN demonstrated enhanced irradiation tolerance [207]. Similar effects have later been reported in Ceria and Zirconia by Weber and coworkers [203-205]. Grain growth from an average diameter of 7 nm to approximately 30 nm, similar to that reported in NC metals, was clearly demonstrated in NC zirconia after 35 dpa of irradiation by 2 MeV Au beam [203]. MD simulation in conjunction with experimental observations suggested disorder based mechanisms driving the grain growth in nanostructured ceramics [205]. Jiao *et al.* also reported a decrease in the density of the irradiation induced defects in ZrN as a function of grain size, as shown in TEM characterizations in Fig. 2.12 [206]. Initial studies by Shen *et al.* have shown enhanced irradiation tolerance is not limited to NC nitrides. In NC $MgGa_2O_4$ irradiated by 300 keV Kr ions, a significant decrease in displacement damage relative to the single crystal counterpart was observed [209]. Amorphization occurs in single crystal specimens, whereas NC specimen shows little indication of amorphization as shown in Fig.

2.13. Similar phenomenon was observed via *in situ* Kr ion irradiation studies of $CePO_4$ nanocrystals [214].

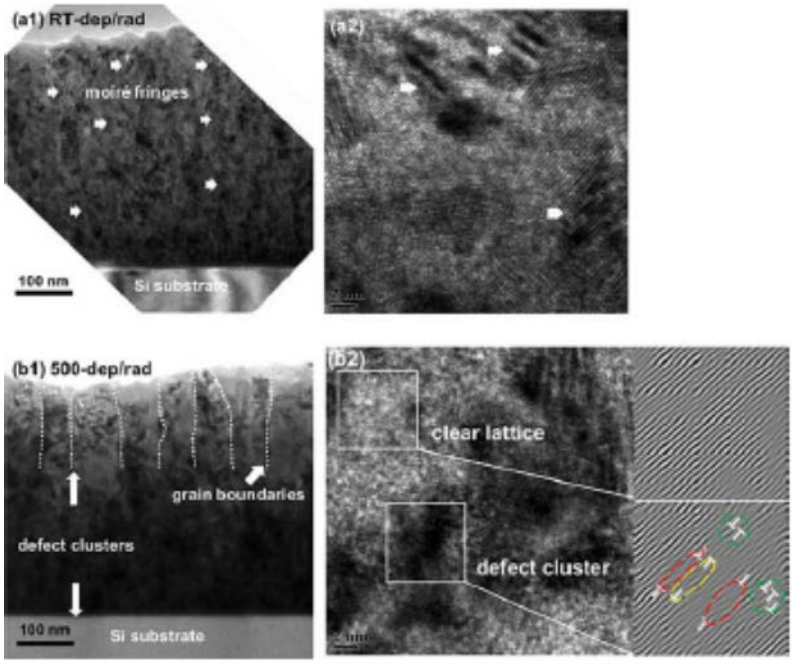

Fig. 2.12. (a1) Bright field TEM image of irradiated NC ZrN film. (a2) HRTEM of the irradiated NC ZrN film shows low density of defect clusters. (b1-b2) TEM and HRTEM image of larger-grained ZrN film. A high density of defect clusters were formed inside grains [206].

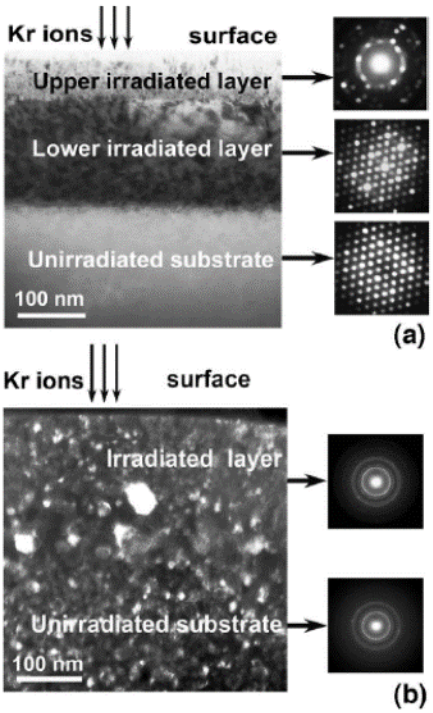

Fig. 2.13. Cross-sectional TEM images and corresponding diffraction patterns obtained from irradiated polycrystalline $MgGa_2O_4$ samples. a) CG $MgGa_2O_4$ irradiated to a dose of 12 dpa. Selected diffraction pattern shows that amorphization occurs in the upper irradiated region of the specimen, whereas the lower and unirradiated regions remain single crystal. b) NC $MgGa_2O_4$ specimen irradiated to a dose of 96 dpa remain its NC characteristics, with little indication of amorphization [209].

However, size effect on radiation damage in NC ceramics is a very complex subject, as the propensity to amorphization, phase transformation, and other microstructural evolution may take precedence prior to any benefit provided by the numerous defect sinks in these NC ceramics [215, 216]. The chemistry and atomic arrangement in oxides can be complex and the heat treatment of NC structure may alter the atomic structure to some extent as is exemplified in the work by Zhang *et al.* in pyrochlore $Gd_2(Ti_{0.65}Zr_{0.35})_2O_7$ [211]. The interplay between damage, grain size, and annealing temperature needed for phase change can be seen in Fig. 2.14. As grain size is less than 100 nm, the critical dose for amorphization of $Gd_2(Ti_{0.65}Zr_{0.35})_2O_7$ increases rapidly to ~ 2 dpa. Whereas for the same material with an average grain size of 100-400 nm, there is little variation

in amorphization dose, ~ 0.73 dpa. Furthermore, during the coarsening of grain size at high annealing temperature, the occupancy of Gd in 16c position changes from 0.57 to 0.8, making the interpretation of size effect on radiation damage more complicated. In general, the slower diffusion kinetics in ceramics requires that the GB density need to be greatly increased to demonstrate enhanced radiation tolerance to a magnitude comparable to NC metallic systems.

Although a large number of studies show that NC ceramics have enhanced radiation resistance, there are cases where the opposite phenomena were observed. For instance, bulk ZrO_2 is know to be one of the most radiation resistant ceramics [217-220], showing no evidence of irradiation induced amorphization at high dose, such as 110 dpa [221]. However Meldrum et al showed that merely 1 dpa of Xe ion irradiation (1MeV) is sufficient to amorphize ZrO2 nanoparticles (3 nm in diameter) embedded in SiO_2 matrix [213]. It was argued that tetragonal nanograins raise the system free energy high enough to facilitate amorphization. It is interesting to see that NC cubic ZrO_2 film is stable against amorphization [203]. The study on amorphization resistance of NC SiC is mixed with opposite observations. One the one hand it has been shown that stacking faults in NC SiC improve radiation resistance [222, 223], but on the other hand, NC SiC has been shown to reduce the amorphization resistance in some cases[224-230]. The complexity arises from the internal microstructure (phases) of SiC, radiation temperature and even ion sources[231].

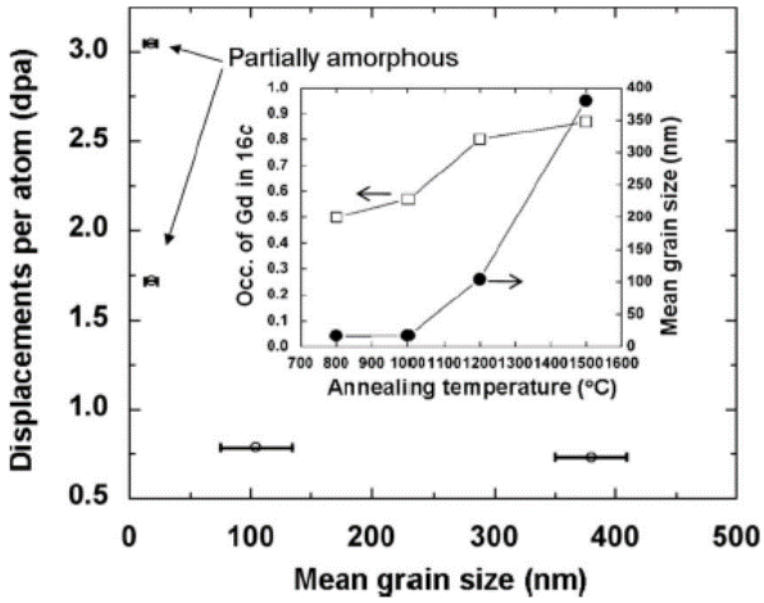

Fig. 2.14. Grain size dependent critical amorphization dose in pyrochlore $Gd_2(Ti_{0.65}Zr_{0.35})_2O_7$ after annealing at different temperatures. Inset shows the relationship of grain size and degree of disorder that occurs on annealing [211].

2.4. The need to refine GB sink strength model

2.4.1. Complexity of GB nature on radiation damage in NC metals

The radiation tolerance of NC metallic materials is directly related to the nature of GB structure and the radiation environment [178, 232-235]. The potential complexity is nicely demonstrated in the work of Uberuaga *et al.* [232], as well as the work by Arjhangmehr and Feghhi [178]. Both of these studies examined the role of GB angle, GB character, the distance of the cascade to the boundary, and the damage states already present in the GB. The resulting microstructure can also be dependent on the cascade type that occurs (semi-spheroid, semi-ellipsoid, or fragmented distribution) [178]. The large variation in the predicted defect density

suggests that the detailed GB character, structure, and radiation history play a significant role in the radiation damage from each cascade and boundary interaction.

The sink strength was investigated in great detail as a function of the GB character by Tschopp *et al.* utilizing molecular statistics simulations [233]. This study surveyed a significant number of GBs and outlined some interesting findings:

1) Certain GB sites have higher vacancy/interstitial formation energy than bulk lattices, indicating that these sites will preferentially capture (annihilate) radiation induced point defects.

2) Although both low-angle GBs (LAGBs) and high-angle GBs (HAGBs) are effective sinks for point defects, the sink efficiency depends on the exact GB character with a general rule that HAGBs are more efficient defect sinks due to their lower point defect formation energy.

3) Point defect (vacancy or interstitial) formation energy also decreases with increasing misorientation angles for LAGBs (less than 15°), but less so for HAGBs as shown in Fig. 2.15.

4) The simulation also shows that there is a greater tendency for interstitials to segregate to GBs than vacancies. This observation suggests that GBs are in fact biased defect sinks. Another implication of this finding is that the nature of GBs (GB energy and misorientation angle etc.) may change during long-term radiation as the preferential absorption of interstitials will gradually change the atomic configuration of the GBs.

Clearly, such atomistic view on GB defect sinks has not been taken into account when developing the analytical GB sink strength formulas.

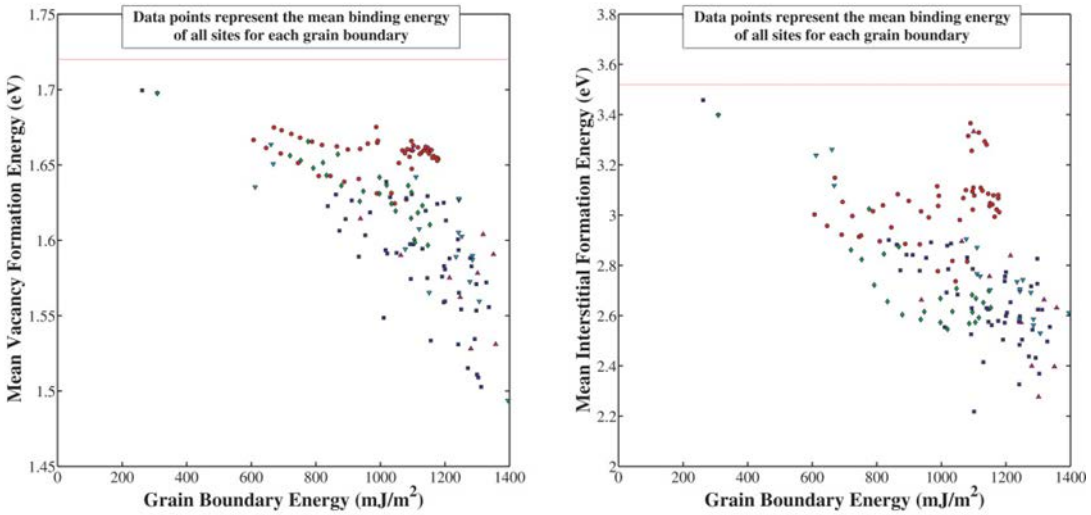

Fig. 2.15. The decreasing point defect formation energy for vacancies and interstitials with increasing GB energy for BCC Fe simulated for a variety of GBs [233].

One detail that appears to be very important is the defect structure present in the boundary either from initial production, mechanical deformation, or previous radiation damage [172, 178]. That being said, most MD simulations have also predicted that a single GB can accommodate multiple cascades without substantial decrease in the sink efficiency and will outperform a single crystal of the same composition with regards to radiation tolerance [184]. The exact structural evolution associated with each new cascade event is not predicted to be the same. This can be seen in the data of damage profiles presented for a pristine and defect loaded boundary. Different from the generally accepted theory that the GBs in NC metals serve as efficient sinks, an MD simulation predicted single crystal W outperforms NC W due to hindered motion of SIAs in this system [168]. Despite this one study, the prevailing view based on numerous studies remains that GBs in NC metals can incorporate the defects produced by multiple sequential cascades in a typical radiation environment. The modeling work by Li *et al.* shows the complexity of the annihilation pathway for a single vacancy near a GB that contains trapped interstitials, as can be seen in Fig. 2.16 [236].

A path with this many local minima suggests a range of complex and evolving defect and boundary structures are possible depending on the local kinetics.

A major limitation in trying to understand defect evolution in NC models utilizing MD simulations is the time limitations associated with the models. To understand the defect evolution near boundaries at relevant time scales, recent work by Dunn *et al.* has attempted to utilize spatially resolved stochastic cluster dynamics (SRSCD) model [154]. Another factor hindering the validation of MD simulations is the limited amount of experimental data available to verify many of the previously mentioned studies due to the difficulty of characterizing GB character and structure during irradiation studies. Advanced microscopy tools, coupled with simulation, have recently been demonstrated to be successful pathways to define the interplay between GB characters and defect absorptions [237-239].

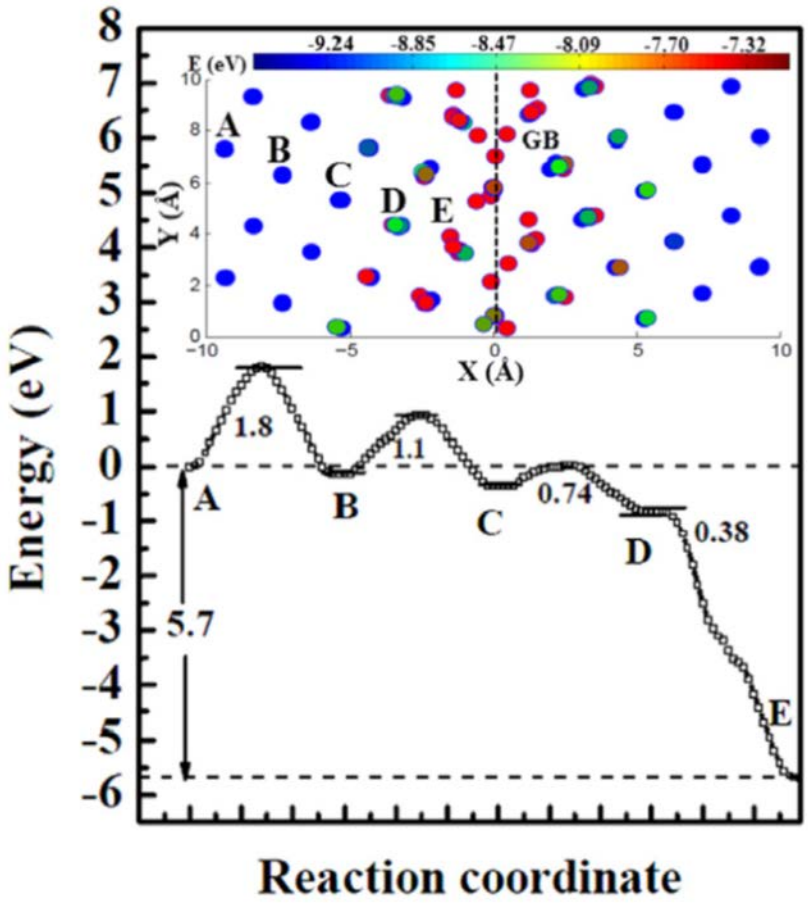

Fig. 2.16. An annihilation path for the vacancy near the GB in tungsten with interstitials trapped at the GB. The axes X and Y are along [310] and $[\bar{1}30]$, respectively [236].

2.4.2. The modified GB sink strength model

The simple rate equation (Eq.2.3) correctly predicts the trend that sink strength of GB is grain size dependent; that is smaller grains have higher sink strength. However there are a couple of issues with this equation. First, the equation predicts that when R reduces to nanometer length scales, the sink strength of GB increases significantly, or sink strength approaches infinity (unrealistically) when grain size reduces to several nm. Second, the equation did not differentiate different types of GBs. For instance there are increasing evidence showing that HAGBs are stronger defect sinks than LAGBs. Third, the sink strength of GBs decays, as GBs are constantly

absorbing point defects because GBs cannot fully recover (self-heal) after absorbing a large number of point defects. NC grains may coarsen during long term irradiation. Thus the assumption that GBs are ideal defect sinks is less likely to hold in continuous, long term, radiation environments.

Detailed derivation of a formula that considers all these factors is beyond the scope of this review, however a simple analytical formula can probably suffice for the current purpose. The absorption of point defects, such as interstitials will require excess free volume on the GB, and HAGBs have greater excess free volume than LAGBs. Hence a fundamental assumption is that not the entire GB area can accommodate point defects, instead there are active sites that can preferentially capture point defects. Thus a factor is introduced when estimating sink strength of GB:

$$k_{gb}^2 = 15 f(\theta,\gamma) / R^2 \tag{2.4}$$

Where $f(\theta, \gamma)$ is a function of GB energy (γ), and misorientation angle (θ), and $f(\theta, \gamma) = 1$ for an ideal HAGBs, and $0 \leq f(\theta) < 1$ for LAGBs. Such a formula has the advantage of integrating the nature of GB (such as sink efficiency) with sink strength, and it may also be consistent with the experimental observations that:

1) the capability of GB sinks to absorb defects decays or alters in some form after long term radiation and grains coarsens, and
2) the GB denuded zone width scales with GB angles, that is HAGBs typically have broader GB denuded zone.

2.4.3. The application of the modified model for interpretation of experimental findings

The aforementioned model can be used to explain some recent studies, where the defect denuded zones appear to vary for different types of GBs. A recent combination of modeling and experimental effort by Han *et al.* has investigated the sink strength of various GBs in He ion implanted Cu at elevated temperature by measuring the resulting denuded zone around each individual boundary [237]. Based on experimental observation of He bubble denuded zone (Fig. 2.17), a simplistic yet elegant model was developed by associating the width of the denuded zone (λ) of an asymmetrical Σ3<110> GB with the misorientation angle (θ) and the width of denuded zone of the coherent twin boundary (CTB) and the symmetric incoherent twin boundary (SITB).

$$\lambda_A = \lambda_{CTB} \cos\theta + \lambda_{SITB} \sin\theta \qquad (2.5)$$

This study indicates that the sink strength of the GBs is strongly related to the GB character [237]. Significant work is needed to substantiate this proposed model at various temperatures, in different material systems and radiation conditions.

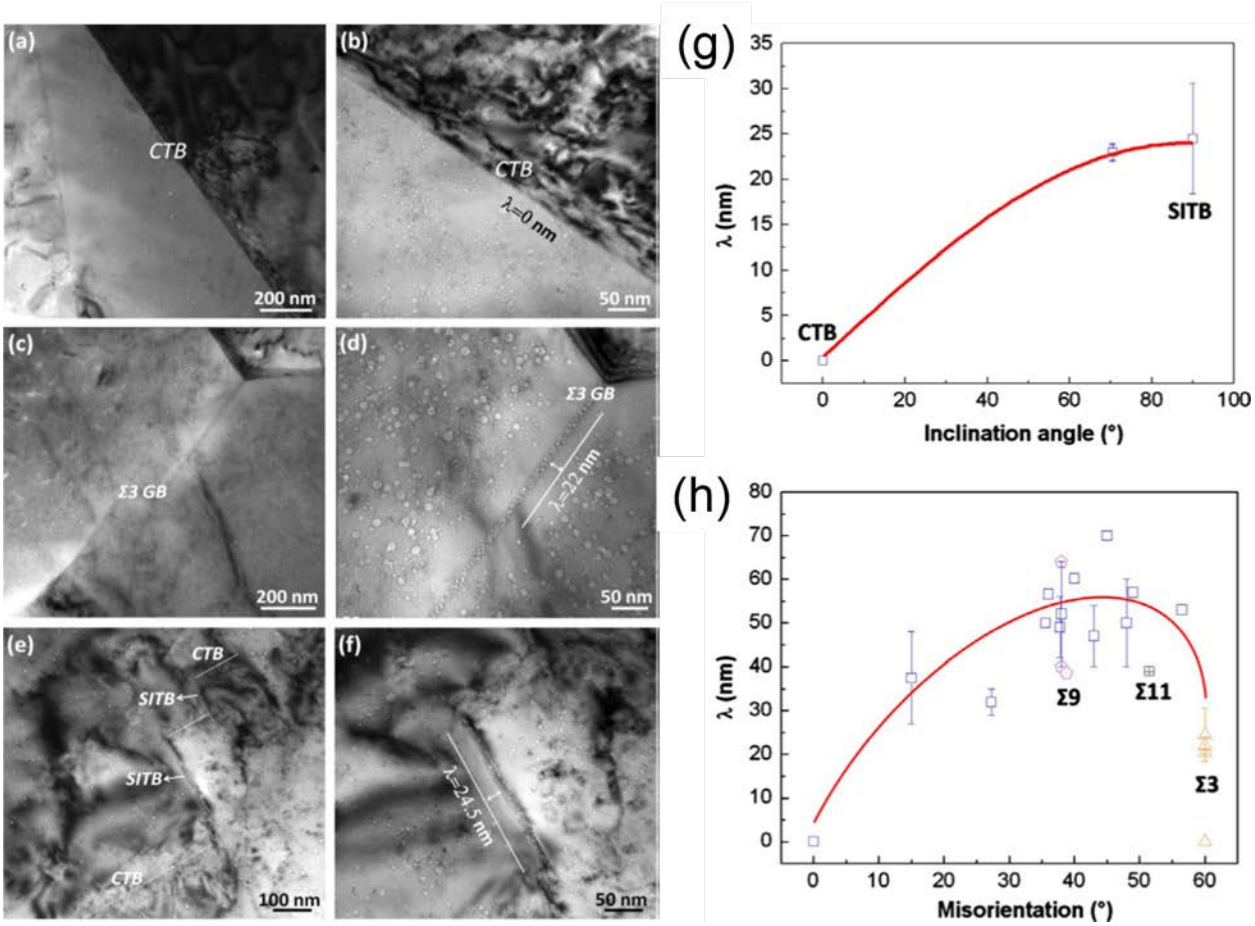

Fig. 2.17. ∑ 3 <110> tilt GBs in Cu irradiated at 450 ºC by 200 keV He ions with a fluence of 2×10^{17} ions cm^2: (a) and (b) show radiation-induced voids but no void denuded zone (VDZ) near a coherent twin boundary (CTB); (c) and (d) show a VDZ near an asymmetric ∑ 3 <110> tilt GB; (e) and (f) show a VDZ at a symmetric incoherent twin boundary (SITB). All images were taken under a defocus of -5 μm. (g-h) The width of the VDZ as a function inclination angle and misorientation angle[237].

This finding was further supported by a very recent *in situ* He ion irradiation TEM study that showed that, even for the same NC Fe grain, not all GBs respond the same during radiation as shown in Fig. 2.18 [181]. It is likely that the GBs surrounding the same grain have different nature and thus as predicted by Eq.2.4, they have different sink capacity. Another interesting observation made during irradiation at elevated temperatures is that cavities in irradiated NC Cu are mainly formed along GBs with much less cavities in the grain interiors [237]. The number density and

average radius of cavities in NC Cu are smaller than those in irradiated single crystal and CG Cu. Although these initial findings are very interesting, the details of the controlling factors and governing mechanisms are not fully clear and require further investigation.

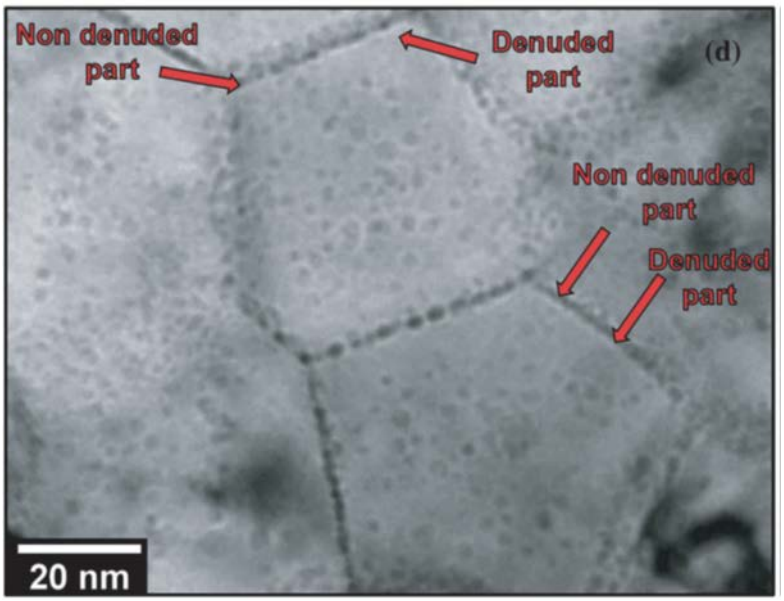

Fig. 2.18. Over-focused bright field TEM image showing partially denuded GBs (pointed by red arrows) in NC Fe irradiated with 10 keV He at 700 K [181].

A large body of literature on radiation damage in nanostructured metals used He ion for radiation studies as He bubbles are one of the concerns in irradiated structural materials. There are abundant studies on He ion irradiation studies in bulk structural materials [240-249] as discussed briefly in sec. 1.3. He bubbles may coalesce and form large voids and lead to blistering and embrittlement after high dose radiation [250-310]. Hence GBs in NC metals and alloys provide an important way to manage He (prohibit the formation or growth of large He filled cavities).

When working with any of these types of advanced TEM characterization techniques, it is often necessary to study the evolution in real time. As such, *in situ* TEM is a powerful tool in

determine the underlying mechanism governing the evolution of NC metals in real time. However, one must understand the limitations associated with sample geometry, experimental conditions, and the effects of electron beam on the observed results during these *in situ* TEM experiments. Recently, Muntifering *et al.* showed that during a sequential *in situ* 3 MeV self-ion irradiation and annealing of NC nickel, the defect evolution kinetics can be greatly influenced by electron beam effects [311]. In Fig. 2.19, the region exposed to the electron beam developed cavities much sooner than those receiving much less electron beam exposure. This experiment was done in metal that should not undergo radiolysis and is well below the knock-on threshold for the nickel, thus eliminating the two major forms of electron beam damage expected in TEM samples. The e-beam facilitated formation of cavities in NC nickel can be attributed to the increasing growth of oxide known to occur in nickel and many other metals exposed to electron beams [311]. As a result, the identification of radiation sink rates and other effects from *in situ* studies should be approached with care.

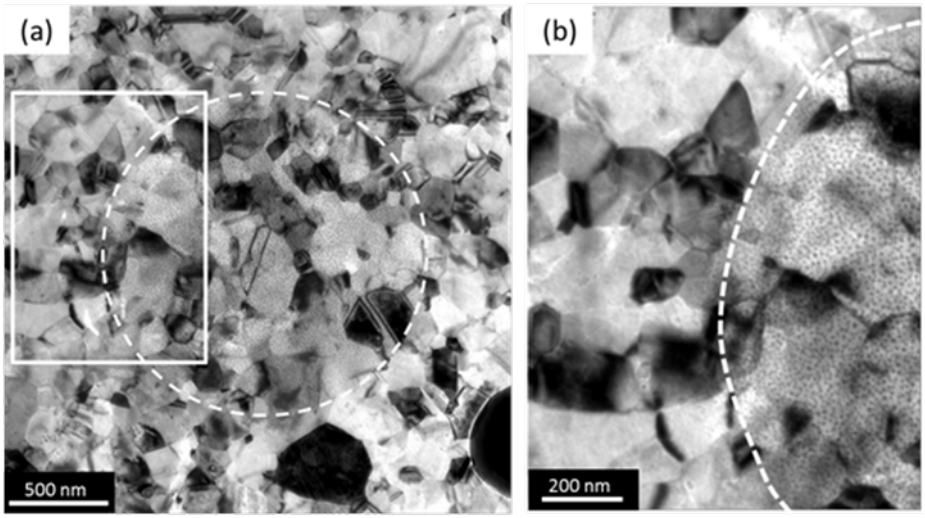

Fig. 2.19. The influence of electron beam on formation of cavities in self-ion irradiated NC Ni. (a) Defocused TEM image after annealing demonstrating that the voids are only present in the

area the electron beam was irradiating during annealing. (b) Higher magnification image of the area boxed in (a) showing drastic different defect density in irradiated NC Ni [311].

2.5 The stability of NC metals in radiation environments

Understanding the absorption of cascades by GBs is only one part of the story. The other major aspect is to understand the mobility of GBs and the associated network present in NC materials as a result of the radiation damage and associated temperature rise. MD simulations have shown that GBs can move over a significant distance in ps after a cascade event [171, 182, 190]. These simulations suggest a fast GB migration mechanism results from either the absorption of the cascade damage or the associated thermal spike. Understanding the extent of grain growth in these types of samples is difficult from post irradiation examination, so *in situ* irradiation TEM has been the tool of choice to examine the structural evolution from displacement damage. A global radiation induced grain growth model was put forward by Kaoumi *et al.* for a range of monolithic metal system based on a thermal spike assumption[200]. This analytical model is expressed as:

$$\boldsymbol{D}^3 - \boldsymbol{D}_0^3 = \boldsymbol{K}\Phi\boldsymbol{t} = [36\boldsymbol{\gamma}\boldsymbol{d}_{\boldsymbol{spikes}}\boldsymbol{\chi}\boldsymbol{\delta}\frac{\boldsymbol{V}_{\boldsymbol{at}}\boldsymbol{\nu}\sqrt{\frac{3}{5}}\Gamma(\frac{8}{3})\boldsymbol{k}_{\boldsymbol{B}}^{5/3}}{10\boldsymbol{\pi}\boldsymbol{C}_0^{2/3}\boldsymbol{\kappa}_0}\frac{\boldsymbol{Q}^{5/3}}{\boldsymbol{E}_{\boldsymbol{a}}^{8/3}}]\Phi\boldsymbol{t} \qquad (2.6)$$

In this equation, the final grain diameter (D) is dependent on the initial grain size (D_0), the average thermal spike size (d_{spike}), the number of thermal spikes per ion (χ), the thermal spike energy (Q), ion flux (Φ), thermal conductivity (κ_0), heat capacity (c_0), atomic volume (V_{at}), GB surface energy (γ), activation energy for atomic jump in the thermal spike (E_a), the gamma function (Γ), and the Boltzmann's constant (k_B). This model is a derivation of the classical thermal grain growth model with the addition of an empirically derived term to incorporate the deviation from classical grain growth due to the ion irradiation damage. This is done by assuming that during a

cascade event that GBs migrate due to atomic jumps and variations of local curvature resulting from the thermal spike. These atomic jumps promote the migration of GBs and the local curvature dictates the direction of boundary migration. The grain size distribution was obtained directly from TEM micrographs and videos captured during *in situ* ion irradiation TEM observations, as seen in Fig. 2.20 [200].

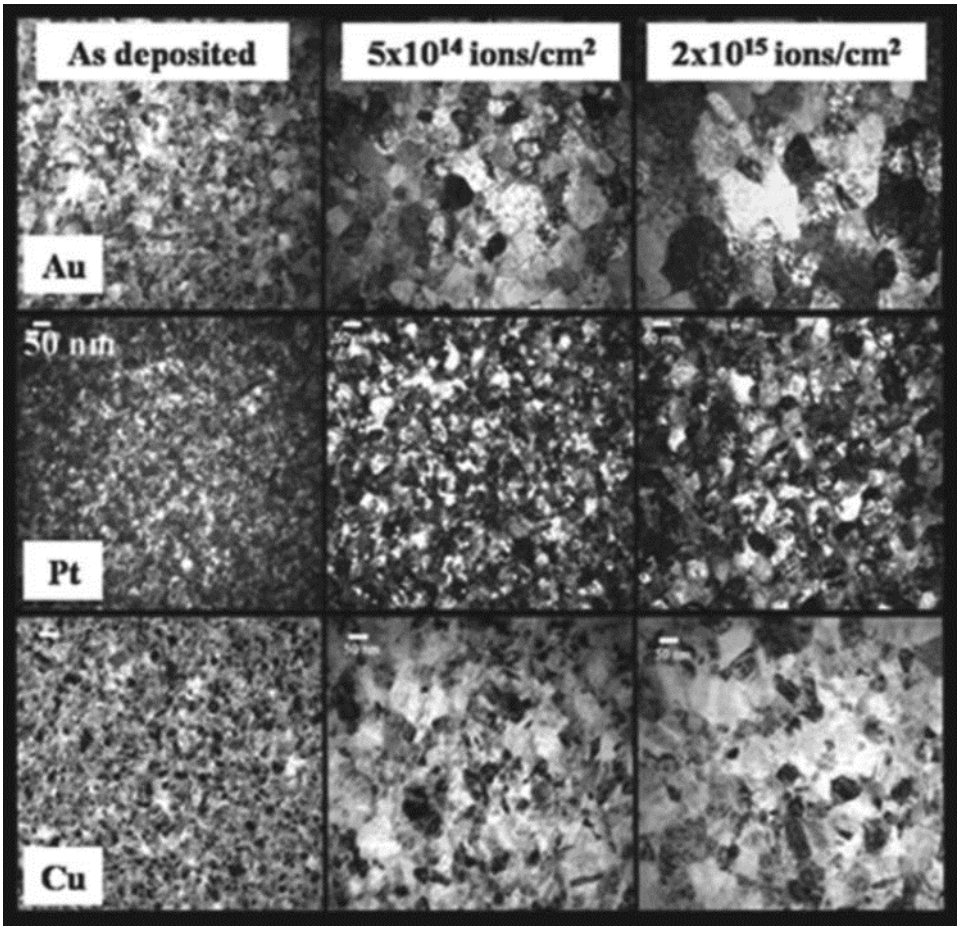

Fig. 2.20. Sequence of bright-field TEM images taken at different ion doses showing grain growth induced by ion irradiation at room temperature; from left to right: as deposited, 5×10^{14} ions/cm^2, 2×10^{15} ions/cm^2; from top to bottom: pure Au thin-film irradiated with 500 keV Ar ions, Pt irradiated with 500 keV Ar ions, and Cu irradiated with 500 keV Kr ions [200].

The understanding of this effect was furthered by Bufford *et al.* [201] that combined *in situ* self-ion irradiation of NC Au film with precession electron diffraction (PED) and mesoscale

modeling of GB stability. In this study, it was shown that both global texture and overall GB network character could evolve during irradiation induced grain growth. In addition, it was shown a single boundary associated with one of the larger grains migrate until it hit a set of sub-grain [201]. The overlaid GB character map and bright-field images before and after irradiation can be directly compared to the mesoscale model and the associated prediction for radiation induced grain growth, as can be seen in Fig. 2.21. Additional post irradiation examination work utilizing PED and other advanced characterization techniques has suggested that non-equilibrium phases may be prone to grain growth over the thermodynamically preferred phase in systems ranging from pure metals to complex ceramics [156, 210]. Very recently, this has been taken further by Yu *et al.* who reported *in situ* Kr ion irradiation induced grain rotation in NC Ag, Cu, and Ni and associated it with significant in-plane strain [26]. The understanding of the complex interaction of GBs, groves, and thin film effects during radiation is still an area requiring significant research.

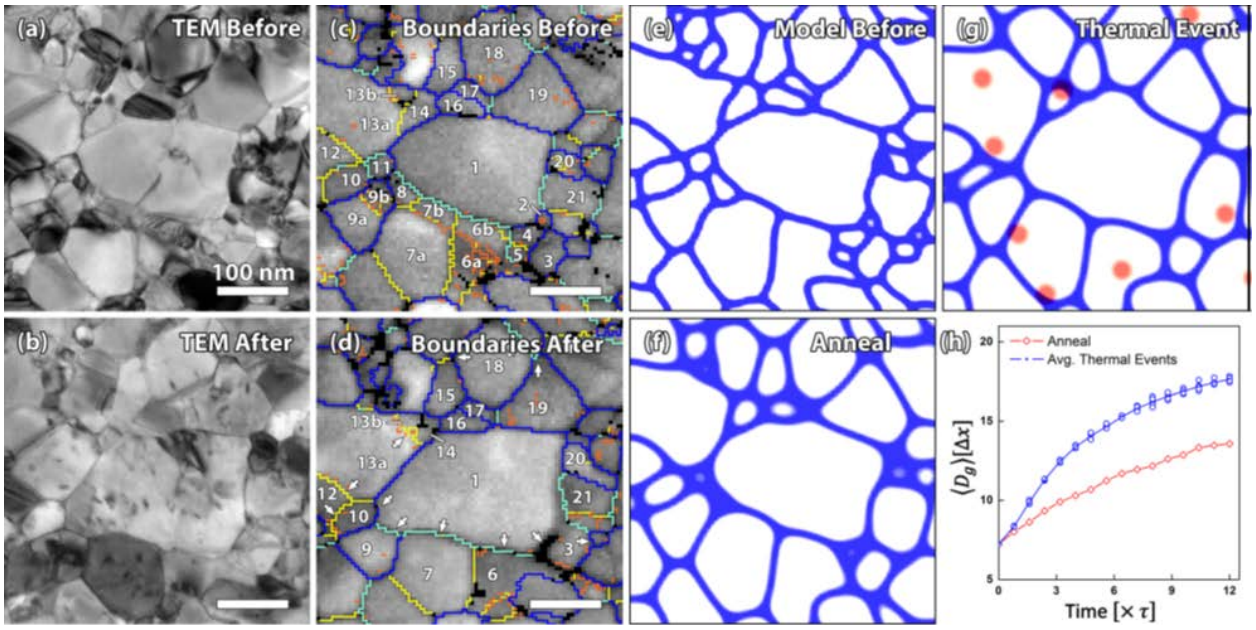

Fig. 2.21. Bright field TEM micrographs of NC Au (a) and (b) and index maps (c) and (d) with GBs highlighted before and after irradiation. Orange, yellow, cyan, and blue indicate GBs with

misorientation angles in the respective ranges of $\varphi<3^{o}$, $3^{o}<\varphi<15^{o}$, $15^{o}<\varphi<30^{o}$, and $30^{o}<\varphi$. Grains are numbered clockwise from the bottom right. Arrows in (d) indicate directions that boundaries moved. (e) Phase field representation of the structure shown in (c). (f) Grain structure after homogenous annealing. (g) Snapshot taken during simulated irradiation. Red spots indicate one set of thermal events. In panels (e)–(g), white (blue) regions represent grain (boundary) regions. (h) Average grain diameter as a function of characteristic time. Red diamonds show the homogenous anneal, while blue circles indicate 5 thermal event runs. The blue line shows the average of these 5 runs [201].

In addition to GB coarsening due to ion irradiation, two recent and somewhat surprising observations were made regarding the potential for strikingly minimal interaction between GBs and voids in irradiated NC Ni samples. In this study Muntifering *et al.* show, by utilizing *in situ* TEM irradiation and annealing in combination with PED, that defect size and shape were not limited to the size of the underlying NC grains [202]. At this damage level, the grain structure is no longer observable via traditional TEM imaging conditions due to the large amount of defects. However, PED orientation and grain structure maps in Fig. 2.22 clearly show the underlying microstructure and the cavities that seem to have no associated correlation to the underlying GB structure [202]. Similarly, Vetterick *et al.* showed that the presence of voids at a GB can decrease the mobility of a GB by four orders of magnitude via a Zener pinning like mechanism [162]. The combined observation of cavities growing straight through boundaries or pinning GBs demonstrate the large number of competing mechanisms that are active in NC samples exposed to radiation. It is our opinion that the dominant mechanism and subsequent radiation tolerance will be highly dependent on the composition, and the character of the GB (not just the average grain size), as well as the radiation environment that the sample will be exposed to during the operational lifetime of relevant components.

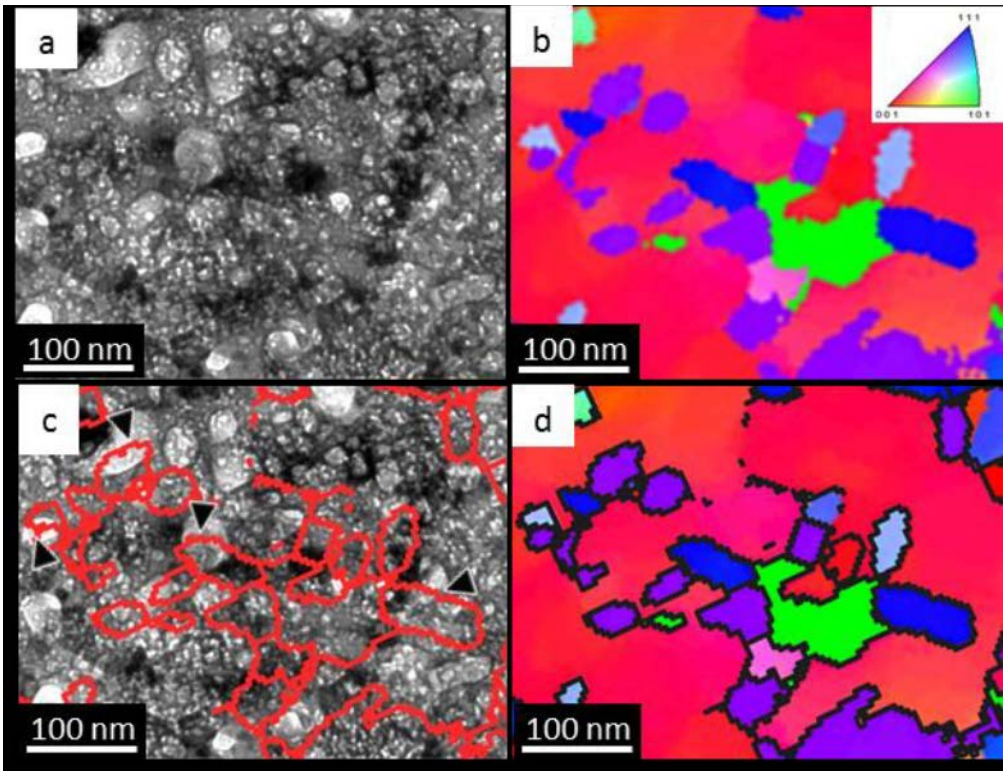

Fig. 2.22. (a) Under-focus BF TEM image of cavities in helium implanted then self-ion irradiated NC nickel film after annealing to 400°C. (b) Orientation map of (a) revealing the grain structure and strong texture, inverse pole Fig. color chart is inset. (c) GBs (red) overlaid on (a) demonstrating that many cavities cross GBs, several examples of which are highlighted with black arrows. (d) Orientation map with GBs emphasized in black [202].

2.6 Challenges and future outlooks

Research into radiation response in NC materials has been limited, but is rapidly increasing. There are many research and engineering challenges ahead of us, such as: elucidating the role of GB character, GB stability, validation in realistic radiation environments, and commercial scale processing of the bulk nanostructured materials. The vast majority of studies investigating radiation stability in NC materials only focus on the average grain size. A small subset of those have started to look at the role of grain size distribution [180]. However, it was not until very recently that GB character was being considered in the design and characterization of radiation

tolerant materials [181, 237]. Because of experimental limitations, the character has typically been limited to the GB orientation and does not include discussion of the GB plane or GBs defects that are expected to play a significant role (based on predictions from MD simulations). Further experimental and modeling work is needed to determine how local GB character, composition, and defect distribution alters the response of GBs as defect sinks. This will be important not only for model systems to advance the basic understanding of the underlying physics, but also for commercial alloys with complex interplay in the chemistry and structural effects in radiation environments.

As shown in section 2.5 the stability of NC materials in radiation environments, the unique ability of GBs to absorb cascade damage and any implanted or transmutated species can be significantly compromised by irradiation induced grain growth. Additionally, recent observation by one of the coauthors suggests that GBs in NC materials produced by methods such as severe plastic deformation and sputter deposition are not equilibrium structures, and therefore exhibit drastically different behavior under irradiation [239]. For any of the materials suggested above or any other NC materials, the concern of grain stability will need to be addressed. Fortunately, this stability is currently being addressed in the thermal and mechanical stability of NC metals through alloying [312, 313], the tailored introduction of stable oxides in pure metal systems [314, 315], the production of ODS alloys [316, 317], or through various combinations thereof [150, 152, 167, 313, 318-383]. Although there is still much controversy over the balance played between thermodynamic and kinetic driving forces in alloy stabilized NC systems, it has been shown empirically that many of the systems predicted by the theory (Fig. 2.23) to be stable and demonstrated significantly enhanced thermal stability at temperatures as high as 1100 ºC [313]. It is the opinion of these authors that these binary systems provide a rich material landscape for

exploring the radiation tolerance in general, as has been previously demonstrated in bulk CG binary systems [239], and may present many more unexpected effects in NC metals due to the complex GB networks. It has also been shown that NC metals can be stabilized against thermal grain growth by the addition of oxides distributed at the GBs [384]. We suggest that utilizing such a strategy might also mitigate radiation induced grain growth that has been observed in high purity NC metals [201]. The addition of oxides may not only minimize grain growth, but might also enhance some of the other properties as has been seen in bulk ODS alloys [150]. In general, the next step in radiation tolerant NC systems may be multiphase alloys.

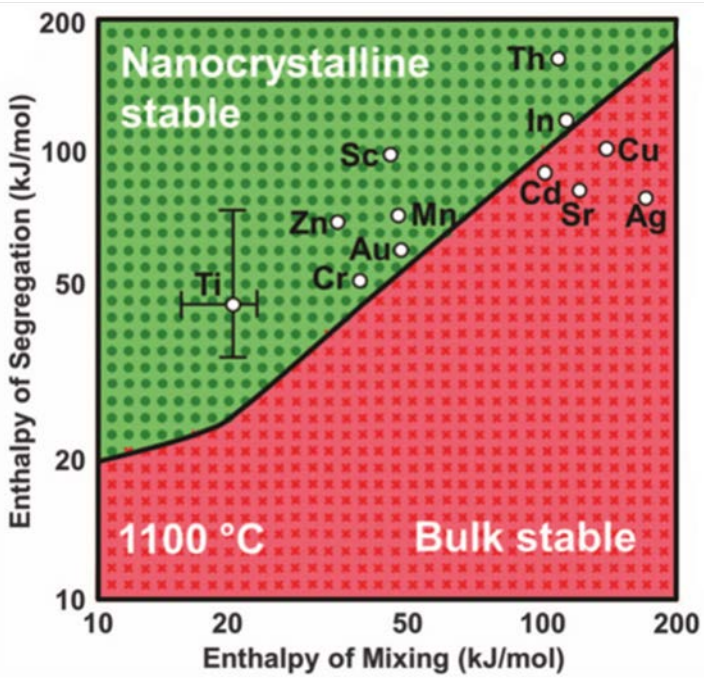

Fig. 2.23. NC materials are desirable in a wide variety of applications; however, the energy associated with the high fraction of GBs inherent in a NC material leads to instability of the nanoscale structure in a monolithic material. It has been experimentally observed that alloying elements can in some cases stabilize a NC microstructure. This Fig. show the significance of solute on and segregation profiles on the stability and mobility of GBs at the NC length scale [313].

To truly examine the roles of these alloys, new developments of characterization tools are needed to explore the structural evolution with the necessary information on the local phase and chemistry. Advancement in characterization tools should greatly advance the fundamental understanding with increased spatial, chemical, and temporal resolution. The enhanced understanding of local microstructural details including GB character and defect and compositional distribution are important for predicting material response to radiation environments. Development of advanced characterization tool will have to include significant advancement in data processing and large-scale non-destructive characterization of nanostructured materials, which will probably require the use of national and global infrastructures like the US Department of Energies (DOE) – Nuclear Energies, Nuclear Science User Facilities and DOE Basic Energy Sciences, Nanoscale Science Research Centers (NSRCs) and other similar international research infrastructures.

The two other aspects needed for the regulatory approved incorporation of NC systems into nuclear applications are validation in realistic radiation environments and commercial scale processing of the nanostructured materials. These two steps are as important, if not more important, as those mentioned previously, but have been to date studied much less. The vast majority of the particle beams chosen in the experiments on NC materials are keV helium ions. The damage type (Frenkel pair vs. cascade damage) and the new dopant introduced during radiation are not necessarily the same observed in specimen subject to the typical neutron spectra and associated transmutations. The difference in damage and damage rates between neutron and ion irradiation is a well-known, but still intensely debated topic in the nuclear energy field [154, 198, 385]. It has been suggested that altering the temperature can compensate for the elevated damage rate and that utilizing triple beam facilities can incorporate any synergistic effects resulting from transmutation.

The development of triple beam facilities and other accelerator developments can be found in the detailed review by Chao [151]. To our knowledge, only a limited set of studies on the different structural evolution as a function of sequential vs. concurrent exposure of NC systems to heavy ion irradiation (displacement cascades), gas implantation (transmutated species), and temperature have been published [202, 311, 386]. All of these studies have shown a drastic change in internal structure as a function of irradiation history.

In a similar manner, the processing of these systems to industrial scale can utilize the advancements made in the last decade or more in processing of nanostructured materials. This ranges from the work developed for electrochemical coating over areas as large as semi-truck bumpers [387] to severe plastic deformation for bulk structural materials [388, 389]. A review of other possible routes to produced bulk nanostructured metals was completed by Beyerlein *et al.* [152]. Despite the challenges facing the field before regulatory approval could ever be considered, the future looks peachy at least through rose colored glasses!

Chapter 3. Radiation damage in metallic and ceramic nanolayers

As mentioned in Chapter 1, it is a major challenge to design "radiation immune" materials that resist radiation damage while maintaining materials' high strength and toughness. Recently, a strategy of incorporating a high-density of heterophase layer interfaces as defect sinks to enhance damage resistance has been investigated significantly. Among various defect sinks, layer interfaces are unique in many aspects. Physically coherent and incoherent interfaces can be constructed between materials with different lattice mismatch [390, 391]. Chemically, various types of chemical bonds can be formed across interface planes [392]. Furthermore, the mechanical behaviors of multilayered nanocomposites, including ductility, yield strength, hardness etc., can be tailored [393, 394]. Geometrically, the layer thickness of each constituent can be precisely controlled down to 1 nm, providing ample opportunity to investigate the size effect on radiation damage in nanomaterials. Hence nanolayer composites have been increasingly used as model systems to explore the role of interfaces under different irradiation conditions. The improved understanding on interactions between interfaces (defect sinks) and radiation-induced defects has provided significant insight into the design of advanced radiation-tolerant structural nanomaterials.

3.1. Sink strength of nanolayers

Rate theory has been widely used to describe the evolution of radiation-induced damage. In 1970, the concept of "sink strength" was initiated by Wiedersich to simplify the solution of the steady defect concentration [395]. Meanwhile, it has been used as a determinant to reflect the strength or affinity of certain sink for radiation-induced defects. Later, the concept was broadened by Brailsford, Bullough, Hayns, Rauh, Wood *et al.* to explore different types of defect sinks [135, 396-400].

Although the sink strength of GBs has been developed as described in Chapter 2, until now, there is no formula to describe the sink strength of interfaces in nanolayers. To develop such an equation, we start with the idea of sink strength for thin foil surfaces [135]. By using the Cartesian coordinate, the point defect concentration, c, within a thin foil can be described by:

$$D\frac{d^2c}{dx^2} + K - Dk_{sc}^2 c = 0 \quad (3.1),$$

where x axis is perpendicular to the foil surface, D is point defect diffusion coefficient, K is defect production rate, k_{sc}^2 is the sink strength from all the microstructure within the foil. For a thin foil with a thickness of $2l$, the solution to the formula given the boundary condition ($c = 0$ when $x = 0$, i.e. free surface is an ideal defect sink) and symmetry condition ($dc/dx = 0$ when $x = l$), is given by

$$c(x) = \frac{K}{Dk_{sc}^2}\left[1 - \frac{\cosh k_{sc}(x-l)}{\cosh k_{sc} l}\right] \quad (3.2).$$

It can be shown that the sink strength of free surfaces can be written as

$$k_s^2 = \frac{k_{sc}/l}{\coth(k_{sc}l) - \frac{1}{k_{sc}l}} \quad (3.3).$$

In the extreme case, when $k_{sc}l \to 0$, i.e. for thin foils where free surface defect sinks dominate, the previous equation can be written as

$$k_s^2 = \frac{3}{l^2} \quad (3.4).$$

Similarly for A/B nanolayers with equal individual layer thickness, h, if we assume that layer interface is an ideal defect sink, then the sink strength of nanolayers can be written as:

$$k_h^2 = \frac{2k_{sc}/h}{\coth(k_{sc}h/2) - \frac{2}{k_{sc}h}} \quad (3.5).$$

When $k_{sc}h \to 0$, we arrive that:

$$k_h^2 = \frac{12}{h^2} \qquad (3.6).$$

Note this formula also assumes that the columnar grain size of each layer is much greater than h, that is the in-plane grain size is sufficiently large to be considered as single crystal like. Thus the overall sink strength of nanolayers (without the consideration of GB sinks within the layers) is underestimated.

With the ideal boundary conditions, the defect flux into two ideal interfaces (F^{ideal}) across the layer can be estimated as:

$$F^{ideal} = \frac{2D}{h}\frac{dc}{dx}|_{x=0} = \frac{2K}{k_{sc}h}\tanh k_{sc}h/2 \qquad (3.7).$$

For free surface, the boundary condition for an ideal sink (c = 0 when x = 0) applies well. However, for the heterophase boundary in nanolayers, limited defect concentration is presented at the interface and this value is closely correlated with the sink efficiency, η. Note that in the simplified Eq. 3.6, the intrinsic nature of layer interfaces, such as coherency strain, misfit dislocation density (interfacial energy), and heat of mixing etc., is not considered. Here we introduce the concept of sink efficiency (η) as the ratio of defect flux into interface (F^{real}) to the defect flux into a perfect sink interface (F^{ideal}) [401, 402],

$$\eta = \frac{F^{real}}{F^{ideal}} \qquad (3.8).$$

By replacing the ideal sink boundary condition by

$$F^{real} = \frac{2D}{h}\frac{dc}{dx}|_{x=0} = \eta F^{ideal} \qquad (3.9),$$

we obtain the particular solution

$$c(x) = c_1 e^{k_{sc}x} + c_2 e^{-k_{sc}x} + \frac{K}{Dk_{sc}^2} \quad (3.10).$$

where

$$c_1 = \frac{-K\eta}{k_{sc}^2 D} \frac{e^{-k_{sc}h/2}}{e^{k_{sc}h/2} + e^{-k_{sc}h/2}}$$
$$c_2 = \frac{-K\eta}{k_{sc}^2 D} \frac{e^{k_{sc}h/2}}{e^{k_{sc}h/2} + e^{-k_{sc}h/2}} \quad (3.11).$$

When η=1, the solution is the same as Eq. 3.2. The correlated sink strength of layer interfaces changes to:

$$k_h^2 = \frac{k_{SC}^2}{\frac{k_{SC}h}{2\eta}\coth(k_{SC}h/2) - 1} \quad (3.12).$$

When $k_{SC}h \to 0$, it evolves to:

$$k_h^2 = \frac{k_{SC}^2}{\frac{1}{\eta} + \frac{k_{SC}^2 h^2}{12\eta} - 1} \quad (3.13).$$

It is noted that when η is considered, the formula of sink strength becomes much more complicated. But the general trend remains the same, that is sink strength increases with η. When $\eta \to 1$, this equation reduces to a format similar to (Eq. 3.6):

$$k_h^2 = \frac{12\eta}{h^2} \quad \text{(Eq. 3.14)}$$

η is large for incoherent, immiscible layer interfaces with high interfacial energy, whereas η is small (but > 0) for coherent and miscible layer interfaces with low-to-intermediate interfacial energy. In addition, η may keep evolving with irradiation time/fluence as the characteristics of layer interfaces may continuously evolve during irradiation [232].

3.2. Phenomena of defect-interface interactions

Before examining the detailed mechanisms on how layer interfaces interact with radiation-

induced defects, several experimental observations are presented first to show that such intimate interactions do exist in nanolayers.

Absorbing radiation-induced defects by layer interfaces

Room temperature *in situ* Kr ion irradiation experiments were employed to investigate the role of interfaces in absorbing radiation-induced defects [403]. As shown in Fig. 3.1, a radiation-induced dislocation loop migrated towards the immiscible Ag/Ni layer interface during radiation, followed by its absorption at the layer interface.

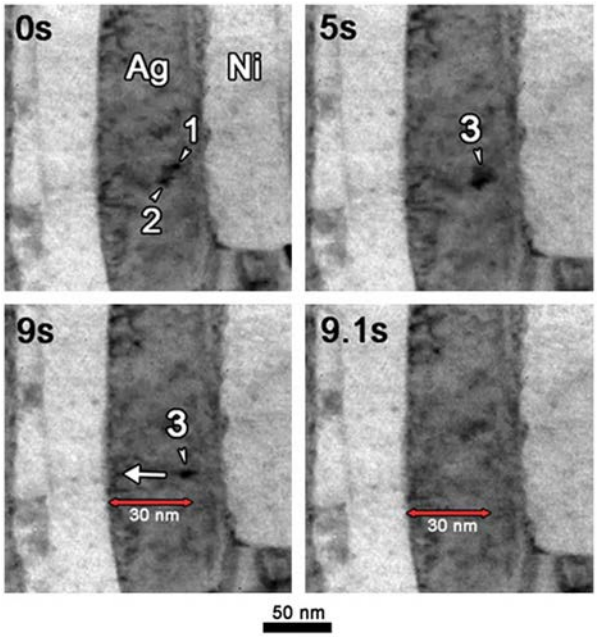

Fig. 3.1. *In situ* observation of dislocation loops absorbed by layer interface over a dose range of 0.131–0.133 dpa ($0.262–0.266\times10^{14}$ ions/cm^2). Loops were indicated by white arrows. Two loops nucleated at 0 s, then reached a quasi-steady state. They merged to form one larger dislocation loop, ~ 6 nm in diameter, by 5 s. The loop was stable until 9 s. Within 0.1 s, the loop diffused left towards the layer interface and nearly disappeared. The big arrow indicates the migration route [403].

Distance dependent defect concentration profile

In principle, since layer interfaces can act as defect sinks, the defect concentration near the interface should be lower than that away from the interface. To validate this hypothesis, recently, Mao *et al.* proposed a method to estimate the local vacancy concentration in Cu layer near Cu/Nb interface [404]. Fig. 3.2a shows the profile of the local steady-state vacancy concentration plotted as a function of distance in samples, which implies that the Cu/Nb interface is an efficient defect sink. Another example is on Cu/Fe nanolayers by *in situ* Cu ion irradiation experiment in TEM (Fig. 3.2b). The evolution of defect clusters under irradiation has been quantified in real time. An increase in defect-generation frequency is observed further away from the Cu/Fe layer interfaces and the defect-generation frequency reaches a maximum near the center of the Cu layers [405].

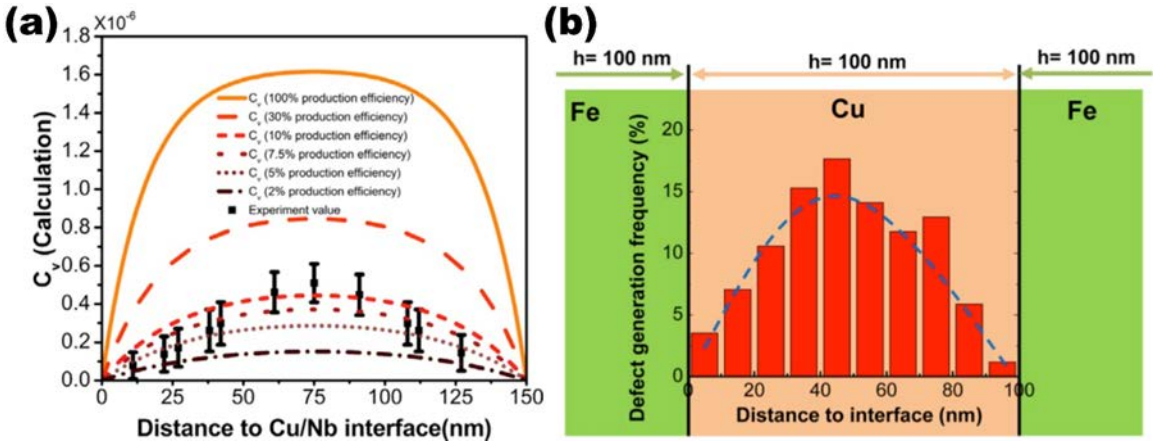

Fig. 3.2 (a) Sink strength of Cu/Nb nanolayers (from experiments): The local steady-state vacancy concentration plotted as a function of distance in samples irradiated to 8×10^{14} at 300ºC along with calculated vacancy concentration profile based on a steady-state rate equation and varying defect production efficiency [404]. (b) A statistical study on the accumulative frequency of defect clusters generated in Cu layers in Cu/Fe 100 nm nanolayers acquired during *in situ* Cu ion irradiation (3MeV) in TEM (0.25-0.31 dpa in 160 s). Fewer defects are identified near the Cu/Fe interfaces during radiation. The defect-generation frequency reaches a maximum in the center of the Cu layers. The dashed line is a visual guide that delineates the defect cluster-concentration profile [405].

Layer thickness dependent defect concentration

According to Eq. 3.13, a higher population of layer interfaces (or smaller h) leads to higher sink strength. The corresponding mean defect concentration in layers is expected to be lower as well. As shown in He ion irradiated Cu/Nb nanolayers (in Fig. 3.3), layer thickness dependent distribution of void density was observed [406]. Meanwhile, a void depleted zone at the interface was identified. Similar scenarios have been studied by He ion and proton irradiation in immiscible Ag/Ni nanolayers [403].

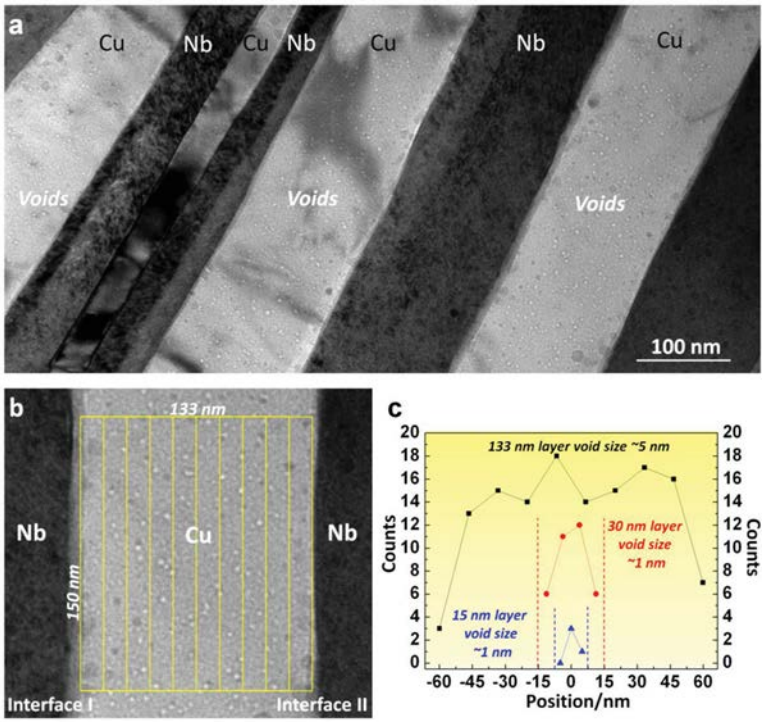

Fig. 3.3. Interface affected zone in He ion irradiated Cu/Nb nanolayers. Bubble distribution in layered structure (Cu/Nb with high-energy interfaces). (a) He ion irradiation-induced voids in Cu layers in irradiated ARB Cu/Nb nanolayers with 135 nm individual layer thickness. (b) Illustration of the method to determine the void number density in Cu layers. (c) The plot of the number density of voids as a function of distance from the center of the layer in 133 nm-, 30 nm-, and 15 nm-thick Cu layers. For each layer thickness, voids were counted over a length of 150 nm in Cu layers [406].

Void denuded zone at the layer interface

Generally, defect concentrations near interfaces are reduced in comparison to the steady-state concentration in the interiors of layers. When local concentration is less than the critical

concentration needed for void nucleation, a void denuded zone may form near the interface [407]. As shown in Fig. 3.4, a clear void denuded zone in He ion irradiated SiOC/Fe multilayers has been observed [408].

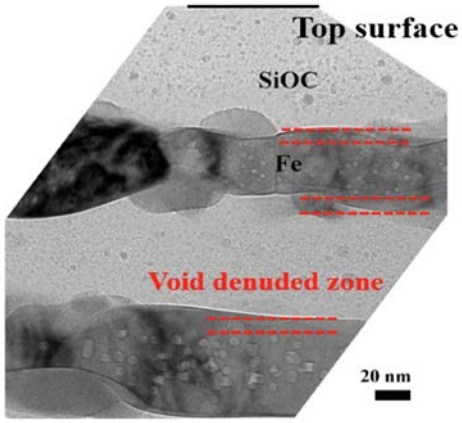

Fig. 3.4. Void denuded zone in He ion irradiated SiOC/Fe multilayer: Typical cross-sectional TEM images from SiOC/Fe multilayers. The formation of nanovoids in the SiOC/Fe multilayer after 600 °C irradiation to 10.7 dpa [408].

3.3. Size effect on mitigation of radiation damage in nanolayers

The initial motivation for investigation on radiation damage in nanolayered composites hinges on the hypothesis that certain types of layer interfaces can absorb radiation induced defects, and thus alleviate radiation damage [409, 410]. The studies on radiation damage in nanolayer systems can be classified into two categories: one on sink efficiency and the other one on sink strength. As pointed out in [411], sink efficiency describes the ability of a single, specific interface to absorb defects from the neighboring grains, which is related to the interface feature, such as misfit dislocation patterns at the interface; while sink strength describes the net effect of defect traps (distributed throughout the material) on the average radiation induced defect concentration [396]. Thus it is often accepted that sink strength may depend on the sink efficiency of the interface

and the thickness of the layers (size dependence of radiation damage) as described in Eq. 3.13 and 3.14.

The influences of various types of interfaces on size dependent radiation resistance have been studied in numerous nanolayer systems, including metallic nanolayers with FCC/BCC, FCC/FCC, BCC/BCC, BCC/HCP, FCC/HCP interfaces, metal/amorphous, and metal/ceramics nanolayers. Among them, FCC/BCC system attracts intensive attention both theoretically and experimentally. Thus, we will review more studies on FCC/BCC systems, as these studies would also shed insights on radiation tolerance in other nanolayer systems.

The FCC/BCC systems reported in literature include Cu/Nb (experiments [307, 404, 406, 409, 410, 412-422] and modeling [401, 423-438]), Cu/V [121, 439, 440], Cu/Mo [441, 442], Cu/W [443-446], Cu/Fe [405, 447], Ag/V [448, 449] and Ni/Fe [450, 451]. Different types of interfaces have various sink efficiencies. Most FCC/BCC systems explored experimentally show a clear trend that radiation damage is alleviated by decreasing h. Some of these examples in Cu/Nb [410], Cu/V [121] and Cu/Fe nanolayers [447] are shown in Fig. 3.5.

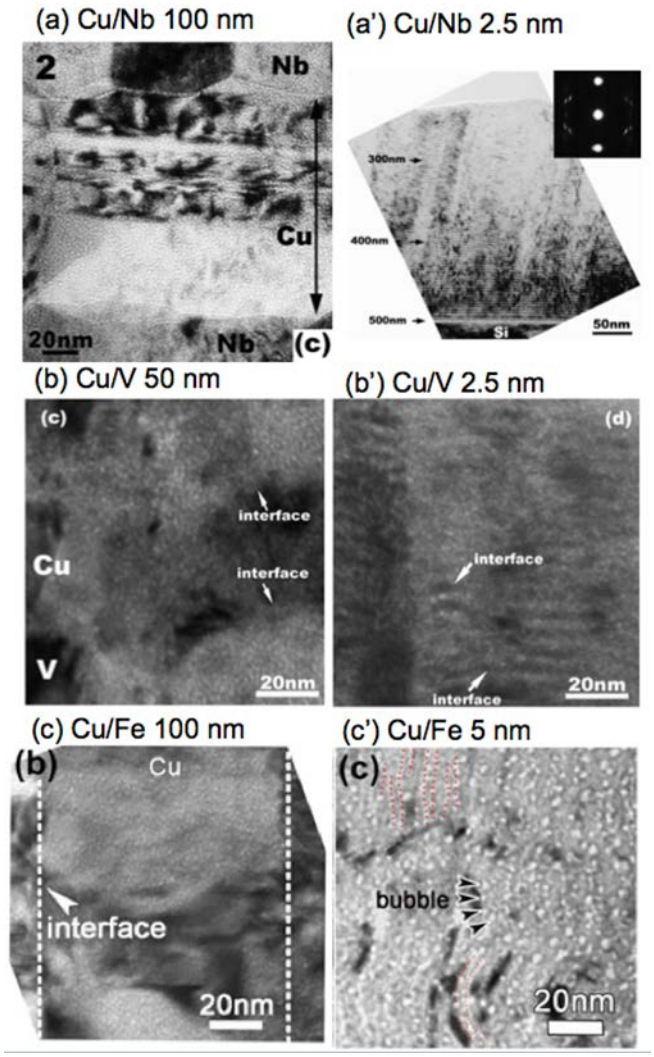

Fig. 3.5. Several FCC/BCC multilayer systems showing layer interfaces can suppress He ion irradiation damage: Cross-section TEM micrographs of several FCC/BCC nanolayer systems showing size effect (layer thickness dependent evolution of He bubble density) (a, a') Cu/Nb [410], (b,b') Cu/V [121] and (c,c') Cu/Fe [447]. In general, He bubble density is much lower in nanolayers with small h.

In general, layer interfaces promote the recombination of opposite type of point defects and hence reduce the accumulative radiation damage, such as defect (He bubble) density and swelling. A systematic study on He bubble induced swelling in Cu/V nanolayers clearly shows continuous swelling reduction with decreasing h (Fig. 3.6) [121]. However, the derivation of correlation between swelling and h from the simplified diffusion equation (Eq. 3.1) is non-trivial.

Other factors, such as the migration of other defects (e.g. di-vacancies) besides point defects, temperature dependent vacancy-interstitial mutual recombination, need to be considered to provide a better estimation of swelling. In addition, with increasing population of He bubbles generated inside layers, the void sink strength has to be involved in the diffusion equation as well.

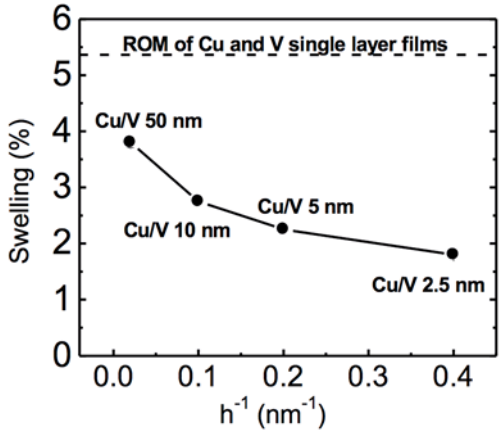

Fig. 3.6. He bubble induced swelling (measured from step height) in Cu/V nanolayers [121]. Swelling vs. 1/h in ion irradiated Cu/V nanolayers, where h is individual layer thickness, shows a continuous swelling reduction with decreasing layer thickness. The rule-of-mixture (ROM) swelling in irradiated Cu and V single layer films is also shown by the horizontal dash line.

Although there are abundant studies on size effect on radiation damage in nanolayers, the research on the influence of fluence (dose) on size dependent radiation response of nanolayers remains limited. Fu *et al.* demonstrated that the bubble density in He ion irradiated Cu/V is strongly tied to the radiation fluence [440] (Fig. 3.7), that is the magnitude of peak bubble density increases with (He ion) fluence before reaches a saturation. Furthermore size effect on alleviation of radiation damage remains prominent in these fluence dependent radiation studies.

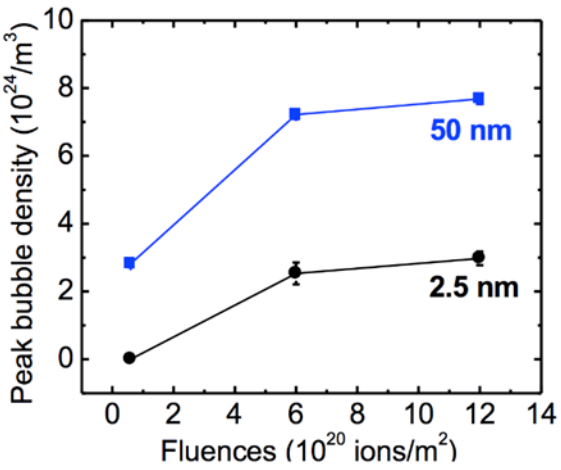

Fig. 3.7, Size effect vs dose dependence: Plot of peak He bubble density, obtained from XTEM micrographs taken at the same under-focus distance of 400 nm, as a function of fluence for ion irradiated Cu/V 50 and 2.5nm multilayers [440].

3.4. Nature of interface on irradiation response of nanolayers

The roles of various types of interfaces in alleviation of radiation damage have been studied in numerous nanolayer systems. Different types of interfaces exhibit various sink efficiencies. Three important interface characteristics (misfit dislocation arrays, coherency stress, and miscibility) are highlighted here to uncover their respective influences on interface-defect interaction.

3.4.1. Incoherent immiscible interface - Influence of misfit dislocation arrays

As described in Chapter 1, radiation can induce various types of vacancy and interstitial clusters. When these clusters migrate to layer interfaces, they may break down into point defects and in turn modify the interface structure simultaneously [424, 452]. Layer interfaces promote the recombination of these vacancies and interstitials. However, He bubbles at interfaces are different as the inert gas atoms stabilize vacancy clusters at interfaces.

He is a byproduct of neutron capture (n,α) reactions. As He solubility in most metals is extremely low [453-455], it tends to migrate and get trapped by defects. For instance, He can rapidly combine with vacancy and their clusters to reduce their formation energy, leading to the formation of He bubbles. Pressurized He bubbles may grow continuously to become pressurized voids and embrittle the irradiated materials [433]. At least two strategies have been applied to delay the transformation of He bubbles into voids and extend the lifetime of irradiated materials: 1) maximize the critical bubble diameter beyond which bubbles transform into voids, or 2) increase the number density of stable He bubbles by maximizing the number of He bubble nucleation sites [411]. The interests of introducing nanolayers with high-density interfaces to manage He bubbles arise from the assumption that certain types of layer interfaces can store He atoms and provide abundant nucleation sites of He bubbles, especially when h is only a few nm.

Threshold He concentration

The hypothesis of He storage at layer interface was proposed in 2005 [409]. It follows, there is a critical He concentration, below which, He atoms are distributed uniformly along layer interface without forming He bubbles. The hypothesis for threshold He concentration to form He bubbles has later been validated in He ion irradiated Cu/V [121], Cu/Nb (synthesized by sputtering [426] and accumulative roll bonding [420]), Cu/Mo [441] nanolayers via nuclear reaction analysis (NRA) and through-focus cross-sectional TEM studies (Fig. 3.8).

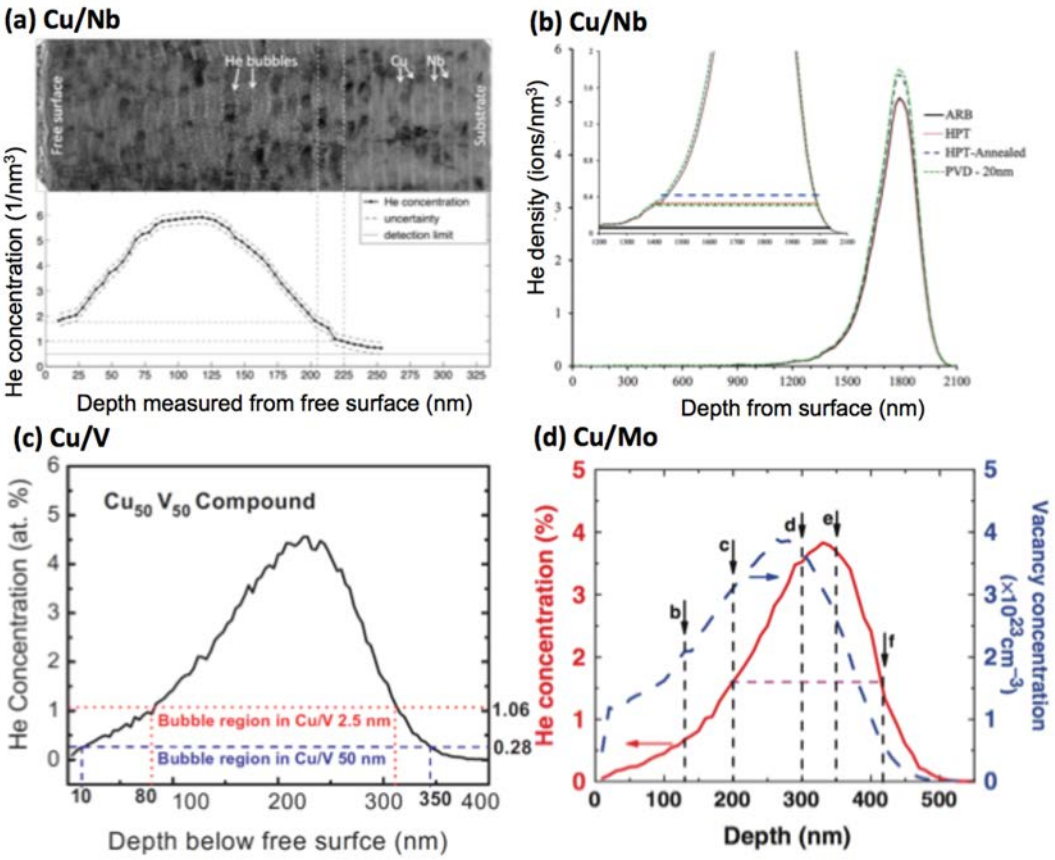

Fig. 3.8. Experimental evidence for threshold He concentration to form He bubbles in nanolayers [121, 420, 426, 441]: (a) Cross-section TEM image of He ion irradiated Cu/Nb 5.6 nm nanolayer and the corresponding He concentration profile show no He bubbles were detected in the surface region when He concentration is < 1.4/nm^3 [426]. (b) In Cu/Nb nanolayers deformed by accumulative roll bonding (ARB) or high pressure torsion (HPT), similar phenomenon was observed. Horizontal lines in inset Fig. show and the range where He bubbles were observed for each specimen [420]. (c) The minimum He concentration beyond which He bubbles are detectable in Cu/V 2.5 nm is 1 at.%, ~ 4 times greater than that (0.26 at.%) in Cu/V 50 nm nanolayers [121]. (d) The He (solid curve) and vacancy concentration (dashed curve) profiles of He irradiated Cu/Mo 5 nm films. Note that locations c and f have the same He concentration, but the vacancy concentration at c is a lot greater [441].

When converted to number of He atoms per unit of interface area, the critical concentrations at which He bubbles are observed in sputtered and roll-bonded Cu/Nb, Cu/V and Cu/Mo are ~ 8.5 [426], ~1.1-5.8 [420], ~1.9 [121] and ~3 [411, 441] atoms/nm^2, respectively. The different interfacial He storage capacity is ascribed to different density of misfit dislocation intersections (MDIs) at interfaces, which will be discussed later.

Beside the He storage capacity of different interfaces, He/vacancy ratio can also affect the formation of He bubbles. As shown in Fig. 3.8d, Stopping and Range of Ions in Matter (SRIM) simulation predicts that the He concentration in Cu/Mo nanolayers is identical at locations c and f. However, He bubbles clearly align along the layer interfaces at location f, while not at location c. A major difference is that the location f, at the tail of radiation zone, has much lower vacancy concentration than that in region c [32]. Greater vacancies will trap more He atoms and form tiny He-vacancy clusters, not detectable in TEM. At the tail of the irradiated specimen, where the vacancy concentration is low, He can migrate readily to the layer interfaces instead of being captured, by vacancies. Hence, He can combine with vacancies at the interface to nucleate bubbles.

Bubble nucleation

The nature of interfaces determines their He storage capacity. Several studies reported that the MDI density dominates the density of He atoms stored at the interfaces. Interface with a higher density of MDIs can store more He atoms, as shown in Fig. 3.9a-c. The information of MDIs can be achieved by atomistic simulations [424] or O-lattice theory [423, 436]. For the same interfacial crystallography, misfit dislocation densities increase following Cu/V < Cu/Mo < Cu/Nb. With known He storage capability, it can be calculated that each MDI can store ~ 25 He atoms in both Cu/Nb and Cu/V without forming a He bubble [304], which is far beyond expectation from the solubility of He in metals. Motivated by this observation, Kashnath *et al.* initiated the study on the state of He atoms at interfaces and proposed a new class of He precipitates at interfaces: nanoscale platelets [431].

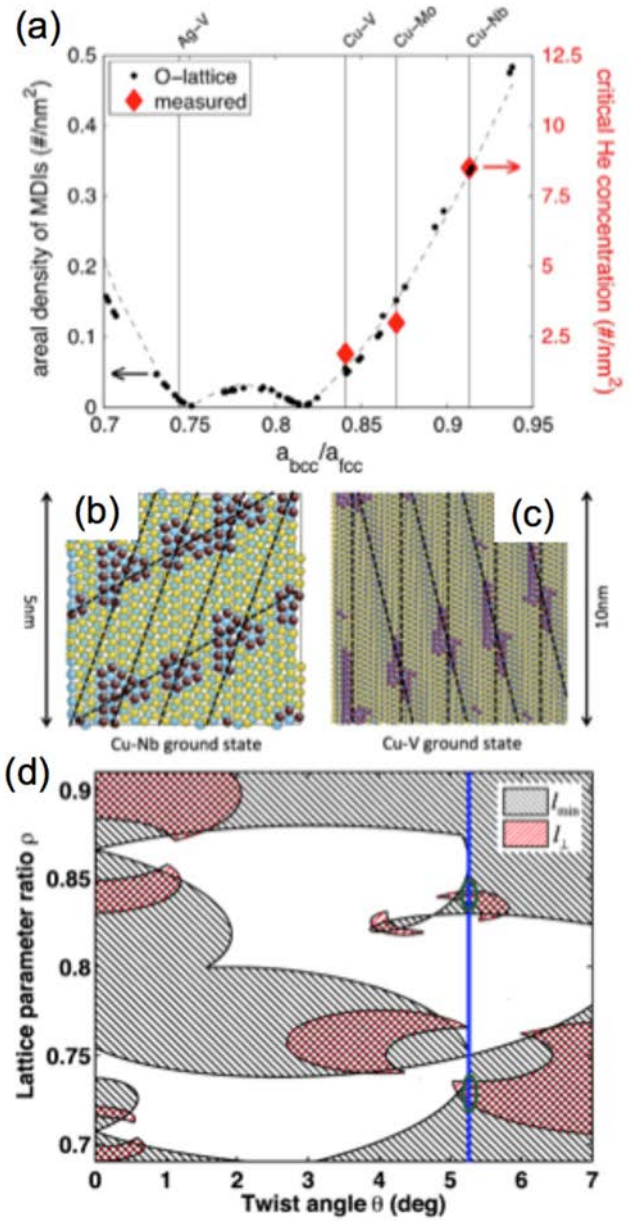

Fig. 3.9. (a) Black dots are areal densities of MDIs calculated by O-lattice theory for a range of FCC/BCC pairs with different lattice parameter ratios, but identical interface crystallography (Kurdjumov–Sachs orientation relation and closest-packed interface planes). Red diamonds are measured critical He concentrations to detect He bubbles in TEM. The dashed line is a visual guide [304]. (b) and (c) show the MDIs in Cu/Nb and Cu/V interfaces. Dashed lines indicate interface misfit dislocations [304, 426]; (d) The solution space for the design problem is the intersection of envelopes satisfying the restriction on l_{min} imposed by design criterion 1(black hatching) as well as the restriction on $l_{\perp}$ imposed by criteria 2 and 3 (red hatching). The vertical blue line at $\theta \approx 5.26^{o}$ denotes interfaces synthesized by PVD. Ovals highlight the intersection of the solution space with this line [436].

He atoms near interfaces prefer to migrate towards interfaces and stay thereafter [433]. Among dislocation lines, MDIs and coherent structures (separated by misfit dislocations) at interfaces, MDIs are the favorite sites for He trapping, where He platelets form by wetting high-energy interface regions. As shown in Fig. 3.10, the He platelets remain stable under irradiation up to ~ 20 He atoms. The clusters are two atomic layer thick and expand as flat platelets by increasing the interface area they occupy, consistent with the previous experimental observation of ~ 25 atoms. When their sizes increase beyond 20 He atoms, however, the clusters grow by increasing their thickness one layer at a time while maintaining a constant area along the interface, forming 3D bubbles. Thus, stable storage of He at interfaces leads to less He-induced swelling prior to bubble/void formation as the volume of such platelets is nearly three times smaller than that of bubbles in FCC Cu.

He platelet-to-bubble transitions are driven by a competition among three types of pressure acting on interfacial He-filled cavities [152, 417, 431]: the mechanical pressure P_{He} of the trapped He gas, the osmotic pressure P_V due to the flux of radiation-induced vacancies to the cavity, and the capillary pressure P_C arising from the surface energy of the cavity. P_{He} and P_V tend to expand the cavity while P_C tends to shrink it. If the three pressures reach balance, i.e.,

$$P_{He} + P_V = P_C \tag{3.15}$$

then the cavity is in equilibrium: it neither expands nor contracts [152]. Platelets have higher capillary pressures than spherical bubbles, which balances the mechanic and osmotic pressures. However, when a platelet grows beyond the “heliophilic” interface region and reaches surrounding “heliophobic” interface region, the capillary pressure drops and the He platelet tends to transform to spherical He bubble.

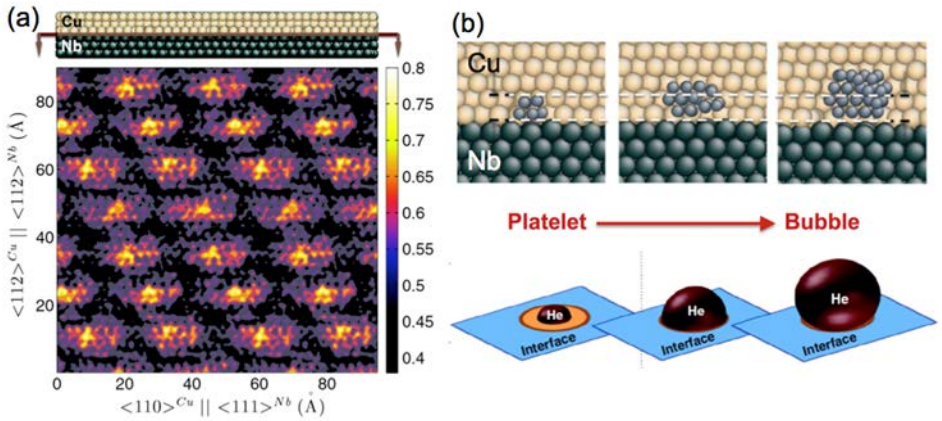

Fig. 3.10. He platelet – bubble transition at Cu/Nb interface: Location dependence of γ_{CuNb} (J/m^2), looking normal to the interface plane. (a) Patches of highest energy coincide with MDIs. Atomistic modeling of the evolution of He–vacancy clusters at an MDI at a Cu/Nb interface. (b) These clusters initially grow as flat platelets by wetting regions of high interface energy. Later on, the He platelet transforms into a more equiaxed precipitate above approximately 20 He atoms [431].

With the understanding of the role of MDIs, Yuryev and Demkowicz [436] developed a solution space (Fig. 3.9d) to search an optimized interface design that allows the bubbles to connect in one direction to form channels and to separate bubble channels far enough that they do not interact with each other in the other direction. This approach can be realized by tuning two parameters that influence MDI distributions: the ratio of cubic lattice parameters in the neighboring crystals and the twist angle describing the relative rotation of the crystals parallel to the interface plane. The essential idea of this study lies in the hypothesis that He atoms can migrate out of the material through these bubble channels instead of forming large bubbles/voids. Therefore, the design of dislocation patterns at interfaces becomes an important topic [435, 456].

Another interesting experimental study on the sink efficiency of different interfaces is shown in Fig. 3.11. Significant variations in interfacial Cu vacancy sink efficiency (η) were measured for interfaces including approximately ideal Cu/Nb sinks with Kurdjumov-Sachs (KS) ($\eta > 0.9$) interfaces, a moderate Cu/V sink with KS interfaces ($\eta \approx 0.9$), and an ineffective

heteroepitaxial Cu/Ni sink ($\eta < 0.5$) [422]. The trend is qualitatively consistent with predictions from MD simulations, that is the average point defect absorption probability should be the highest for the Cu/Nb interfaces and the lowest for the Cu/Ni interfaces [429].

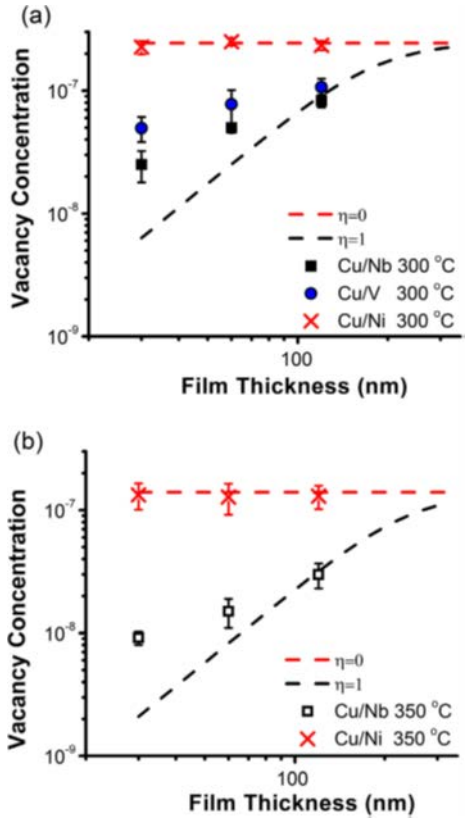

Fig. 3.11. Vacancy concentration at the center of the film plotted as a function of film thickness measured at (a) 300ºC and (b) 350ºC. Calculated trends for the bounding sink efficiencies of η = 0 and η = 1, assuming a defect production efficiency of 1%, are plotted as a guide [422].

3.4.2. Immiscible coherent interfaces – The influence of coherency stress

Prior studies on radiation damage in nanolayers suggest that incoherent interfaces with high-density misfit dislocations and MDIs are more efficient in alleviating radiation damage. One evidence is that coherent twin boundaries in nanotwinned Cu without misfit dislocations do not reduce the density of He bubbles comparing to the single crystal Cu under He ion irradiation [457]. However, as will be shown extensively in Chapter 4, nanotwinned metals have outstanding

radiation tolerance as TBs are effective defect sinks. Furthermore several studies show that immiscible coherent interfaces may also play a positive role in mitigating radiation damage. In He ion irradiated (100) Cu/ Co with coherent FCC/FCC interface [458], a clear size dependence is observed. He bubbles nucleate and align along the coherent Cu/Co interfaces (Fig. 3.12a-b), presumably due to the following reasons. First, the interaction between radiation induced defects and coherent interface may create disconnections at interfaces, which serve as defect sinks. Second, the coherency stress may promote defect migration towards layer interfaces [438]. Third, the coherent Cu/Co interface may inhibit bubble growth, similar to the radiation response of incoherent interfaces. In fully coherent immiscible FCC Cu/Fe 0.75 nm nanolayers [447], He bubbles nucleate and align within the Cu layers (Fig. 3.12c-d). The alignment of abundant He bubbles inside the Cu layers consumes a large amount of He atoms and vacancies, and the interface confinement prohibits the coarsening of He bubbles, thus suppresses the formation of voids. The alignment of He bubbles in narrow nanolayers is, to some extent, similar to the construction of directional He storage/transportation channels to store more He atoms by reducing the spacing of MDIs in one direction [436].

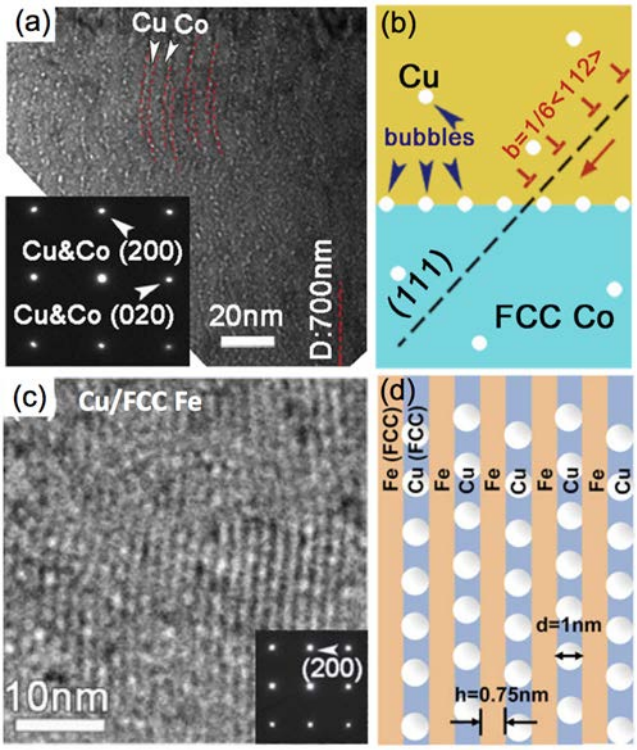

Fig. 3.12. (a) XTEM image and schematics show that in He ion irradiated immiscible coherent Cu/Co 5 nm nanolayers, clear alignment of He bubbles along layer interfaces. The embedded SAD pattern shows that the film retained epitaxial structure with fully coherent FCC (100) Cu/ Co interface [458]; (c-d) The fully coherent FCC Cu/Fe interface in Cu/Fe 0.75 nm nanolayers subjected to He ion irradiation to 2.5 dpa. He bubbles prefer to nucleate in Cu layers and are constricted to reside inside the Cu layers, resulting in smaller bubble size compared to bubbles in other Cu/Fe nanolayers with larger h [447].

Recently, Vattre *et al.* proposed that the reduced defect migration energies/barriers near interface might be primarily responsible for the enhancement in sink strength, inducing a preferential drift of point defects towards interfaces [438]. As shown in Fig. 3.13a-b, the reduced defect migration barriers arise from the elastic field in the layered structure. The sink strength of interface for both vacancies and interstitials with elastic interaction (blue line in Fig. 3.13c-d) is significantly higher than that without elastic interaction (orange line in Fig. 3.13c-d). Furthermore, the recombination of vacancies and interstitials could also be promoted by the emission of interstitials from the interface into layer interior [430], which is similar to another observation near

GBs [183].

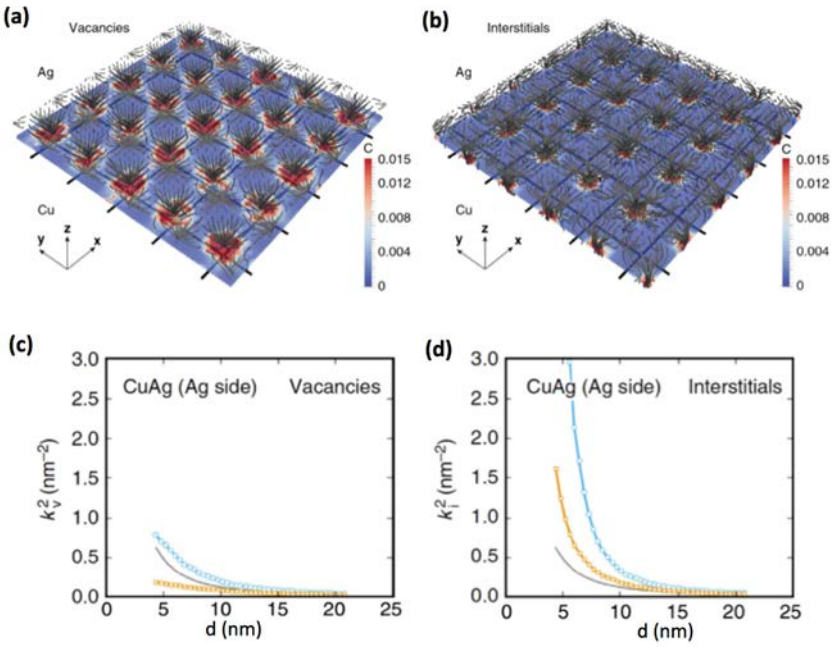

Fig. 3.13. Interface stress enhance the sink strength of layer interfaces: (a-b) Migration paths and local concentrations of (a) vacancies and (b) interstitials on the Ag side of the semicoherent Ag–Cu interface. Migration paths are shown as grey lines originated from 1 nm away from the interface. The square grid of black lines represents interface dislocations. The normalized concentrations of point defects are plotted in a plane located two atomic distances away from the interface. Any normalized concentration values higher than 0.015 are shown as equal to 0.015. (c-d) Enhancement in sink strength of semicoherent interfaces. Sink behaviors of Ag–Cu interfaces for (c) vacancies and (d) interstitials in Ag as a function of layer thickness, d. Orange and blue lines correspond to the object kinetic Monte Carlo (OKMC) calculations without saddle point anisotropy and with the fully anisotropic interaction model, respectively [438].

3.4.3. Miscible layer interface – radiation induces intermixing

Immiscible nanolayer systems retain the layer interfaces under radiation as the positive heat of mixing between the layer constituents thermodynamically drives the demixing process to maintain chemically distinct layer interfaces during radiation or annealing. In contrast, irradiation of miscible nanolayer systems can induce significant interdiffusion (e.g. Cu/Ni [459]), resulting in

the formation of intermetallics (e.g. Al/Nb [460], Al/Ti [461, 462] and Fe/W [463]) or amorphous structure (e.g. Ni/Ti [464, 465]). Taking Al/Nb nanolayer as an example [460], Fig. 3.14 shows the chemistry of layer interface in surface, peak damage and unirradiated regions of He ion irradiated Al/Nb nanolayers. The peak damage region clearly shows interdiffusion between Al and Nb, forming intermetallics at interfaces.

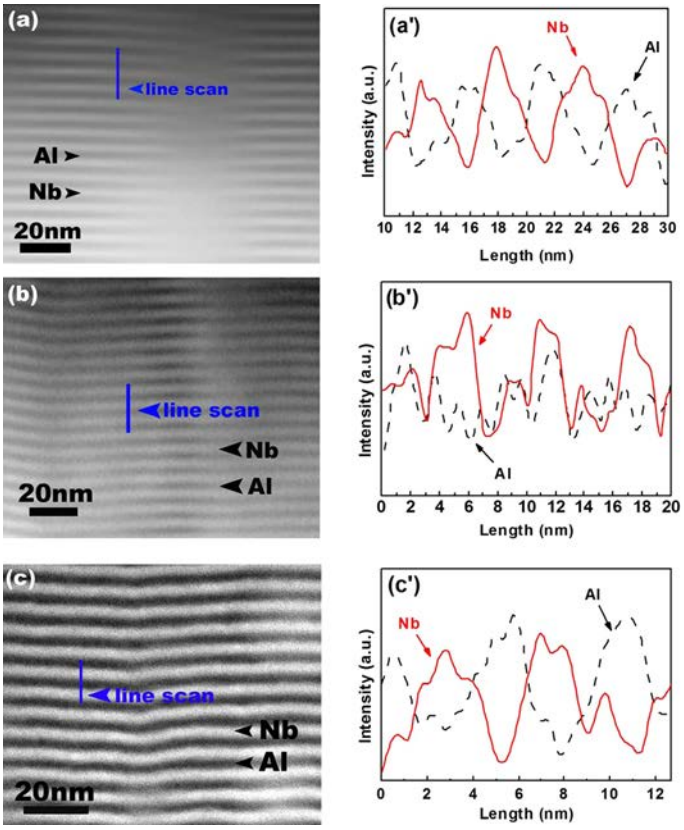

Fig. 3.14. STEM micrographs of He ion irradiated Al/Nb 2.5nm multilayers at (a) surface, (b) peak damage, and (c) unirradiated region. Distinctive layer interfaces are clearly resolved in all regions. Figures (a')–(c') show the corresponding composition analyses along line markers. Modulated composition profiles are revealed in (a') and (c'), but intermixing clearly occurs in region (b') [460].

3.5. Alternative mechanisms to reduce defect density in nanolayers

The role of interfaces is not just limited to the annihilation of defects at layer interfaces. The sandwiched layers can provide a sweeping channel for dislocations to annihilate defects with opposite nature. *In situ* TEM snapshots have captured one such typical defect annihilation process in Fe/Fe_2Zr nanolayers [466]. A dislocation loop A (outlined in circle in Fig. 3.15(a)) nucleated at 0.755 dpa migrated until it encountered and annihilated loop B within the same layer. The Fe_2Zr layers have become amorphous after slight radiation and the crystal/amorphous layer interface confines the migration of dislocation loops within the Fe layers. It remains unclear if such a mechanism may also operate in other multilayer systems given limited studies to date. Further studies on radiation damage in multilayers with crystal/amorphous interfaces are necessary to substantiate such a mechanism.

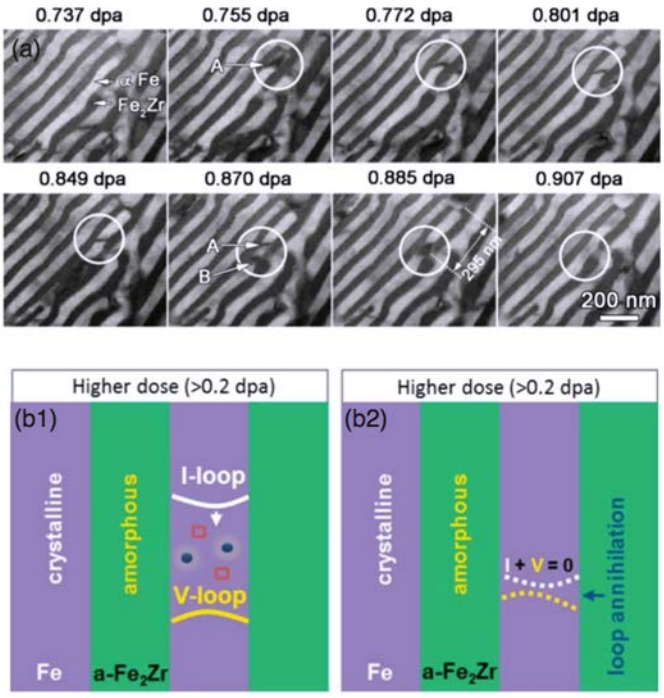

Fig. 3.15. *In situ* evidence showing the Fe/amorphous Fe_2Zr interface assisted defect annihilation in Fe layers. (a) *In situ* TEM snapshots of dislocation loop migration over a dose range of 0.737–0.907 dpa (over 70 s) in confined nanolaminates. At 0.755 dpa, a dislocation loop A was generated and started to migrate within the α-Fe layer, as outlined by the circle. Loop A migrated over a

distance of 295 nm by 0.885 dpa before it encountered loop B. The two loops then interacted and combined with each other. (b) Schematics of the defect removal mechanism illustrating the migration of dislocation loops in α-Fe channels confined by the crystal/amorphous layer interface and the recombination of dislocation loops with opposite nature [466].

3.6. Radiation damage in ceramic nanolayers - amorphization and nanocrystallization

Radiation damage in ceramic nanolayers is a complex subject due to the complicated structure of oxide compounds, the higher bonding energy of ceramics, electrostatic effects, and penchant for preserving stoichiometry in compounds [467]. Certain ceramic nanolayers, such as CrN/AlTiN [468, 469] and TiN/MgO [470], can effectively remove radiation induced defects as layer interfaces can act as defect sinks, and suppress amorphization [471].

Amorphization is an important issue for irradiated ceramics [472]. Some ceramics have a higher tendency for amorphization under radiation than others [473]. For instance, in $CeO_2/SrTiO_3$ system [474], enhanced amorphization at interfaces was observed because (1) layer interfaces act as biased sinks for different types of defects, that is interface steps attract cation interstitials, leaving behind an excess of immobile vacancies; and (2) defects at interface steps induce significant structural and chemical distortions.

However, in TiN/AlN nanolayers [471], suppression of amorphization in AlN layers and the reduction of irradiation-induced softening were observed (Fig. 3.16). A clear size dependent reduction of radiation damage was observed in these nanolayers. More specifically when h = 10-20 nm, the TiN/AlN nanolayers show the best He ion irradiation tolerance, and a critical layer thickness of more than 5 nm is necessary to prevent severe intermixing. This study suggests that both the interface characteristics and the critical length scale (layer thickness) contribute to the reduction of the He ion irradiation-induced damages in nitride-based ceramic nanolayers. Note that prior studies show that polycrystalline AlN is resistant to radiation induced amorphization

under 700 MeV Bi ion irradiation. Hence it is likely the amorphization resistance of AlN also depends on the types of ion source for radiation studies [475]. In addition, TiN/AlN nanolayers also have good radiation resistance against Ar [476, 477] and Xe [478] ion irradiation to 92-127 dpa. The interfaces remain intact although radiation may lead to lateral grain growth in individual layers.

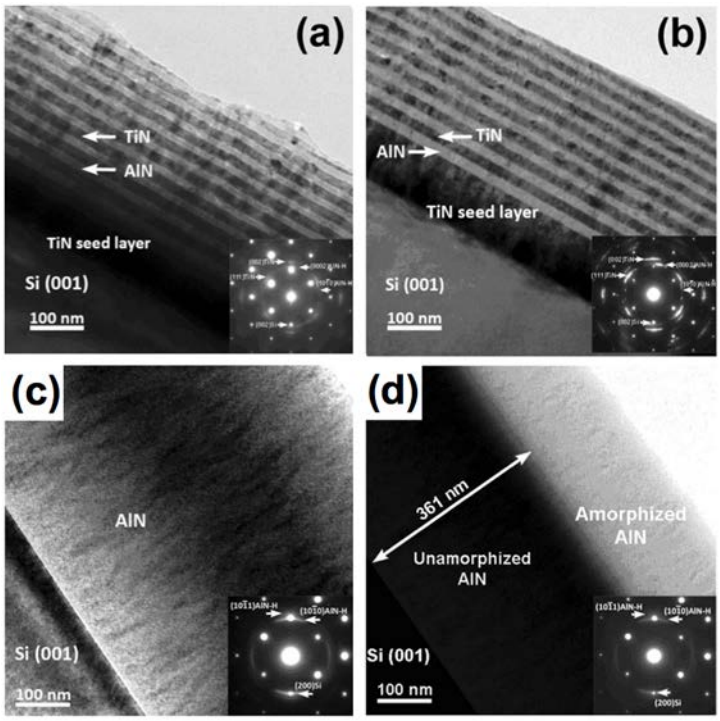

Fig. 3.16. Suppression of amorphization in AlN in by TiN/AlN layered structure under radiation. Low magnification cross-sectional TEM micrographs and SAD patterns of (a) as-deposited and (b) ion irradiated TiN/AlN 20 nm nanolayers after He ion irradiation to ~ 4 dpa. No amorphization is detected. (c-d) In contrast, He ion radiation on as-deposited single layer AlN induced obvious amorphization [471].

Uberuaga *et al.* [479] pointed out that the phase of layer constituents may have an influence on the defect evolution during radiation. They compared radiation damage of $SrTiO_3$ (STO) coupled with three different types of oxides [473, 480, 481], forming near perfectly coherent interfaces and discovered that, under similar radiation conditions, the behavior of STO in the three

systems is very different (Fig. 3.17). In the case of $BaTiO_3$/ STO, no amorphization was observed; in the case of STO/$LaAlO_3$, the STO side amorphized significantly; in the TiO_2/STO sample, the formation of a defect denuded zone at the interface in the TiO_2 side was observed. The drastic difference in radiation response of the materials with same chemistry but different types of interface is surprising as atomistic modeling reveals that there are no thermodynamic trap states for defects at these interfaces (Fig. 3.17d). Based on these interesting observations, Uberuaga *et al.* hypothesize that the controlling parameters (that dictate radiation response of the materials) are the defect properties within each of the bulk phases and that the interface simply acts as a transition point between the two materials. Using a reaction-diffusion model, they demonstrated that the formation and migration energies of defects within each phase determine the eventual response at the interface. The formation energies dictate the direction of flow of defects, while the migration energies dictated the rates of defect flow.

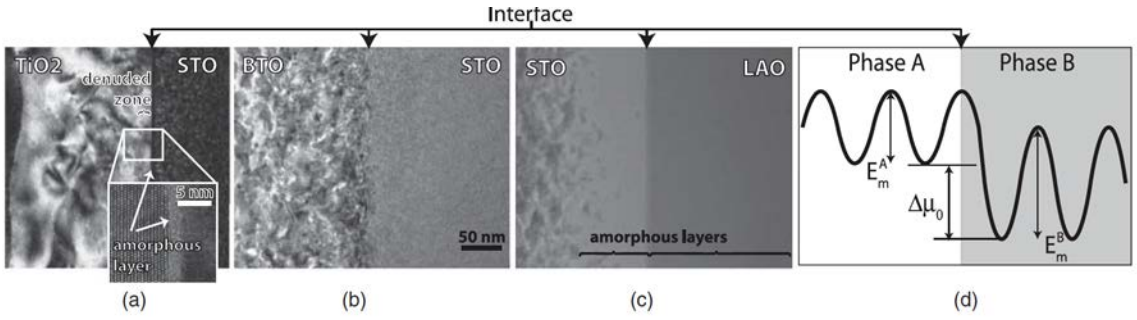

Fig. 3.17. Examples of the irradiation response of different oxide heterointerfaces [479]: (a) $TiO_2/SrTiO_3$, (b) $BaTiO_3/SrTiO_3$, and (c) $SrTiO_3/LaAlO_3$. In each case, the film thickness was between 250 and 300 nm and the irradiation conditions were chosen such that about 3 - 4 dpa occurred just under the interface. In each case, the energy of the implanted Ne and the total fluence were (left) 250 keV, 1.11×10^{16} ions/cm^2, (middle) 300 keV, 1.55×10^{16} ions/cm^2, and (right) 260 keV, 8.23×10^{16} ions/cm^2. The positions of the denuded zone and amorphous layers are labeled. The scale bar for all three images is the same. (d) Schematic of the typical energetic landscape for point defects as determined from atomistic calculations. Details about these experiments and the corresponding atomistic calculations can be found in [479].

Meanwhile, *in situ* radiation experiments reveal the suppression of nanocrystallization in amorphous Y_2O_3 layers by Fe/Y_2O_3 layer interface [482, 483]. As shown in Fig. 3.18, after Kr ion irradiation to 7.8 dpa, the as-deposited amorphous Y_2O_3 in the Fe/Y_2O_3 50 nm nanolayer crystallized, in contrast to little crystallization in 10 nm-thick Y_2O_3 layers, implying size dependent enhancement of radiation tolerance [483]. Within the interface affected zones (~10 nm), interfaces absorb radiation induced defects and produce interfacial stress to mitigate radiation induced crystallization.

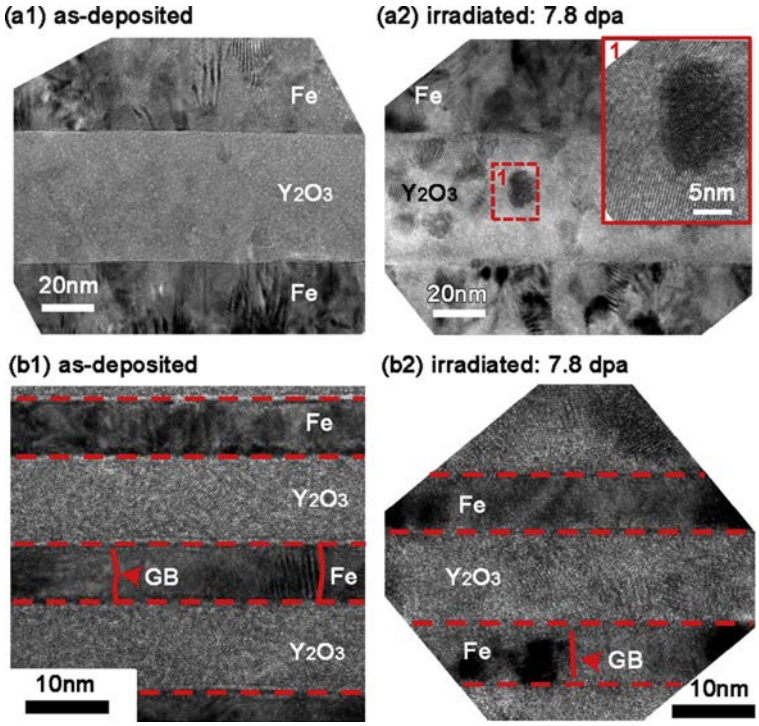

Fig. 3.18. Suppression of nanocrystallization in amorphous Y_2O_3 in Fe/ Y_2O_3 nanolayers [483]. *In situ* Kr ion irradiation studies (room temperature) showing the evidence of suppression of crystallization in oxide layers by Fe/Y_2O_3 interface in Fe/Y_2O_3 multilayers. Comparison of microstructures of Fe/Y_2O_3 50 nm and Fe/$Y_2O_3$10 nm nanolayers before (a1 and b1) and after (a2 and b2) Kr ion irradiation (up to 7.8 dpa) (a1) as-deposited Y_2O_3 in Fe/Y_2O_3 50 nm nanolayer has primarily amorphous phase with some embedded nanograins, (a2) subsequent radiation of Fe/Y_2O_3 50 nm leads to extensive crystallization in the 50 nm thick Y_2O_3 layers. A typical nanograin is shown in the embedded HRTEM image in Fe/Y_2O_3 10 nm nanolayers. Comparison of micrographs before (b1) and after irradiation (b2) shows insignificant variation in microstructure in Fe and Y_2O_3 layers. Y_2O_3 in irradiated Fe/Y_2O_3 10 nm multilayer remains predominantly amorphous.

3.7. Size effect on hardening in irradiated nanolayers

Radiation introduces significant microstructure damage in form of drastic increase in defect density, and in turn prominent irradiation hardening. Irradiation hardening is manifested by increase in yield strength, hardness, flow stress and is often accompanied by loss of toughness and ductility [484, 485] . Hence radiation hardening may be used as an indirect probe to evaluate the influence of radiation damage on deformability of the irradiated materials. Most radiation experiments pertaining to this chapter were conducted by He or heavy ions, the radiation damage resides in shallow surface (a few hundreds of nms to a couple of micrometers). Consequently irradiation hardening in nanolayers is typically measured by nano/micro mechanical testing techniques, such as nanoindentation [486, 487], and micropillar compression in SEM [414, 421, 488] and TEM [419]. Nanoindentation is the most widely used method to probe irradiation hardening. One of the earlier systematic irradiation hardening measurements of metallic nanolayers were performed on He ion irradiated Cu/V system [439] with various h and fluences. Size dependent irradiation hardening has been uncovered: the magnitude of irradiation hardening decreases with decreasing h (Fig. 3.19a). Correlated microscopy studies show that for multilayers with smaller h, the density of He bubbles is significantly reduced, and hence irradiation hardening (due primarily to He bubbles) is expected to be less prominent than that in multilayers with greater h. This size dependent hardening phenomena has also been observed in a variety of other He ion irradiated nanolayers, including Ag/V [448] and Ag/Ni [403] (Fig. 3.19a). Notice that these are immiscible nanolayer systems with incoherent FCC/BCC or FCC/FCC interfaces. Surprisingly, in He ion irradiated immiscible (100) FCC Cu/Co nanolayers with coherent interface, an opposite trend was observed: the magnitude of irradiation hardening increases with decreasing h [458]. In the as-deposited FCC Cu/Co nanolayers, as both Cu and Co have low SFE, mobile Shockley

partials are predominant plasticity carriers. The peak strength of Cu/Co multilayers is determined by the interface barrier strength to the transmission of partials. After He ion irradiation, however, He bubbles align preferentially along the Cu/Co layer interface, consequently partials may have to go through a constriction (to become full dislocations) at the interface before transmission across the layer interface, leading to significant increase in yield strength of the irradiated multilayers with smaller h [458]. There are limited studies on dose and size dependent radiation damage in nanolayers. An example of He ion irradiated Cu/V nanolayers in Fig. 3.19b show that irradiation hardening reaches saturation at lower fluence for multilayers with greater h [440].

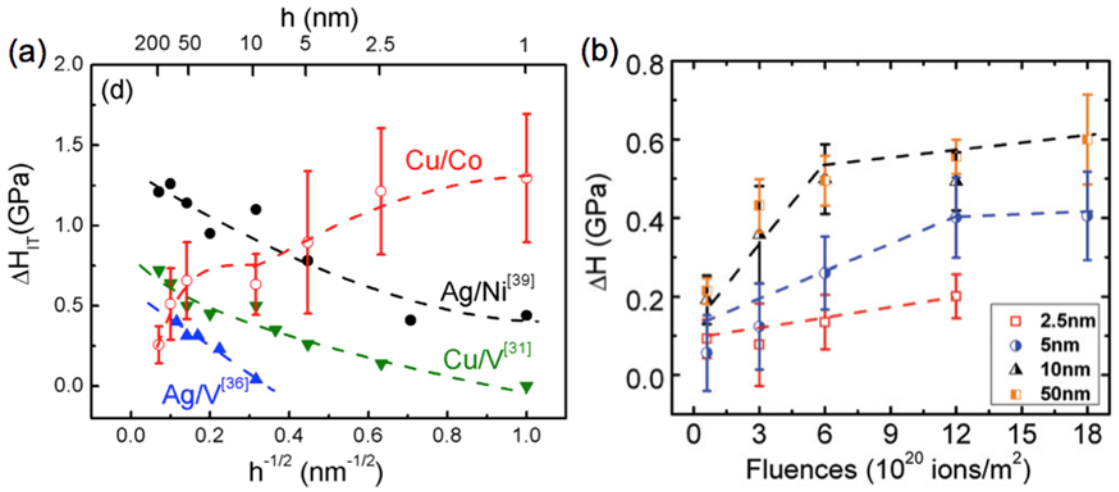

Fig. 3.19. (a) Less irradiation hardening in He ion irradiated Ag/V, Ag/Ni, Cu/V nanolayers with smaller h [458]. (b) Fluence dependence of irradiation hardening in He ion irradiated Cu/V nanolayers [440]. Irradiation hardening approaches saturation at lower fluence in multilayers with greater h.

Although the nanoindentation technique is successful in probing irradiation hardening in irradiated nanolayers, this technique applies a non-uniform stress and strain underneath the tip, thereby leading to the complication of interpreting plastic flow behavior. The development of the micropillar compression test technique has opened new routes to acquire stress-strain curves from

nominally uniaxial compression tests of specimens with small volume [489-491]. Li *et al.* studied compressive flow behavior of He ion irradiated Cu/Nb nanolayers containing uniformly distributed He bubbles [414]. The flow strength of irradiated Cu films increases by more than a factor of 2 due to the introduction of high-density He bubbles (Fig. 3.20a). In contrast in He ion irradiated Cu/Nb nanolayers, the magnitude of irradiation induced strengthening (increase in yield strength) is much less and decreases with decreasing h (Fig. 3.20c-d). When h decreases to 2.5 nm, the Cu/Nb 2.5 nm nanolayer shows insignificant hardening and little loss in deformability. SEM images of Cu/Nb 70 nm micropillars (in Fig. 3.20e) show morphological evolution of as-deposited and irradiated pillars before and after compression. The irradiation induced increase in shear strength has also been studied via *in situ* compression of Cu [492] and Cu-Nb alloy and Cu/Nb nanolaminate pillars in TEM [419].

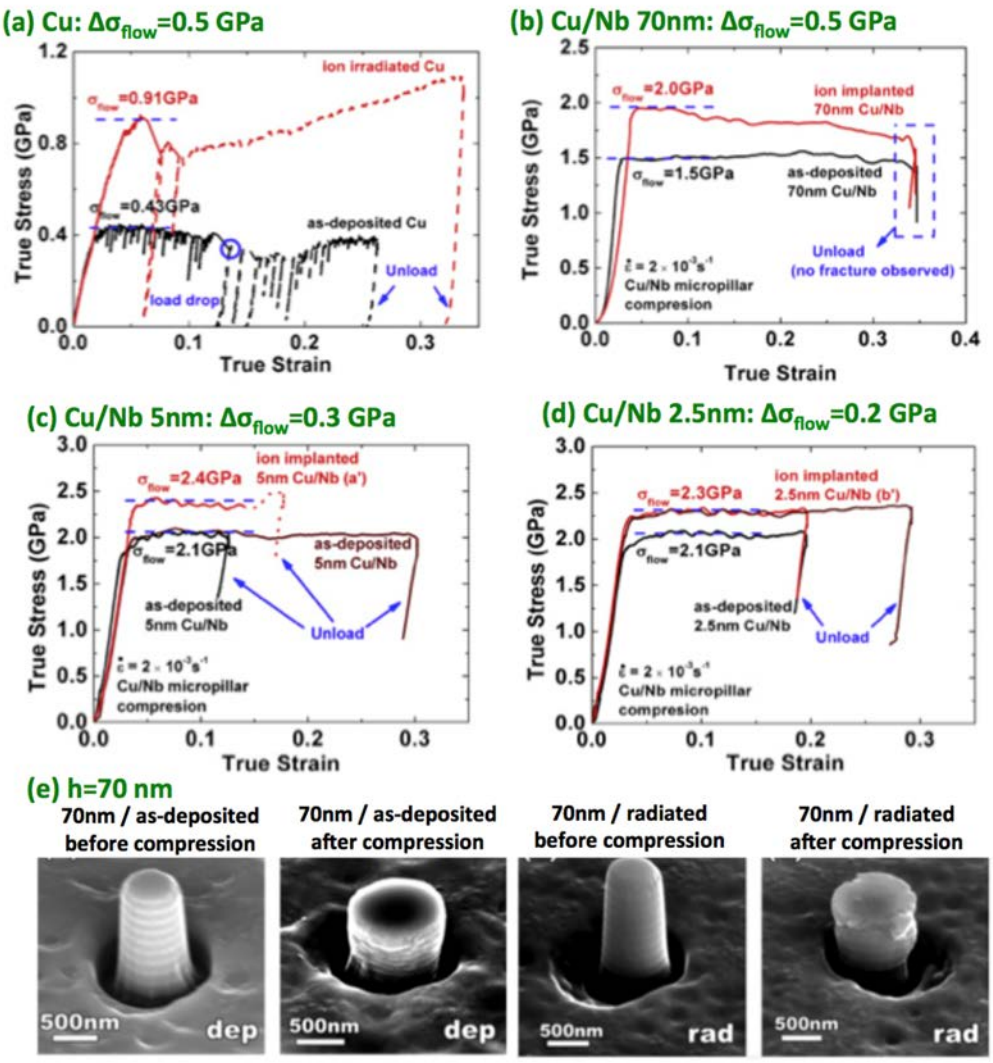

Fig. 3.20. Radiation induced strengthening and variation in plastic deformation ability measured by micropillar compression tests in He ion irradiated Cu/Nb nanolayers. True stress–strain behavior of (a) single-crystal Cu pillar, (b) Cu/Nb 70 nm, (c) Cu/Nb 5 nm, and (d) Cu/Nb 2.5 nm nanolayer pillars before and after He ion irradiation. (e) SEM images of Cu/Nb 70 nm micropillars before and after radiation and pillar compression (Reorganized from [414]).

The irradiation induced hardening mechanisms of nanolayers are very complicated as they are not only determined by the type, dimension, and density of irradiation induced defect clusters, but also by h. Before we discuss the details of the irradiation hardening in nanolayers, the correlated mechanical behavior with various layer thickness will be briefly described. Generally, three regimes have been characterized to describe the size dependent strengthening in as-deposited

nanolayers. (1) When h is large (typically > 50 nm), the strengthening depends on the pile-up of gliding dislocations, and thus follows the classical Hall-Petch strengthening model. (2) At the intermediate layer thickness (when h = 10 - 50 nm), the flow strength of nanolayers is determined by the confined layer slip (CLS) model, and typically follows the Orowan bowing mechanism. (3) When h is small (less than 5 nm), interface barrier strength for a single gliding dislocation dominates the strength of the film (referred to literature [390] for more details). Thus, the understanding on the fundamental mechanisms of irradiation hardening in nanolayers should couple multiple strengthening mechanisms together.

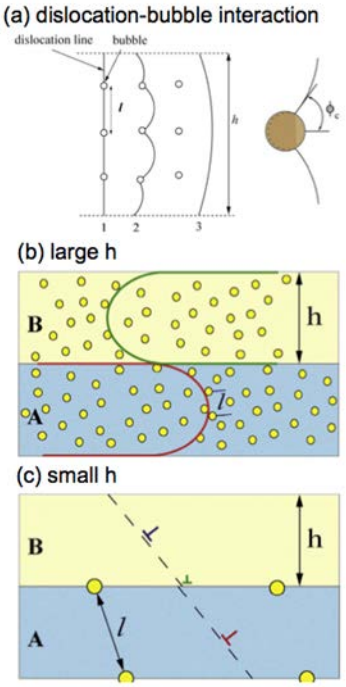

Fig. 3.21. Schematic illustration of gliding dislocation interaction with obstacles (nanoscale He bubbles in this case) of spacing *l*. Φ_C is the semicritical angle at which the dislocation breaks away from the pinning obstacle. (b-c) Schematic illustration of the bubble distribution in nanolayers (the circles indicate bubbles). (b) When h is a few tens of nanometers, h >> *l*, the strengthening mechanism is dominated by the confined layer slip (CLS) model. Gliding dislocations in a given layer are confined by the interfaces and nanoscale bubbles, resulting in a term that adds to the CLS stress; (c) when h is a few nanometers, h < *l*, the yield strength is determined by the crossing of single dislocations across interfaces containing a distribution of nanoscale He bubbles [448].

Irradiation hardening of nanolayers is contributed by both layer constituents and interfaces.

At large layer thickness, (h > 5 nm), the hardening behavior in nanolayers is similar to that in monolithic metals. Radiation induced dislocation loops and He bubbles are generally treated as weak obstacles to the migration of dislocations. The Friedel–Kroupa–Hirsch (FKH) model is commonly used to describe irradiation strengthening ($\Delta\sigma$) arising from weak obstacles [493-495]

$$\Delta\sigma = \frac{1}{8} M\mu b d N^{2/3} \quad (3.16),$$

where M is the Taylor factor (~3 for polycrystalline FCC and BCC metals). μ is the shear modulus, b is the magnitude of Burgers vector of the primary glide dislocations, d and N are the respective average defect diameter and density that can be determined from TEM experiments. This model was initially developed to account for interaction between gliding dislocations and dislocation loops or small cavities without He atoms [493], and yet works well to describe He bubble induced hardening.

A more sophisticated hardening model can be derived from the Orowan model. For strong (impenetrable) obstacles with a separation spacing l, the Orowan model assumes that the glide dislocation bows to a semicircle with a radius of $l/2$ between obstacles. However, it has been shown that the model overestimates the strengthening due to weak obstacles, and thus the Orowan model is modified to [448, 496]:

$$\tau = \frac{\mu b}{2\pi l} \ln\left(\frac{l}{r}\right) (cos\varphi_c)^{1/2} \quad (3.17),$$

where φ_c is half of a critical bow-out angle between lines of a dislocation cutting an obstacle shown schematically in Fig. 3.21a. When $\varphi_c = 0$, this equation reduces to the Orowan formula. The average obstacle spacing l_s is then given by

$$l_s = \frac{1}{\sqrt{2Nr}} \quad (3.18),$$

where r is the radius of the defect cluster, and N is the defect density. For weak obstacles, $0 < \varphi_c < \pi/2$, the spacing of obstacles only involves the two adjacent obstacles on the dislocation line.

Friedel [494] proposes that l is given by:

$$l = \frac{l_s}{\sqrt{cos\varphi_c}} \quad (3.19),$$

Substitution of Eq. (3.19) into Eq. (3.17) yields the Friedel equation [494]:

$$\tau = \frac{\mu b}{2\pi l_s} \ln\left(\frac{l}{r\sqrt{cos\varphi_c}}\right) (cos\varphi_c)^{3/2} \quad (3.20),$$

which is used to predict the radiation hardening with known critical bow-out angle between lines of a dislocation cutting an obstacle. The bow-out angle can be estimated by [497]:

$$cos\varphi_c = \frac{\ln(\alpha \bar{D}/b)}{\ln(l/b)} \quad (3.21),$$

where α = 1 - 4, $\bar{D}$ is a harmonic mean of l and d, given by,

$$\frac{1}{\bar{D}} = \frac{1}{d} + \frac{1}{l} \quad (3.22),$$

where d is the bubble diameter. Theoretically, this model can treat most of the irradiation induced defects. For example, interstitial loops could be treated as a strong obstacle and φ_c= 0. A more simplified Orawan model is [498] written as:

$$\Delta\sigma = M\alpha'\mu b\sqrt{Nd} \quad (3.23),$$

where b, N and d carry the same physical meanings as defined previously. α' is the average barrier strength of the radiation-induced defect clusters [498]. This model is acceptable only when all obstacles have identical strength, arranged on a square lattice in the slip plane [For details see [496]]. In conclusion, radiation hardening from defects, such as bubble, dislocation loops and SFTs, can be tackled by dispersed barrier hardening model appropriately.

When layer thickness is small (h < 5 nm), in pristine nanolayers, the strength of the nanolayers is determined by the transmission of a single dislocation across the interface. In He ion irradiated nanolayers, a high density of He bubbles decorate at interface and therefore, are

responsible for the irradiation hardening. Multiple factors, including interface shear strength and bubble distribution at interfaces, contribute to the flow stress enhancement after irradiation. Recently, a series of micropillar compression tests have been performed on He ion implanted Cu/Mo, Cu/V and Cu/Nb nanolayers with individual layer thickness of 5 nm, in which the implanted He concentration was tuned to correlate with the density of MDIs, so that the average He concentration at each MDI was approximately equal (shown in Fig. 3.22) [421]. After implantation, the flow stress enhancement is proportional to the strength of the un-implanted nanolayer systems. The interfaces with higher density of MDIs and lower shear resistance tend to provide enhanced hardening [421].

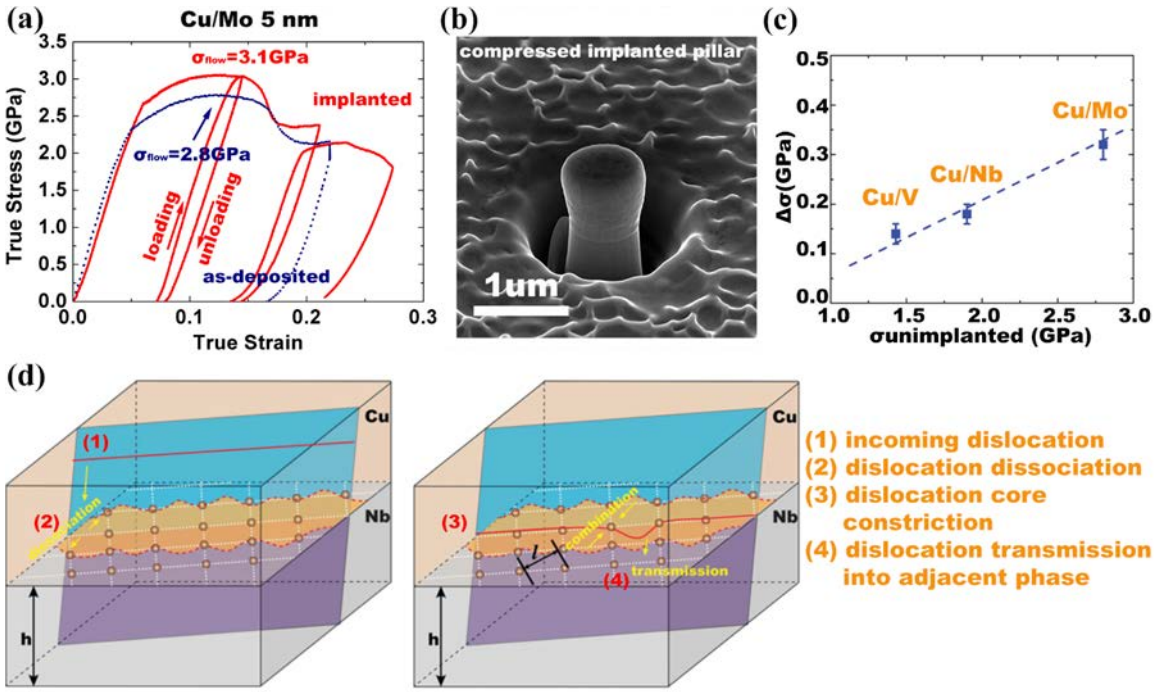

Fig. 3.22. (a) Compressive stress versus strain curves of Cu/Mo 5 nm nanolaminate pillar before (blue) and after (red) 0.8 at.% helium implantation and (b) corresponding SEM image of a compressed implanted nanopillar. (c) Flow stress enhancement introduced by interfacial helium bubbles in He ion irradiated Cu/Mo, Cu/V, and Cu/Nb 5 nm nanolaminate is proportional to the strength of the un-implanted sample. (d) Schematic illustration of the interaction behavior of interfacial bubbles with incoming gliding dislocations (step 1, where the circles indicate bubbles). When the dislocation glides towards and reaches the interface, its core dissociates (step 2) and

spreads along the interface to an extent dependent upon the interfacial shear strength, marked in orange. With higher applied stress, the dislocation trapped at the interface must collapse its core to transmit into the adjacent phase (step 3), which will be affected by the shear strength of the interface as well as the interactive force with interfacial helium bubbles. [421]

In summary, irradiation hardening in nanolayers relies on the relationship between bubble spacing and layer thickness. The increase of shear stress ($\Delta\tau$) due to He bubbles is obtained by the balance between the dislocation line force and resistance from all obstacles with separation distance l and the layer thickness h. The dependence of hardening increment due to bubbles ($\Delta\tau$) on the interface spacing (h) for a variety of multilayers was found to fit the phenomenological form:

$$\Delta\tau = \tau_i \left(1 - \frac{l}{\sqrt{2}h}\right) \quad (3.24).$$

where τ_i is average shear strength to obstacles. When the average bubble spacing is equal to or greater than the layer thickness, bubble hardening is negligible compared to the confined layer slip stress for single dislocations in multilayers. Finally, we summarize the literature to date on radiation damage on nanolayers in Table 3.1.

Table 3.1. Summary of current studies on radiation damage in nanolayers.

	Miscibility	**Coherent/incoherent**	**Radiation source**	**Modeling**
Metallic nanolayers				
FCC/BCC systems				
Cu/Nb	Immiscible	Incoherent	He ion [307, 409, 410, 412-418, 420, 421, 426, 434]; Kr ion [404, 419, 422]	MD [363, 412, 424, 426-434, 437, 499]; Reaction-diffusion model [401]; O-lattice theory [436];

				OKMC [438]
Cu/V	Immiscible	Incoherent	He ion [121, 439, 440]; Kr ion [422]	MD [426]
Cu/Mo	Immiscible	Incoherent	He ion [441, 442]	
Cu/W	Immiscible	Incoherent	He ion [443, 444, 446]	DFT [445]
Cu/Fe	Immiscible	Incoherent	He ion [447]; Cu ion [77]	
Ag/V	Immiscible	Incoherent	He ion [206, 448, 449]	Monte Carlo [363]
Ni/Fe	Miscible	Incoherent	Fe ion [451]	MD [450]
Cu/Ni	Miscible	Coherent/incoherent	Kr ion [422]	MD [459]
Al/Nb	Miscible	Incoherent	He ion [460]	
FCC/FCC systems				
Ag/Ni	Immiscible	Incoherent	He ion [39]; Proton [39]; Kr ion [403]	
Cu/FCC Co	Immiscible	Coherent/incoherent	He ion [458]	
Cu/FCC Fe	Immiscible	Coherent	He ion [447]	
BCC/BCC systems				
Fe/W	Miscible	Incoherent	He ion [463]	Monte Carlo [363]
Cr/W	Miscible	Incoherent	Xe ion [500]	
BCC/HCP systems				
Zr/Nb		Incoherent	γ-ray [501]	
Ta/Ti	Miscible	Incoherent	Ar ion [502]	Monte Carlo [363]
FCC/HCP systems				
Al/Ti	Miscible	Incoherent	Ar ion [461, 462]	MD [503, 504]
Metal/Amorphous (Crystal/Amorphous)				
Fe/SiOC			He ion [505-507] Kr ion [508, 509]	
Cu/Ta	Immiscible	Incoherent	He ion [510]	
Fe/Y_2O_3			He ion [482]; Kr ion [511]	DFT [392]
Cu/CuZr			He ion [487]	
Fe/TiO_2			He ion [512]	
Metal/Ceramics (Crystal/Crystal)				
FeCr/MgO			Ni ion [513]	

$FeCr/TiO_2$			Ni ion [514]	
$FeCr/Y_2O_3$			Ni ion [515]	
W/ZrO_2			Au ion [516]	
Zr/SiC			Xe ion [517]	
Ceramic nanolayers				
CrN/AlTiN			Ar ion [468, 469]	
TiN/MgO			He ion [470]	
$CeO_2/SrTiO_3$				MD [474]
TiN/AlN			He ion [471]; Ar ion [476, 477]; Xe ion [478]	
$BaTiO_3$/ STO			Ne ion [473]	Reaction–diffusion model [479]
$(Ti,Al)N/Ti_2AlN_x$			Ar ion [518]	

Note: Miscibility and coherency are marked in metal/metal systems only.

3.8. Challenges and future outlooks

Although the radiation studies on nanolayer systems have been investigated over a decade, there are still many unexplored subjects. First, most studies on nanolayers focus on He ion irradiation to a dose of several dpa. More comprehensive studies should be conducted by neutron irradiation and heavy ion irradiation, especially to a high dpa level.

Second, current radiation studies on nanolayers are mostly performed at room temperature. The stability of interface subjected to radiation at elevated temperatures (relevant to the service temperatures of materials in nuclear reactors) needs to be examined. Radiation induced dimension and density of defects are expected to be temperature dependent. Radiation damage in nanolayers at elevated temperatures remains a poorly understood subject.

Third, the combination of layer interfaces and MDIs on defect (such as He) management should be considered from a comprehensive point of view. A recent study [363] has shed some light on radiation tolerance of irradiated Cu/Nb, Ag/V, Fe/W, and Ti/Ta interfaces.

Fourth, experimentally there are limited studies on radiation damage in HCP based nanolayers. Meanwhile, mechanical testing of irradiated nanomaterials is limited mostly to nanoindentation and few micropillar compression studies. Tensile tests on irradiated nanomaterials are necessary to validate their application as structural materials in reactor environment.

Finally a majority of theoretical studies on radiation damage in nanolayers focus on point defects. The interaction of dislocation loops and 3D defects, such as voids/bubbles with layer interfaces should also be considered in future simulation studies.

Chapter 4. Radiation damage in nanotwinned metals

Nanotwinned (NT) metals can be synthesized by introducing nanotwins into monolithic metals via pulsed electrodeposition [519] or magnetron sputtering techniques [520-523]. By controlling depostion temperature, deposition rate, and the orientation of growth twins, the average twin spacing can be tailored from a few to tens nanometers. Twin boundaries (TBs) strengthen materials drastically by impeding dislocation motion due to the slip discontinuity, without losing ductility and work-hardening capability due to symmetrical slips across the boundary [524-526]. As a result, NT metals acquire a combination of high strength and strong work hardening capability [519, 527-536]. Moreover, TBs have long been recognized as effective defect sinks in irradiated materials as manifested decades ago in a series of works by Makin [537], Norris [538], King [539-541], Smith [540, 541] and Zinkle [3] *et al.* Different defect-TB interaction mechanisms have been proposed but variations remain that whether a denuded zone can form at a coherent twin boundary (CTB) [537, 538, 542]. Some experiments and simulations point out that a CTB has limited effects on alleviating radiation damage [457, 543], while others provide real time evidence that TBs can act as effective sinks and diffusion channels for radiation induced defects, and consequently, enhance the radiation tolerance of the NT materials [29, 544, 545].

In this chapter, we will start with revisiting the atomic structure of TBs. In particular, we will put more emphases on the structure and behavior of an incoherent twin boundary (ITB) because increasing evidence indicates that a CTB is often defective, containing ITB steps. It is thereby likely that the radiation response of a CTB is signified by that of an ITB. We will procede by highlighting several recent progresses on the radiation response of NT metals and end this chapter by summarizing possible open questions.

4.1. Twin boundaries in FCC metals

TBs are classified into two types: CTBs and ITBs. A CTB is a twin terrace plane (or twin plane), and an ITB is the lateral boundary of a twin. Corresponding to the crystallography of the twin, a CTB is atomically flat without intrinsic dislocations while an ITB contains twinning dislocations. Corresponding to the crystallography of the Σ3 twin in FCC structure, Σ3{111}nt and Σ3{112} TBs are commonly observed (Fig. 4.1a-b), and referred to as CTB and ITB, respectively. Given that the mechanisms of defect-TB interactions are inevitably built up on the structure of CTBs and ITBs, we first give a brief introduction to the atomic configuration of TBs.

4.1.1 Defective CTB

CTBs are widely described as perfect interfaces in early studies and the ability of CTBs in strengthening, maintaining the ductility and minimizing the electron scattering is well documented [519-522, 525, 527]. Recently, Li *et al.* discovered by *in situ* HRTEM mechanical testing and MD simulations that CTBs not only act as barriers to slip transmission [546-548], but also react with a lattice dislocation to facilitate the multiplication of partial dislocations, forming imperfect/defective CTBs (Fig. 4.1d-e) [415, 549]. Further study by Wang *et al.* pointed out that as-grown CTBs in NT Cu are inherently defective with kink-like steps and curvature. The imperfections on CTBs consist of incoherent segments and partial dislocations, which play a crucial role on the deformation mechanisms and defect-TB interactions.

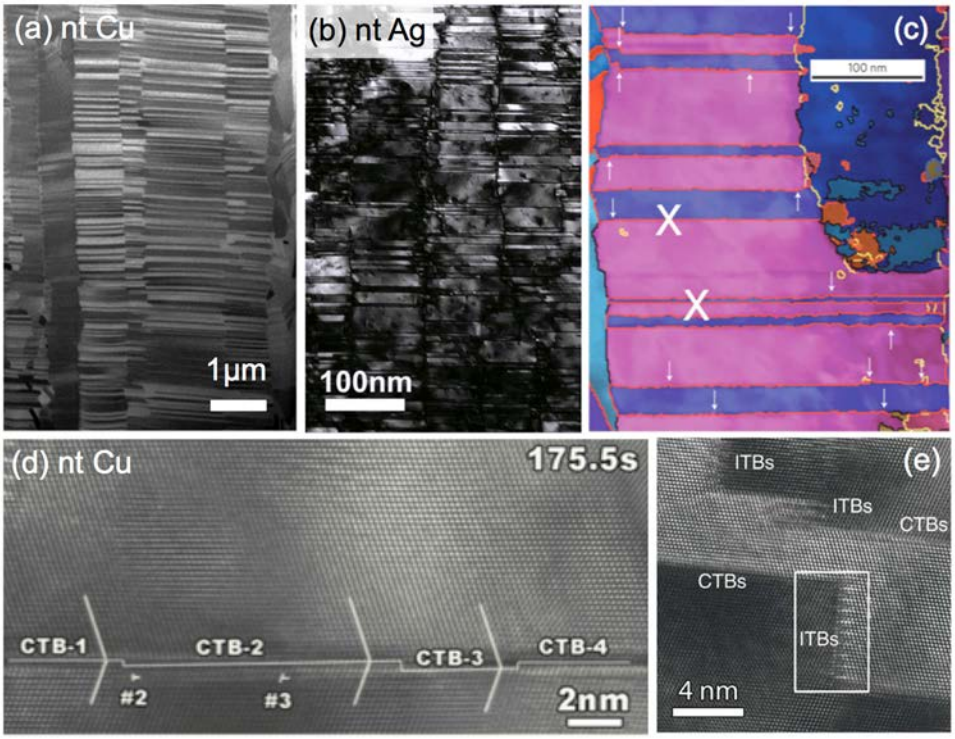

Fig. 4.1. TEM micrographs of NT (a) Cu [550] and (b) Ag [527]; (c) defective CTBs prevailing in deformed NT structure [551]; (d) HRTEM snapshots showing the interaction of lattice glide dislocation with a CTB, forming defective CTB [552]; (e) TEM micrograph of CTB-ITB junctions in NT Cu [549].

4.1.2 Dislocation structures of ITB

Σ3{112} ITBs are of great interest, since they are low energy, thermally stable boundaries that separate one column from the others in NT metals. Atomistic simulations were employed to investigate the structure and stability of Σ3 GBs in FCC metals, such as Cu with low SFE and Al with high SFE [415, 529, 530, 553-560]. Taking Cu as an example, three sets of tilt Σ3 GBs have been studied with respect to the tilt axis parallel to <111>, <112>, and <110>, respectively. Results show that only Σ3{111} and Σ3{112} GBs are thermodynamically stable and the others tend to dissociate into terraced interfaces, which is consistent with TEM observation [521].

Σ3{112} ITBs show different structures with respect to their SFE [546] and play a crucial role in determining mechanical response of NT metals [536, 561], in particular when the height of ITBs is a few nanometers thick [526, 562]. Σ3{112} ITBs can be represented as a set of partial dislocations on every {111} plane with a repeatable sequence b_1: b_2: b_3, where Burgers vector of a pure edge dislocation b_1 is equal to $1/6[11\bar{2}]$, and two mixed partial dislocations (b_2 and b_3) with opposite sign screw components are equal to $1/6[\bar{2}\,11]$ and $1/6[1\,\bar{2}\,1]$, respectively (Fig. 4.2) [526]. The sum of the Burgers vectors in one triple unit equals zero.

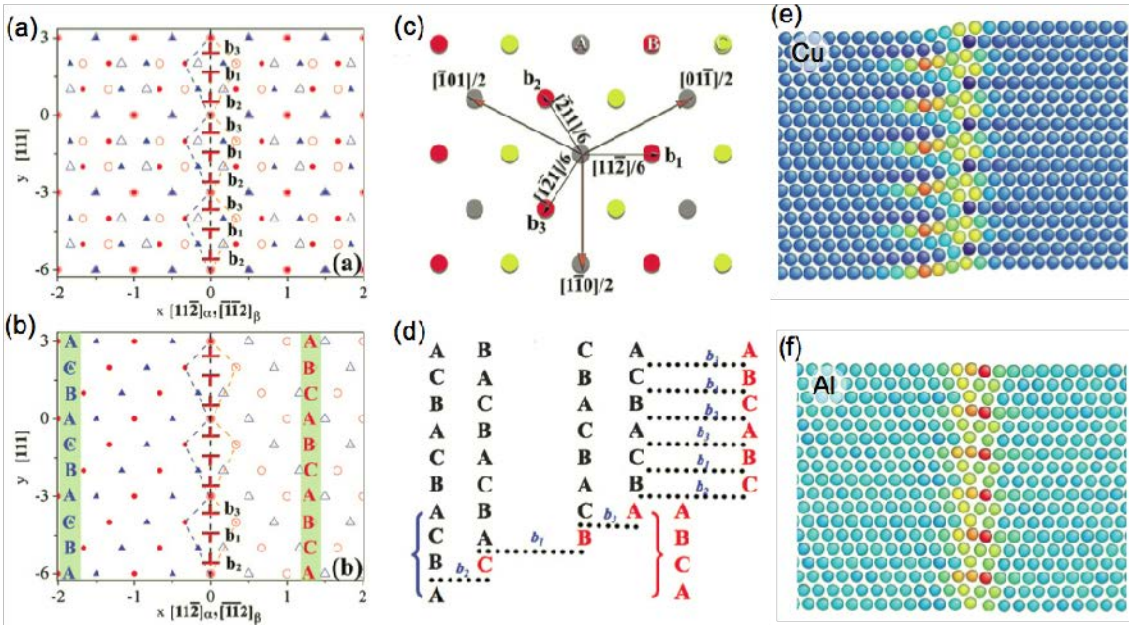

Fig. 4.2. (a-d) Dichromatic pattern of a [110] Σ3{112} ITB showing the atomic structure of the boundary: (a) Dichromatic pattern of an ITB containing a set of partial dislocations on every (111) plane with a repetitive sequence b_2:b_1:b_3, and (b) the equivalent bicrystal structure of an ITB. The dashed lines outline the boundary atoms belonging to two grains. (c) Plan-view of (111) plane stacking and three partials. b_1 is a pure edge dislocation, b_2 and b_3 are mixed partial dislocations with opposite sign screw components. (d) Schematic illustration of the glide of the three partials to create a twin. The solid symbols represent atoms in grain α and the empty symbols represent atoms in grain β. The repeatable pattern with a unit involving three {111} planes is delineated by solid lines. (e) and (f) show relaxed atomic structures of Σ3{112} in Cu and Al, respectively [561].

In the absence of external stress, the dissociation of partial dislocations in ITBs can occur spontaneously because of a reduction in core energy. Molecular statics calculations for ITBs in FCC metals under zero applied stress [561] revealed that ITBs can dissociate into two phase boundaries (PBs), bounding the 9R phase, that contain different arrays of partial dislocations, and the separation distance between the two PBs scales inversely with increasing SFE (Fig. 4.2e-f) [526, 561]. The study of shear response of ITBs in FCC metal reveals possible migration mechanisms of ITBs [561]. For FCC metals with low SFE, one of the two PBs migrates through the collective glide of partials, referred to as the phase-boundary-migration (PBM) mechanism. This has been observed by *in situ* nanoindentation test in TEM [526]. For metals with high SFE, ITBs experience a coupled motion (migration and sliding) through the glide of interface disconnections, referred to as the interface-disconnection-glide (IDG) mechanism [561]. This has been recently confirmed in NT Al [536].

4.2 Radiation effects of CTB

4.2.1 Point defect-CTB interaction

Annihilation of point defects by GBs gives birth to denuded zones of point defects or precipitates upon irradiation or quenching [538, 542, 563, 564] since it is energetically favorable for point defects to nucleate at or migrate to GBs. In contrast, the formation energies of vacancies and interstitials at CTBs are close to those in perfect lattice [457]. So the defect denuded zones (DDZs) at the vicinity of CTBs are generally not expected. Pioneering work of Makin has shown that CTBs have no DDZs [537]. However, by quenching Au from near the melting point, Segall has identified a CTB can act as a very effective vacancy sink to annihilate stacking fault tetrahedron (SFTs) [542]. In case of irradiation, Norris has pointed out that TBs may be effective

on capturing vacancies [538]. Later a systematic microscopic work by King and Smith has shown that defect evolution at CTBs is different from that in matrix [541]. So far, debates still remain on the validity of the sink effect of CTBs in irradiation environments [457, 543]. Energetically, a perfect CTB is not favorable to absorb defects, but this no longer holds true for a defective CTB. Recent studies have found that the interaction of CTBs and defects could induce twin steps containing dislocations [552, 565]. The formation energy at these twin steps is generally lower than that in perfect lattice/CTB. Taking NT Cu as an example, the interstitial formation energy decreases from 3.06 eV in Cu lattice to 0.98 eV at a twin step with a Frank dislocation [29]. These steps provide the fast-diffusion channels to promote the defect migration and annihilation mainly due to the confinement of migration from 3D to 1D along a dislocation line.

Interactions between CTBs and point defects (or clusters) were recently revisited in real time by Li and coworkers [566]. NT Ag was irradiated under electron microscope at room temperature using 1 MeV Kr ions and the microstructural evolution was captured [566]. As shown in Fig. 4.3a1, a CTB is originally straight. At 11 s, a mobile interstitial loop formed at the vicinity of the CTB (Fig. 4.3a2), causing the distortion of the CTB. Later the loop was captured by the curved CTB at 13 s (Fig. 4.3a3) and eventually absorbed by the CTB at 16 s (Fig. 4.3a4). As shown in Fig. 4.3a5, the P1 puddle on the CTB was later replaced by two neighboring curved sections, labeled as P2 and P3 at 18 s and the two SFTs were then gradually absorbed before the CTB recovered at 25 s (Fig. 4.3a7).

Based on these observations, a hypothetical mechanism of point defect-CTB coupling is illustrated in Fig. 4.3b. It was proposed that the nature and content of point defects on each side of the boundary determines the morphological evolution of the CTB. First, the local stress field generated by the small interstitial loop deforms the CTB. Second, the absorption of the interstitials

results in a locally interstitial-rich boundary. Third, when the vacancy-rich SFTs approach the CTB, the interstitial-rich CTB prompts the interstitials to rapidly redistribute themselves along the CTB into two smaller puddles right next to each SFT. Eventually, the recombination of vacancies and interstitials zeros the former events and the local structure of the CTB is healed.

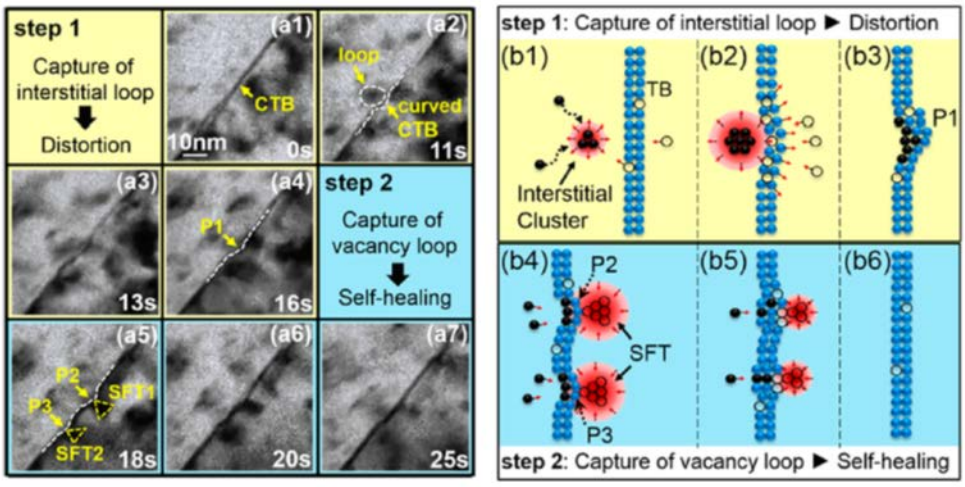

Fig. 4.3. Interaction between Kr ion irradiation induced dislocation loops and CTB in NT Ag. (a1−a4) *In situ* video snapshots of a dislocation loop interacting with a CTB. The CTB was curved during the interaction from 11s to 16s, as indicated by P1. (a5−a7) *In situ* video snapshots of the self-healing of the CTB via absorption of SFTs. At 18s, P1 transformed into two smaller curved sections, labeled as P2 and P3. At 20s, two SFTs approached to the curved CTB, causing gradual evolution of the boundary. The CTB eventually recovered (self-healed) at 25s. (b1−b6) Schematics of the self-healing mechanism of CTB. The stress field of the interstitial loop firstly curves the CTB and the formation of SFTs later changes the distribution of interstitials at CTB, generating two smaller puddles right next to each SFT. Finally, the annihilation of interstitials with SFTs leads to the self-healing of the CTB [566].

The fact that the CTBs can be recoverable sinks for point defects brings up other questions, such as whether there are defect-free zones at the boundaries and how would the boundaries alter the migration kinectics of nearby defects. Statistical anyalyes on defect activities near CTBs have been reported [566]. The accumulative defect concentration within a twin in Kr irradiated Ag was evaluated using the *in situ* irradiation video captured during 0.6 to 1 dpa. As shown in Fig. 4.4a,

Zone C exhibited the lowest defect density after overlapping numerous video frames, indicating the existence of TB affected zone (TBAZ), which is analogous to the defect-denuded zone at GBs. The width of the TBAZ is 2-5 nm. By tracking dozens of distinguishable defects, the global diffusivity D^{Global} was calculated as $D^{Global} = L^2/4t$, where $\boldsymbol{L}$ is the average of accumulative diffusion distance of the defects and t is defect's lifetime. Note that the lifetime is the sum of migration and dwell time. Fig. 4.4b shows that the D^{Global} in Zone A (D_A^{Global}) is 40 ± 7 nm^2/s, which is ~ 3 times of that in Zone B (D_B^{Global} = 13 ± 2 nm^2/s). The reason that defect clusters in Zone A diffuses faster than those in Zone B is because the defect clusters in Zone B are more remotely distributed from one another, and therefore their interactions become less active, resulting in longer dwell time.

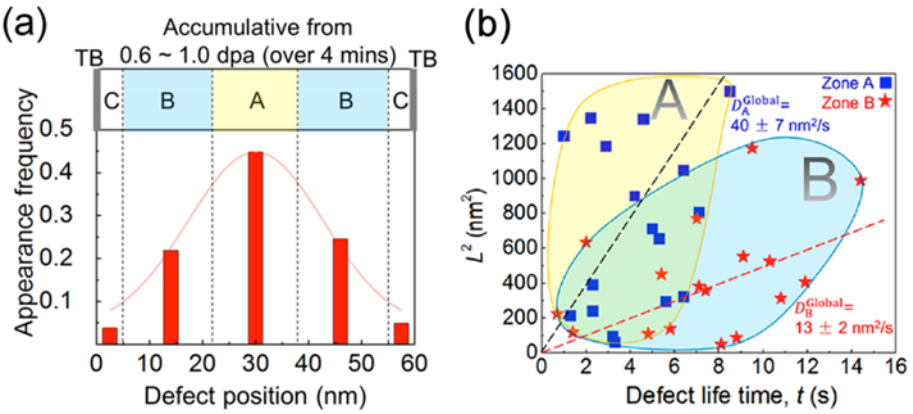

Fig. 4.4. (a) Existence of TB affected zone (TBAZ) in irradiated NT Ag. The accumulative defect concentration (0.6−1.0 dpa over 4 min) in Zone A (shown as appearance frequency) is significantly higher than those in Zone B. Zone C (closest to TBs) has the lowest accumulative defect concentration. Different defect migration kinetics in Zone A and B in irradiated NT Ag. (b) The global diffusivity, derived by fitting the plot of L^2 as a function of defect lifetime (t) as indicated by the dashed lines is 40 ± 7 nm^2/s for defect clusters in Zone A, ~ three times larger than that in Zone B, 13 ± 2 nm^2/s [566].

Following the derivation of sink strength for thin foils with free surfaces, the sink strength of CTBs with an average twin spacing, t, can be described as:

$$k_t^2 = \frac{k_{sc}/t}{[\frac{k_{sc}t}{4}\coth(k_{sc}t/2) - \frac{1}{k_{sc}t}]} \quad (4.1)$$

When $k_{sc}t \to 0$,

$$k_t^2 = \frac{12}{t^2} \quad (4.2)$$

Furthermore as there are different types of TBs, we assume that the sink strength of TBs is related to the coherency and energy of TBs, and can be described as follows:

$$k_t^2 = \frac{12 f(\gamma_t, \rho_{step})}{t^2} \quad (4.3)$$

where γ_t is the TB energy, f is related to TB characteristics, such as TB energy and the density of ITB steps etc.

4.2.2 Formation of ITB due to dislocation-CTB interactions

Despite that this section reviews the role of CTBs, it is more likely that the irradiation induced or preexisted twin steps (small ITBs) are active sinks. We thus should examine the mechanisms of the formation of ITBs during irradiation. So far the irradiation induced CTB-to-ITB transition is not readily available in literature but there are extensive studies on this type of transition triggered by applied stress. It has been proposed that depending on the characteristics of the dislocations and the driving stress, possible dislocations react at CTBs include cross-slip into the twinning plane to cause twin growth or de-twinning, formation of a sessile stair-rod dislocation at the CTB, and transmission across the CTB [2, 11-14, 22-23, 26]. After transmission, a Shockley partial dislocation is left at the CTB and a set of partials finally form an ITB. Fig. 4.5 illustrates the dislocation multiplication mechanisms.

During irradiation, a large amount of dislocations are generated and frequently interact with the high density CTBs, possibly through the mechanisms as described above. As a result, large quantities of ITB steps form and continue to interact with defects. Therefore, in the next section we turn our focus to the radiation effects of ITBs.

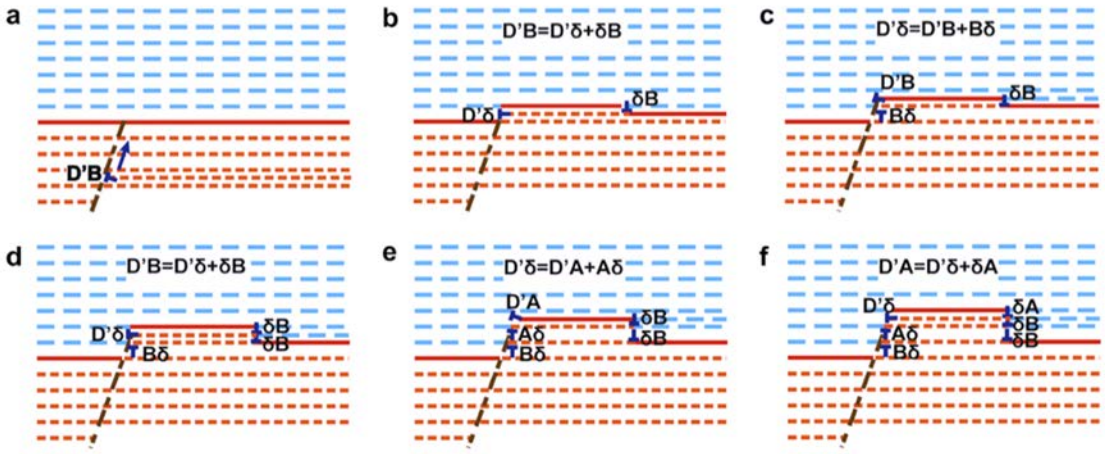

Fig. 4.5. (a–f) Schematic illustration of the dislocation multiplication mechanism through the interaction of a mixed dislocation D'B with the TB. A detailed description of the propagation process is given in the literature [552].

4.3. Radiation effects of ITB

4.3.1 Point defect-ITB interactions

ITBs separate one column from the others in NT metals. Corresponding to dislocation structure of ITBs, Fig. 4.6a illustrates defect structures associated with a twinned column. In contrast to the CTB, the formation and transformation of point defects at the ITB is more energetically favorable. Molecular statics simulations on NT Cu have shown that defects prefer to nucleate at ITBs and migrate faster than those inside the crystal. The formation energy for an interstitial at ITBs (~1.3 eV) is much lower than that within the crystal lattice (~ 3 eV) (Fig. 4.6b),

implying interstitials prefer to stay at TBs. Furthermore interstitials in grain interior experience very low migration energy (~ 0.11 eV), permitting their rapid migration to nearby TBs. Once arrived at ITBs, defects can be transported rapidly (similar to 1D diffusion) along fast diffusion channels and the recombination/neutralization of defects with opposite types is significantly enhanced. For ITBs consisting of sets of 3 adjacent Shockley partials, there are two fast diffusion paths along dislocation lines that experiences the kinetic barrier of 0.34 eV for channel 1 at tensile sites sandwiched by two partial dislocations (b_1 and b_3) (Figs. 4.6b-c), and 0.01 eV for expeditious 1D crowdion diffusion in channel 2 (Figs. 4.6b-d). In addition, if nanovoids exist at ITBs to store radiation induced damage, the radiation tolerance is further enhanced, as recently reported in NT Cu with nanovoids [565], which will be revisted later. It is worth mentioning that the kinetic energy barrier is as low as 0.01-0.16 eV for channels along ITB-CTB junctions in NT Cu, which is significant in NT structure with abundant ITB-CTB junctions.

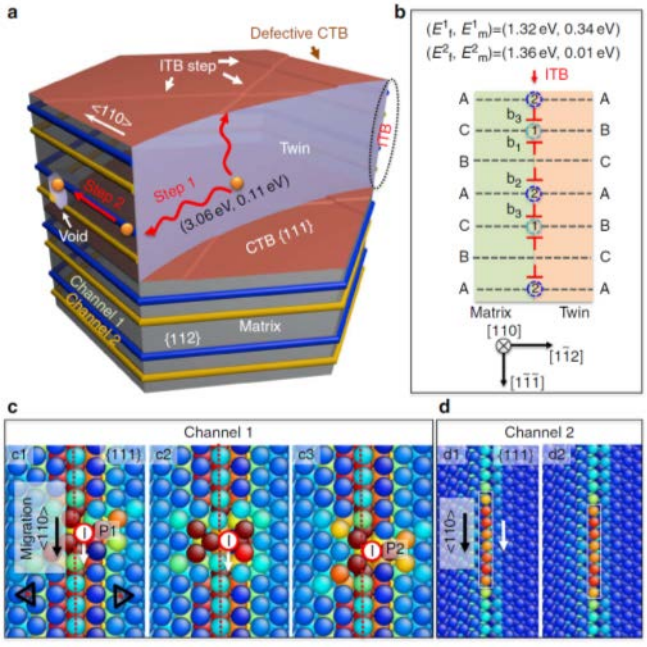

Fig. 4.6. Absorption and diffusion of interstitials in NV-NT Cu. (a) Fast interstitial diffusion pipes enabled by ITB-CTB networks in NT Cu. (b) Two fast diffusion channels at ITBs and (c, d) the corresponding diffusion mechanisms. (c) For the channel 1, an interstitial initially stays at a

dislocation core in an {111} layer sandwiched between b_1 and b_3. The interstitial then migrates downward to another low-energy site, with energy at the same level as its initial low-energy site. (d) For the channel 2, an interstitial has a spreading core associated with the distributed free volume along dislocation line. The migration of the distributed interstitial requires a very low energy barrier (0.01 eV) displaying a crowdion-type of behavior [29].

4.3.2 Irradiation-induced ITB migration and dislocation-ITB interactions

Other than point defects, ITBs frequently interact with dislocations, resulting in the change of dislocation content within ITBs. Previous *in situ* nanoindentation studies have revealed that repetitive dislocation-ITB interactions can induce steps [536, 567], where dislocation transmission eventually occurs, and ITB steps migrate to further accommodate plasticity at high stresses [567, 568]. MD simulations show that before absorption of the lattice dislocations, ITBs migrated and dissociated into two tilt walls bounding a volume of 9R phase due to applied shear stress. The dissociation of ITBs is associated with crystal rotation [561]. Continued dislocation-ITB interactions in twinned Al led to accumulation of residual dislocations, which appeared as steps along the initially straight ITB [536]. These steps eventually grew pronounced enough to provide sites for dislocation transmission across the ITB or the nucleation of dislocations in the adjacent grain.

The local variation of the ITB structure during irradiation can trigger the migration of the ITB, in contrast to morphological variations of the CTB as discussed in the previous sections. Li *et al.* examined the migration of vicinal ITBs in self-ion irradiated Cu, as shown in Fig. 4.7, and ascribed the ITB migration to collective glide of an array of mobile partials due to defect-ITB interaction [569]. In addition, Yu and coworkers presented *in situ* evidence of ITB migration for Kr irradiated NT Ag as shown in Fig.4.8 [570]. The tiny kink in box1 disappeared due to ITB migration after 86s.

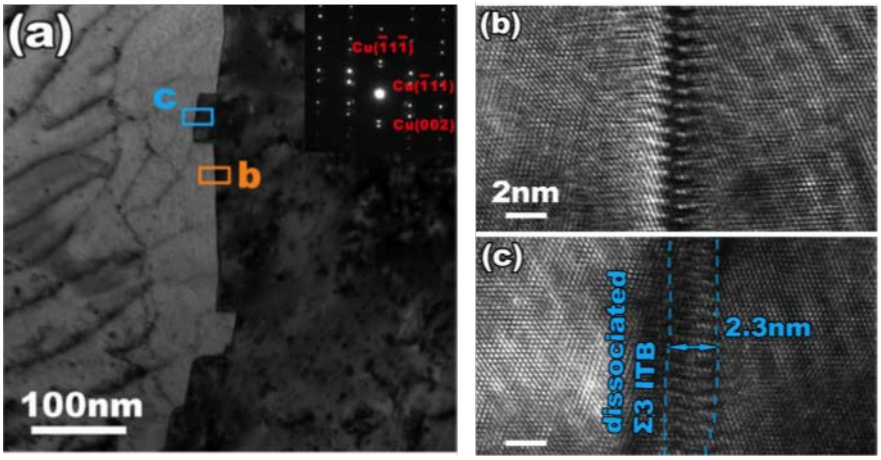

Fig. 4.7. (a) Bright field TEM image of an ITB generated after irradiation to 8.5 dpa. The inset shows the corresponding diffraction pattern, which confirms the Σ3 ITB orientation. (b) and (c) high resolution TEM images of the boundary before and after migration, respectively. After migration, the width of the boundary is around 2.3 nm. The Cu films were fabricated by e-beam evaporation on a sapphire substrate at 300℃ and the irradiation was performed using 4.5 MeV Cu^{3+} ions to the doses of 5.55 and 27.9×10^{14} ions/cm^2 [569].

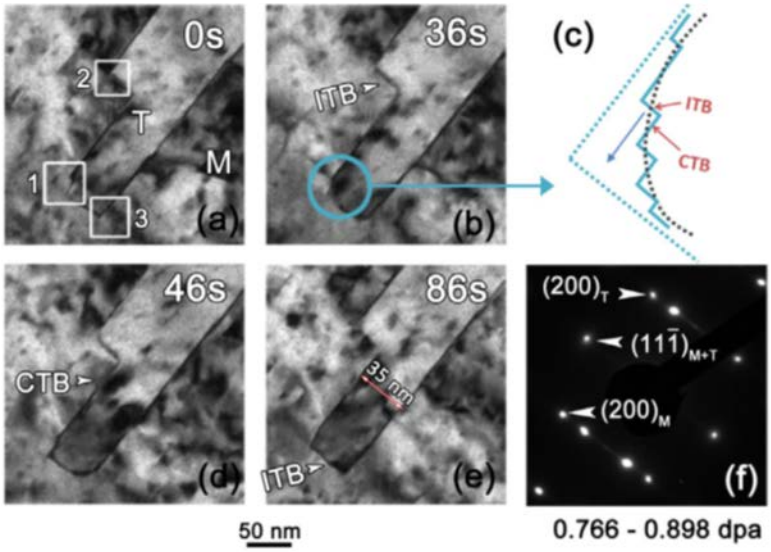

Fig. 4.8. Continuous migration and recovery of TBs. Snapshots recorded during *in situ* irradiation in TEM and corresponding schematics showing the continuous evolution of twin boundaries over a dose range of 0.766–0.898 dpa. Observation was performed along the [011] direction. (a) At 0 s, box 1 shows a small kink at the junction between an ITB and a CTB, while boxes 2 and 3 each outline a right angular corner that consists of an ITB and CTB pair. (b) By 36 s, the sharp corners in boxes 2 and 3 have become blunted, and the kink in box 1 has evolved into a curved boundary. (c) The corresponding magnified schematic for box 1 shows that the curved corner consists of

numerous minuscule steps of ITBs and CTBs. (d) At 46 s, the corner in box 1 has become sharp again, while the bottom corner in box 3 appears more blunted (with mixtures of ITB and CTB steps). (e) The kink in box 1 has nearly disappeared by 86 s. (f) SAD pattern indicating the existence of twins with Σ3 {111} CTBs [570]. Videos are available online in the original reference.

The mechanisms of ITB migration due to the interaction between ITB and irradiation induced defects have been described as follows. From the perspective of point defect-ITB interactions, irradiation leads to supersaturated vacancies close to the ITBs, and interstitials may emit from the TBs to annihilate neighboring vacancies [569]. As a result, the local stress between vacancies within the matrix and interstitials in the boundary could drive Shockley partials at ITBs to glide, which is associated with ITB migration, as shown in Fig. 4.9a. Energetically, the collective glide of Shockley partials within Σ3 {112} ITB generates zero strain, thus the strain energy remains constant during ITB migration.

From the perspective of dislocation and ITB interactions, as shown in Fig. 4.9b [570], a perfect dislocation loop can be absorbed by an ITB, forming of a Frank partial by

$$\frac{1}{2}[\bar{1}\bar{1}0]+\frac{1}{6}[112]\longrightarrow\frac{1}{3}[\bar{1}\bar{1}1] \qquad (4.4)$$

As a result, an array of parallel Frank partials could be formed during radiation along ITBs. These partials could grow by absorbing vacancies if they are intrinsic faults (vacancy-type), causing the ITB to migrate leftwards as shown in Fig. 4.9c. Equivalently, the intrinsic Frank partials could also shrink by absorbing interstitials to propagate rightwards. Therefore, the ITBs in a NT metal could migrate back and forth via dislocation climb by absorbing interstitials or vacancies. Besides, it is also likely that the migration of 1/6[112] Shockley partials at the ITB could be directly driven by local stress field formed by excessive defects, which is analogous to the mechanism of ITB migration under applied stress. In summary, the glide of Shockley partials

and climb of Frank partials, may operate alternatively or simultaneously to effectively advance or retreat ITBs during irradiation.

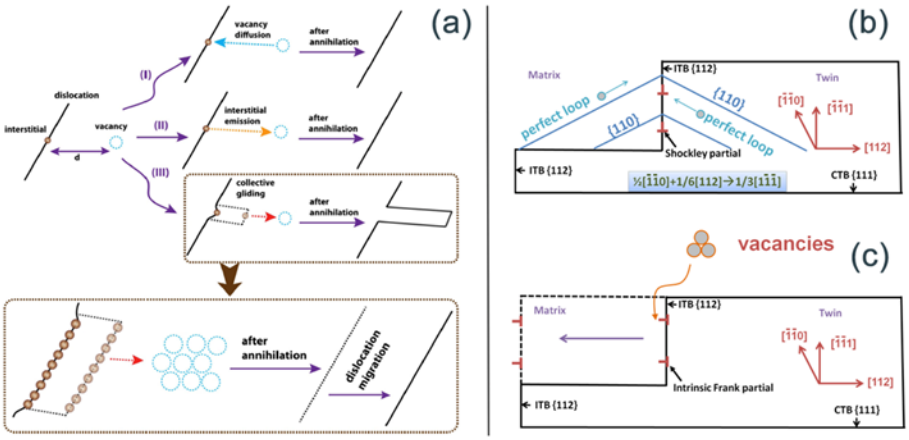

Fig. 4.9. (a) Schematic illustration representing three interstitial-vacancy annihilation mechanisms [569]. (b-c) Schematics of ITB migration mechanisms during irradiation. Schematics illustrating the interaction of a dislocation loop on the {110} plane with Shockley partials on an ITB, leading to the formation of Frank partials at the ITB. The ITB is decorated by an array of 1/3<111> intrinsic Frank partials (due to perfect loop–Shockley partial interactions). The absorption of vacancies can result in the ITB moving leftwards via dislocation climb. The Frank partials can interact with perfect loops again and form mobile Shockley partials, which usually dominate the migration of the ITB. Shockley partials can migrate under local stress induced by irradiation [570].

In addition to the continuous migration of ITBs during irradiation, Fan *et al* recently reported an intriguing observation of rapid migration of sharp ITB tips [571]. A series of TEM snapshots taken during *in situ* irradiation of twinned Cu over 0.1 - 0.2 dpa (in Fig. 4.10a) show the detwinning process through the sharpening and subsequent collapse of a TB due to dislocation loop - ITB interactions. Furthermore, the migration of ITB migration has a strong correlation with the twin thickness (t). Fig. 4.10 (b-d) illustrate the different scenarios of ITB migration in twins with different t. When t is small (< 10 nm), the stress field of a dislocation loop (not in direct contact with the ITB) may be sufficient to drive the rapid detwinning event (Fig. 4.10b). However, for thicker twins (t > 20 nm), the corner of twins (ITB corners) can migrate back and forth due to the climb of Frank partials or glide of Shockley partials, leading to self-healing of ITBs (Fig.

4.10d). For twins with intermediate thickness (10-20 nm), a gradual "sharpening" of ITB from corners occurs (Fig. 4.10c), followed by detwinning [571].

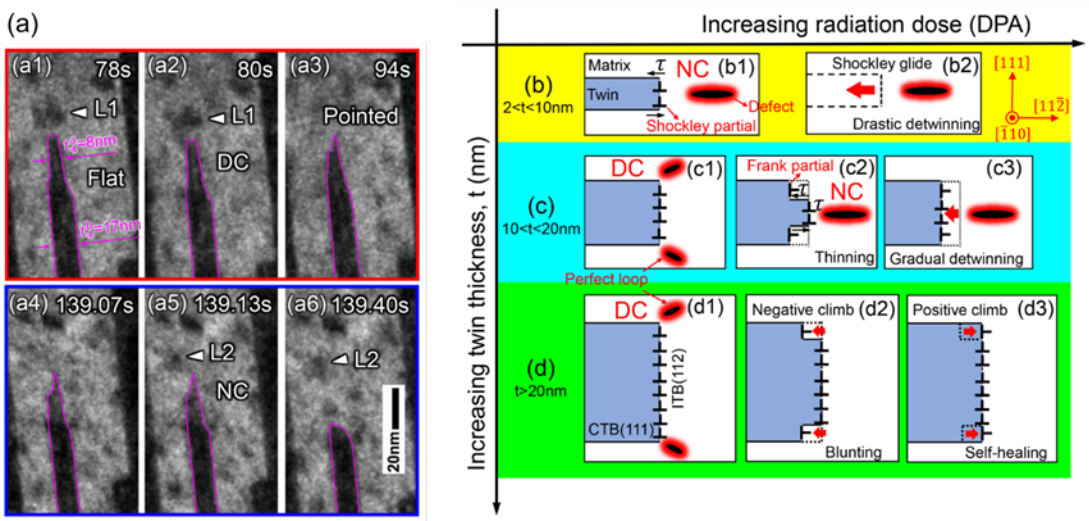

Fig. 4.10. (a) A series of TEM snapshots taken during *in situ* irradiation of NT-Cu over 0.1 to 0.2 dpa, showing the detwinning process for a 17 nm-thick twin with a 8 nm-thick tip. Two irradiation-induced dislocation loops interacting with the ITB are indicated by L1 and L2 [571]. The sharpening (a1-a5) and the subsequent collapsing (a6) processes of the twin are the consequences of dislocation-ITB interactions. (b-d) Schematic illustration of twin thickness-dependent detwinning during radiation. (b1) - (b2) When twin thickness (t) < 10 nm, drastic detwinning occurs due to the glide of Shockley partials on ITBs. (c1) - (c3) For medium-thick twins (10 < t < 20nm), the gradual detwinning starts from the corner, and then, followed by collapses of the sharpened tip. (d1) - (d3) In thick twins (t > 20 nm), the corner of twins (ITB corners) can migrate back and forth due to the climb of Frank partials or glide of Shockley partials [571]. This phenomenon was observed through *in situ* TEM studies shown in Fig. 4.8.

During irradiation, energetic ITBs tend to migrate to reduce the area of CTBs (and consequent energy stored in CTBs) with the driving force F (=$2\gamma_T$/t, where γ_T is excess energy of CTB and t is twin thickness). Friction force (F_P, or Peierls barrier), for the migration of ITBs increases with the twin thickness, as partial dislocations in the ITB migrate collectively [526]. When t is small, the driving force is greater than the friction stress ($F > F_P$), hence ITB can migrate to reduce the area of CTBs (Fig. 4.10 b and c) [562]. While $F < F_P$, ITB would not migrate. Clearly, the migration velocity must exhibits twin thickness dependence. As shown in

Fig. 4.11a, Chen *et al.* have identified that the velocity of ITBs decreases progressively with the increasing twin thickness and the critical thickness (t^*) for ITB migration is ~ 10 nm [562]. They found that when $t > t^*$, detwinning could begin from the corner but will easily reverse back. This is because the driving force, in this case, for ITB migration is negligible as the detwinning does not change the total area of CTBs (does not reduce the energy stored at TBs). In addition, if ITB migration is induced by the interaction with defects, then it is nature to imaging that ITB migration velocity is also affected by the defect generation rate that is control by dose rate during irradiation experiments. Fig. 4.11b shows the dependence of ITB migration on dose rate at room temperature. The average ITB migration velocity (V_{ITB}, nm/s) decreases rapidly with increasing twin thickness at a high dose rate (2.5×10^{-3} dpa/s) as compared to that at lower dose rates ($0.43\text{-}1.98 \times 10^{-3}$ dpa/s) [571]. The data at non-irradiation condition [572] ($K_3 = 0$ dpa/s) are also plotted (black) as a reference.

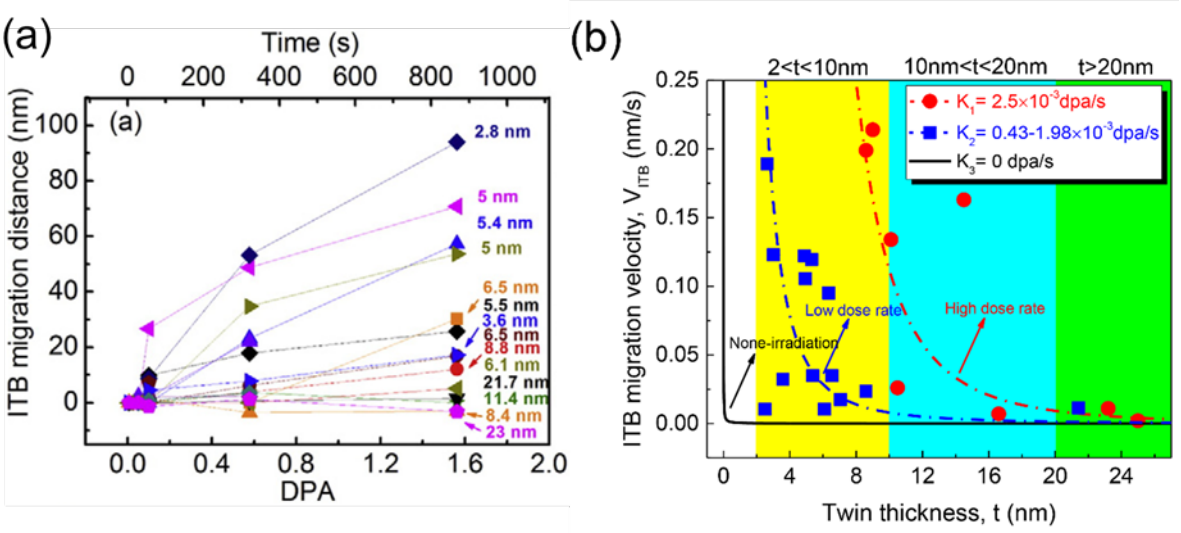

Fig. 4.11. The dependence of ITB migration on twin thickness and dose rate at room temperature. (a) The plot of twin length over radiation dose for numerous twins. The migration velocity of ITBs (the slope of each set of data) decreases progressively with the increasing twin thickness. The critical film thickness, t^*, is ~ 10 nm [562]. (b) The average ITB migration velocity (V_{ITB})

decreases rapidly with increasing twin thickness at a high dose rate ($K_1 = 2.5 \times 10^{-3}$ dpa/s, red data) as compared to that at a low dose rate ($K_2 = 0.43\text{-}1.98 \times 10^{-3}$ dpa/s, blue data) [571]. The data at non-irradiation condition [572] ($K_3 = 0$ dpa/s) are also plotted (black) as a reference.

4.4. 3D defect-TB interactions

4.4.1 SFT-TB interactions: mechanisms and experiments

SFTs are a dominant type of vacancy clusters in irradiated FCC metals with low-to-intermediate SFE [573-575]. SFTs, once formed [44, 576], are very stable, and can be annihilated when interacting with interstitials or dislocations [577-581]. Based on MD simulations as shown in Fig. 4.12, Niewczas and Hoagland [545] suggested that Σ3 {111} CTBs could lead to the destruction of SFTs via interaction of partial dislocations (on CTBs) with SFTs. King and Smith studied the mechanism of point defect absorption by GBs and Σ3 {111} CTBs in electron-beam irradiated Al and Cu, and showed that TBs may be biased sinks for dislocation loops [541]. It is likely that these CTBs are defective, and SFTs actually interact with tiny ITB steps at the CTBs. To investigate the interaction between TBs on SFTs, NT Ag has been irradiated by Kr ions at room temperature within a TEM (Fig. 4.13a) [39]. Clear twin size dependence has been shown, that is fewer SFTs were formed in Ag with finer twins after irradiation to 1 dpa (Fig. 4.13b). It is also suggested that SFT-TB interactions result in a large number of truncated SFTs and high density stacking faults (SFs) at TBs and within twin matrix [582], consistent with the prior MD simulations. The existence of SFs is confirmed by both elongated diffraction dots and streaking lines in the insets of Fig. 4.13a.

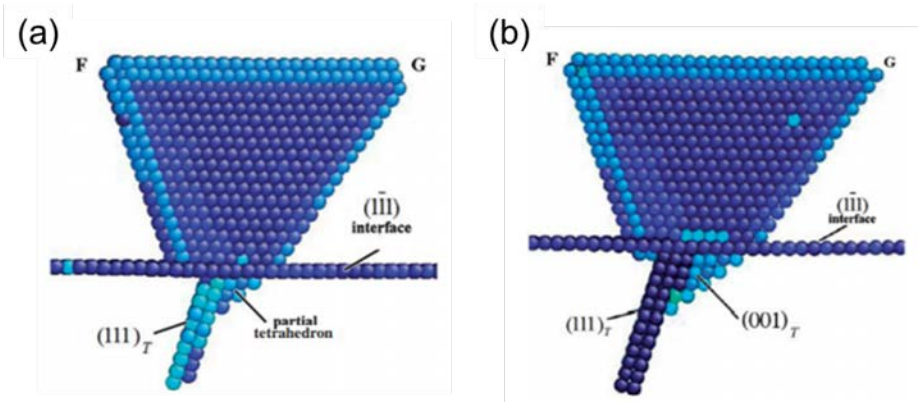

Fig. 4.12. MD simulation results showing the destruction of a large SFT in apex-down configuration by a growing twin [545]. (a) the parent SFT partially incorporated into the twin lattice, and (b) the destruction of the parent SFT during further twin growth.

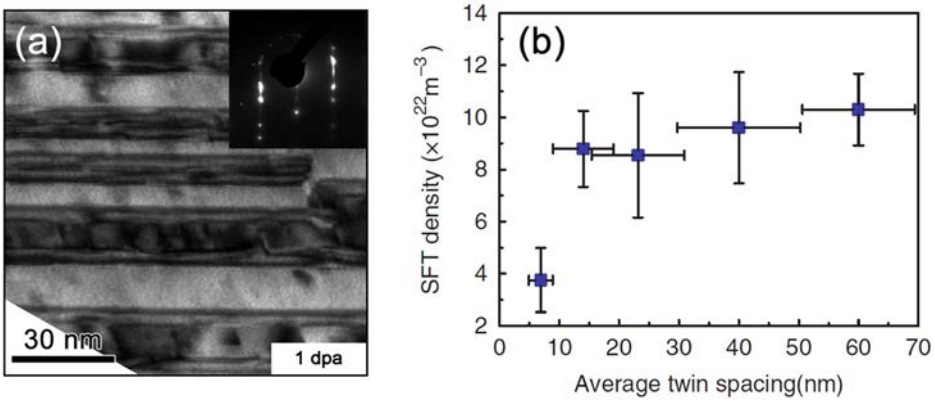

Fig. 4.13. (a) XTEM of fine twinned Ag (t=8 nm) irradiated by 1MeV Kr ion at room temperature up to 1 dpa, showing relatively low defect density. The inset selected area diffraction (SAD) pattern shows strong intensity of streaking lines, implying the formation of a high density of stacking faults, which were observed along TBs. (b) The density of SFTs decreased sharply at smaller average twin spacing. All specimens were irradiated up to 1 dpa [39].

The *in situ* evidence of annihilation of SFTs by TBs is shown in Fig. 4.14a and b, wherein the apex of an SFT approached a CTB at 0 s and disappeared by 10 s. In the meantime, the twin thickness reduced from 8 to 7 nm. After post-irradiation analyses, as shown by the HRTEM image in Fig. 4.14c, two typical SFT morphology has been revealed. SFT-a was truncated from its apex and SFT-b lost part of the base. The consequence of such interactions is the generation of high density stacking faults as shown in Fig.4.14c and d. The volume fraction of irradiation induced

stacking faults is estimated to be ~ 10%. Similar results have been reported in Kr irradiated NT Cu [582].

The interaction mechanisms have been schematically proposed although the knowledge at atomic level is limited by the time and space resolution of current technique [39]. When the SFT is approached by a TB from its base as shown in Fig. 4.14e, a 1/6[121] Shockley partial at the TB could interact with the stair-rod dislocations 1/6<110> in the SFT, forming new mobile Shockley partials (1/6[211] and 1/6[112]) which propagate on ABD and ACD faces of the SFT. Consequently, the Frank loops on the faces are unfaulted and the SFT eventually collapsed [575]. These studies might have brought up potential approaches to elminate SFTs in irradiated FCC metals, that is, introduing large density of ITBs or defective CTBs.

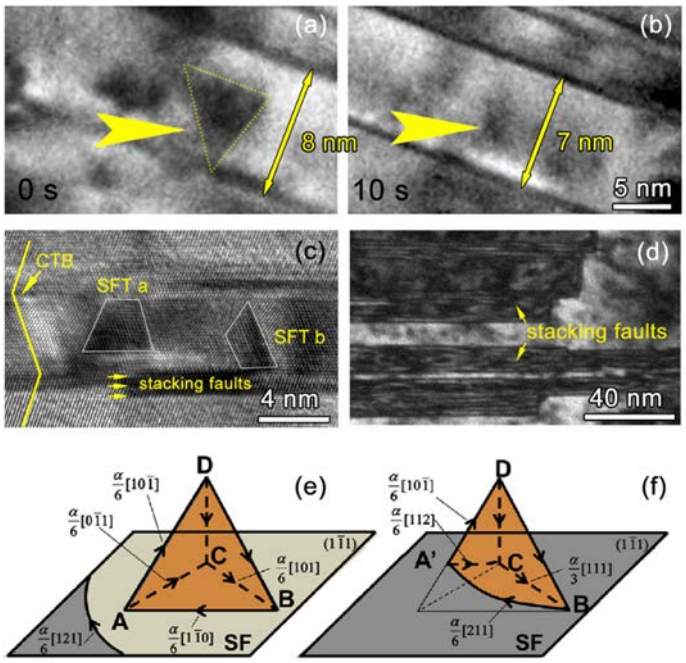

Fig. 4.14. (a-b) *In situ* observation of an SFT interacting with TBs over a dose range of 0.075–0.081 dpa. The apex of the SFT was in contact with a TB at 0 s and started to evolve. At 10 s, the SFT had a core barely discernible and the twin spacing shrank by 1 nm. (c) HRTEM image of two truncated SFTs at TBs. SFT-a was truncated from its apex, whereas SFT-b was destructed from its base. (d) TEM micrograph showing high density stacking faults induced by SFT–TB interactions reside along CTB and within in twin interior [39]. (e-f) Schematic illustration of a Shockley partial

migrating on the base plane of the SFT. The mobile Shockley partial interacts with two sessile stair-rod dislocations, AB and AC, generates two mobile Shockley partials on the surfaces of the SFT, ABD and ACD, which continue to glide on the SFT surface and lead to the collapse of the SFT [582].

4.4.2 Helium bubbles in NT metals

Previous sections have unveiled that TBs can serve as active defect sinks through facilitating the recombination of point defects and favoring interactions between TB dislocations and defect clusters. It is thus natural to hypothesize that TBs might exert similar effects on the nucleation and distribution of helium bubbles. However, unlike high angle GBs, CTBs in NT Cu subjected to high dose He ion irradiation were not found to curtail the formation of vacancy and interstitial clusters [457]. These observations have been rationalized through atomistic simulations, which show that the formation energies of vacancies and interstitials at CTBs are nearly identical to those of Cu matrix, in contrast to the heterophase interfaces in nanolayers [424] or high angle GBs in NC metals [583]. In addition, SFTs and loops were not observed in the specimens as He prevents vacancies from forming those types of clusters. Systematic studies by Han *et al.* on GB sink efficiencies of He irradiated Cu have shown that the variation in the width of the bubble free zone was related to the misorientation angle and GB plane normal [237]. CTBs have barely shown any bubble free zone since their inclination angle is 0°(Fig. 2.17g-h). It should be noted that these studies focused solely on CTBs. Given that the excess volume at ITBs can store He atoms during irradiation, it is likely that bubble nucleation at ITBs is different from that at CTBs. But the coupling between He bubbles and ITBs remains unclear.

4.5. Anomalous defect concentration distribution in NT metals

The statistics of the defect concentration distribution in a 60-nm-thick twin in NT Ag irradiated at room temperature up to 0.6 to 1.0 dpa is shown in Fig. 4.4 [566]. The accumulative defect concentration is higher in the center of twins, as the defect density would be lower near defect sinks. However, in a follow-up study, Li *et al.* have reported that the distribution of defects in NT Ag depends on twin spacing. When t = 20 nm in irradiated NT Ag in an ultra-low-dose regime (<0.025 dpa) defect concentration is greater near TBs [584] as shown in Fig. 4.15. At such an early stage of irradiation, well before the steady-state defect concentration is established, the distribution of defect density is controlled more by kinetics rather than thermodynamics. To explain the anomalous defect concentration distribution in NT Ag, a hypothesis has been proposed as shown in Fig. 4.16 [584]. A defect cluster is assumed to be in one of the two stages, migration and absorption, before being annihilated. Therefore, the competition between defect migration time (τ_t) and absorption time (τ_a) determines the defect concentration distribution at an early stage or radiation where kinetics play an important role. For instance, in fine twins (Fig. 4.16b), since defects are closer to TBs as compared to thick twins (Fig. 4.16c), so τ_t is likely to be smaller than τ_a. As a consequence, defect clusters will build up near the TBs as shown in Fig. 4.16b.

The anomalous defect concentration distribution has also been observed in Kr ion irradiated nanovoid-nanotwinned Cu [585]. Radiation damage in such an interesting structure will be discussed in detail in section 4.7. A series of *in situ* TEM snapshots in Fig. 4.17 demonstrate the defect morphology evolution up to 0.1 dpa at low and high dose rate in irradiated NT Cu with nanovoids. Qualitatively, the TEM micrographs show that a majority of the irradiation-induced defect clusters (black dots) were located near domain boundaries, especially in stage 1 of low dose

radiation (Fig. 4.17a–c). The anomalous phenomenon observed further proves that TBs are effective defect sinks and may significantly enhance the radiation tolerance.

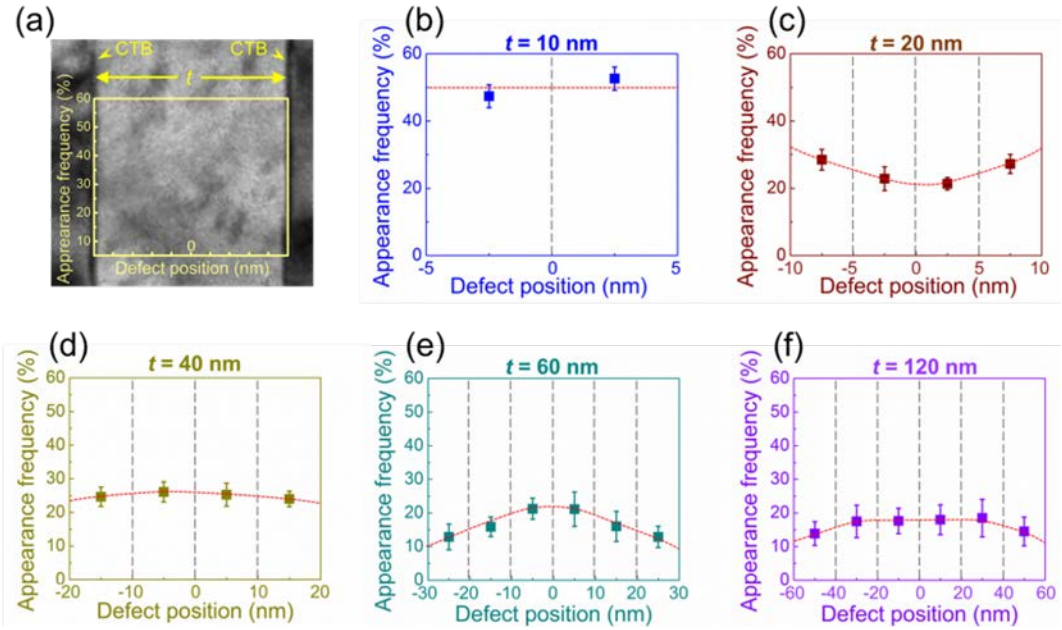

Fig. 4.15. Accumulative appearance frequency of defect clusters during 0.025 dpa in Kr ion irradiated NT Ag with respect to defect position for twins with different thicknesses. (a) The position of 0 (center axis) is defined as the center of the twinned crystals. The left and right Y axis represent the two twin boundaries. (b) When t = 10 nm, defect clusters distributed nearly uniformly. (c) When t = 20 nm, more defects appeared close to twin boundaries. (d-f) When t > 20nm, the center of twins tends to accumulated more defects than the areas near TBs [584].

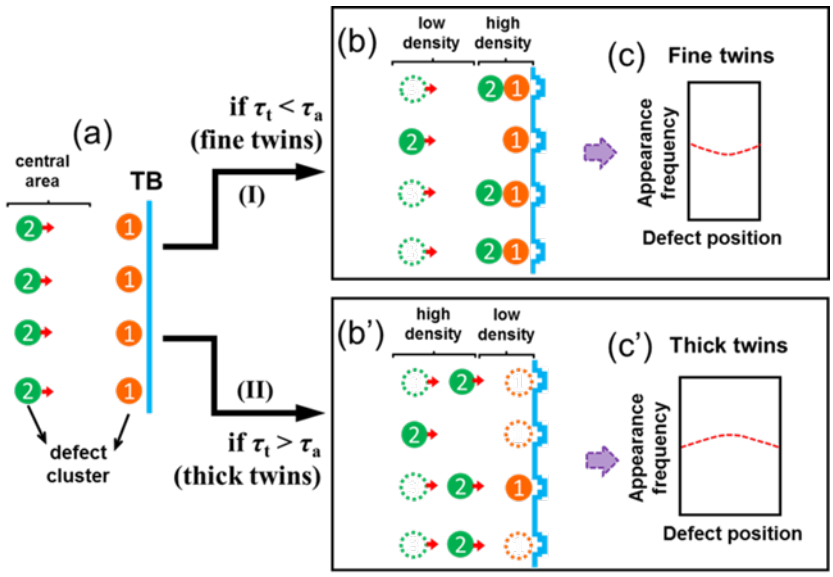

Fig. 4.16. Schematics illustrating the opposite types of defect distribution in twinned metals. Case I: $\tau_t < \tau_a$ (a-b-c); and case II: $\tau_t > \tau_a$ (a-b'-c'). τ_t is the time for a defect cluster to travel (migrate) to twin boundaries (defect sinks), and τa is the time it takes for a twin boundary to absorb adjacent defect clusters. (b) In case I (a-b-c), when twins are very fine, as $\tau_t < \tau_a$, defects (labeled as "2"s) arrive at twin boundary before predecessors (marked as "1"s) can be absorbed, and thus defect clusters pile-up near the TBs, and consequently leads to higher defect density near the TBs (c). Note that the TBs are distorted while attempting to absorb adjacent defect clusters. Case II: The scenario becomes the opposite for thick twins, it is likely that $\tau_t > \tau_a$, that is the arrival of group 2 defect clusters takes longer time than the absorption of defect clusters (group 1 adjacent to TBs). (c') Thus the central area exhibits higher defect density [584].

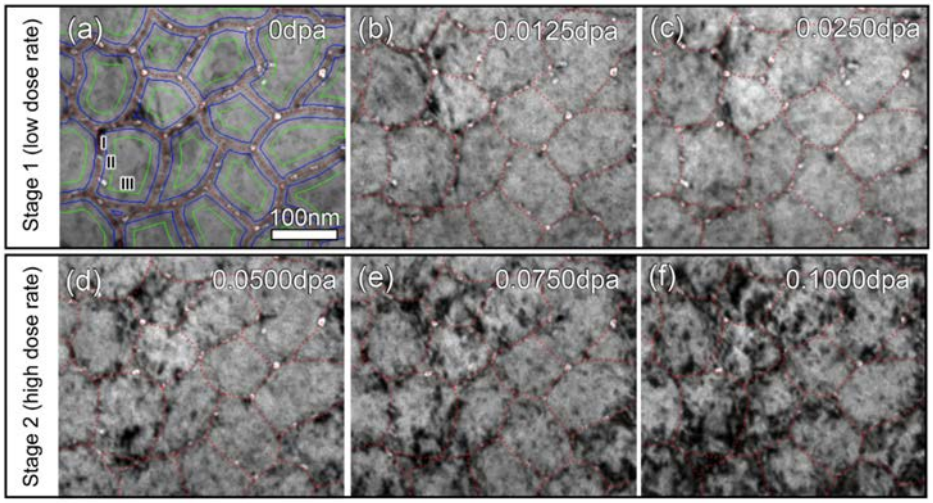

Fig. 4.17. Bright-field TEM snapshots showing the accumulation and distribution of defect clusters during *in situ* Kr^{++} ion irradation of NV-NT Cu up to a dose of 0.1 dpa. Each doamin is divided into three equal-area regions, as marked in (a) by I, II and III that are bounded by red, blue and green lines, and the irradiation-indcued defects show preferential distribution in Region I. (a-c) The defect evolution in stage 1 of low dose rate from 0 to 0.025 dpa. (d- f) The defect evolution in stage 2 of high dose rate from 0.025 to 0.1 dpa [585].

4.6. Healing of nanovoids and alleviation of irradiation damage by nanovoid-nanotwinned architechture

Previous studies show NT Ag [39] and Cu [582] exhibit improved radiation tolerances than their CG counterpart due to the unique features of NT structure. In this section, we discuss the possibility of void healing enabled by nanotwins. In general, continuous intense radiation leads to

high-density voids with increasing void size. Some voids can be removed by annealing at elevated temperatures when plenty of mobile interstitials are activated. So the void shrinkage can be used as a measure of the mobility of interstitials within the materials. In a recent work by Chen and coworkers, nanovoids were intentionally introduced into NT Cu, forming nanovoid-nanotwin Cu (NV-NT) [29]. Fig. 4.18a-b shows the as-prepared Cu contained abundant nanovoids primarily surrounding columnar domain boundaries. Fig. 4.18c shows high-density CTBs with an average twin thickness of ~ 15 nm, and ITBs that were decorated by a large number of nanovoids with an average diameter of ~ 10 nm. These 3D voids distributed at different depth in the film are introduced during magnetron sputtering process, and void density can be controlled by tailoring deposition rate, substrate temperature as well as epitaxy between film and substrate. HR TEM image in Fig. 4.18d shows atomic structure of CTBs and ITBs. Fig. 4.18e displays a conceptual schematic of NV-NT metals that contain ITB-CTB networks and nanovoids along ITBs. Fig. 4.18f shows diffusion channels associated with dislocations at CTBs and ITBs that could potentially transport interstitials and their clusters towards nanovoids.

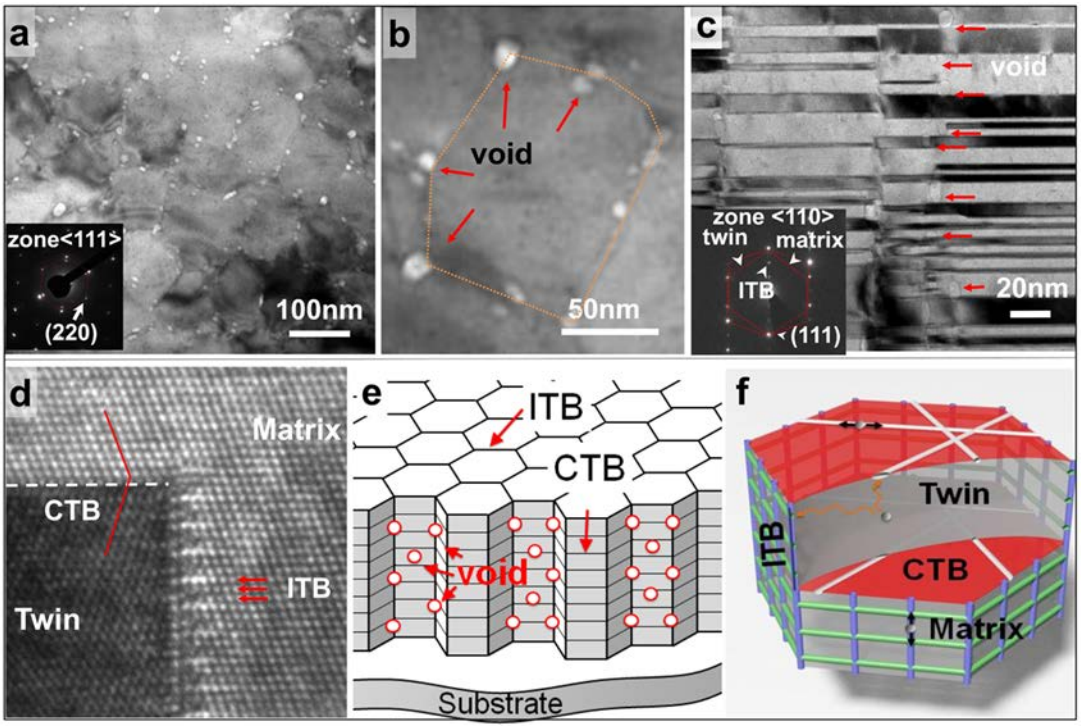

Fig. 4.18. (a–b) Plan-view transmission electron microscopy (TEM) micrograph showing the as-prepared NV-NT Cu film containing abundant nanovoids primarily surrounding columnar domain boundaries. (c) Cross-section TEM micrograph shows high-density Σ3{111} coherent twin boundaries (CTB) with an average twin thickness of ~ 15 nm, and Σ3{112} incoherent twin boundaries (ITBs), which were decorated by a large number of nanovoids with an average diameter of ~10 nm. The inserted selected area diffraction (SAD) pattern confirms the formation of epitaxial NT Cu. (d) High-resolution TEM image of CTBs and ITBs. (e) A conceptual schematic of metals with CTB and ITB networks and nanovoids. (f) Inside a typical columnar grain radiation-induced interstitials or their loops can rapidly migrate towards ITBs, where they can migrate rapidly to nanovoids [29]. Videos are available online in the original reference.

Radiation response of NV-NT Cu was investigated via *in situ* Kr ion irradiation studies. TEM snapshots compare the drastic difference in evolution of microstructure during irradiation of coarse grained (CG) (Fig. 4.19a) and NV-NT Cu (Fig. 4. 19b). During initial radiation of CG Cu by 0.1 displacements-per-atom (dpa), there was a rapid, prominent increase in density of defect clusters; the density of dislocation loops increased monotonically with dose and a high-density of dislocation segments were observed by 1.56 dpa. In contrast, in NV-NT Cu, the density of dislocation loops increased slightly with dose accompanied by a gradual elimination of nanovoids.

By 0.56 dpa, a significant decrease of void density was observed. By 1.56 dpa, voids were mostly removed.

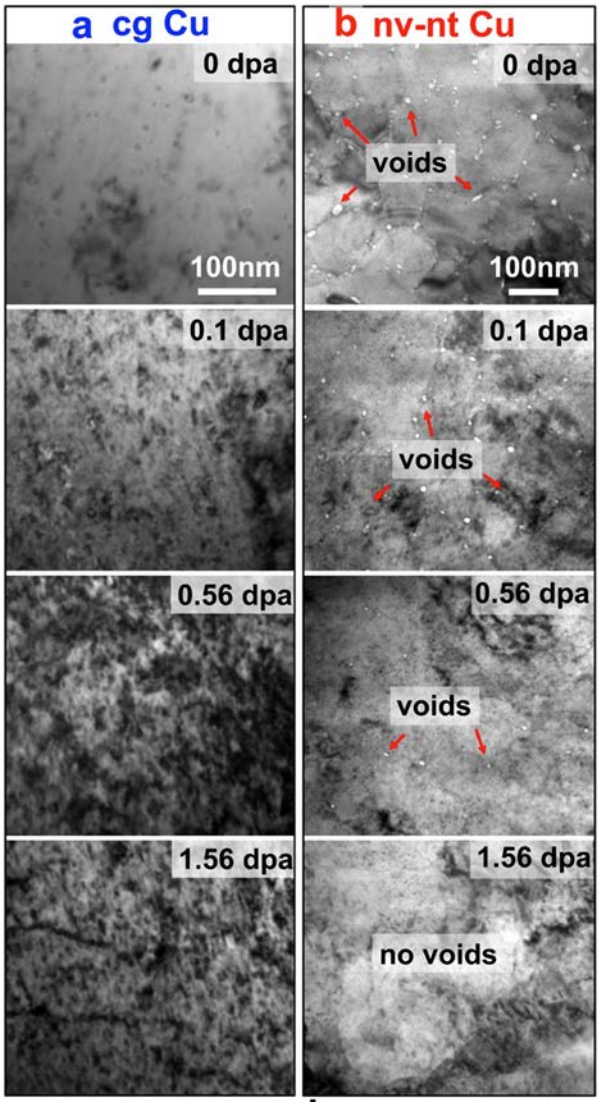

Fig. 4.19. Superior radiation tolerance and void shrinkage in NV-NT Cu as evidenced by *in situ* Kr ion irradiation studies. TEM snapshots in (a) and (b) compare drastically different evolution of microstructure during *in situ* Kr ion irradiation of coarse grained (CG) and NV-NT Cu. (a) During initial radiation of CG Cu by 0.1 displacements per atom (dpa), there is a rapid and prominent increase in density of defect clusters, the density of dislocation loops increased monotonically with dose and high-density dislocation segments were observed by 1.56 dpa (b) In contrast, in NV-NT Cu, the density of dislocation loops increased slightly with dose accompanied by a gradual elimination of nanovoids [29].

The superior irradiation tolerance is ascribed to ITB-CTB network and nanovoids. The

significance of such ITB-CTB networks has been covered in Section 4.1 (Fig. 4.6), and here we focus on the role of nanovoids. During *in situ* radiation experiments, absorption of interstitial loops by nanovoids was frequently observed. MD simulation reveals dynamic process through which a void absorbs a neighboring dislocation loop (Fig. 4.20). Three scenarios subjected to self-ion irradiations, were compared, including a stand-alone Frank (interstitial) loop, a pair of nanovoid and Frank loop in immediate contact, and the similar pair that are separated by ~ 1 nm. During irradiation, the individual Frank loop was disturbed, but only slightly changes its shape after a cascade (Fig. 4.20a-c). In parallel the Frank loops immediately contacting the void (Fig. 4.20d-f) or slightly separated from the void (Fig. 4.20g-i) were prominently absorbed by the void after radiation. The amount of net interstitials (inside a Frank loop) absorbed by a void depends on the energy and fluence of primary knock-on atoms and the detailed absorption mechanisms is discussed in [565].

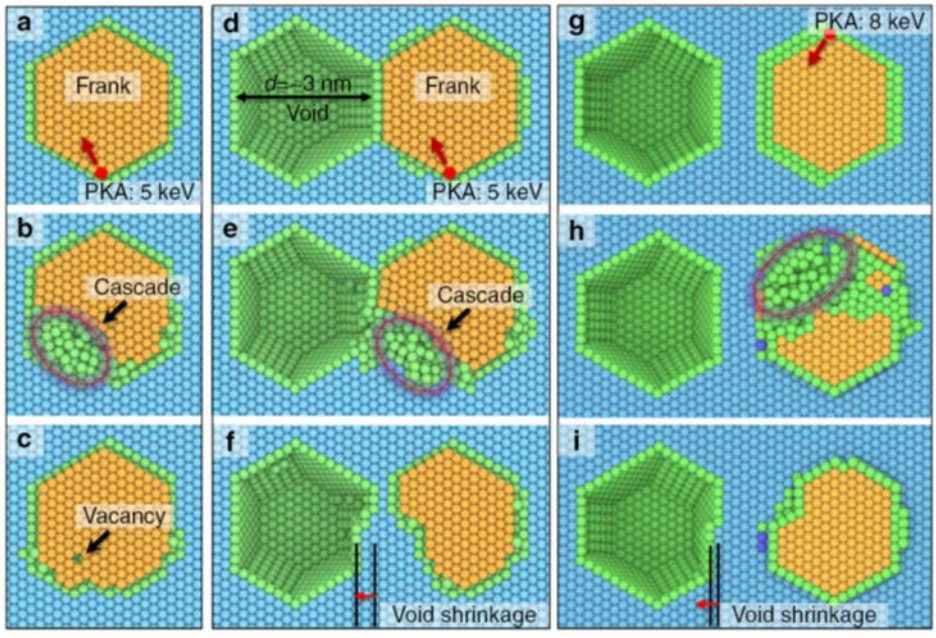

Fig. 4.20. Two-dimensional projected view of interstitial loop–nanovoid interactions. (a) For a stand-alone Frank loop, a 5 keV primary knock-on atom (PKA) generates a cascade at one corner of the loop (b). During the quenching process, the cascade shrinks, accompanied by the recovery

of the Frank loop. After the retreat of the cascade, the Frank loop evolves back to its original configuration, except a vacancy at the loop and an interstitial out of the loop (a Frenkel pair) (c). (d) For a Frank loop immediately next to a void (d = 3 nm), a similar cascade is performed. (e) Accompanying the retreat of the cascade, the interstitials are absorbed into the void (f), leading to a shrinkage of the void and substantial removal of the Frank loop. No defects appear out of the Frank loop. (g) For a Frank loop ~ 1 nm away from a void (d = 3 nm), a similar cascade generated by an 8 keV PKA is performed (h). The interstitials of the Frank loop are attracted into the void (i), leading to shrinkage of the void and Frank loop. No defects appear out of the Frank loop in cases d and h [565].

4.7. Summary and future outlook

In this chapter, we briefly summarized several significant characteristics on the radiation response of NT metals. First, there are significant number of *in situ* irradiation studies that show both CTBs and ITBs can effectively engage and eliminate irradiation induced defects, and TB affected zones clearly exist in heavy ion irradiated NT metals. Second, a direct consequence of these interactions is TB migration. Such migration events may have profound impact on the design of irradiation tolerant materials. Meanwhile the migration of TBs lead to detwinning, a process that depends on twin thickness. There is clearly a need to explore how to enhance the stability of TBs during irradiation and investigate the irradiation response of NT alloys. Third, it is encouraging to see that TBs can destruct SFTs, which are typically considered as a very stable defect clusters. Fourth, the influence of TBs on He ion irradiation resistance of NT metals remain a topic that needs further investigation. The role of CTBs and ITBs on He bubble nucleation and growth may be an interesting subject for future studies. Forth, in spite of abundant *in situ* evidence on defect-TB interactions, simulations that reveal the underlying physics remain extremely limited. Finally, there is abundant opportunity to investigate the mechanical behavior of irradiated NT metals and alloys.

Chapter 5. Radiation damage in nanoporous, nanowires and nanoparticles

Metallic nanoporous (NP) materials, nanowires and nanoparticles as shown in Fig. 5.1a-c with large surface-to-volume ratios exhibit unique properties that enable potential applications, such as energy storage, catalysts, filters, gas sensors. [524, 586-593]. For instance, NP Au has been found to possess remarkable catalytic activity towards oxidation reactions as compared to its bulk counterpart [594]. It has also been reported that the strength of NP materials can be dramatically improved by reducing the length scale of ligaments and pores. NP Au with high porosity can be as strong as bulk Au and the ligaments in NP Au can approach the theoretical yield strength of Au when the ligament diameter reduces to approximately 10 nm, as shown in Fig. 5.1d-e [595]. Besides, the Young's modulus of ZnO nanowires is shown to increase with decreasing wire diameter as shown in Fig. 5.1f, and when wire diameter is greater than 200 nm, the Young's modulus reaches that of bulk ZnO [596]. The emergence of unique and sometimes not inherently expected properties occur throughout the set of materials due with high surface-to-volume ratios (nanoporous, nanowires and nanoparticles). This chapter will examine the radiation tolerance of these surface dominated materials.

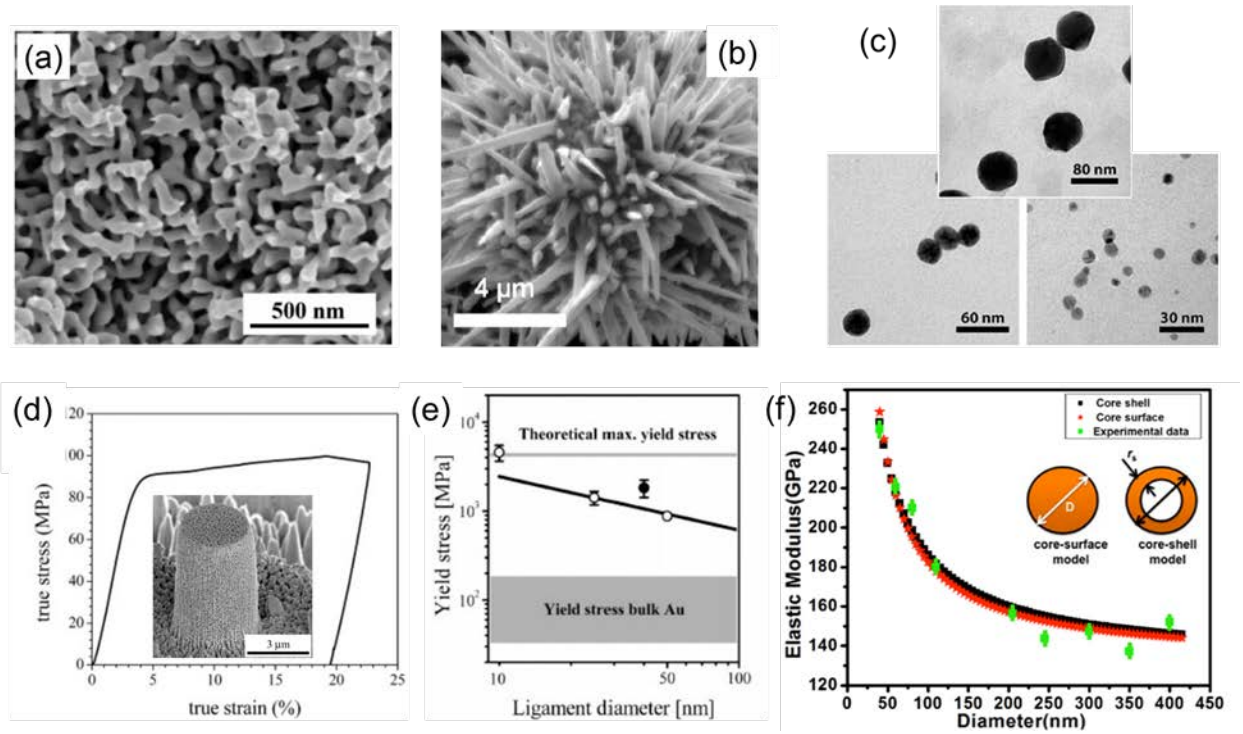

Fig. 5.1 SEM micrograph of (a) open-cell foam morphology of NP Au [595] and (b) as-received ZnO nanowires [597]. (c) *In situ* TEM images of as-deposited Au nanoparticles on carbon grids [598]. (d) The Stress-strain curve of a NP Au pillar. The embedded SEM micrograph shows the NP Au pillar used for uniaxial microcompression tests. Despite its high porosity, the NP Au is as strong as bulk Au (10-200 MPa) [595]. (e) The yield strength of NP Au increases with decreasing ligament diameter [595]. (f) The Young's modulus as a function of wire diameter for ZnO nanowires [596].

5.1. Sink strength of Nanoporous materials

Cellular model and embedding model have been developed to describe the sink strength of a void [135]. The cellular model works well for an array of uniformly distributed voids, whereas the embedding model applies when voids are randomly distributed. The results derived from the two models are in qualitative agreement with each other. Hence, to simplify the discussion, we will briefly summarize the major conclusion derived from the cellular model. When voids are the only defect sinks in materials, the concentration of defects can be described by

$$D[\frac{d^2c}{dr^2}+\frac{2}{r}\frac{dc}{dr}]+K=0 \qquad (5.1)$$

We assume voids are uniformly distributed within a material, as shown schematically in Fig. 5.2, where a is the void radius. When $r = a$, $c = 0$; and when $r = R_c$, $dc/dr = 0$. Hence R_c can be approximated as the void-to-void separation distance. The solution of c becomes

$$c(r)=\frac{K}{D}\frac{(r-a)}{6ar}[2R_c^3-(r+a)ar] \qquad (5.2)$$

The sink strength for voids can thus be calculated as:

$$k_V^2=4\pi aC_V^0 f_c \qquad (5.3)$$

where $C_V^0=\frac{3}{4\pi R_0^3}$, $R_0^3=R_c^3-a^3$, and

$$f_c=\frac{5(R_c^3-a^3)^2}{[5R_c^6-9aR_c^5+5a^3R_c^3-a^6]} \qquad (5.4)$$

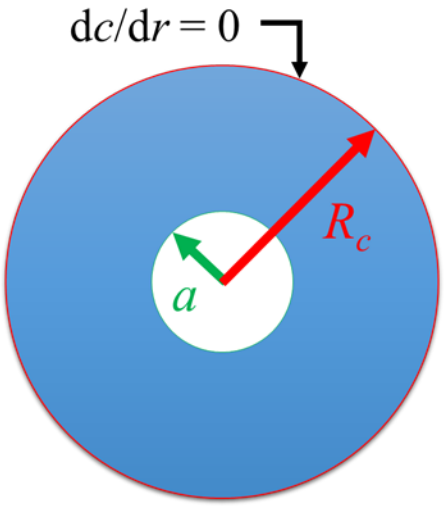

Fig. 5.2. Schematics of a void and the boundary of a void influenced zone. The void radius is a (when $r = a$, $c = 0$); and when $r = R_c$, $dc/dr = 0$.

5.2. Free surface – defect interactions in nanoporous materials

5.2.1 Capture of radiation-induced defect clusters by free surface

The superior radiation tolerance of NP structures arises from abundant free surfaces, which are considered as perfect defect sinks. *In situ* irradiation experiments have been performed to directly examine the nucleation, growth and absorption of defect clusters in NP Ag [599] and NP Au [40]. Fig. 5.3 shows the direct evidence of the removal of defect clusters by the free surface of NP Ag. Irradiation-induced defect clusters, including individual dislocation loops, SFTs and dislocation segments, in NP Ag were absorbed by either free surface or grain boundary triple junction.

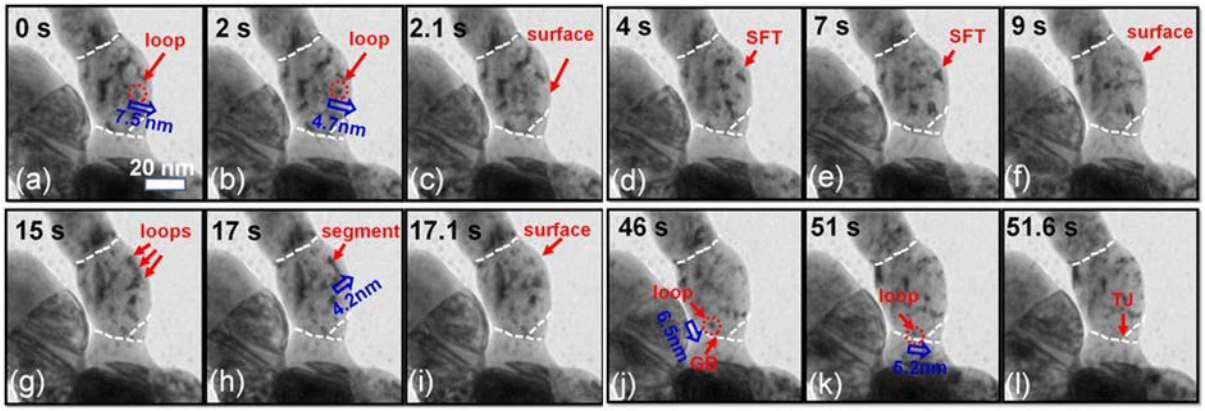

Fig. 5.3 *In situ* video snapshots showing several representative events of defect capture by free surface or triple junctions (TJs) during Kr ion irradiation of NP Ag at room temperature over 1.18-1.27 dpa. (a–c) Evidence of rapid absorption of individual dislocation loops by the free surface. A loop migrated towards the free surface and was immediately removed by the free surface within 0.1s. (d–f) A stacking fault tetrahedron (SFT) was gradually removed by the free surface from 7 to 9 s. (g–i) A dislocation segment was rapidly absorbed by the free surface. (j–l) The absorption of a dislocation loop by a TJ in the ligament [599].

5.2.2 Radiation induced void shrinkage

Void swelling in irradiated metallic materials is widely observed at elevated temperatures [69-72]. Hence it is surprising that void shrinkage is observed during *in situ* Kr ion irradiation of NP Ag at room temperature [81]. Several *in situ* video snapshots in Fig.5.4 showing the shrinkage of nanovoids during irradiation of NP Au at room temperature. In this case, most of the vacancies are bound in the form of sessile defect clusters, and thus there may be insufficient vacancies to support void growth. Meanwhile, there is a continuously biased flock of interstitials and their clusters to nanovoids during irradiation. As shown in Fig.5.4(a1-a4), three nanovoids with the diameter of 15, 12 and 11 nm continuously shrank during irradiation. One of the voids (marked by red arrows) was completely removed, and the diameter of the other two nanovoids decreased substantially. As void contracts via the absorption of irradiation-induced defects, the void shrinkage rate is determined by the defect capture rate. A recent study on nanovoid-nanotwinned Cu shows the existence of significant tensile stress surrounding nanovoids, and smaller voids generate higher stress fields near void surfaces compared to larger voids [29]. Consequently, smaller voids may capture defects more rapidly during irradiation than larger voids, and lead to their higher shrinkage rate. This rationale is in agreement with the experimental observation (Fig. 5.4b) that shows the normalized diameter reduction, $\Delta d/d$, is inversely proportional to the initial defect diameter in NP Au. The green dashed line is the result of fitting for all data, while the red and blue dash lines are fitting results by choosing the data in the range of $d < 16$ nm and $d > 30$ nm, respectively. The difference between the fitting results indicates that normalized diameter of the smaller voids contract faster than larger voids [40].

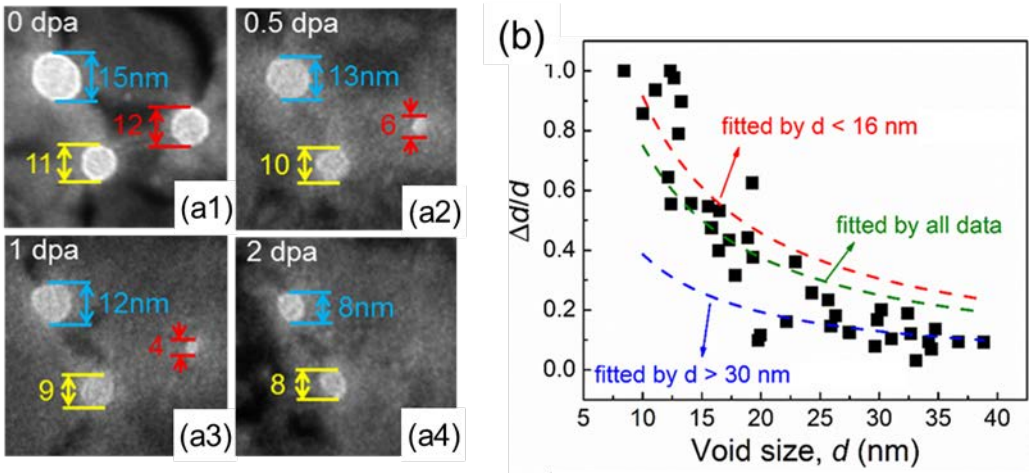

Fig. 5.4 *In situ* irradiation snapshots showing the shrinkage of nanopores in Au under Kr irradiation at room temperature. (a1) Three pristine pores with the size of 15, 12 and 11 nm before irradiation. (a2-a3) Under irradiation up to 1 dpa, defects migrated towards the nanopores, and the size of pores continuously decreased. (a4) By 2 dpa, the size of the other two nanopores decreased from 15 to 8 nm and from 11 to 8 nm, separately. (b) The normalized diameter reduction, Δ d/d, as a function of pore size. The olive dashed line is the result of fitting for all data, and the red dashed line and blue dashed line are fitting results by choosing the data in the range of d < 16 nm and d > 30 nm, respectively [40].

Irradiation temperature-dependent void shrinkage has also been studied [600]. The shrinkage rate of voids in NP Au decreases with increasing irradiation temperature as shown in Fig. 5.5. For Au irradiated at room temperature most vacancies are tied up in sessile vacancy clusters (SFTs, vacancy loops) formed directly in the displacement cascades. Consequently, the mobility of vacancies and the void nucleation and growth are strongly suppressed. Thus, more interstitials arrive at nanopores, leading to the shrinkage of nanopores. At higher irradiation temperature, the mobility of vacancies increases, and the recombination rate between interstitials (and clusters) and vacancies (and clusters) increases. Because nanopores absorb fewer defects at elevated temperatures, the nanopore shrinkage rate decreases. No obvious growth of nanopores was observed at high temperatures.

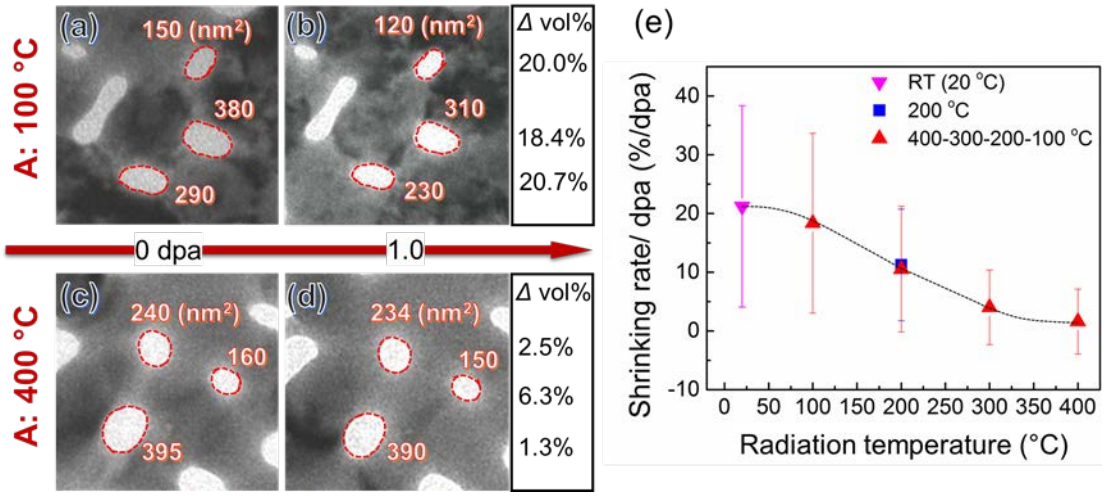

Fig. 5.5. (a-d) *In situ* video snapshots showing the temperature-dependent pore shrinkage in NP Au at two different temperatures, 100 °C (a-b) and 400 °C (c-d). At 100 °C, three nanopores with areas of 150, 380 and 290 nm^2 decrease by 20%, 18.4% and 20.7% in volume, respectively after irradiation to 1 dpa. As a comparison, three nanopores barely shrink at 400 °C, by 2.5%, 6.3 % and 1.3%. (e) Statistic data showing the temperature-dependent shrinkage of nanopores during irradiation of NP Au. Average pore shrinkage rate (%/dpa) decreases with increasing irradiation temperature, from ~21%/dpa at RT [40] to1.6%/dpa at 400 °C [600].

Void shrinkage has also been observed in other materials systems including self-ion irradiated Si [601] and e-beam irradiated Mg [602, 603]. For instance, *in situ* TEM micrographs in Fig. 5.6 show the shrinkage of a single nanocavity in Si during self-ion irradiation at ~ 21 °C up to a fluence of 3×10^{15} ions/cm^2. Xu *et al.* performed *in situ* TEM studies on pure Mg under electron-beam irradiation at room temperature [603]. Voids first formed a platelet shape and then gradually evolved into a nearly equiaxial geometry. Atomistic simulations implied that the initial growth along the longitudinal direction is controlled by slow nucleation kinetics of vacancy layers on basal facets and anisotropic vacancy diffusivity [603]. The subsequent growth along platelet thickness direction is driven by thermodynamics to reduce surface energy. Zheng *et al.* used *in situ* HRTEM techniques to demonstrate the layer-by-layer growth of atomic planes at the nanopore periphery, and when the spreading of electron-beam led to the shrinkage and removal of nanopores as shown in Fig. 5.7 [602]. The authors attributed the healing of nanopores in magnesium alloys

to the e-beam-induced anisotropic diffusion of Mg atoms in the vicinity of nanopore edges.

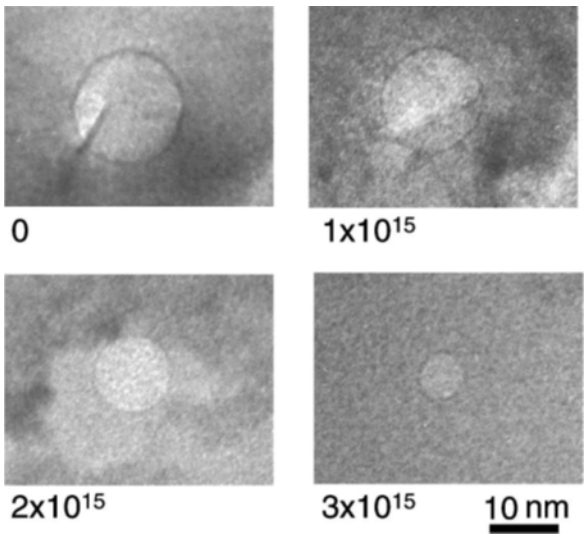

Fig. 5.6. *In situ* TEM micrographs showing the shrinkage of a single nanocavity in Si during self-ion irradiation at ~ 21 °C up to a fluence of 3×10^{15} ions/cm^2 [603].

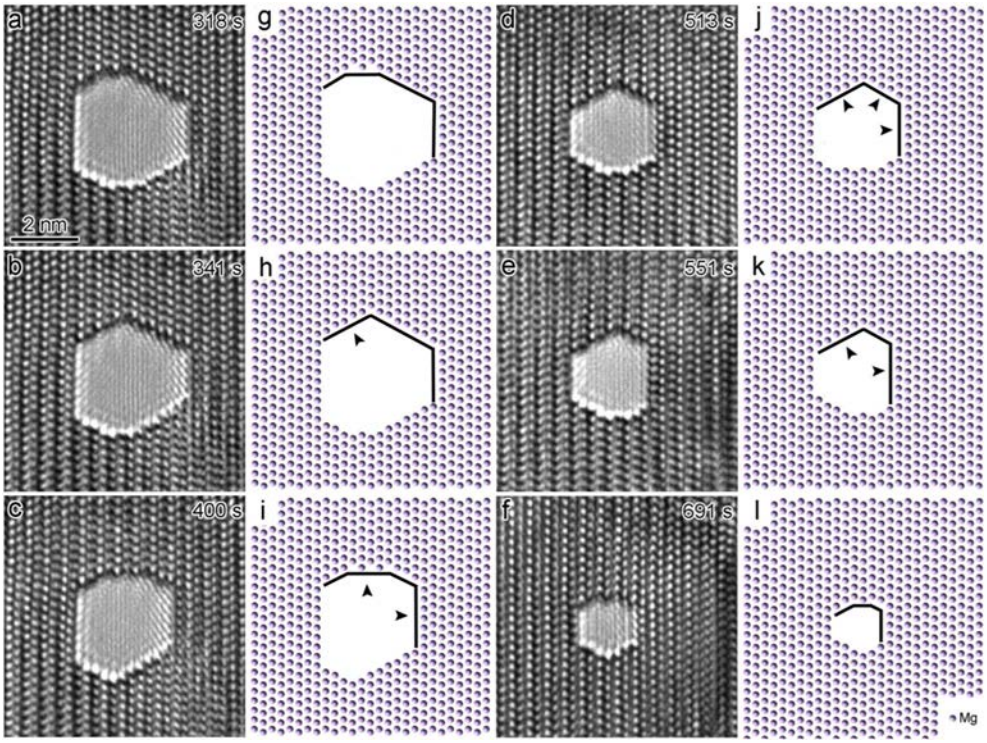

Fig. 5.7. Electron-beam-assisted healing of nanopores in magnesium alloy (86wt.%Mg, 9wt.%Al, 1wt.% Zn and 4 wt.% Sn). (a-f) sequential high-resolution TEM images showing the alteration of nanopore morphology during continuous e-beam irradiation. (g-l) Schematic illustration corresponding to (a-f), respectively [602].

5.3. Size effect in irradiated nanoporous materials and nanowires

5.3.1 Size effect in nanoporous materials

It has been reported in the literature that radiation resistance of NP metals depends on the ligament size of NP metals and the irradiation conditions [604]. Ion irradiation experiments on Au nanofoams have been performed to design the window of radiation tolerant NP Au in terms of ligament size and irradiation dose-rate [604]. Au nanofoams were synthesized by electrochemically dealloying Si from evaporated amorphous Si-Au thin films. During dealloying, as Si is etched away, Au atoms self-assemble into a nanocrystalline porous network. TEM image in Fig. 5.8a shows the ligament diameter is 10-20 nm with a pore size of 20-50 nm, leading to an approximate density of 35-45%. The ion irradiation experiments were performed at room temperature with 45 keV Ne ions to a dose of $4.5\times10^{14}/cm^2$ at dose-rate of$\sim1\times10^{13}$ ions/cm^2/s. Fig. 5.8b shows that the foam structure was unaltered by an irradiation under these conditions, suggesting the stability of the foam structure and the radiation resistance. For comparison, Fig. 5.8c shows significant irradiation damage was accumulated in a single crystal Au under the same irradiation conditions, Ne bubbles and dislocation loops were formed, which are the typical defect clusters formed in FCC metals irradiated at this condition. Fig. 5.8d shows the HRTEM image of irradiated NP Au with the absence of clear defect clusters in the matrix.

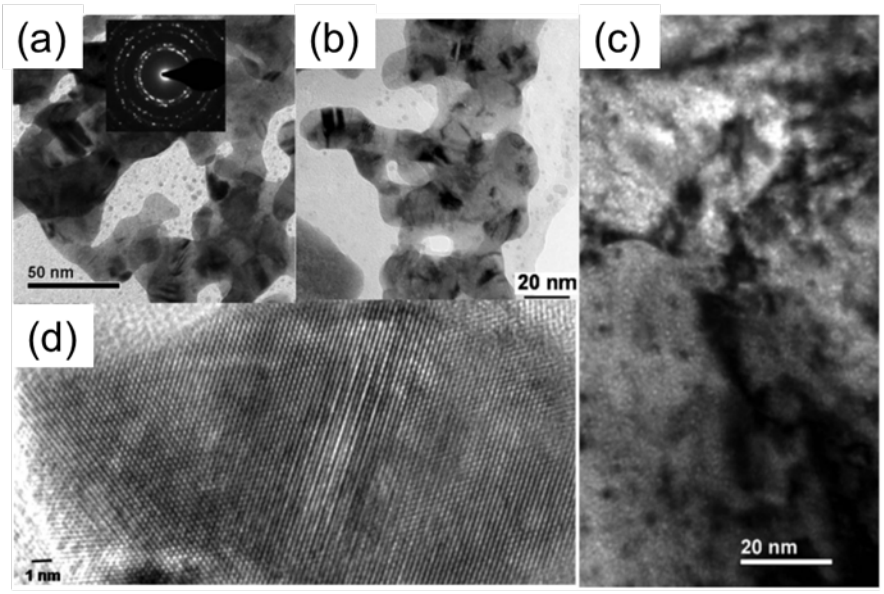

Fig. 5.8. Microstructural evolution of NP Au under irradiation. Irradiation of NP Au was performed with 45keV Ne^+ to a dose of $4.5\times10^{14}/cm^2$ at 300 K. (a) Unirradiated NP Au showing that the ligaments are polycrystalline. (b) Microstructure of irradiated NP Au. (c) Under-focused bright-field TEM images of single crystal Au film after irradiation at the same condition, showing the formation of Ne bubbles and dislocation loops. (d) HRTEM image of irradiated NP Au. No radiation damage was observed in (b) and (d) [604].

In situ irradiation experiments have been performed to study NP Ag that was synthesized by dealloying of $Ag_{23}Cu_{77}$ sputtered film [599]. As shown in Fig. 5.9a, the average ligament size in NP Ag is ~40 nm, and average island size is ~ 150 nm, as shown in Fig. 5.9 a-b. Fig. 5.9 (c-h) compares the microstructural evolution in NP and CG Ag under Kr ion irradiation at room temperature. By 0.02 dpa, a large number of defect clusters were formed in CG Ag (Fig. 5.9d), whereas NP Ag remained intact (Fig. 5.9g). At 0.25 dpa, both the size and density of defect clusters were significantly increased in CG Ag (Fig. 5.9e), while only a few small defect clusters formed in the ligaments of NP Ag (Fig. 5.9h). Similar results have been reported in NP Au that was prepared by dealloying of rolled $Ag_{65}Au_{35}$ leaves (Fig. 5.10a) [40]. *In situ* Kr ion irradiation at room temperature was performed in both NP and CG Au, and the TEM snapshots from *in situ* videos compared the microstructure evolution of CG and NP Au irradiated at the same conditions.

These defect clusters included dislocation loops and SFTs. From 0 to 0.02 dpa (Fig. 5.10 b and b'), a few defect clusters formed in NP Au, whereas defect density increased rapidly in CG Au. By 0.2 dpa, both the diameter and density of defect clusters in CG Au increased significantly (Fig. 5.10c'), while only a few defect clusters were generated in NP Au. Kr ion irradiation caused a gradual and moderate increase of defect density in NP Au up to 0.5 dpa (Fig. 5.10 b-d). At the same irradiation condition, CG Au had accumulated significantly more defects by 0.5 dpa (Fig. 5.10 b'-d').At 0.5 dpa (Fig. 5.10 d and d'), the average diameter of defect clusters in NP Au appeared much smaller than that in CG Au.

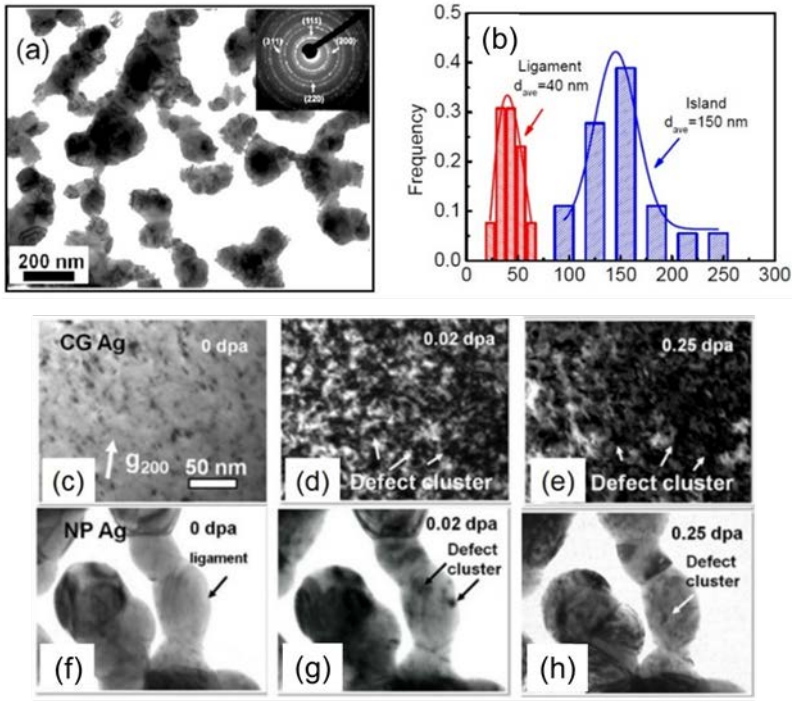

Fig. 5.9. (a) Bright field TEM micrograph of NP Ag. (b) Statistics show the average ligament size is ~ 40 nm, and average island size is ~ 150 nm. (c-h) The drastic difference between microstructures of CG (c-e) and NP (f-h) Ag subjected to Kr ion irradiation at room temperature at different doses. (d, g) After irradiation at 0.02 dpa, CG Ag was swamped with a high density of defect clusters, whereas NP Ag remained intact. (e, h) By 0.25 dpa, there was a significant increase in both the size and density of defect clusters in CG Ag, while only a few defect clusters were observed in the ligaments of NP Ag [599].

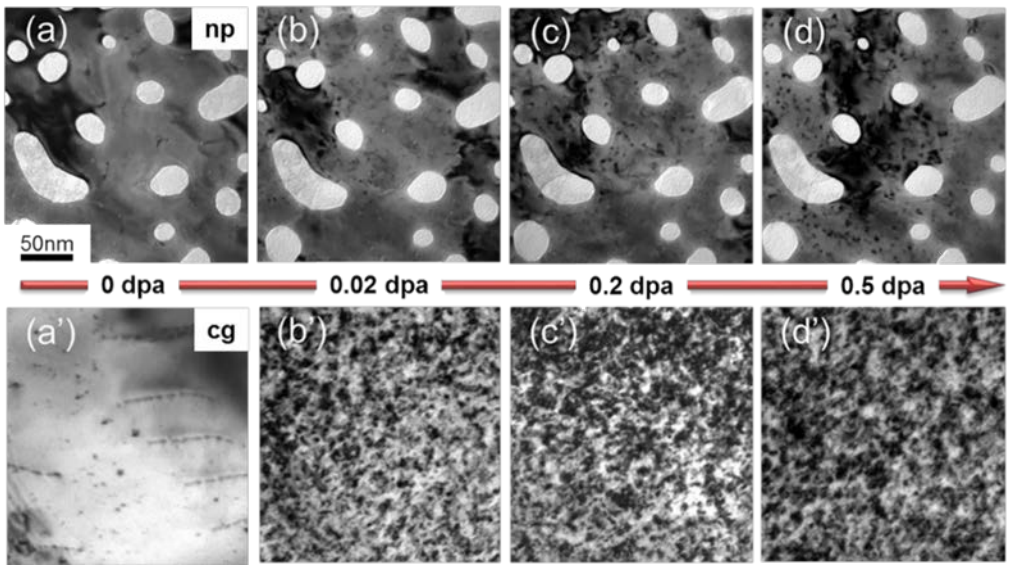

Fig. 5.10. TEM snapshots obtained from *in situ* radiation video revealed drastically different irradiation response between NP and CG Au subjected to *in situ* Kr ion irradiation at room temperature. (a-a') Before irradiation, both NP and CG Au appeared relatively clean with few preexisting defects. (b-d) TEM snapshots show a gradual and moderate increase of defect density in irradiated NP Au, up to 0.5 dpa. (b'-d') In contrast, CG Au had accumulated much more defects rapidly by 0.5 dpa [40].

In a follow-up study, Li *et al* performed temperature dependent *in situ* Kr ion irradiation studies in NP Au by performing a series of isothermal experiments (Fig. 5.11a) [600]. Such a temperature based "jump" test has the advantage of obtaining defect accumulation statistics in one *in situ* experiment, and thus significantly increase the efficiency of *in situ* studies. As shown in Fig. 5.11b, the defect density in NP Au decreases at elevated temperatures. It is worth mentioning that in addition to the studies of NP Au, *in situ* irradiation of porous Mg has also been reported [605]. Although, straightly speaking, the pore size in the Mg used in the study is not in the nanoscale regime, the results were similar to what have been observed in NP Au. Defects accumulated rapidly in CG Mg, but gradually and moderately in porous Mg as shown in Fig. 5.12 [605].

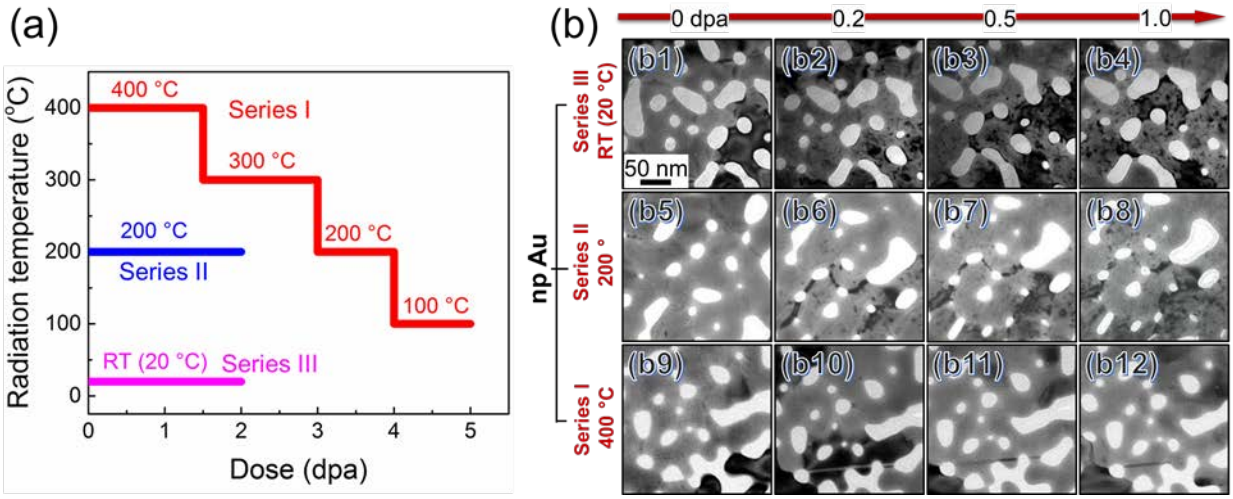

Fig. 5.11. (a) The summary of *in situ* irradiation experiments on NP Au reported in [600]. Series I: temperature-jump tests (400→300→200→100 °C); Series II: at constant 200 °C and Series III: at room temperature (RT). (b) The corresponding TEM snapshots obtained from *in situ* videos show irradiation response of NP Au at various irradiation temperatures. Before irradiation, NP Au contained little defects (b1, b5, b9). (b2-b4) During irradiation, many defects were accumulated in NP Au at RT with dose up to 1 dpa. (b5-b8) At 200 °C, irradiation induces fewer defects in NP Au, and much fewer defects in NP Au at 400 °C (b10-b12). Therefore, defect density decreases with increasing irradiation temperature.

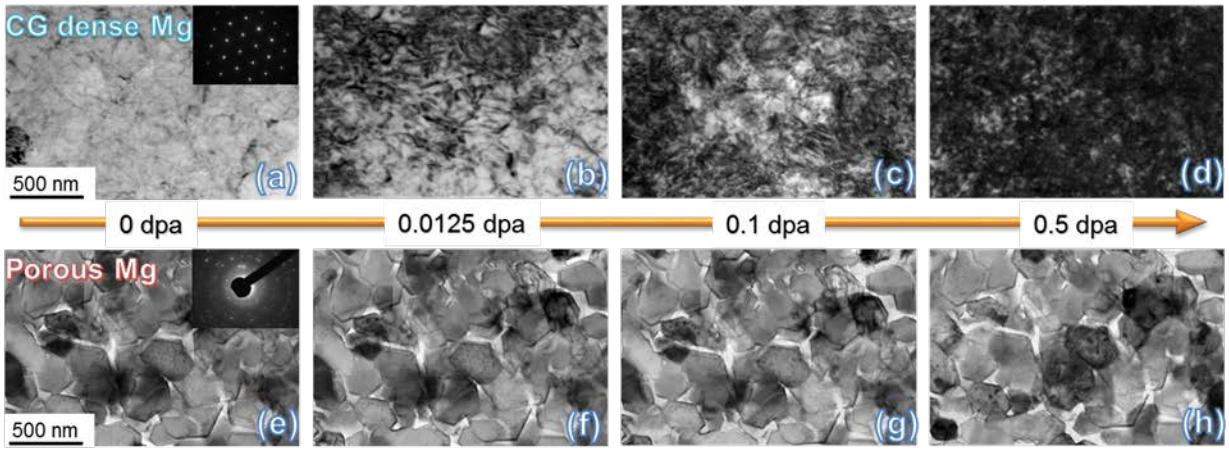

Fig. 5.12. TEM snapshots obtained from *in situ* irradiation video reveal drastically different irradiation response between CG and porous Mg subjected to Kr ion irradiation at room temperature [605]. (a-d) During irradiation of CG Mg, the number of defects increased rapidly by 0.0125 dpa. By 0.5 dpa, tons of defects were introduced during irradiation. (e-h) In contrast, a gradual and moderate increase of defect density were observed in irradiated porous Mg up to 0.5 dpa.

Fig. 5.13 shows the statistics of the size and density evolution of the defect clusters in NP and CG Au at RT and during the temperature-jump test. The average saturated size of defect clusters is ~ 10 and ~ 4 nm in CG and NP Au, respectively (Fig. 5.13a). The defect density in both CG and NP Au reached saturation at a similar dose, ~0.1 dpa (Fig. 5.13b) [40]. Clearly, the free surface plays a major role in removing the irradiation-induced point defects and defect clusters in NP Au. Although a moderate reduction of defect cluster density (a factor of 2) and cluster size (a factor of ~2.5) in irradiated NP Au compared to CG Au was observed, the difference of point defect concentration in the matrix would be substantial. Fig. 5.13c and 5.13d show the statistics obtained from temperature based jump tests of NP Au and CG Au. The saturation defect size in NP Au (5.13c) is ~ 4 nm and has little temperature-dependence. In contrast, in irradiated CG Au, saturation defect size is ~ 10 nm at RT, and decreases monotonically to ~ 4 nm with increasing temperature to 400 °C. The large difference of defect size in CG Au and NP Au irradiated at RT indicating that the free surface of nanopores in NP Au clearly inhibits the growth of defects in NP Au by absorbing both vacancies and interstitials. Due to an active thermal vacancy-interstitial recombination process, it is thought that the growth of defect clusters is suppressed. Therefore, defect size in NP Au and CG Au irradiated at 400 °C is similar, ~ 4 nm. The saturation defect density in both NP Au and CG Au decreases gradually with increasing irradiation temperature (5.13d).

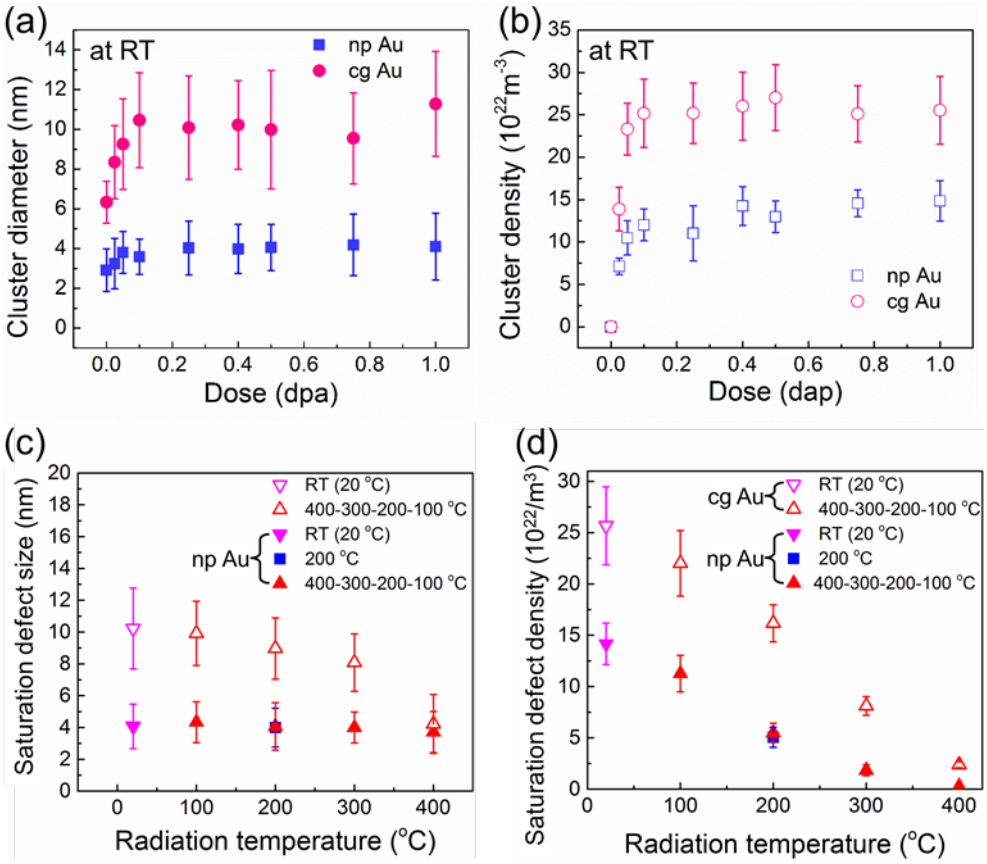

Fig. 5.13. (a-b) Statistics of defect size and density evolution as a function of dose in NP Au and CG Au irradiated at RT [40]. (a) The average defect cluster diameter is ~ 10 and ~ 4 nm for CG and NP Au, respectively. (b) The saturated defect density in NP Au is around half of that in CG Ag. (c-d) Statistics of defect size and density evolution as a function of irradiation temperature in NP Au and CG Au. (c) The saturation defect size in NP Au is ~ 4 nm and has little temperature-dependence. In contrast, in irradiated CG Au, saturation defect size is ~ 10 nm at RT, and decreases monotonically to ~ 4 nm with increasing temperature to 400 °C. (d) Saturation defect density in both NP Au and CG Au decreases gradually with increasing irradiation temperature [600].

One may speculate if most of the nanovoids were removed during irradiation, then the irradiation resistance of NP metals may degrade during subsequent irradiation. However, the foregoing studies show that the existence of nanovoids significantly delays damage accumulation in NP metals by more than an order of magnitude. Deliberate introduction of nanovoids with desirable distribution of sizes and various density may significantly prolong the radiation stability

of irradiated metallic materials. Further investigations on the stability of nanovoids are necessary before this concept can be transferred into a practical reactor application.

MD simulations show that radiation resistance of NP Au depends on the size of the ligament compared to collision cascade size and the migration distance of defects in the time interval between collision cascades [41]. Fig. 5. 14 shows the window of radiation tolerance of Au foam under Ne ion irradiation at room temperature in terms of ligament size vs. dose-rate. When the ligament size is comparable to the cascade size, the emission of planar defects, including stacking faults and twins, and the melting and breaking of ligaments were observed. Porous metals with ligaments comparable or smaller than cascade size are not applicable for the harsh radiation environments, while those with ligament size larger than the migration distance of defects in the time interval between cascades would accumulate irradiation damage in a similar way as conventional materials. In between these dimensions, the foam is immune to irradiation damage by the annihilation of defects at free surfaces.

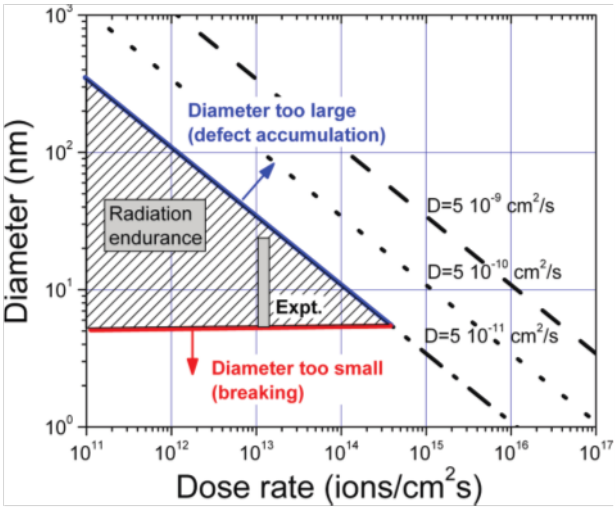

Fig. 5.14. Size effect on stability and design of radiation tolerant NP metals. Irradiation damage resistant ligaments are those within the triangular area. The upper critical limit was estimated for three different diffusivities (D) of defect clusters [604].

5.3.2 Size effect on radiation damage in nanowire materials

In addition to NP materials, size effect on the irradiation tolerance has also been observed in nanowires. Recent work by Sun *et al.* has shown that ZnO nanowires have a distinct defect denuded zone (DDZ) under *in situ* Kr ion irradiation, as can be seen in Fig. 5.15 [597]. This DDZ ranges from the surface of the nanowire to a region in the core of the nanowire that contains a high-density of dislocation loops characterized using high-resolution TEM in Fig. 5.15f. The defect density as a function of distance across the wire in Fig. 5.15g shows that the defect density is the highest in the center of the irradiated ZnO nanowires, and decreases rapidly toward free surfaces. The peak defect density decreases with decreasing wire diameter as shown in Fig. 5.15 h [597].

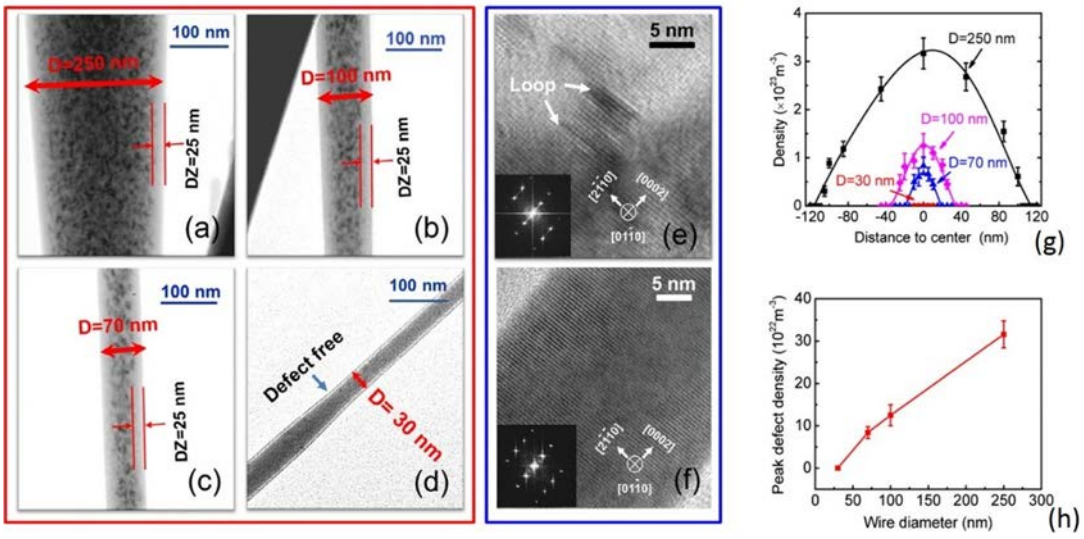

Fig. 5.15. Defect denuded zone (DDZ) in ZnO nanowires with different diameters revealed by *in situ* Kr ion irradiations up to 5 dpa. (a) A TEM micrograph showing a DDZ with a width of ~25 nm for a ZnO nanowire with an average diameter D of ~250 nm, a similar width of DDZ was also displayed in nanowires with D of 100 nm (b) and 70 nm (c). Meanwhile the density of defect clusters appeared to reduce with decreasing wire diameter. (d) When D = 30 nm, no clear evidence of dislocation loops can be observed, that is the wire of this diameter is immune to irradiation-induced damage. (e) High-resolution TEM (HRTEM) image showing dislocation loops in irradiated nanowire with D of 70 nm. The dislocation loops, with ~5 nm in diameter, were located

on {0001} planes. (f) HRTEM image of the irradiated nanowire (D = 30 nm) showing the absence of dislocation loops. (g) Defect cluster density versus the distance to the center of wires with diameters of 30–250 nm. (h) Wire size dependent peak dislocation loop density, that is ZnO nanowire with smaller diameter has lower peak defect density [597].

Through MD simulations as shown in Fig. 5.16, Zhang *et al.* have shown that the vacancy formation energy decreases from 1.02 to 0.96 eV from the bulk region to the surface in Au nanowires [606]. At a region of ~ 3 - 6 nm to the surface, the formation energies of the vacancies decrease, indicating that vacancies attract each other. When the vacancy-surface distance is below 1 nm, the vacancy formation energy drops quickly, providing the driving force for vacancies to migrate toward the surfaces. Consequently, the gradient distribution of vacancy clusters emerges. It is worth mentioning that the formation energy of point defects in certain nanolayer systems, such as immiscible Cu/Nb multilayers [607], decreases much greater (from ~ 1.25 to ~ 0.2 eV in Cu and ~ 2.75 to ~ 1.1 eV in Nb) from the bulk region to the layer interface as compared to nanowires.

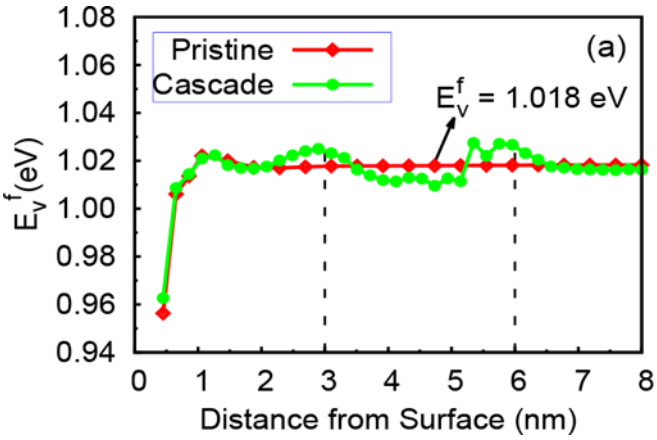

Fig. 5.16. The vacancy formation energy as a function of the vacancy-surface distance in Au nanowires [606].

In addition to the expected DDZ that affects the overall defect density in the wire as a function of wire diameter, the *in situ* Kr ion irradiation study on ZnO nanowires shows size dependent swelling and a non-uniform DDZ that is influenced by the existence of preexisting defect clusters in the wires [597]. Under irradiation, the preexisting large dislocation loops (L1-L3 in Fig. 5.17a) migrated along the prismatic plane of the ZnO nanowire at ~ 2 nm/s during radiation before they became stationary. By 1.5 dpa, as shown in Fig. 5.17b, these preexisting dislocation loops are pinned by the radiation-induced small dislocation loops. Swelling of the ZnO nanowires along the radial direction was observed. Radiation-induced radial strain (ε), ($\varepsilon = (d - d_0)/d_0$, where d_0 and d are the wire diameter before and after radiation) increases with doses and the magnitude of strain decreases for nanowires with smaller diameters (Fig. 5.17c). Interestingly nanowires with diameters of 30 nm or smaller have no swelling. Fig. 5.17d shows that a high-density of small radiation-induced dislocation loops are trapped by the preexisting large dislocation loops, leading to the formation of dumbbell-shape distribution of defect clusters, accompanied by the DDZs near the surface.

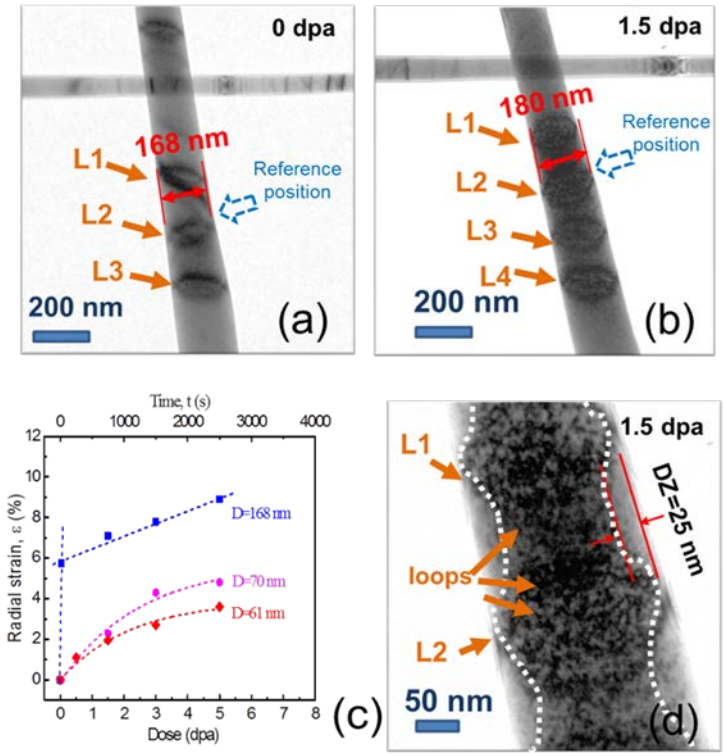

Fig. 5.17. Radiation-induced strain and the influence of internal defect sinks on loop distribution. (a) Bright field TEM image of several preexisting dislocation loops (L1-L3) in ZnO nanowire prior to irradiation. (b) After Kr ion irradiation up to 1.5 dpa, a high density of defect clusters was observed near an array of hexagonal shaped preexisting dislocation loops (L1- L3). The wire diameter (measured from the same location) swelled from 168 to 180 nm, and the dash arrows show the reference position for the measurements. Notice that another loop (L4) migrated upward along wire axial direction during radiation. (c) Comparison of irradiation-induced swelling (radial strain) in wires of various diameters shows that wires of larger diameter (D = 168 nm) swelled rapidly to ~ 9.0% by 5 dpa. In contrast, wires of smaller initial diameter, 61 nm, swelled gradually and moderately to ~ 3.6%. (d) Magnified TEM micrograph of the loops L1 and L2 in Fig. 6.11b shows that a large number of small dislocation loops were trapped by pristine dislocation loops, and consequently a dumbbell distribution of small loops was observed [597].

MD simulations have also shown an interesting phenomenon, surface roughening after 20keV self-ion irradiation of Au nanowires [608]. As shown in Fig. 5.18, a Au nanowire with the diameter of 8.2 nm had relatively smooth surface after ion bombardment of 80 ps (5.18a). After 170 ps, a large crater was formed on the nanowire surface. It is argued that the formation of craters at the surface of Au nanowires is due to the microexplosion of hot atoms when the PKA energy is high enough (> 10 keV in the case of Au nanowires). Such a crater formation phenomenon is likely

to affect the stability of metallic nanowires during irradiation. There is, however, no experimental evidence to validate such a prediction.

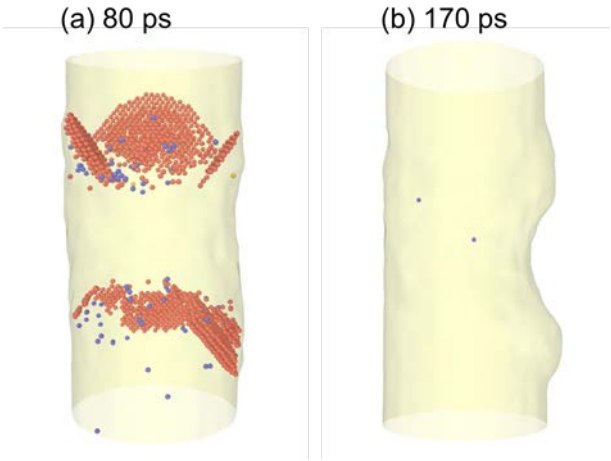

Fig. 5.18. MD simulations illustrate the surface roughening in a 8.2 nm-thick Au nanowire after 20 keV self-ion irradiation [608]. (a) Irradiation process at 80 ps, and (b) a crater formed on the surface of Au nanowire after 170 ps, leading to a rough surface.

5.4. Irradiation-induced structural change of nanoparticles

The nanoscale effect on radiation damage in metallic nanoparticles is dominated by the increased sputtering present in the particles due to the increasing surface-to-volume ratio. A simple analytical model accounting for the local curvature and depth of the damage in the particle among other factors regarding sputtering yield appears to be a good fit and valid at least to a first order [609]. The size effect on sputtering yield and the corresponding fundamental mechanisms during self-ion irradiation have been reported by Bufford *et al.* [598]. By investigating the mechanisms via *in situ* TEM, the changes in mechanism due to particle size can be directly observed (Fig. 5.19). As the size of the particle decreases below a threshold of 10 nm, a transition between cratering to particle disintegration was observed. In Fig. 5.19a (g'-i'), the violent disintegration of a single 5

nm particle to form five smaller nanoparticles was observed due to a single ion strike. Although these mechanisms may have ties with those seen in the surface reconstruction that occurs in bulk and thin films exposed to ionizing radiation [610-612], the detailed mechanisms appear much different due to the free surfaces in multiple directions and, as such, these two dominant mechanisms (cratering and disintegration) warrant further discussion and research.

In a complementary modeling effort, Kissel and Urbassek used MD simulations to predict the disintegration of 4 nm Au particles bombarded with 100 keV Au ions (Fig. 5.19b) [613]. This study exploring the role of ion energy on the particle evolution showed that the classical linear-cascade sputtering is active in addition to a thermal aspect that results in enhanced sputtering yield from the Au nanoparticle. In these small particles, sputtering can result in the mass disintegration of Au particle in less than 20 ps and the release of Au clusters of up to 100 atoms [613]. This MD simulation effort agrees very well with the structural evolution seen experimentally in the 5 nm nanoparticle that was hit by a single 46 keV Au ion in Fig. 5.18b [598].

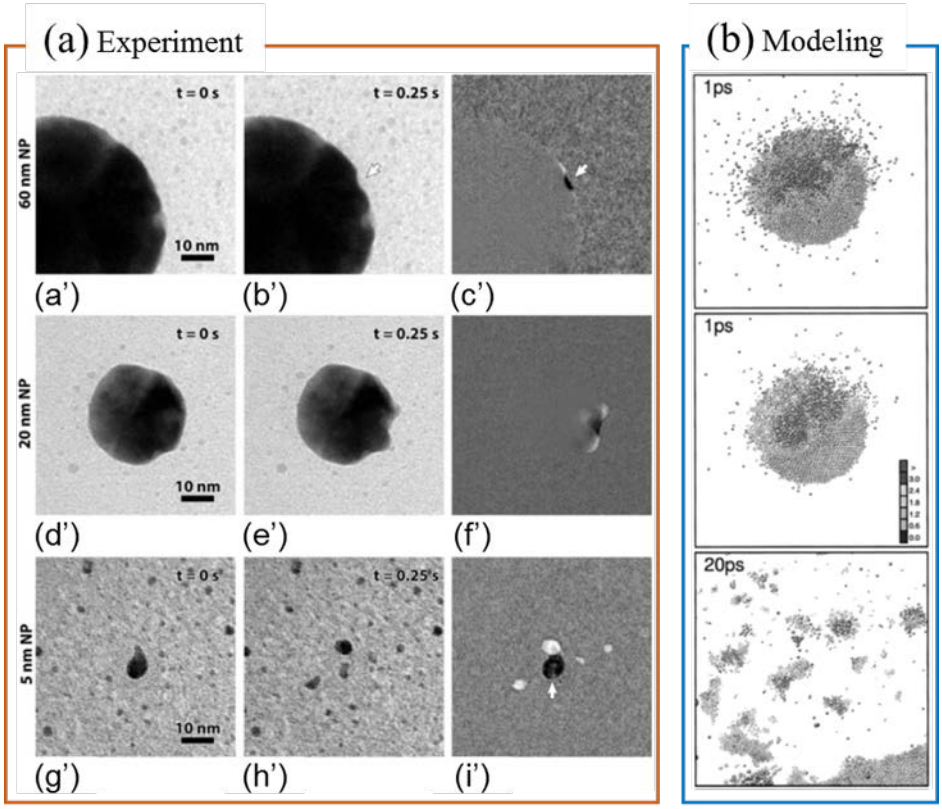

Fig. 5.19. Irradiation-induced nanoparticle disintegration (experiment (a) and modeling (b)). (a) Effects of single 46 keV Au ions in Au nanoparticles of decreasing size. Note that the magnification is similar for all micrographs. Each pair of micrographs is separated by 1 frame, about 0.25 s here. (a'–c') A single ion strike in a 60 nm nanoparticle created a surface crater, marked by the white arrow. (c') The difference image highlights the change between (a') and (b'); features present only in (a) are dark and newly formed features present only in (b') appear light. (d'–f') A single ion creating a crater in a 20 nm nanoparticle. (f') The difference image. (g'–i') An approximately 5 nm teardrop-shaped nanoparticle was initially surrounded by a number of previously sputtered particles. (h') The nanoparticle exploded, leaving several particles nearby. (i') Difference image showing the locations of the old and new particles. The white arrow indicates a fragment from (h') that is difficult to see in (i') because it overlapped with the original nanoparticle location [598]. (b) Perspective (top) and cross-sectional (middle) view of the Au nanoparticle at t =1 ps after atom bombardment. Bottom: Perspective view at t=20 ps. Atoms are shaded according to their local temperature in units of the melting temperature of Au [613].

Although ceramic nanoparticles often have novel size-dependent optical, magnetic, electrical and piezoelectric properties, their behavior in radiation environments remains poorly understood due to the minimal studies performed to determine the evolution of their microstructures, mechanical and physical properties, and band gap stability. In addition to the

sputtering effects seen in metallic nanoparticles, nanoscale ceramics generally appear to undergo considerable microstructural evolution. An example of the disintegration of SnO_2 exposed to 4.6 MeV Pb ion beam to a dose of 5×10^{12} ions/cm^2 is shown in Fig. 5.20. The drastic structural evolution from 100 nm single crystal particles to interconnected much smaller nanoparticles with dimensions on the order of a few nm is a result of the thermal spike in the SnO_2 [614]. The extremely fine nanoparticles formed in the SnO_2 may have unique properties that worth further studies.

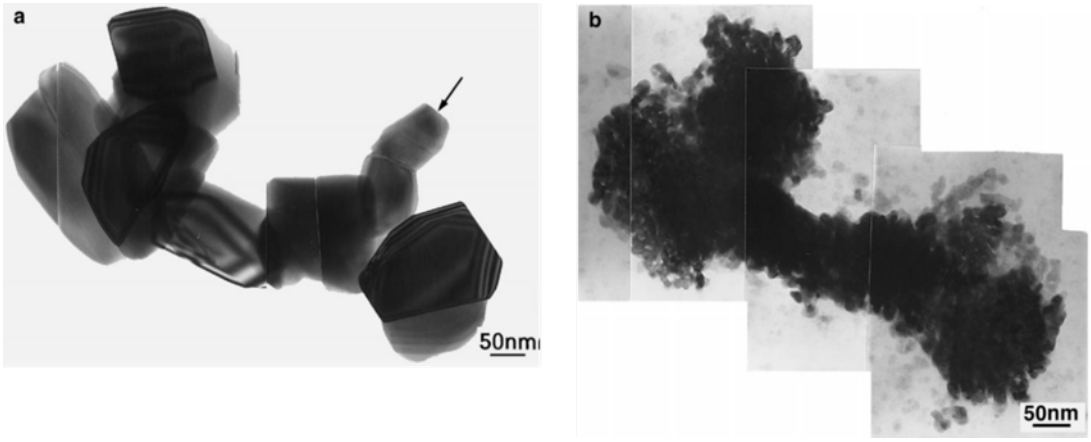

Fig. 5.20. Disintegration of SnO_2 nanoparticles by irradiation. Pd ion beam induced microstructure evolution Tin oxide nanograins: (a) Before irradiation, the SnO_2 nanoparticles are faceted with dimension of ~ 100 nm. (b) After radiation with 5×10^{12} Pb ion/cm^2, extremely fine SnO_2 nanoparticles form. The arrow shows a small grain that partially disappears after ion irradiation [614].

In addition to forgoing discussions, many other *in situ* irradiation studies have been performed as a function of particle size [598, 615], dimensional ratio [616, 617], and orientation etc. For example, a swift heavy ion study, using 1 GeV Pb, found an inverse relationship between the initial nanocluster on the target and the average sputtered particle size collected [618]. In contrast, Jarvi *et al.* predicted that during light ion irradiation the size of the particle plays no role in the sputtering yield [619]. Another MD simulation by Kissel *et al.* probed the interaction of

irradiated Au with an underlying Au substrate during a cascade event [620]. This simulation performed as a function of energy showed that the particle can not only be sputtered rapidly, but also be ejected from the surface due to thermal spike, and a crater can be produced in the substrate [620]. It should be noted although it appears generally accepted that the sputtering yield of nanoparticles is enhanced compared to bulk and thin film systems, it remains unclear what term and alteration should be added to the classical Thompson distribution to best represent the observed mechanisms. The subject of enhanced sputtering yield in nanoparticles is an area requires future research. Summarizing the experimental and modeling effort looking at radiation damage in Au nanoparticles has demonstrated three active regimes.

1) For particles with a diameter of less than ~10 nm, radiation results in atomization and violent disintegration of the nanoparticle.
2) Radiation of particles with dimensions of ~10-100 nm results in cratering with filaments and cluster sputtering.
3) When the particle diameter is greater than ~100 nm, radiation results in internal defect formation and sputter yields reach near normal rates.

Although a majority of the work to date has focused on Au nanoparticles, some study has been performed in other metallic nanoparticle systems. A limited set of models have looked at Fe nanoparticles to determine the size at which enhanced radiation stability may be possible [621]. Moving beyond monolithic metal systems, an interesting example of internal structural evolution due to just a 5 keV He ion beam is seen in the irradiation-induced destabilization of the icosahedral structures in FePt nanoparticles [622]. This low energy light ion implantation at a dose as low as 10^{17} ions/cm^2 is enough to drastically alter the structure of the icosahedral particles, but surprisingly not that of the $L1_0$ particles [622]. Fig. 5.21a shows a FePt nanoparticle, which is a

previously multiply twinned particle, has transformed into an FCC single crystal particle after 5 keV He ion irradiation at a maximum fluence of 3×10^{17} ions/cm^2 [622]. However, the He implantation was found to lower the $L1_0$ ordering temperature of the FePt nanoparticles. This minor change in the structure and transition temperatures from a relatively minimal radiation exposure had observable changes on the properties of the irradiated FePt nanoparticles [623]. Javri *et al.* utilized MD simulations to highlight how the transition from icosahedral to single crystalline morphology can happen from even a single cascade event. MD simulations show that this transition occurs due to the melting and resolidification of the entire nanoparticle, as shown in Fig. 5.21b [624]. The evolution from icosahedral structure to single crystal nanoparticles appears to be a global response to ionizing irradiation, as it has also be been observed with a similar transition mechanism through a disordered phase [625].

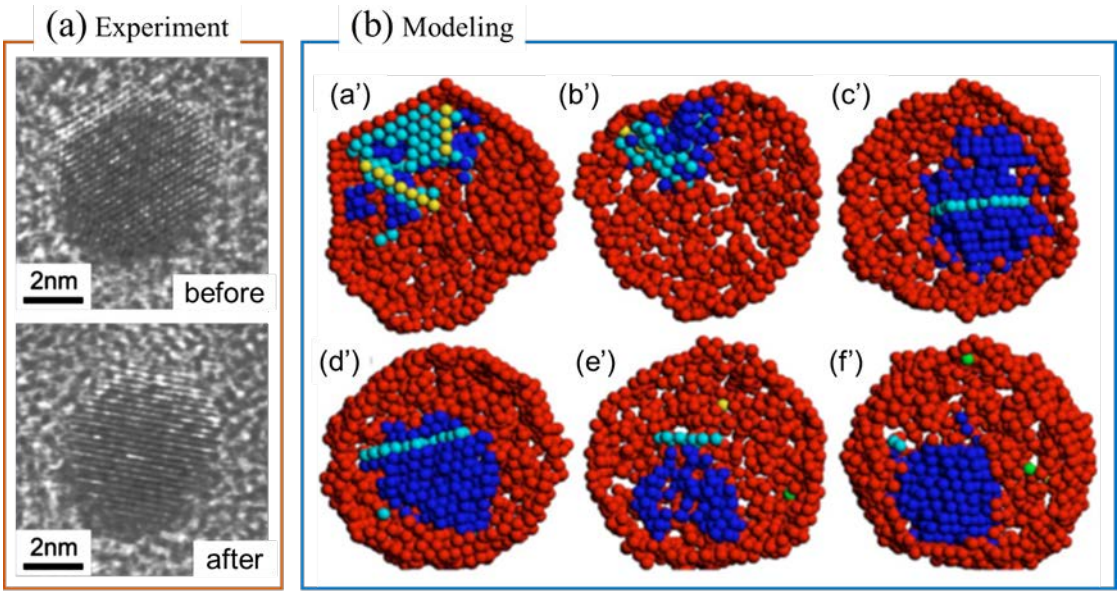

Fig. 5.21. Radiation-induced crystal structure change of FePt nanoparticles (experiment (a) and modeling (b)). (a) A FePt nanoparticle, which exhibits multiply twinned structure before irradiation (top) has transformed into an FCC single crystal particle (bottom) after 5 keV He irradiation at a maximum fluence of 3×10^{17} ions/cm^2. (b) MD simulation results show the transition from icosahedral to single crystalline morphology in a partly molten cluster. The upper

part shows snapshots of the transition. The atoms, from darkest to lightest, are FCC (blue), surface (red), HCP (light blue), and fivefold symmetry axis (yellow). Liquid atoms are not shown. Initially (a'), the cluster is a partly molten icosahedron but at some point the liquid part absorbs the solid almost completely (b'). The solid then recrystallizes with only one twin boundary between two FCC components (c'). The boundary exists for several nanoseconds (d') but migrates in the crystalline part of the cluster. At some point it reaches the liquid boundary (e') and vanishes, leaving a single crystalline solid part (f') [624].

In addition to free-standing nanoparticles, nanocomposites embedded with nanoparticles have demonstrated enhanced performance under radiation environments. These low-dimensional structures can be produced in large quantity by bulk processing technique [6], film deposition [626], or ion implantation [149, 627, 628]. Because of the extensive studies [6, 13, 282, 482, 511, 629-661] and prior excellent review on the response of ODS steels to radiation environments [6] and models discussing the radiation response of yttria nanoparticle explicitly [662], this system will not be discussed as an embedded nanoparticle system in this review. The reader is referred to two separate overview papers by Meldrum *et al.* that nicely describe the potential for forming nanoparticles in bulk systems by ion implantation and the future opportunities in the field [628].

The most common application of embedded nanoparticles in radiation environments, in addition to ODS steel, appears to focus on metal nanoparticles embedded in glass. An example from Ramjauny *et al.* can be seen in Fig. 5.22 [663]. In this work, it was shown that the initial embedded Au nanoparticles can be destroyed by 4 MeV heavy ion irradiation at a dose of 10^{16} ions/cm^2. This can also result in the formation of new precipitate phase. It was also shown that by controlling temperature or nuclear stopping power, a bimodal size distribution of the particles was achievable [663].

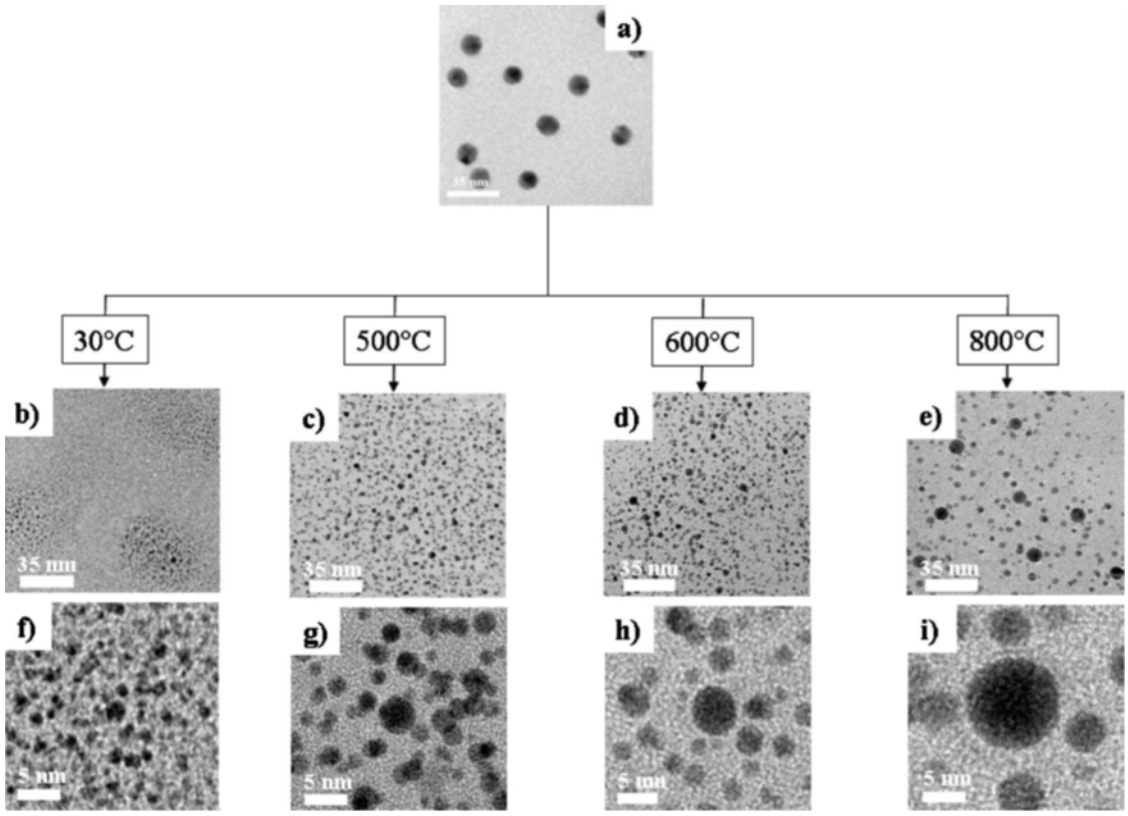

Fig. 5.22. Irradiation-induced microstructural change of nanoparticles at high temperatures. (a) Bright field TEM micrograph of an as-prepared sample. Bright field TEM micrographs of samples irradiated with 4 MeV Au ions at a fluence of 8×10^{16} ions/cm^2 for increasing temperatures: (b) and (f) 30 °C, (c) and (g) 500 °C, (d) and (h) 600 °C, and (e) and (i) 800 °C. Magnification of the previous micrographs are also shown: (f) 30 °C, (g) 500 °C, (h) 600 °C, and (i) 800 °C. The ion irradiation direction is normal to the plane [663].

The large variation in structure of embedded Au nanoparticles was thoroughly investigated to control the particle size and distribution [664]. It has also been shown that subsequent ion irradiation under limited condition can results in the Au particles being elongated in a mica matrix [627]. Ridgway *et al.* proposed a thermodynamic argument for the elongation of Au nanoparticles due to swift heavy ions [665], despite the far-from-equilibrium conditions. In addition to the work on Au, it was shown that embedded particles of a range of compositions can be formed or tailored through controlled ion beam modification. These systems include embedded: Ag [666], Pt [667], Co [668], amorphous Cu [669], ZnO [670], solid state Xe [671], and many more [628] under the

right irradiation conditions. In addition to amorphous silica and mica most commonly used in these studies, a range of other matrices with intriguing properties can be utilized including matrix as exotic as $CdNbO_3$ [672] or Poly (VinyliDene Fluoride) (PVDF) [673]. In theory, embedded nanoparticles can be produced using an immiscible pair of implanted species and matrix, as well as many other systems that will be kinetically limited. Once created, the structure of these embedded particles can be tailored through a combination of ion irradiation and thermal processing. Systems containing embedded nanoparticles are already finding applications in harsh radiation environments, as is highlighted in the use of erbium-doped-nanoparticle optical fibers for space applications [674]. A nice study reviewing the potential to tailor shape and size of embedded nanoparticles can be found in the reference from Ridgway *et al.* [675]. It should be noted that radiation damage in metallic materials with nanoprecipitate is a subject that has also been intensively studied [13, 676-690], but not covered in the current review due to space and time limitations. With an improved fundamental understanding on the subject, a multitude of engineering applications varying from quantum bridges [691] to color changing artwork [692] is possible!

5.5 The influence of free surface on the defect migration kinetics

In situ radiation study provides abundant information to investigate defect migration kinetics in materials under irradiation. Global and instantaneous diffusivities of defect clusters under irradiation have been determined. The global diffusivity (D_g) is the diffusivity averaged over a long period of time (including migration and dwell time) for numerous defect clusters, whereas instantaneous diffusivity (D_i) is measured only during the migration process [599]. Fig. 5.23a shows typical examples of measured migration distance (diffusion length X) of individual defect clusters (4 nm in diameter) in both CG and NP Ag. In order to determine the global diffusivity of

defect clusters, the migration of a large number of defect clusters has been studied statistically. Fig. 5.23b shows diffusion length square (X^2) vs. accumulative time for numerous defect clusters with similar size (4 nm in diameter) for both CG and NP Ag. Assuming one-dimensional diffusion, the diffusivity of defect clusters (D) can be estimated by

$$D = X^2 / 2t \qquad (5.5),$$

where t is the diffusion time. A linear fit of these data shows that D_g of defect clusters (d_{defect} = 4 nm) in CG Ag is 78 nm^2/s, much greater than that in NP Ag, ~12 nm^2/s. Fig. 5.23c compares the size-dependent variation of D_g for CG and NP Ag. Basically, D_g reduced rapidly from 105 to 45 nm^2/s with increasing size of defect clusters in CG Ag. A similar trend is observed in NP Ag. However, for the same dimension of defect clusters, D_g in NP Ag is consistently much lower than that in CG Ag. Similar techniques have been applied to determine D_i as shown in Fig. 5.23d. Basically, there is no clear size-dependent variation of D_i for CG and NP Ag. Nonetheless, the average value of D_i in NP Ag, ~350 nm^2/s, is much less than that in CG Ag, ~1200 nm^2/s. The value of D_i in both CG and NP Ag is at least an order of magnitude greater than their respective D_g.

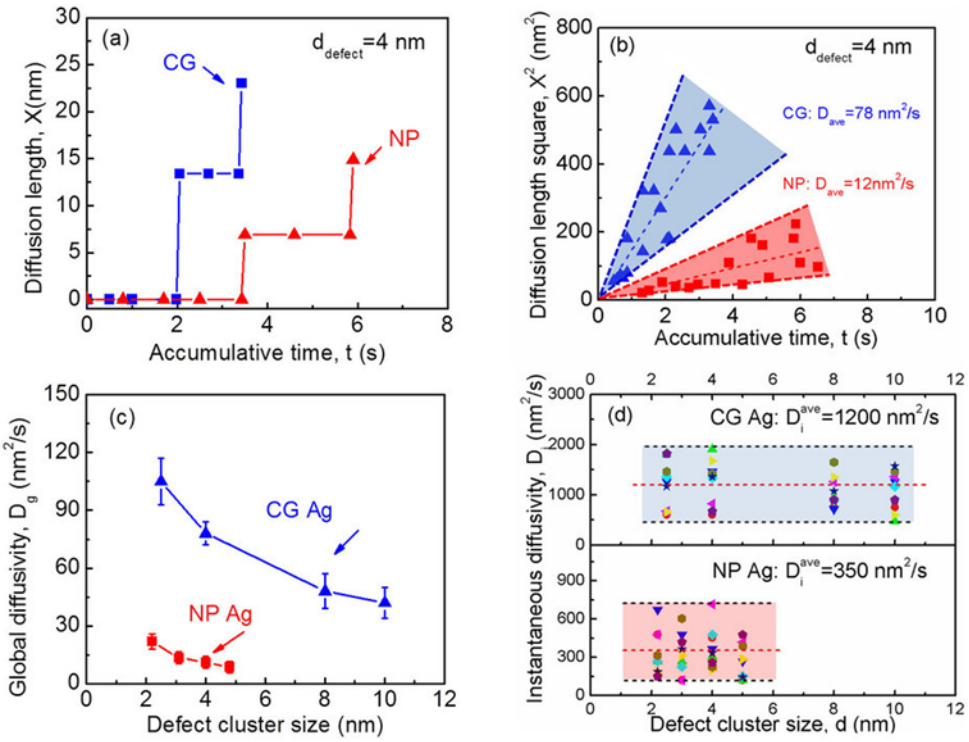

Fig. 5.23 Determination of global and instantaneous diffusivities of defect clusters in CG and NP Ag. (a) A representative plot of diffusion length (X) versus accumulative time for individual defect clusters with a diameter of 4 nm in CG and NP Ag. (b) Plots of diffusion length square (X^2) vs. accumulative time for a large number of defect clusters with a similar average size of 4 nm. The average global diffusivity was estimated to be ~78 and 12 nm^2/s in CG and NP Ag, respectively. (c) The global diffusivity (D_g) of defect cluster in NP Ag is consistently lower than that in its CG counterpart. (d) The instantaneous diffusivity (D_i) in CG and NP Ag was estimated to be 1200 and 350 nm^2/s, respectively [599].

The migration kinetics of defect clusters has been examined in NP Au under irradiation at different dose-rates [40]. The global diffusivity of defect clusters was determined by using the same estimation method [40]. Like the migration behaviors in NP Ag [599], most defect clusters migrate in a 'stick-slip' manner that is a defect cluster migrates instantaneously within a fraction of a second, and then stays for a while (dwelling time) before its next movement. Fig. 5.24a shows D_g of defect clusters in NP Au at two dose-rates, 3.2×10^{-3} and 5.0×10^{-4} dpa/s. The global diffusivity is greater at higher dose-rate. Fig. 5.24b shows the instantaneous diffusivity of the

defect clusters in the irradiated NP Au varies from 200 to 800 nm^2/s, and the average value of the instantaneous diffusivity did not show a clear dependence on the dose-rate.

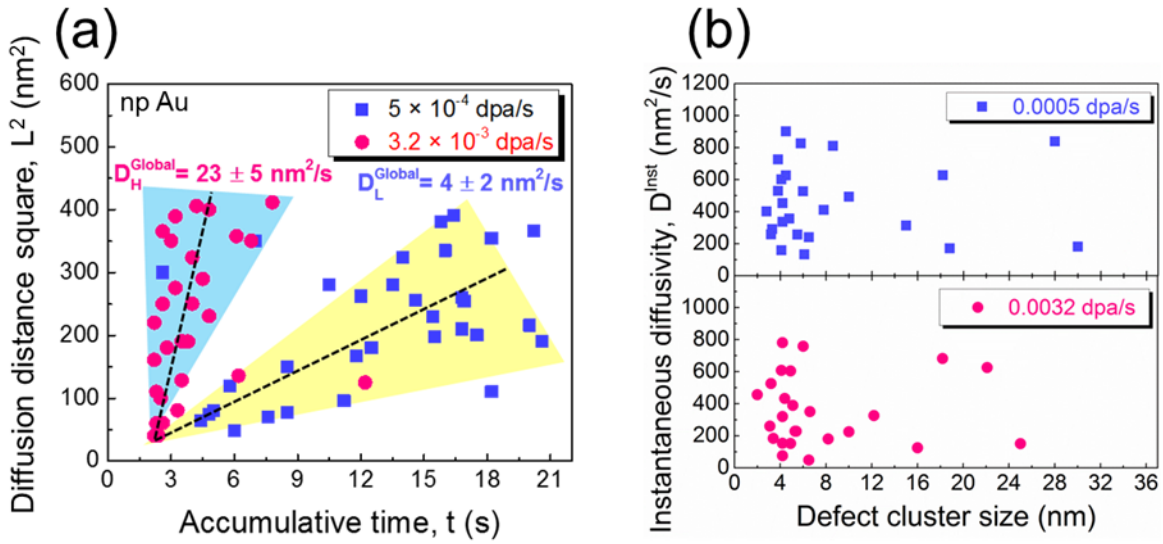

Fig. 5.24 Determination of global and instantaneous diffusivities of defect clusters in NP Au under irradiation at dose-rates of 5.0×10^{-4} and 3.2×10^{-3} dpa/s. (a) The global diffusivity of defect clusters in NP Au was significantly reduced when the dose-rate decreased from 3.2×10^{-3} to 5×10^{-4} dpa/s. (b) The instantaneous diffusivity of defect clusters in irradiated NP Au varies from 200 to 800 nm^2/s, and the average value of instantaneous diffusivity shows little dependence on dose-rate and cluster diameter [40].

5.6. Summary and future work

Understanding the response of low-dimensional nanomaterials to radiation environments have become the cornerstone of modern electronics and have been essential for the development of advanced nuclear systems. Despite enormous research efforts for development of nanomaterials with novel physical properties, the fundamental understandings on the irradiation tolerance of NP materials, nanoparticles and nanowires remain limited. The free surfaces can act as defect sinks and remove the radiation-induced defect clusters, including dislocation loops, segments and SFTs

at room temperature. However, the radiation response of these low-dimensional materials in harsher environments, such as neutron radiation at elevated temperatures with high flux is largely unknown. Diffusivities of defect clusters in NP pure metals under irradiation have been measured by the *in situ* technique. It is shown that the response of nanoparticles to irradiation conditions cannot be entirely predicted from the bulk response, and varies drastically among these low-dimensional materials. Further work on the solute redistribution of low-dimensional alloys and corresponding mechanical property evolution under irradiation is necessary, and the window of radiation tolerance of low-dimensional materials in various irradiation conditions needs to be established. Coupling of multiscale modeling and experimental observations improves our understanding of radiation behavior of low-dimensional materials and predicts the performance of low-dimensional materials in harsh irradiation environments.

Chapter 6. Summary and future outlook

Radiation damage in nanostructured materials has emerged as a new arena that bridges among the community of nanostructured materials, radiation effects, physics, mechanics and modeling and simulation. There are significant challenges and opportunities in front of us.

A paramount challenge remains how to discover and design advanced materials that are eventually "immune" from radiation to hundreds of dpa. Significant progress has been made to explore the impacts of various types of defect sinks in nanostructured materials on alleviation of radiation damage. However there are abundant scientific questions that remain to be addressed. The followings are some outstanding issues from a long list of scientific problems that deserve prompt attention.

1. How to design defect sinks that have "self-healing" capability?

It is well known that most defect sinks evolve during interaction with radiation induced defect clusters. Consequently these defect sinks may lose their capability to continuously absorb or eliminate radiation induced defect clusters. Perhaps the ideal defect sinks should have "self-healing" capability, so that these sinks can retain their ability to eliminate radiation induced damage while recovering at the same time. Although there are some limited success in using precipitate (such as TiC etc.) to alleviate radiation damage in austenitic stainless steels, and ODS steels, there is a need to design advanced radiation resistant materials with progressively greater sink strength and self-healing capability. The concept of work hardening and dislocation recovery is, to some extent, analogous to the search for such type of ideal defect sinks.

2. How to combine the advantages of several types of defect sinks into one material system to achieve superior radiation tolerance?

In each of previous chapters, a particular type of defect sinks is the primary defects in nanostructured materials. It is natural to suspect that an innovative combination of these defects into defective networks may be an effective approach to tackle radiation induced damage. There are numerous successful examples in the literature already, including ODS alloys with grain boundaries and phase boundaries, nanotwinned metals with nanopores, etc. Clearly a lot could be done to design nanomaterials with defective networks to handle the transportation and elimination of radiation induced defects. An analogous example is the city's infrastructure, consisting of drains and underground tunnels, that can effectively defeat flood.

3. How to significantly enhance the thermal stability of defect sinks?

The introduction of most defects put materials into a state further away from equilibrium, as these defects store excess energy. Thermodynamically, most of these defects can be removed at elevated temperature (by annealing) with few exceptions (such as oxides nanoprecitates in ODS steels). As most radiation environment encounter intermediate-to-high temperatures, the thermal stability of most defect sinks is clearly a major concern. There are increasing studies on enhancement of thermal stability in nanostructured materials. A nature combination of outstanding thermal and radiation stability may enable unprecedented radiation tolerance in nanomaterials.

4. How do defect sinks engage and absorb radiation induced defect clusters?

Although there are abundant examples showing the significant reduction of defect density in nanomaterials, fundamental questions remain on how defect sinks interact and eliminate these defect clusters? Modeling and simulations using various tools are necessary to address these fundamental physics questions. In fact modeling studies on radiation induced damage in nanomaterials remain a largely unexplored territory.

5. What is the influence of nanomaterials on nucleation and growth of defects under radiation? As defect sinks in nanomaterial are closely spaced, these sinks may drastically change the formation of point defects in their neighborhood. At an atomistic level, such a phenomenon can be explored in greater detail via MD simulations.

6. What is the impact of defect sinks on mobility and kinetics of radiation induced defect clusters? *In situ* radiation inside a transmission electron microscope remains a critical tool to answer this question. The major facility in the US, IVEM at Argonne National Laboratory, the new facility at Sandia National Laboratory and in situ radiation facilities worldwide have produced a significant amount of data in this aspect. Continuous upgrade of the existing facility and establishment of new facility worldwide are necessary. Combination of in situ studies with modeling is critical to understand and predict the kinetics of defect clusters in irradiated nanomaterials.

7. What is influence of radiation damage on mechanical properties of irradiated nanostructured materials? This appears as an obvious question. However this subject is, surprisingly, a large empty space to date. A combination of advanced nanomechanical testing with radiation capability is necessary to evaluate the mechanical behavior of irradiated nanomaterials.

8. How to fabricate high quality bulk nanostructured materials with enhanced radiation tolerance? The nanostructured materials have spent two decades to explore the synthesis of bulk nanostructured materials. Many of their success can be translated to the nanomaterials for nuclear application. Severe plastic deformation, such as equal channel angular pressing, can now process large amount of materials in a short time. Consolidation of nanocrystalline powders (prepared by ball milling or chemical synthesis) by sintering can produce bulk nanostructured materials.

9. How to synthesize large-scale radiation resistant coatings? Many of the previous chapters have discussed the radiation tolerance of nanostructured coatings consisting of metallic or ceramic materials. Fabrication of large scale coatings is a possibility given the maturity of industry in using a variety of coating techniques. The radiation resistance of these coatings need to be rigorously evaluated.

As described in foregoing section, investigation of radiation damage in nanomaterials is an emerging and active research subject, rich in materials science, physics, chemistry and mechanics. Such a new arena brings many aspects of nanomaterials together, and may eventually lead to significant applications of novel nanomaterials for advanced nuclear energy applications.

Acknowledgements

We acknowledge Prof. Engang Fu from Peking University and Dr. Qing Su from University of Nebraska, Lincoln, for providing data and discussion. X.Z. and J.L. acknowledge financial support by NSF-DMR-Metallic Materials and Nanostructures Program under grant no. 1643915, and partial support by NSF under grant no. 1611380. Work by M.L.T. was supported by the U.S. Department of Energy, Office of Science, Basic Energy Sciences, under Award # DE-SC0008274. KY.Y. acknowledges financial supports from National Science Foundation of China (51501225) and Start-up Program of China University of Petroleum-Beijing (2462014YJRC019 and 2462015YQ0602). M.N., and L.S. acknowledge financial support from the DoE Office of Nuclear Energy, Nuclear Energy Enabling Technologies, award DE-NE0000533. L.S. also acknowledges financial support by NSF under award no. 1130589. H.W. and X. Z. acknowledge the funding support from the U.S. Office of Naval Research (N00014-17-1-2087 and N00014-16-1-2465), and start-up program from Purdue University. K.H. acknowledges partial support by the LDRD program at Sandia National Laboratories and the Division of Materials Science and Engineering, Office of Basic Energy Sciences, U.S. Department of Energy. This work was performed, in part, at the Center for Integrated Nanotechnologies, an Office of Science User Facility operated for the US Department of Energy (DOE) Office of Science by Los Alamos National Laboratory [Contract DE-AC52-06NA25396] and Sandia National Laboratories [Contract DEAC04-94AL85000]. Sandia National Laboratories is a multi-program laboratory managed and operated by Sandia Corporation, a wholly-owned subsidiary of Lockheed Martin Co., for the U.S. Department of Energy's National Nuclear Security Administration under contract DE-AC04-94AL85000. The IVEM facility at Argonne National Laboratory is supported by DOE-Office of Nuclear Energy. C.S. acknowledges support through the INL Laboratory Directed

Research & Development (LDRD) Program under DOE Idaho Operations Office Contract DE-AC07-05ID14517. The authors would like to thank M. Blair for assistance with preparation for the document. JW acknowledges the support by the Nebraska Center for Energy Sciences Research. N.L. acknowledges the support of the U.S. Department of Energy through the Los Alamos National Laboratory (LANL) / Laboratory Directed Research & Development (LDRD) Program. N.L. and Y.C. was supported, in part, by the Center for Integrated Nanotechnologies, an Office of Science User Facility operated for the U.S. Department of Energy (DOE) Office of Science. LANL, an affirmative action/equal opportunity employer, is operated by Los Alamos National Security, LLC, for the National Nuclear Security Administration of the U.S. Department of Energy under contract DE-AC52-06NA25396.

References

[1] S.J. Zinkle, G.S. Was, Materials challenges in nuclear energy, Acta Materialia, 61 (2013) 735-758.
[2] S.J. Zinkle, 1.03 - Radiation-Induced Effects on Microstructure* A2 - Konings, Rudy J.M, in: Comprehensive Nuclear Materials, Elsevier, Oxford, 2012, pp. 65-98.
[3] S.J. Zinkle, K. Farrell, Void swelling and defect cluster formation in reactor-irradiated copper, Journal of Nuclear Materials, 168 (1989) 262-267.
[4] M.A. Nastasi, J.W. Mayer, SpringerLink (Online service), Ion implantation and synthesis of materials.
[5] S.J. Zinkle, J.T. Busby, Structural materials for fission & fusion energy, Materials Today, 12 (2009) 12-19.
[6] G.R. Odette, M.J. Alinger, B.D. Wirth, Recent Developments in Irradiation-Resistant Steels, Annual Review of Materials Research, 38 (2008) 471-503.
[7] S. Ukai, M. Fujiwara, Perspective of ODS alloys application in nuclear environments, Journal of Nuclear Materials, 307 (2002) 749-757.
[8] M.S. El-Genk, J.-M. Tournier, A review of refractory metal alloys and mechanically alloyed-oxide dispersion strengthened steels for space nuclear power systems, Journal of Nuclear materials, 340 (2005) 93-112.
[9] L.L. Hsiung, M.J. Fluss, S.J. Tumey, B.W. Choi, Y. Serruys, F. Willaime, A. Kimura, Formation mechanism and the role of nanoparticles in Fe-Cr ODS steels developed for radiation tolerance, Physical Review B, 82 (2010) 184103.
[10] M. Alinger, G. Odette, D. Hoelzer, On the role of alloy composition and processing parameters in nanocluster formation and dispersion strengthening in nanostuctured ferritic alloys, Acta Materialia, 57 (2009) 392-406.
[11] A. Hirata, T. Fujita, Y. Wen, J. Schneibel, C.T. Liu, M. Chen, Atomic structure of nanoclusters in oxide-dispersion-strengthened steels, Nature materials, 10 (2011) 922.
[12] G.R. Odette, D.T. Hoelzer, Irradiation-tolerant nanostructured ferritic alloys: Transforming helium from a liability to an asset, Jom, 62 (2010) 84-92.
[13] E.A. Marquis, Core/shell structures of oxygen-rich nanofeatures in oxide-dispersion strengthened Fe-Cr alloys, Applied Physics Letters, 93 (2008).
[14] G.R. Odette, Recent progress in developing and qualifying nanostructured ferritic alloys for advanced fission and fusion applications, Jom, 66 (2014) 2427-2441.
[15] C.A. Williams, P. Unifantowicz, N. Baluc, G.D. Smith, E.A. Marquis, The formation and evolution of oxide particles in oxide-dispersion-strengthened ferritic steels during processing, Acta Materialia, 61 (2013) 2219-2235.
[16] E. Aydogan, N. Almirall, G. Odette, S. Maloy, O. Anderoglu, L. Shao, J. Gigax, L. Price, D. Chen, T. Chen, Stability of nanosized oxides in ferrite under extremely high dose self ion irradiations, Journal of Nuclear Materials, 486 (2017) 86-95.
[17] A. Anders, Metal plasma immersion ion implantation and deposition: a review, Surface and Coatings Technology, 93 (1997) 158-167.
[18] P.K. Chu, S. Qin, C. Chan, N.W. Cheung, L.A. Larson, Plasma immersion ion implantation—A fledgling technique for semiconductor processing, Materials Science and Engineering: R: Reports, 17 (1996) 207-280.

[19] J.F. Gibbons, Ion implantation in semiconductors—Part II: Damage production and annealing, Proceedings of the IEEE, 60 (1972) 1062-1096.
[20] S. Pearton, C. Vartuli, J. Zolper, C. Yuan, R. Stall, Ion implantation doping and isolation of GaN, Applied physics letters, 67 (1995) 1435-1437.
[21] J.S. Williams, J.M. Poate, Ion implantation and beam processing, Academic Press, 2014.
[22] J.F. Ziegler, Ion Implantation Science and Technology 2e, Elsevier, 2012.
[23] J. Erlebacher, M.J. Aziz, E. Chason, M.B. Sinclair, J.A. Floro, Spontaneous pattern formation on ion bombarded Si (001), Physical review letters, 82 (1999) 2330.
[24] J. Li, D. Stein, C. McMullan, D. Branton, M.J. Aziz, J.A. Golovchenko, Ion-beam sculpting at nanometre length scales, Nature, 412 (2001) 166-169.
[25] S.J. Zinkle, B.N. Singh, Microstructure of neutron-irradiated iron before and after tensile deformation, Journal of nuclear materials, 351 (2006) 269-284.
[26] K.Y. Yu, Y. Chen, J. Li, Y. Liu, H. Wang, M.A. Kirk, M. Li, X. Zhang, Measurement of Heavy Ion Irradiation Induced In-Plane Strain in Patterned Face-Centered-Cubic Metal Films: An in Situ Study, Nano Letters, 16 (2016) 7481-7489.
[27] H. Wangyu, Z. Bangwei, H. Baiyun, G. Fei, J.B. David, Analytic modified embedded atom potentials for HCP metals, Journal of Physics: Condensed Matter, 13 (2001) 1193.
[28] W. Wolfer, Fundamental properties of defects in metals, Comprehensive nuclear materials, 1 (2012) 1-45.
[29] Y. Chen, K.Y. Yu, Y. Liu, S. Shao, H. Wang, M. Kirk, J. Wang, X. Zhang, Damage-tolerant nanotwinned metals with nanovoids under radiation environments, Nature communications, 6 (2015).
[30] C. Sun, M. Song, K. Yu, Y. Chen, M. Kirk, M. Li, H. Wang, X. Zhang, In situ Evidence of Defect Cluster Absorption by Grain Boundaries in Kr Ion Irradiated Nanocrystalline Ni, Metallurgical and Materials Transactions A, 44 (2013) 1966-1974.
[31] S. Zinkle, R. Sindelar, Defect microstructures in neutron-irradiated copper and stainless steel, Journal of Nuclear Materials, 155 (1988) 1196-1200.
[32] A. Kozlov, V. Panchenko, K. Kozlov, I. Russkikh, A.V. Kozlov, Evolution of radiation defects in nickel under low-temperature neutron irradiation, The Physics of Metals and Metallography, 115 (2014) 39-45.
[33] N.H. Packan, Voids in neutron irradiated aluminum, (1970).
[34] M. Kiritani, Similarity and difference between fcc, bcc and hcp metals from the view point of point defect cluster formation, Journal of nuclear materials, 276 (2000) 41-49.
[35] S. Zinkle, B. Singh, Analysis of displacement damage and defect production under cascade damage conditions, Journal of nuclear materials, 199 (1993) 173-191.
[36] R. Averback, T.D. de La Rubia, Displacement damage in irradiated metals and semiconductors, Solid State Physics, 51 (1997) 281-402.
[37] R. Stoller, G. Odette, B. Wirth, Primary damage formation in bcc iron, Journal of Nuclear Materials, 251 (1997) 49-60.
[38] R. Averback, Atomic displacement processes in irradiated metals, Journal of nuclear materials, 216 (1994) 49-62.
[39] K.Y. Yu, D. Bufford, C. Sun, Y. Liu, H. Wang, M.A. Kirk, M. Li, X. Zhang, Removal of stacking-fault tetrahedra by twin boundaries in nanotwinned metals, Nature Communications, 4 (2013).

[40] C.F. Jin Li, J. Ding, S. Xue, Y. Chen, Q. Li, H. Wang & X. Zhang, In situ heavy ion irradiation studies of nanopore shrinkage and enhanced radiation tolerance of nanoporous Au, Scientific Reports, 7 (2017).
[41] J. Silcox, P. Hirsch, Direct observations of defects in quenched gold, Philosophical Magazine, 4 (1959) 72-89.
[42] B. Wirth, V. Bulatov, T.D. De La Rubia, Atomistic simulation of stacking fault tetrahedra formation in Cu, Journal of nuclear materials, 283 (2000) 773-777.
[43] R.E. Voskoboinikov, Y.N. Osetsky, D.J. Bacon, Computer simulation of primary damage creation in displacement cascades in copper. I. Defect creation and cluster statistics, Journal of Nuclear Materials, 377 (2008) 385-395.
[44] B.P. Uberuaga, R.G. Hoagland, A.F. Voter, S.M. Valone, Direct transformation of vacancy voids to stacking fault tetrahedra, Phys Rev Lett, 99 (2007) 135501.
[45] S.J. Zinkle, Microstructures and Mechanical Properties of Irradiated Metals and Alloys, in: V. Ghetta, D. Gorse, D. Mazière, V. Pontikis (Eds.) Materials Issues for Generation IV Systems: Status, Open Questions and Challenges, Springer Netherlands, Dordrecht, 2008, pp. 227-244.
[46] M. Rieth, S.L. Dudarev, S.M. Gonzalez de Vicente, J. Aktaa, T. Ahlgren, S. Antusch, D.E.J. Armstrong, M. Balden, N. Baluc, M.F. Barthe, W.W. Basuki, M. Battabyal, C.S. Becquart, D. Blagoeva, H. Boldyryeva, J. Brinkmann, M. Celino, L. Ciupinski, J.B. Correia, A. De Backer, C. Domain, E. Gaganidze, C. García-Rosales, J. Gibson, M.R. Gilbert, S. Giusepponi, B. Gludovatz, H. Greuner, K. Heinola, T. Höschen, A. Hoffmann, N. Holstein, F. Koch, W. Krauss, H. Li, S. Lindig, J. Linke, C. Linsmeier, P. López-Ruiz, H. Maier, J. Matejicek, T.P. Mishra, M. Muhammed, A. Muñoz, M. Muzyk, K. Nordlund, D. Nguyen-Manh, J. Opschoor, N. Ordás, T. Palacios, G. Pintsuk, R. Pippan, J. Reiser, J. Riesch, S.G. Roberts, L. Romaner, M. Rosiński, M. Sanchez, W. Schulmeyer, H. Traxler, A. Ureña, J.G. van der Laan, L. Veleva, S. Wahlberg, M. Walter, T. Weber, T. Weitkamp, S. Wurster, M.A. Yar, J.H. You, A. Zivelonghi, Recent progress in research on tungsten materials for nuclear fusion applications in Europe, Journal of Nuclear Materials, 432 (2013) 482-500.
[47] J. Marian, B.D. Wirth, J.M. Perlado, Mechanism of Formation and Growth of $〈100〉$ Interstitial Loops in Ferritic Materials, Physical Review Letters, 88 (2002) 255507.
[48] D.J. Bacon, F. Gao, Y.N. Osetsky, The primary damage state in fcc, bcc and hcp metals as seen in molecular dynamics simulations, Journal of Nuclear Materials, 276 (2000) 1-12.
[49] M.L. Jenkins, Z. Yao, M. Hernández-Mayoral, M.A. Kirk, Dynamic observations of heavy-ion damage in Fe and Fe–Cr alloys, Journal of Nuclear Materials, 389 (2009) 197-202.
[50] M. Kirk, X. Yi, M. Jenkins, Characterization of irradiation defect structures and densities by transmission electron microscopy, Journal of Materials Research, 30 (2015) 1195-1201.
[51] M. Downey, B. Eyre, Neutron irradiation damage in molybdenum, Philosophical Magazine, 11 (1965) 53-70.
[52] P. Loubeyre, R. LeToullec, J. Pinceaux, H. Mao, J. Hu, R. Hemley, Equation of state and phase diagram of solid He 4 from single-crystal x-ray diffraction over a large P-T domain, Physical review letters, 71 (1993) 2272.
[53] D. Maher, B. Eyre, Neutron irradiation damage in molybdenum, Philosophical Magazine, 23 (1971) 409-438.
[54] K. Lacefield, J. Moteff, J. Smith, Neutron radiation damage in tungsten single crystals, Philosophical Magazine, 13 (1966) 1079-1081.

[55] M. Kiritani, Y. Maehara, H. Takata, Electron Radiation Damage and Properties of Point Defects in Molybdenum, Journal of the Physical Society of Japan, 41 (1976) 1575-1583.
[56] S. Fukuzumi, T. Yoshiie, Y. Satoh, Q. Xu, H. Mori, M. Kawai, Defect structural evolution in high purity tungsten irradiated with electrons using high voltage electron microscope, Journal of nuclear materials, 343 (2005) 308-312.
[57] H. Xu, R.E. Stoller, Y.N. Osetsky, D. Terentyev, Solving the Puzzle of <100> Interstitial Loop Formation in bcc Iron, Physical review letters, 110 (2013) 265503.
[58] M.-C. Marinica, F. Willaime, J.-P. Crocombette, Irradiation-Induced Formation of Nanocrystallites with C 15 Laves Phase Structure in bcc Iron, Physical review letters, 108 (2012) 025501.
[59] D.J. Bacon, A review of computer models of point defects in hcp metals, Journal of Nuclear Materials, 159 (1988) 176-189.
[60] D. Bacon, Point defects and clusters in the hcp metals: their role in the dose transition, Journal of nuclear materials, 206 (1993) 249-265.
[61] M. Griffiths, Evolution of microstructure in hcp metals during irradiation, Journal of Nuclear Materials, 205 (1993) 225-241.
[62] S. Yamada, T. Kameyama, Observation of c-component dislocation structures formed in pure Zr and Zr-base alloy by self-ion accelerator irradiation, Journal of Nuclear Materials, 422 (2012) 167-172.
[63] M. Griffiths, A review of microstructure evolution in zirconium alloys during irradiation, Journal of Nuclear Materials, 159 (1988) 190-218.
[64] A. Khan, Z. Yao, M. Daymond, R. Holt, Effect of foil orientation on damage accumulation during irradiation in magnesium and annealing response of dislocation loops, Journal of Nuclear Materials, 423 (2012) 132-141.
[65] A. Wolfenden, K. Herschbach, K. Müller, T. Stober, Neutron irradiation damage in magnesium single crystals, Radiation Effects, 39 (1978) 177-180.
[66] V. Levy, Determining the Nature of Dislocation Loops Observed in Mg, J. Microscopie, 19 (1974) 1-16.
[67] A. Jostsons, R. Blake, J. Napier, P. Kelly, K. Farrell, Faulted loops in neutron-irradiated zirconium, Journal of Nuclear Materials, 68 (1977) 267-276.
[68] M. Griffiths, D. Faulkner, R. Styles, Neutron damage in α-titanium, Journal of Nuclear Materials, 119 (1983) 189-207.
[69] L.K. Mansur, Void swelling in metals and alloys under irradiation: an assessment of the theory, Nuclear Technology, 40 (1978) 5-34.
[70] D. Norris, The use of the high voltage electron microscope to simulate fast neutron-induced void swelling in metals, Journal of Nuclear Materials, 40 (1971) 66-76.
[71] E. Little, D. Stow, Void-swelling in irons and ferritic steels: II. An experimental survey of materials irradiated in a fast reactor, Journal of Nuclear Materials, 87 (1979) 25-39.
[72] F. Garner, H. Brager, D. Gelles, J. McCarthy, Neutron irradiation of FeMn, FeCrMn and FeCrNi alloys and an explanation of their differences in swelling behavior, Journal of Nuclear Materials, 148 (1987) 294-301.
[73] N. Packan, K. Farrell, J. Stiegler, Correlation of neutron and heavy-ion damage: I. The influence of dose rate and injected helium on swelling in pure nickel, Journal of Nuclear Materials, 78 (1978) 143-155.
[74] A.D. Brailsford, R. Bullough, M.R. Hayns, Point defect sink strengths and void-swelling, Journal of Nuclear Materials, 60 (1976) 246-256.

[75] S. Sharafat, N.M. Ghoniem, M. Anderson, B. Williams, J. Blanchard, L. Snead, Micro-engineered first wall tungsten armor for high average power laser fusion energy systems, Journal of Nuclear Materials, 347 (2005) 217-243.
[76] F.A. Garner, M.B. Toloczko, B.H. Sencer, Comparison of swelling and irradiation creep behavior of fcc-austenitic and bcc-ferritic/martensitic alloys at high neutron exposure, Journal of Nuclear Materials, 276 (2000) 123-142.
[77] J. Stubbins, F. Garner, Swelling and microstructure of high purity nickel irradiated with fast neutrons in EBR-II, Journal of nuclear materials, 191 (1992) 1295-1299.
[78] K. Farrell, J. Houston, Suppression of radiation damage microstructure in aluminum by trace impurities, Journal of Nuclear Materials, 83 (1979) 57-66.
[79] Y.V. Konobeev, A. Dvoriashin, S. Porollo, F.A. Garner, Swelling and microstructure of pure Fe and Fe–Cr alloys after neutron irradiation to~ 26dpa at 400° C, Journal of nuclear materials, 355 (2006) 124-130.
[80] S. Ohnuki, D. Gelles, B. Loomis, F. Garner, H. Takahashi, Microstructural examination of simple vanadium alloys irradiated in the FFTF/MOTA, Journal of nuclear materials, 179 (1991) 775-778.
[81] J.H. Evans, Void swelling and irradiation-induced void shrinkage in neutron irradiated molybdenum and TZM, Journal of Nuclear Materials, 88 (1980) 31-41.
[82] M. Song, Y.D. Wu, D. Chen, X.M. Wang, C. Sun, K.Y. Yu, Y. Chen, L. Shao, Y. Yang, K.T. Hartwig, X. Zhang, Response of equal channel angular extrusion processed ultrafine-grained T91 steel subjected to high temperature heavy ion irradiation, Acta Materialia, 74 (2014) 285-295.
[83] C. Sun, S. Zheng, C.C. Wei, Y. Wu, L. Shao, Y. Yang, K.T. Hartwig, S.A. Maloy, S.J. Zinkle, T.R. Allen, H. Wang, X. Zhang, Superior radiation-resistant nanoengineered austenitic 304L stainless steel for applications in extreme radiation environments, Sci Rep, 5 (2015) 7801.
[84] S. Zinkle, K. Farrell, H. Kanazawa, Microstructure and cavity swelling in reactor-irradiated dilute copper-boron alloy, Journal of nuclear materials, 179 (1991) 994-997.
[85] F. Garner, D. Porter, Reassessment of the swelling behavior of AISI 304 stainless steel, in, Hanford Engineering Development Lab., 1982.
[86] P. Dubuisson, D. Gilbon, J. Séran, Microstructural evolution of ferritic-martensitic steels irradiated in the fast breeder reactor Phénix, Journal of nuclear materials, 205 (1993) 178-189.
[87] M. Toloczko, F. Garner, C. Eiholzer, Irradiation creep and swelling of the US fusion heats of HT9 and 9Cr-1Mo to 208 dpa at~ 400 C, Journal of Nuclear Materials, 212 (1994) 604-607.
[88] N.M. Ghoniem, G.L. Kulcinski, The use of the fully dynamic rate theory to predict void growth in metals, Radiation Effects, 41 (1979) 81-89.
[89] S.K. McLaurin, G.L. Kulcinski, R.A. Dodd, Effects of temperature and helium on void formation in self-ion irradiated aluminum, Journal of Nuclear Materials, 117 (1983) 208-212.
[90] B.N. Singh, J.H. Evans, Significant differences in defect accumulation behaviour between fcc and bcc crystals under cascade damage conditions, Journal of Nuclear Materials, 226 (1995) 277-285.
[91] N.I. Budylkin, E.G. Mironova, V.M. Chernov, V.A. Krasnoselov, S.I. Porollo, F.A. Garner, Neutron-induced swelling and embrittlement of pure iron and pure nickel irradiated in the BN-350 and BOR-60 fast reactors, Journal of Nuclear Materials, 375 (2008) 359-364.

[92] T.D. Ryan, A. Taylor, Heavy Ion-Induced Void Formation in Pure Nickel, in: S.T. Picraux, E.P. EerNisse, F.L. Vook (Eds.) Applications of Ion Beams to Metals, Springer US, Boston, MA, 1974, pp. 675-685.
[93] F.A. Garner, J.F. Stubbins, Saturation of swelling in neutron-irradiated molybdenum and its dependence on irradiation temperature and starting microstructural state, Journal of Nuclear Materials, 212 (1994) 1298-1302.
[94] J.D. Elen, G. Hamburg, A. Mastenbroek, Voids in vanadium, niobium and molybdenum by fast neutron irradiation at high temperatures, Journal of Nuclear Materials, 39 (1971) 194-202.
[95] G.L. Kulcinski, J.L. Brimhal, High-temperature heavy ion bombardment of molybdenum, niobium and TZM, in, Belgium, 1972.
[96] B.A. Loomis, A. Taylor, S.B. Gerber, Void swelling of Nb and Nb-1% Zr induced by 58Ni+ bombardment, Journal of Nuclear Materials, 56 (1975) 25-37.
[97] F.W. Wiffen, The microstructure and swelling of neutron irradiated tantalum, Journal of Nuclear Materials, 67 (1977) 119-130.
[98] K. Yasunaga, H. Watanabe, N. Yoshida, T. Muroga, N. Noda, Microstructure of tantalum irradiated with heavy ions, Journal of Nuclear Materials, 258–263, Part 1 (1998) 879-882.
[99] W.J. Weber, G.L. Kulcinski, R.G. Lott, P. Wilkes, H.V. Smith, Ion simulation study of void formation in high purity vanadium, in, United States, 1976.
[100] J. Matolich, H. Nahm, J. Moteff, Swelling in neutron irradiated tungsten and tungsten-25 percent rhenium, Scripta Metallurgica, 8 (1974) 837-841.
[101] D. Faulkner, C.H. Woo, Void swelling in zirconium, Journal of Nuclear Materials, 90 (1980) 307-316.
[102] A. Jostsons, P.M. Kelly, R.G. Blake, K. Farrell, Neutron irradiation-induced defect structures in zirconium, American Society for Testing and Materials, Special Technical Publication, (1978) 46-61.
[103] C.D. Cann, D. Faulkner, K. Nuttall, R.C. Styles, A.J. Shillinglaw, C.K. Chow, A.J. Rogowski, Irradiation growth in zirconium and zirconium alloys irradiated in the Dounreay fast reactor, in, Canada, 1986, pp. 77.
[104] W.G. Wolfer, Advances in void swelling and helium bubble physics, Journal of Nuclear Materials, 122 (1984) 367-378.
[105] S. Rokkam, A. El-Azab, P. Millett, D. Wolf, Phase field modeling of void nucleation and growth in irradiated metals, Modelling and simulation in materials science and engineering, 17 (2009) 064002.
[106] Y. Li, S. Hu, X. Sun, F. Gao, C.H. Henager, M. Khaleel, Phase-field modeling of void migration and growth kinetics in materials under irradiation and temperature field, Journal of Nuclear Materials, 407 (2010) 119-125.
[107] S. Di, Z. Yao, M.R. Daymond, X. Zu, S. Peng, F. Gao, Dislocation-accelerated void formation under irradiation in zirconium, Acta Materialia, 82 (2015) 94-99.
[108] Y. Dai, G. Odette, T. Yamamoto, The Effects of Helium in Irradiated Structural Alloys-1.06, (2012).
[109] R.E. Stoller, The influence of helium on microstructural evolution: Implications for DT fusion reactors, Journal of nuclear materials, 174 (1990) 289-310.
[110] N. Packan, K. Farrell, Simulation of first wall damage: effects of the method of gas implantation, Journal of Nuclear Materials, 85 (1979) 677-681.

[111] A. Jostsons, K. Farrell, Structural damage and its annealing response in neutron irradiated magnesium†, Radiation Effects, 15 (1972) 217-225.
[112] J.L. Brimhall, G.L. Kulcinski, H.E. Kissinger, B. Mastel, Microstructural analysis of neutron irradiated titanium and rhenium, Radiation Effects, 9 (1971) 273-278.
[113] M. Griffiths, Microstructure evolution in h.c.p. metals during irradiation, Philosophical Magazine A: Physics of Condensed Matter, Structure, Defects and Mechanical Properties, 63 (1991) 835-847.
[114] S. Donnelly, The density and pressure of helium in bubbles in implanted metals: a critical review, Radiation Effects, 90 (1985) 1-47.
[115] W. Han, E. Fu, M.J. Demkowicz, Y. Wang, A. Misra, Irradiation damage of single crystal, coarse-grained, and nanograined copper under helium bombardment at 450 C, Journal of Materials Research, 28 (2013) 2763-2770.
[116] F. Zhang, X. Wang, J.B. Wierschke, L. Wang, Helium bubble evolution in ion irradiated Al/B 4 C metal metrix composite, Scripta Materialia, 109 (2015) 28-33.
[117] J. Hetherly, E. Martinez, Z. Di, M. Nastasi, A. Caro, Helium bubble precipitation at dislocation networks, Scripta Materialia, 66 (2012) 17-20.
[118] K.Y. Yu, Y. Liu, C. Sun, H. Wang, L. Shao, E.G. Fu, X. Zhang, Radiation damage in helium ion irradiated nanocrystalline Fe, Journal of Nuclear Materials, 425 (2012) 140-146.
[119] H. Iwakiri, K. Yasunaga, K. Morishita, N. Yoshida, Microstructure evolution in tungsten during low-energy helium ion irradiation, Journal of nuclear materials, 283 (2000) 1134-1138.
[120] P. Johnson, F. Lawson, Helium gas-bubble superlattice formation in molybdenum, Nuclear Instruments and Methods in Physics Research Section B: Beam Interactions with Materials and Atoms, 243 (2006) 325-334.
[121] E. Fu, A. Misra, H. Wang, L. Shao, X. Zhang, Interface enabled defects reduction in helium ion irradiated Cu/V nanolayers, Journal of Nuclear Materials, 407 (2010) 178-188.
[122] N.F. Carnahan, K.E. Starling, Equation of state for nonattracting rigid spheres, The Journal of Chemical Physics, 51 (1969) 635-636.
[123] A. Driessen, E. Van der Poll, I.F. Silvera, Equation of state of solid He 4, Physical Review B, 33 (1986) 3269.
[124] H. Mao, R. Hemley, Y. Wu, A. Jephcoat, L. Finger, C. Zha, W. Bassett, High-pressure phase diagram and equation of state of solid helium from single-crystal X-ray diffraction to 23.3 GPa, Physical review letters, 60 (1988) 2649.
[125] J.H. Evans, An interbubble fracture mechanism of blister formation on helium-irradiated metals, Journal of Nuclear Materials, 68 (1977) 129-140.
[126] R. Mills, D. Liebenberg, J. Bronson, Equation of state and melting properties of He 4 from measurements to 20 kbar, Physical Review B, 21 (1980) 5137.
[127] J.P. Hirth, J. Lothe, Theory of dislocations, (1982).
[128] W. Wolfer, Dislocation loop punching in bubble arrays, Philosophical Magazine A, 59 (1989) 87-103.
[129] T. Schober, R. Lasser, J. Golczewski, C. Dieker, H. Trinkaus, Dilatometric measurements of helium densities in bubbles arising from tritium decay in tantalum, Physical Review B, 31 (1985) 7109.
[130] X. Zhang, E. Fu, A. Misra, M. Demkowicz, Interface-enabled defect reduction in He ion irradiated metallic multilayers, Jom, 62 (2010) 75-78.

[131] D. Kramer, H.R. Brager, C.G. Rhodes, A.G. Pard, Helium embrittlement in type 304 stainless steel, Journal of Nuclear Materials, 25 (1968) 121-131.
[132] M.R. Gilbert, S.L. Dudarev, S. Zheng, L.W. Packer, J.-C. Sublet, An integrated model for materials in a fusion power plant: transmutation, gas production, and helium embrittlement under neutron irradiation, Nuclear Fusion, 52 (2012) 083019.
[133] H. Trinkaus, On the modeling of the high-temperature embrittlement of metals containing helium, Journal of Nuclear Materials, 118 (1983) 39-49.
[134] L.K. Mansur, Theory and experimental background on dimensional changes in irradiated alloys, Journal of Nuclear Materials, 216 (1994) 97-123.
[135] R. Bullough, M.R. Hayns, M.H. Wood, Sink Strengths for Thin-Film Surfaces and Grain-Boundaries, Journal of Nuclear Materials, 90 (1980) 44-59.
[136] S.J. Zinkle, L.L. Snead, Designing Radiation Resistance in Materials for Fusion Energy, Annu Rev Mater Res, 44 (2014) 241-267.
[137] S.J. Zinkle, A. Moslang, Evaluation of irradiation facility options for fusion materials research and development, Fusion Eng Des, 88 (2013) 472-482.
[138] S.J. Zinkle, Fusion materials science: Overview of challenges and recent progress, Phys Plasmas, 12 (2005).
[139] M.L. Jenkins, M.A. Kirk, W.J. Phythian, Experimental Studies of Cascade Phenomena in Metals, Journal of Nuclear Materials, 205 (1993) 16-30.
[140] C. Dimitrov, B. Sitaud, X. Zhang, O. Dimitrov, U. Dedek, F. Dworschak, Radiation-induced defects in solid solutions and intermetallic compounds based on the Ni-Al system: I. Low-temperature electron-irradiation damage, Journal of Physics: Condensed Matter, 4 (1992) 10199.
[141] R.J. Arsenault, The possibility of irradiation damage affecting the rate-controlling mechanism of slip in body-centered cubic metals and solid solutions, Acta Metallurgica, 15 (1967) 1853-1859.
[142] E.M. Schulson, The ordering and disordering of solid solutions under irradiation, Journal of Nuclear Materials, 83 (1979) 239-264.
[143] H. Venker, P. Giesecke, K. Ehrlich, Influence of fast diffusing substitutional elements on the swelling behaviour of Ni-and Cu-alloys, in: Radiation effects in breeder reactor structural materials, 1977.
[144] Y.N. Osetsky, D. Rodney, D.J. Bacon, Atomic-scale study of dislocation–stacking fault tetrahedron interactions. Part I: mechanisms, Philosophical Magazine, 86 (2006) 2295-2313.
[145] B.D. Wirth, V.V. Bulatov, T.D. de la Rubia, Dislocation-Stacking Fault Tetrahedron Interactions in Cu, Journal of Engineering Materials and Technology, 124 (2002) 329-334.
[146] P. Szelestey, M. Patriarca, K. Kaski, Computational study of a screw dislocation interacting with a stacking-fault tetrahedron, Modelling and Simulation in Materials Science and Engineering, 13 (2005) 541-551.
[147] Y.N. Osetsky, R.E. Stoller, Y. Matsukawa, Dislocation–stacking fault tetrahedron interaction: what can we learn from atomic-scale modelling, Journal of Nuclear Materials, 329–333, Part B (2004) 1228-1232.
[148] R.A. Andrievskii, Effect of Irradiation on the Properties of Nanomaterials, Phys Met Metallogr+, 110 (2010) 229-240.

[149] L.M. Wang, S.X. Wang, R.C. Ewing, A. Meldrum, R.C. Birtcher, P.N. Provencio, W.J. Weber, H. Matzke, Irradiation-induced nanostructures, Mat Sci Eng a-Struct, 286 (2000) 72-80.
[150] S. Wurster, R. Pippan, Nanostructured metals under irradiation, Scripta Materialia, 60 (2009) 1083-1087.
[151] A.W. Chao, W. Chou, Reviews of Accelerator Science and Technology, Volume 2: Medical Applications of Accelerators, World Scientific, 2010.
[152] I.J. Beyerlein, A. Caro, M.J. Demkowicz, N.A. Mara, A. Misra, B.P. Uberuaga, Radiation damage tolerant nanomaterials, Materials Today, 16 (2013) 443-449.
[153] I. Adlakha, K.N. Solanki, Atomic-scale investigation of triple junction role on defects binding energetics and structural stability in a alpha-Fe, Acta Materialia, 118 (2016) 64-76.
[154] A. Dunn, R. Dingreville, E. Martinez, L. Capolungo, Identification of dominant damage accumulation processes at grain boundaries during irradiation in nanocrystalline alpha-Fe: A statistical study, Acta Materialia, 110 (2016) 306-323.
[155] G. Valles, M. Panizo-Laiz, C. Gonzalez, I. Martin-Bragado, R. Gonzalez-Arrabal, N. Gordillo, R. Iglesias, C.L. Guerrero, J.M. Perlado, A. Rivera, Influence of grain boundaries on the radiation-induced defects and hydrogen in nanostructured and coarse-grained tungsten, Acta Materialia, 122 (2017) 277-286.
[156] S. Rajasekhara, P.J. Ferreira, K. Hattar, Microstructural Evolution Of Nanocrystalline Nickel Thin Films Due To High-Energy Heavy-Ion Irradiation, Aip Conf Proc, 1525 (2013) 630-635.
[157] J. Gruber, H. Lim, F. Abdeljawad, S. Foiles, G.J. Tucker, Development of physically based atomistic microstructures: The effect on the mechanical response of polycrystals, Comp Mater Sci, 128 (2017) 29-36.
[158] Z. Chen, L.J. Kecskes, K.G. Zhu, Q.M. Wei, Atomistic simulations of the effect of embedded hydrogen and helium on the tensile properties of monocrystalline and nanocrystalline tungsten, Journal of Nuclear Materials, 481 (2016) 190-200.
[159] O. El-Atwani, J.E. Nathaniel, A.C. Leff, B.R. Muntifering, J.K. Baldwin, K. Hattar, M.L. Taheri, The role of grain size in He bubble formation: Implications for swelling resistance, Journal of Nuclear Materials, 484 (2017) 236-244.
[160] P.M. Piaggi, E.M. Bringa, R.C. Pasianot, N. Gordillo, M. Panizo-Laiz, J. del Rio, C.G. de Castro, R. Gonzalez-Arrabal, Hydrogen diffusion and trapping in nanocrystalline tungsten, Journal of Nuclear Materials, 458 (2015) 233-239.
[161] M. Samaras, P.M. Derlet, H. Van Swygenhoven, M. Victoria, Atomic scale modelling of the primary damage state of irradiated fcc and bcc nanocrystalline metals, Journal of Nuclear Materials, 351 (2006) 47-55.
[162] G.A. Vetterick, O. El-Atwani, J.K. Baldwin, M.R. Tonks, M.L. Taheri, Quantification of void pinning effects during grain growth of nanocrystalline iron, Journal of Nuclear Materials, 481 (2016) 62-65.
[163] R.E. Stoller, P.J. Kamenski, Y.N. Osetsky, Length-Scale Effects in Cascade Damage Production in Iron, Mater Res Soc Symp P, 1125 (2009) 109-+.
[164] L.L. Liu, Z. Tang, W. Xiao, Z. Wang, Self-healing mechanism of irradiation defects near Sigma=11(113) grain boundary in copper, Mater Lett, 109 (2013) 221-224.
[165] O. El-Atwani, J.A. Hinks, G. Greaves, J.P. Allain, S.A. Maloy, Grain size threshold for enhanced irradiation resistance in nanocrystalline and ultrafine tungsten, Mater Res Lett, 5 (2017) 343-349.

[166] O. El-Atwani, J.E. Nathaniel, A.C. Leff, J.K. Baldwin, K. Hattar, M.L. Taheri, Evidence of a temperature transition for denuded zone formation in nanocrystalline Fe under He irradiation, Mater Res Lett, 5 (2017) 195-200.
[167] B. Muntifering, S.J. Blair, C. Gong, A. Dunn, R. Dingreville, J.M. Qu, K. Hattar, Cavity Evolution at Grain Boundaries as a Function of Radiation Damage and Thermal Conditions in Nanocrystalline Nickel, Mater Res Lett, 4 (2016) 96-103.
[168] N.Y. Park, P.R. Cha, Y.C. Kim, H.K. Seok, S.H. Han, S.C. Lee, S. Cho, H.J. Jung, Radiation damage in nano-crystalline tungsten: A molecular dynamics simulation, Met Mater Int, 15 (2009) 447-452.
[169] A. Misra, L. Thilly, Structural metals at extremes, Mrs Bull, 35 (2010) 965-976.
[170] M. Samaras, P.M. Derlet, H. Van Swygenhoven, M. Victoria, Stacking fault tetrahedra formation in the neighbourhood of grain boundaries, Nucl Instrum Meth B, 202 (2003) 51-55.
[171] W. Voegeli, K. Albe, H. Hahn, Simulation of grain growth in nanocrystalline nickel induced by ion irradiation, Nucl Instrum Meth B, 202 (2003) 230-235.
[172] M. Samaras, P.M. Derlet, H. Van Swygenhoven, M. Victoria, Radiation damage near grain boundaries, Philosophical Magazine, 83 (2003) 3599-3607.
[173] J. Xu, J.B. Liu, S.N. Li, B.X. Liu, Y. Jiang, Self-healing properties of nanocrystalline materials: a first-principles analysis of the role of grain boundaries, Phys Chem Chem Phys, 18 (2016) 17930-17940.
[174] X.Z. Xiao, D.K. Song, H.J. Chu, J.M. Xue, H.L. Duan, Mechanical properties for irradiated face-centred cubic nanocrystalline metals, P Roy Soc a-Math Phy, 471 (2015).
[175] A. Kilmametov, A. Balogh, M. Ghafari, C. Gammer, C. Mangler, C. Rentenberger, R. Valiev, H. Hahn, Radiation effects in bulk nanocrystalline FeAl alloy, Radiat Eff Defect S, 167 (2012) 631-639.
[176] R.A. Andrievski, Behavior of Radiation Defects in Nanomaterials, Rev Adv Mater Sci, 29 (2011) 54-67.
[177] X.Z. Xiao, H.J. Chu, H.L. Duan, Effect of grain boundary on the mechanical behaviors of irradiated metals: a review, Sci China Phys Mech, 59 (2016).
[178] A. Arjhangmehr, S.A.H. Feghhi, Irradiation deformation near different atomic grain boundaries in alpha-Zr: An investigation of thermodynamics and kinetics of point defects, Scientific Reports, 6 (2016).
[179] G.M. Cheng, W.Z. Xu, Y.Q. Wang, A. Misra, Y.T. Zhu, Grain size effect on radiation tolerance of nanocrystalline Mo, Scripta Materialia, 123 (2016) 90-94.
[180] O. El-Atwani, A. Suslova, T.J. Novakowski, K. Hattar, M. Efe, S.S. Harilal, A. Hassanein, In-situ TEM/heavy ion irradiation on ultrafine-and nanocrystalline-grained tungsten: Effect of 3 MeV Si, Cu and W ions, Materials Characterization, 99 (2015) 68-76.
[181] O. El-Atwani, J. Nathaniel II, A. Leff, J. Baldwin, K. Hattar, M. Taheri, Evidence of a temperature transition for denuded zone formation in nanocrystalline Fe under He irradiation, Mater Res Lett, (2016) 1-6.
[182] M. Samaras, P.M. Derlet, H. Van Swygenhoven, M. Victoria, Computer simulation of displacement cascades in nanocrystalline ni, Phys Rev Lett, 88 (2002) 125505.
[183] X.M. Bai, A.F. Voter, R.G. Hoagland, M. Nastasi, B.P. Uberuaga, Efficient annealing of radiation damage near grain boundaries via interstitial emission, Science, 327 (2010) 1631-1634.

[184] D. Chen, J. Wang, T.Y. Chen, L. Shao, Defect annihilation at grain boundaries in alpha-Fe, Scientific Reports, 3 (2013).
[185] B. Singh, On the influence of grain boundaries on void growth, Philosophical Magazine, 28 (1973) 1409-1413.
[186] I. Skorvanek, R. Gerling, The influence of neutron irradiation on the soft magnetic and mechanical properties of amorphous and nanocrystalline Fe73. 5Cu1Nb3Si13. 5B9 alloys, Journal of applied physics, 72 (1992) 3417-3422.
[187] O. El-Atwani, J. Hinks, G. Greaves, S. Gonderman, T. Qiu, M. Efe, J.P. Allain, In-situ TEM observation of the response of ultrafine-and nanocrystalline-grained tungsten to extreme irradiation environments, Scientific reports, 4 (2014).
[188] A. Etienne, B. Radiguet, N. Cunningham, G. Odette, R. Valiev, P. Pareige, Comparison of radiation-induced segregation in ultrafine-grained and conventional 316 austenitic stainless steels, Ultramicroscopy, 111 (2011) 659-663.
[189] O. El-Atwani, M. Efe, B. Heim, J.P. Allain, Surface damage in ultrafine and multimodal grained tungsten materials induced by low energy helium irradiation, Journal of Nuclear Materials, 434 (2013) 170-177.
[190] N. Nita, R. Schaeublin, M. Victoria, Impact of irradiation on the microstructure of nanocrystalline materials, Journal of Nuclear Materials, 329 (2004) 953-957.
[191] B. Radiguet, A. Etienne, P. Pareige, X. Sauvage, R. Valiev, Irradiation behavior of nanostructured 316 austenitic stainless steel, J Mater Sci, 43 (2008) 7338-7343.
[192] A. Alsabbagh, R.Z. Valiev, K.L. Murty, Influence of grain size on radiation effects in a low carbon steel, Journal of Nuclear Materials, 443 (2013) 302-310.
[193] A.R. Kilmametov, D.V. Gunderov, R.Z. Valiev, A.G. Balogh, H. Hahn, Enhanced ion irradiation resistance of bulk nanocrystalline TiNi alloy, Scripta Materialia, 59 (2008) 1027-1030.
[194] M. Rose, A.G. Balogh, H. Hahn, Instability of irradiation induced defects in nanostructured materials, Nucl Instrum Meth B, 127 (1997) 119-122.
[195] C. Sun, K.Y. Yu, J.H. Lee, Y. Liu, H. Wang, L. Shao, S.A. Maloy, K.T. Hartwig, X. Zhang, Enhanced radiation tolerance of ultrafine grained Fe-Cr-Ni alloy, Journal of Nuclear Materials, 420 (2012) 235-240.
[196] C. Abromeit, Aspects of Simulation of Neutron Damage by Ion Irradiation, Journal of Nuclear Materials, 216 (1994) 78-96.
[197] F. Vook, H. Stein, Relation of neutron to ion damage annealing in Si and Ge, Radiation Effects, 2 (1969) 23-30.
[198] G.S. Was, J.T. Busby, T. Allen, E.A. Kenik, A. Jenssen, S.M. Bruemmer, J. Gan, A.D. Edwards, P.M. Scott, Emulation of neutron irradiation effects with protons: validation of principle, Journal of Nuclear Materials, 300 (2002) 198-216.
[199] C. Sun, F.A. Garner, L. Shao, X. Zhang, S.A. Maloy, Influence of injected interstitials on the void swelling in two structural variants of 304L stainless steel induced by self-ion irradiation at 500 °C, Nuclear Instruments and Methods in Physics Research Section B: Beam Interactions with Materials and Atoms, 409 (2017) 323-327.
[200] D. Kaoumi, A.T. Motta, R.C. Birtcher, A thermal spike model of grain growth under irradiation, Journal of Applied Physics, 104 (2008) 073525.
[201] D.C. Bufford, F.F. Abdeljawad, S.M. Foiles, K. Hattar, Unraveling irradiation induced grain growth with in situ transmission electron microscopy and coordinated modeling, Applied Physics Letters, 107 (2015) 191901.

[202] B. Muntifering, S.J. Blair, C. Gong, A. Dunn, R. Dingreville, J. Qu, K. Hattar, Cavity Evolution at Grain Boundaries as a Function of Radiation Damage and Thermal Conditions in Nanocrystalline Nickel, Mater Res Lett, (2015) 1-8.
[203] Y.W. Zhang, W.L. Jiang, C.M. Wang, F. Namavar, P.D. Edmondson, Z.H. Zhu, F. Gao, J. Lian, W.J. Weber, Grain growth and phase stability of nanocrystalline cubic zirconia under ion irradiation, Physical Review B, 82 (2010) 184105.
[204] Y. Zhang, P.D. Edmondson, T. Varga, S. Moll, F. Namavar, C. Lan, W.J. Weber, Structural modification of nanocrystalline ceria by ion beams, Phys Chem Chem Phys, 13 (2011) 11946-11950.
[205] D.S. Aidhy, Y.W. Zhang, W.J. Weber, A fast grain-growth mechanism revealed in nanocrystalline ceramic oxides, Scripta Materialia, 83 (2014) 9-12.
[206] L. Jiao, K.Y. Yu, D. Chen, C. Jacob, L. Shao, X. Zhang, H. Wang, Radiation tolerant nanocrystalline ZrN films under high dose heavy-ion irradiations, Journal of Applied Physics, 117 (2015) 145901.
[207] H. Wang, R. Araujo, J.G. Swadener, Y.Q. Wang, X. Zhang, E.G. Fu, T. Cagin, Ion irradiation effects in nanocrystalline TiN coatings, Nucl Instrum Meth B, 261 (2007) 1162-1166.
[208] A. Guglya, I. Neklyudov, R. Vasilenko, Effect of helium ion irradiation on the structure and electrical resistivity of nanocrystalline Cr-N and V-N coatings, Radiat Eff Defect S, 162 (2007) 643-649.
[209] T.D. Shen, S. Feng, M. Tang, J.A. Valdez, Y. Wang, K.E. Sickafus, Enhanced radiation tolerance in nanocrystalline MgGa2O4, Applied Physics Letters, 90 (2007) 263115-263500.
[210] M. Rose, G. Gorzawski, G. Miehe, A.G. Balogh, H. Hahn, Phase stability of nanostructured materials under heavy ion irradiation, Nanostruct Mater, 6 (1995) 731-734.
[211] J. Zhang, J. Lian, A.F. Fuentes, F. Zhang, M. Lang, F. Lu, R.C. Ewing, Enhanced radiation resistance of nanocrystalline pyrochlore Gd2 (Ti0. 65Zr0. 35) 2O7, Applied Physics Letters, 94 (2009) 243110.
[212] A. Audren, I. Monnet, Y. Leconte, X. Portier, L. Thome, M. Levalois, N. Herlin-Boime, C. Reynaud, Structural evolution of SiC nanostructured and conventional ceramics under irradiation, Nucl Instrum Meth B, 266 (2008) 2806-2809.
[213] A. Meldrum, L.A. Boatner, R.C. Ewing, Nanocrystalline Zirconia Can Be Amorphized by Ion Irradiation, Physical Review Letters, 88 (2001) 025503.
[214] F.Y. Lu, Y.Q. Shen, X. Sun, Z.L. Dong, R.C. Ewing, J. Lian, Size dependence of radiation-induced amorphization and recrystallization of synthetic nanostructured CePO4 monazite, Acta Materialia, 61 (2013) 2984-2992.
[215] W.J. Weber, R.C. Ewing, L.M. Wang, The Radiation-Induced Crystalline-to-Amorphous Transition in Zircon, Journal of Materials Research, 9 (1994) 688-698.
[216] W.J. Weber, Models and mechanisms of irradiation-induced amorphization in ceramics, Nucl Instrum Meth B, 166 (2000) 98-106.
[217] R.C. Ewing, A. Meldrum, L.M. Wang, W.J. Weber, L.R. Corrales, Radiation effects in zircon, Rev Mineral Geochem, 53 (2003) 387-425.
[218] A. Meldrum, L.A. Boatner, C.W. White, R.C. Ewing, Ion irradiation effects in nonmetals: formation of nanocrystals and novel microstructures, Mater Res Innov, 3 (2000) 190-204.

[219] A. Meldrum, S.J. Zinkle, L.A. Boatner, M. Wu, R. Mu, A. Ueda, D.O. Henderson, R.C. Ewing, Radiation effects in zircon, hafnon, and thorite: Implications for Pu disposal, Microstructural Processes in Irradiated Materials, 540 (1999) 395-400.
[220] S.X. Wang, L.M. Wang, R.C. Ewing, Irradiation-induced amorphization: Effects of temperature, ion mass, cascade size, and dose rate, Physical Review B, 63 (2001).
[221] M.G.N. Elizabeth L. Fleischer, Mark A. Zaleski, William Hertl, C. Barry Carter and James W. Mayer, Microstructure of hardened and softened zirconia after xenon implantation, Journal of Materials Research, 6 (1991) 1905-1912.
[222] Y.W. Zhang, M. Ishimaru, T. Varga, T. Oda, C. Hardiman, H.Z. Xue, Y. Katoh, S. Shannon, W.J. Weber, Nanoscale engineering of radiation tolerant silicon carbide, Phys Chem Chem Phys, 14 (2012) 13429-13436.
[223] L. Jamison, M.J. Zheng, S. Shannon, T. Allen, D. Morgan, I. Szlufarska, Experimental and ab initio study of enhanced resistance to amorphization of nanocrystalline silicon carbide under electron irradiation, Journal of Nuclear Materials, 445 (2014) 181-189.
[224] K. Imada, M. Ishimaru, H.Z. Xue, Y.W. Zhang, S.C. Shannon, W.J. Weber, Amorphization resistance of nano-engineered SiC under heavy ion irradiation, Journal of Nuclear Materials, 478 (2016) 310-314.
[225] J. Huguet-Garcia, A. Jankowiak, S. Miro, D. Gosset, Y. Serruys, J.M. Costantini, Study of the Ion-Irradiation Behavior of Advanced SiC Fibers by Raman Spectroscopy and Transmission Electron Microscopy, J Am Ceram Soc, 98 (2015) 675-682.
[226] W. Jiang, H. Wang, I. Kim, Y. Zhang, W.J. Weber, Amorphization of nanocrystalline 3C-SiC irradiated with Si+ ions, Journal of Materials Research, 25 (2010) 2341-2348.
[227] S. Intarasiri, L.D. Yu, S. Singkarat, A. Hallen, J. Lu, M. Ottosson, J. Jensen, G. Possnert, Effects of low-fluence swift iodine ion bombardment on the crystallization of ion-beam-synthesized silicon carbide, Journal of Applied Physics, 101 (2007).
[228] W. Jiang, H. Wang, I. Kim, I.T. Bae, G. Li, P. Nachimuthu, Z. Zhu, Y. Zhang, W.J. Weber, Response of nanocrystalline 3C silicon carbide to heavy-ion irradiation, Physical Review B, 80 (2009).
[229] H. Jiang, X. Wang, I. Szlufarska, The Multiple Roles of Small-Angle Tilt Grain Boundaries in Annihilating Radiation Damage in SiC, Scientific Reports, 7 (2017).
[230] N. Swaminathan, P.J. Kamenski, D. Morgan, I. Szlufarska, Effects of grain size and grain boundaries on defect production in nanocrystalline 3C-SiC, Acta Materialia, 58 (2010) 2843-2853.
[231] L. Jamison, K. Sridharan, S. Shannon, I. Szlufarska, Temperature and irradiation species dependence of radiation response of nanocrystalline silicon carbide, Journal of Materials Research, 29 (2014) 2871-2880.
[232] B.P. Uberuaga, L.J. Vernon, E. Martinez, A.F. Voter, The relationship between grain boundary structure, defect mobility, and grain boundary sink efficiency, Scientific Reports, 5 (2015) 9095.
[233] M.A. Tschopp, K.N. Solanki, F. Gao, X. Sun, M.A. Khaleel, M.F. Horstemeyer, Probing grain boundary sink strength at the nanoscale: Energetics and length scales of vacancy and interstitial absorption by grain boundaries in alpha-Fe, Physical Review B, 85 (2012) 064108.
[234] M.A. Tschopp, D.E. Spearot, D.L. McDowell, Chapter 82 Influence of Grain Boundary Structure on Dislocation Nucleation in FCC Metals, 14 (2008) 43-139.

[235] X.M. Bai, B.P. Uberuaga, The Influence of Grain Boundaries on Radiation-Induced Point Defect Production in Materials: A Review of Atomistic Studies, Jom, 65 (2013) 360-373.
[236] X.Y. Li, W. Liu, Y.C. Xu, C.S. Liu, Q.F. Fang, B.C. Pan, J.L. Chen, G.N. Luo, Z.G. Wang, An energetic and kinetic perspective of the grain-boundary role in healing radiation damage in tungsten, Nuclear Fusion, 53 (2013) 123014.
[237] W.Z. Han, M.J. Demkowicz, E.G. Fu, Y.Q. Wang, A. Misra, Effect of grain boundary character on sink efficiency, Acta Materialia, 60 (2012) 6341-6351.
[238] C.M. Barr, G.A. Vetterick, K.A. Unocic, K. Hattar, X.M. Bai, M.L. Taheri, Anisotropic radiation-induced segregation in 316L austenitic stainless steel with grain boundary character, Acta Materialia, 67 (2014) 145-155.
[239] C.M. Barr, L. Barnard, J.E. Nathaniel, K. Hattar, K.A. Unocic, I. Szlufarska, D. Morgan, M.L. Taheri, Grain boundary character dependence of radiation-induced segregation in a model Ni-Cr alloy, Journal of Materials Research, 30 (2015) 1290-1299.
[240] S.J. Zinkle, Effect of H and He irradiation on cavity formation and blistering in ceramics, Nucl Instrum Meth B, 286 (2012) 4-19.
[241] J. Chen, P. Jung, H. Trinkaus, Microstructural evolution of helium-implanted alpha-SiC, Physical Review B, 61 (2000) 12923-12932.
[242] J. Chen, P. Jung, H. Trinkaus, Evolution of helium platelets and associated dislocation loops in alpha-SiC, Physical Review Letters, 82 (1999) 2709-2712.
[243] M. Tokitani, Y. Ohtawa, N. Yoshida, K. Tokunaga, T. Fujiwara, N. Ashikawa, S. Masuzaki, H. Yamada, A. Sagara, N. Noda, A. Komori, L.E. Grp, Micro/nano scale modification of plasma facing components in LHD and its impact on the metal dust generations, Journal of Nuclear Materials, 390-91 (2009) 156-159.
[244] N. Yoshida, H. Iwakiri, K. Tokunaga, T. Baba, Impact of low energy helium irradiation on plasma facing metals, Journal of Nuclear Materials, 337 (2005) 946-950.
[245] N. Yoshida, M. Miyamoto, K. Tokunaga, H. Iwakiri, H. Wakimoto, T. Fujiwara, T. Grp, Microscopic damage of metals exposed to the helium discharges in TRIAM-1M tokamak and its impact on hydrogen recycling process, Nuclear Fusion, 43 (2003) 655-659.
[246] M.H. Cui, Z.G. Wang, L.L. Pang, T.L. Shen, C.F. Yao, B.S. Li, J.Y. Li, X.Z. Cao, P. Zhang, J.R. Sun, Y.B. Zhu, Y.F. Li, Y.B. Sheng, Temperature dependent defects evolution and hardening of tungsten induced by 200 keV He-ions, Nucl Instrum Meth B, 307 (2013) 507-511.
[247] D. Perez, L. Sandoval, S. Blondel, B.D. Wirth, B.P. Uberuaga, A.F. Voter, The mobility of small vacancy/helium complexes in tungsten and its impact on retention in fusion-relevant conditions, Scientific Reports, 7 (2017).
[248] J. Chen, Z.Y. He, P. Jung, Microstructure of helium-implanted α-Al2O3 after annealing, Acta Materialia, 54 (2006) 1607-1614.
[249] P. Song, J. Sun, Z. Wang, M. Cui, T. Shen, Y. Li, L. Pang, Y. Zhu, Q. Huang, J. Lü, Irradiation resistance properties studies on helium ions irradiated MAX phase Ti3AlC2, Nuclear Instruments and Methods in Physics Research Section B: Beam Interactions with Materials and Atoms, 326 (2014) 332-336.
[250] H. Trinkaus, B.N. Singh, Helium accumulation in metals during irradiation - where do we stand?, Journal of Nuclear Materials, 323 (2003) 229-242.
[251] K. Ehrlich, The role of precipitates for the development of irradiation-induced swelling and high-temperature embrittlement in an austenitic stainless steel of type X10 CrNiMoTiB 15 15, Z Metallkd, 94 (2003) 485-491.

[252] G. Dobmann, S.N. Korshunov, M. Kroening, Y.V. Martynenko, I.D. Skorlupkin, A.S. Surkov, Helium and radiation defect accumulation in metals under stress, Vacuum, 82 (2008) 856-866.
[253] X.Y. Tan, L.M. Luo, H.Y. Chen, X.Y. Zhu, X. Zan, G.N. Luo, J.L. Chen, P. Li, J.G. Cheng, D.P. Liu, Y.C. Wu, Mechanical properties and microstructural change of W-Y2O3 alloy under helium irradiation, Scientific Reports, 5 (2015).
[254] J. Xu, C.B. Wang, W. Zhang, C.L. Ren, H.F. Gong, P. Huai, Atomistic simulations of the interactions of helium with dislocations in nickel, Nucl Mater Energy, 7 (2016) 12-19.
[255] H.F. Gong, C.B. Wang, W. Zhang, J. Xu, P. Huai, H.Q. Deng, W.Y. Hu, The energy and stability of helium-related cluster in nickel: A study of molecular dynamics simulation, Nucl Instrum Meth B, 368 (2016) 75-80.
[256] E. Martinez, B.P. Uberuaga, B.D. Wirth, Atomistic modeling of helium segregation to grain boundaries in tungsten and its effect on de-cohesion, Nuclear Fusion, 57 (2017).
[257] R. Liontas, X.W. Gu, E.G. Fu, Y.Q. Wang, N. Li, N. Mara, J.R. Greer, Effects of Helium Implantation on the Tensile Properties and Microstructure of Ni73P27 Metallic Glass Nanostructures, Nano Letters, 14 (2014) 5176-5183.
[258] M.S. Ding, J.P. Du, L. Wan, S. Ogata, L. Tian, E. Ma, W.Z. Han, J. Li, Z.W. Shan, Radiation-Induced Helium Nanobubbles Enhance Ductility in Submicron-Sized Single-Crystalline Copper, Nano Letters, 16 (2016) 4118-4124.
[259] H.F. Gong, C.B. Wang, W. Zhang, P. Huai, W. Lu, Z.Y. Zhu, Atomistic simulation of the trapping capability of He- vacancy defects at Ni Sigma 3(1(1)over-bar2)[110] grain boundary, Modelling and Simulation in Materials Science and Engineering, 24 (2016).
[260] J. Gazda, H.M. Chung, B.A. Loomis, M. Meshii, Effects of heavy-ion irradiation on microstructure of V-4Cr-4Ti alloy at moderate temperatures, Microstructure Evolution during Irradiation, 439 (1997) 349-354.
[261] H.F. Huang, W. Zhang, M. De Los Reyes, X.L. Zhou, C. Yang, R. Xie, X.T. Zhou, P. Huai, H.J. Xu, Mitigation of He embrittlement and swelling in nickel by dispersed SiC nanoparticles, Mater Design, 90 (2016) 359-363.
[262] N. Gao, M. Victoria, J. Chen, H. Van Swygenhoven, Helium-vacancy cluster in a single bcc iron crystal lattice, J Phys-Condens Mat, 23 (2011).
[263] T. Zhang, C. Vieh, K. Wang, Y. Dai, Irradiation-induced evolution of mechanical properties and microstructure of Eurofer 97, Journal of Nuclear Materials, 450 (2014) 48-53.
[264] L. Zhang, C.C. Fu, E. Hayward, G.H. Lu, Properties of He clustering in alpha-Fe grain boundaries, Journal of Nuclear Materials, 459 (2015) 247-258.
[265] C.H. Zhang, K.Q. Chen, Y.S. Wang, J.G. Sun, D.Y. Shen, Formation of bubbles in helium implanted 316L stainless steel at temperatures between 25 and 550 degrees C, Journal of Nuclear Materials, 245 (1997) 210-216.
[266] C.H. Zhang, K.Q. Chen, Y.S. Wang, J.G. Sun, Temperature dependence of bubble structure in 316L stainless steel irradiated with 2.5 MeV He ions, Journal of Nuclear Materials, 258 (1998) 1623-1627.
[267] V. Zell, H. Schroeder, H. Trinkaus, Helium Bubble Formation in Nickel during Hot Implantation, Journal of Nuclear Materials, 212 (1994) 358-363.
[268] J.N. Yu, X.J. Zhao, W. Zhang, W. Yang, F.M. Chu, Defect production and accumulation under hydrogen and helium ion irradiation, Journal of Nuclear Materials, 251 (1997) 150-156.

[269] T. Yamamoto, Y. Wu, G.R. Odette, K. Yabuuchi, S. Kondo, A. Kimura, A dual ion irradiation study of helium-dpa interactions on cavity evolution in tempered martensitic steels and nanostructured ferritic alloys, Journal of Nuclear Materials, 449 (2014) 190-199.
[270] T. Yamamoto, G.R. Odette, P. Miao, D.T. Hoelzer, J. Bentley, N. Hashimoto, H. Tanigawa, R.J. Kurtz, The transport and fate of helium in nanostructured ferritic alloys at fusion relevant He/dpa ratios and dpa rates, Journal of Nuclear Materials, 367 (2007) 399-410.
[271] T. Yamamoto, G.R. Odette, P. Miao, D.J. Edwards, R.J. Kurtz, Helium effects on microstructural evolution in tempered martensitic steels: In situ helium implanter studies in HFIR, Journal of Nuclear Materials, 386-88 (2009) 338-341.
[272] K. Wang, Y. Dai, P. Spatig, Microstructure and fracture behavior of F82H steel under different irradiation and tensile test conditions, Journal of Nuclear Materials, 468 (2016) 246-254.
[273] J. Wang, X. Gao, N. Gao, Z.G. Wang, M.H. Cui, K.F. Wei, C.F. Yao, J.R. Sun, B.S. Li, Y.B. Zhu, L.L. Pang, Y.F. Li, D. Wang, E.Q. Xie, Grain size effects on He bubbles distribution and evolution, Journal of Nuclear Materials, 457 (2015) 182-185.
[274] A. van Veen, R.J.M. Konings, A.V. Fedorov, Helium in inert matrix dispersion fuels, Journal of Nuclear Materials, 320 (2003) 77-84.
[275] H. Ullmaier, J. Chen, Low temperature tensile properties of steels containing high concentrations of helium, Journal of Nuclear Materials, 318 (2003) 228-233.
[276] H. Trinkaus, H. Ullmaier, High-Temperature Embrittlement of Metals Due to Helium - Is the Lifetime Dominated by Cavity Growth or Crack-Growth, Journal of Nuclear Materials, 212 (1994) 303-309.
[277] H. Trinkaus, The effect of cascade induced gas resolution on bubble formation in metals, Journal of Nuclear Materials, 318 (2003) 234-240.
[278] T. Suzudo, T. Tsuru, M. Yamaguchi, H. Kaburaki, An atomistic modeling of He bubble stability at grain boundaries in alpha-Fe, Journal of Nuclear Materials, 442 (2013) S655-S659.
[279] H. Schroeder, Y. Dai, Helium Concentration-Dependence of Embrittlement Effects in Din 1.4970, 13-Percent Cw Austenitic Stainless-Steel at 873-K, Journal of Nuclear Materials, 191 (1992) 781-785.
[280] A.I. Ryazanov, O.K. Chugunov, S.M. Ivanov, S.T. Latushkin, R. Lindau, A. Moslang, A.A. Nikitina, K.E. Prikhodko, E.V. Semenov, V.N. Unezhev, P.V. Vladimirov, Tensile properties and microstructure of helium implanted EUROFER ODS, Journal of Nuclear Materials, 442 (2013) S153-S157.
[281] L. Peng, Y. Dai, Helium-induced hardening effect in ferritic/martensitic steels F82H and Optimax-A irradiated in a mixed spectrum of high energy protons and spallation neutrons, Journal of Nuclear Materials, 417 (2011) 996-1000.
[282] N. Oono, S. Ukai, S. Kondo, O. Hashitomi, A. Kimura, Irradiation effects in oxide dispersion strengthened (ODS) Ni-base alloys for Gen. IV nuclear reactors, Journal of Nuclear Materials, 465 (2015) 835-839.
[283] Y. Nakamura, S. Kitajima, K. Shinohara, S. Ishimoto, T. Shodai, T. Torimaru, K. Yasuda, Low-Temperature Embrittlement of Low-Energy He Implanted Pure Iron and Iron-Based Alloys, Journal of Nuclear Materials, 179 (1991) 749-752.

[284] T. Miura, K. Fujii, K. Fukuya, Micro-mechanical investigation for effects of helium on grain boundary fracture of austenitic stainless steel, Journal of Nuclear Materials, 457 (2015) 279-290.
[285] P. Magnusson, J.C. Chen, W. Hoffelner, High temperature creep of a helium-implanted titanium aluminide alloy, Journal of Nuclear Materials, 416 (2011) 60-64.
[286] P. Magnusson, J. Chen, P. Jung, T. Sauvage, W. Hoffelner, P. Spatig, Helium embrittlement of a lamellar titanium aluminide, Journal of Nuclear Materials, 434 (2013) 252-258.
[287] R.J. Kurtz, H.L. Heinisch, The effects of grain boundary structure on binding of He in Fe, Journal of Nuclear Materials, 329 (2004) 1199-1203.
[288] P. Jung, H. Klein, J. Henry, J. Chen, Effect of implanted deuterium on tensile properties of helium-doped RAFM EUROFER97, Journal of Nuclear Materials, 417 (2011) 1013-1017.
[289] S. Jublot-Leclerc, M.L. Lescoat, F. Fortuna, L. Legras, X. Li, A. Gentils, TEM study of the nucleation of bubbles induced by He implantation in 316L industrial austenitic stainless steel, Journal of Nuclear Materials, 466 (2015) 646-652.
[290] K. Imasaki, A. Hasegawa, S. Nogami, M. Satou, Helium effects on the tensile property of 316FR stainless steel at 650 and 750 degrees C, Journal of Nuclear Materials, 417 (2011) 1030-1033.
[291] E. Gaganidze, C. Petersen, J. Aktaa, Study of helium embrittlement in boron doped EUROFER97 steels, Journal of Nuclear Materials, 386-88 (2009) 349-352.
[292] Y.X. Feng, J.X. Shang, G.H. Lu, Migration and nucleation of helium atoms at (110) twist grain boundaries in tungsten, Journal of Nuclear Materials, 487 (2017) 200-209.
[293] P.D. Edmondson, C.M. Parish, Y. Zhang, A. Hallen, M.K. Miller, Helium bubble distributions in a nanostructured ferritic alloy, Journal of Nuclear Materials, 434 (2013) 210-216.
[294] Y. Dai, J. Henry, Z. Tong, X. Averty, J. Malaplate, B. Long, Neutron/proton irradiation and He effects on the microstructure and mechanical properties of ferritic/martensitic steels T91 and EM10, Journal of Nuclear Materials, 415 (2011) 306-310.
[295] J. Chen, P. Jung, T. Rebac, F. Duval, T. Sauvage, Y. de Carlan, M.F. Barthe, Helium effects on creep properties of Fe-14CrWTi ODS steel at 650 degrees C, Journal of Nuclear Materials, 453 (2014) 253-258.
[296] B. Yao, D.J. Edwards, R.J. Kurtz, G.R. Odette, T. Yamamoto, Multislice simulation of transmission electron microscopy imaging of helium bubbles in Fe, J Electron Microsc, 61 (2012) 393-400.
[297] X. Zhang, C.L. Ren, H. Han, C.B. Wang, H.F. Huang, Y.R. Yin, W. Zhang, G. Lumpkin, P. Huai, Z.Y. Zhu, First-principles prediction of interstitial carbon, nitrogen, and oxygen effects on the helium behavior in nickel, Journal of Applied Physics, 122 (2017).
[298] P.P. Liu, Q. Zhan, Z.Y. Fu, Y.P. Wei, Y.M. Wang, F.M. Wang, S. Ohnuki, F.R. Wan, Surface and internal microstructure damage of He-ion-irradiated CLAM steel studied by cross-sectional transmission electron microscopy, J Alloy Compd, 649 (2015) 859-864.
[299] J.Y. Shi, L. Peng, M.Y. Ye, F. Gao, Molecular Dynamics Study: Effects of He Bubble and Cr Precipitate on Tensile Deformation of Grain Boundaries in alpha-Fe, Ieee T Plasma Sci, 45 (2017) 289-293.
[300] J.H. Chen, L.P. Guo, F.F. Luo, T.C. Li, Y.Y. Ren, J.P. Suo, Synergistic Effects in Reduced-Activation Martensitic Steel under Single and Sequential Helium/Hydrogen Ion Irradiation, Fusion Sci Technol, 66 (2014) 301-307.

[301] Y. Dai, H. Schroeder, Creep-Properties and Microstructures of Helium Implanted Aisi 316l Electron-Beam Weld and Parent Material, Fusion Eng Des, 30 (1995) 261-273.
[302] J. Chen, Y. Long, A first-principles study on the helium doped grain boundary in metal Al, Eur Phys J B, 85 (2012).
[303] M.Q. Hong, Y.Q. Wang, F. Ren, H.X. Zhang, D.J. Fu, B. Yang, X.H. Xiao, C.Z. Jiang, Helium release and amorphization resistance in ion irradiated nanochannel films, Epl-Europhys Lett, 106 (2014).
[304] M.J. Demkowicz, A. Misra, A. Caro, The role of interface structure in controlling high helium concentrations, Curr Opin Solid St M, 16 (2012) 101-108.
[305] D. Terentyev, X. He, Effect of Cr precipitates and He bubbles on the strength of < 1 1 0 > tilt grain boundaries in BCC Fe: An atomistic study, Comp Mater Sci, 50 (2011) 925-933.
[306] J. Wang, X. Gao, Z.G. Wang, K.F. Wei, C.F. Yao, M.H. Cui, J.R. Sun, B.S. Li, L.L. Pang, Y.B. Zhu, P. Luo, H.L. Chang, H.P. Zhang, H.P. Zhu, D. Wang, Y.Y. Du, E.Q. Xie, TEM Characterization of Helium Bubbles in T91 and MNHS Steels Implanted with 200 keV He Ions at Different Temperatures, Chinese Phys Lett, 32 (2015).
[307] M. Zhernenkov, S. Gill, V. Stanic, E. DiMasi, K. Kisslinger, J.K. Baldwin, A. Misra, M.J. Demkowicz, L. Ecker, Design of radiation resistant metallic multilayers for advanced nuclear systems, Applied Physics Letters, 104 (2014).
[308] X.K. Liu, Y. Liu, D.Z. Qian, Z. Zheng, First-principles study of helium atom doped interstitial sites of Al, Acta Phys Sin-Ch Ed, 59 (2010) 6450-6456.
[309] M.A. Tschopp, F. Gao, K.N. Solanki, He-V cluster nucleation and growth in alpha-Fe grain boundaries, Acta Materialia, 124 (2017) 544-555.
[310] E. Martinez, D. Schwen, A. Caro, Helium segregation to screw and edge dislocations in alpha-iron and their yield strength, Acta Materialia, 84 (2015) 208-214.
[311] B. Muntifering, R. Dingreville, K. Hattar, J. Qu, Electron Beam Effects during In-Situ Annealing of Self-Ion Irradiated Nanocrystalline Nickel, in: MRS Proceedings, Cambridge Univ Press, 2015, pp. 13-18.
[312] A.J. Detor, C.A. Schuh, Grain boundary segregation, chemical ordering and stability of nanocrystalline alloys: Atomistic computer simulations in the Ni-W system, Acta Materialia, 55 (2007) 4221-4232.
[313] T. Chookajorn, H.A. Murdoch, C.A. Schuh, Design of stable nanocrystalline alloys, Science, 337 (2012) 951-954.
[314] J. Kacher, P. Elizaga, S.D. House, K. Hattar, M. Nowell, I.M. Robertson, Thermal stability of Ni/NiO multilayers, Mat Sci Eng a-Struct, 568 (2013) 49-60.
[315] D.S. Gianola, S. Van Petegem, M. Legros, S. Brandstetter, H. Van Swygenhoven, K.J. Hemker, Stress-assisted discontinuous grain growth and its effect on the deformation behavior of nanocrystalline aluminum thin films, Acta Materialia, 54 (2006) 2253-2263.
[316] V.V. Sagaradze, A.V. Litvinov, V.A. Shabashov, N.F. Vil'danova, A.G. Mukoseev, K.A. Kozlov, New method of mechanical alloying of ODS steels using iron oxides, Phys Met Metallogr+, 101 (2006) 566-576.
[317] Z. Dapeng, L. Yong, L. Feng, W. Yuren, Z. Liujie, D. Yuhai, ODS ferritic steel engineered with bimodal grain size for high strength and ductility, Mater Lett, 65 (2011) 1672-1674.
[318] A. Bachmaier, G.B. Rathmayr, M. Bartosik, D. Apel, Z. Zhang, R. Pippan, New insights on the formation of supersaturated solid solutions in the Cu-Cr system deformed by high-pressure torsion, Acta Materialia, 69 (2014) 301-313.

[319] K.J. Bryden, J.Y. Ying, Thermal stability and hydrogen absorption characteristics of palladium-yttrium nanoalloys, Acta Materialia, 44 (1996) 3847-3854.
[320] K.A. Darling, M.A. Tschopp, R.K. Guduru, W.H. Yin, Q. Wei, L.J. Kecskes, Microstructure and mechanical properties of bulk nanostructured Cu-Ta alloys consolidated by equal channel angular extrusion, Acta Materialia, 76 (2014) 168-185.
[321] J.B. Dubois, L. Thilly, P.O. Renault, F. Lecouturier, M. Di Michiel, Thermal stability of nanocomposite metals: In situ observation of anomalous residual stress relaxation during annealing under synchrotron radiation, Acta Materialia, 58 (2010) 6504-6512.
[322] Z. Fan, J. Jian, Y. Liu, Y. Chen, M. Song, L. Jiao, H. Wang, X. Zhang, In situ studies on superior thermal stability of bulk FeZr nanocomposites, Acta Materialia, 101 (2015) 125-135.
[323] P.C. Millett, R.P. Selvam, A. Saxena, Stabilizing nanocrystalline materials with dopants, Acta Materialia, 55 (2007) 2329-2336.
[324] M.N. Polyakov, T. Chookajorn, M. Mecklenburg, C.A. Schuh, A.M. Hodge, Sputtered Hf-Ti nanostructures: A segregation and high-temperature stability study, Acta Materialia, 108 (2016) 8-16.
[325] C. Saldana, A.H. King, S. Chandrasekar, Thermal stability and strength of deformation microstructures in pure copper, Acta Materialia, 60 (2012) 4107-4116.
[326] B. Schuh, F. Mendez-Martin, B. Volker, E.P. George, H. Clemens, R. Pippan, A. Hohenwarter, Mechanical properties, microstructure and thermal stability of a nanocrystalline CoCrFeMnNi high-entropy alloy after severe plastic deformation, Acta Materialia, 96 (2015) 258-268.
[327] G.H. Zahid, Y. Huang, P.B. Prangnell, Microstructure and texture evolution during annealing a cryogenic-SPD processed Al-alloy with a nanoscale lamellar HAGB grain structure, Acta Materialia, 57 (2009) 3509-3521.
[328] H.W. Zhang, X. Huang, R. Pippan, N. Hansen, Thermal behavior of Ni (99.967% and 99.5% purity) deformed to an ultra-high strain by high pressure torsion, Acta Materialia, 58 (2010) 1698-1707.
[329] P. Zhang, J.Y. Zhang, J. Li, G. Liu, K. Wu, Y.Q. Wang, J. Sun, Microstructural evolution, mechanical properties and deformation mechanisms of nanocrystalline Cu thin films alloyed with Zr, Acta Materialia, 76 (2014) 221-237.
[330] F. Zhou, X.Z. Liao, Y.T. Zhu, S. Dallek, E.J. Lavernia, Microstructural evolution during recovery and recrystallization of a nanocrystalline Al-Mg alloy prepared by cryogenic ball milling, Acta Materialia, 51 (2003) 2777-2791.
[331] E. Botcharova, J. Freudenberger, L. Schutz, High thermal stability of mechanically-alloyed nanocrystalline Cu-Nb alloys, Int J Mater Res, 97 (2006) 1350-1354.
[332] M.D. Abad, S. Parker, D. Kiener, M.M. Primorac, P. Hosemann, Microstructure and mechanical properties of CuxNb1-x alloys prepared by ball milling and high pressure torsion compacting, J Alloy Compd, 630 (2015) 117-125.
[333] D. Bhattacharya, T.V.C. Rao, K.G. Bhushan, K. Ali, A. Debnath, S. Singh, A. Arya, S. Bhattacharya, S. Basu, Thermal evolution of nanocrystalline co-sputtered Ni-Zr alloy films: Structural, magnetic and MD simulation studies, J Alloy Compd, 649 (2015) 746-754.
[334] H. Kotan, K.A. Darling, M. Saber, C.C. Koch, R.O. Scattergood, Effect of zirconium on grain growth and mechanical properties of a ball-milled nanocrystalline FeNi alloy, J Alloy Compd, 551 (2013) 621-629.

[335] Z. Sadeghian, B. Lotfi, M.H. Enayati, P. Beiss, Microstructural and mechanical evaluation of Al-TiB2 nanostructured composite fabricated by mechanical alloying, J Alloy Compd, 509 (2011) 7758-7763.
[336] K. Santhi, E. Thirumal, S.N. Karthick, H.J. Kim, V. Narayanan, A. Stephen, Structural and magnetic investigations on metastable Ag-Fe nanophase alloy, J Alloy Compd, 557 (2013) 172-178.
[337] K.Y. Zhao, C.J. Li, J.M. Tao, D.H.L. Ng, X.K. Zhu, The synthesis, microstructure, hardness and thermal properties of bulk nanocrystalline Al produced by in situ consolidation with low-energy ball milling, J Alloy Compd, 504 (2010) S306-S310.
[338] J.P. Chu, Y.Y. Hsieh, C.H. Lin, T. Mahalingam, Thermal stability enhancement in nanostructured Cu films containing insoluble tungsten carbides for metallization, Journal of Materials Research, 20 (2005) 1379-1384.
[339] O.K. Donaldson, W.B. Wang, K. Hattar, J.R. Trelewicz, Impurity stabilization of nanocrystalline grains in pulsed laser deposited tantalum, Journal of Materials Research, 32 (2017) 1351-1360.
[340] H. Natter, M. Schmelzer, R. Hempelmann, Nanocrystalline nickel and nickel-copper alloys: Synthesis, characterization, and thermal stability, Journal of Materials Research, 13 (1998) 1186-1197.
[341] R.A. Andrievski, Review of thermal stability of nanomaterials, J Mater Sci, 49 (2014) 1449-1460.
[342] H. Kotan, K.A. Darling, M. Saber, R.O. Scattergood, C.C. Koch, Thermal stability and mechanical properties of nanocrystalline Fe-Ni-Zr alloys prepared by mechanical alloying, J Mater Sci, 48 (2013) 8402-8411.
[343] A. Molinari, I. Lonardelli, K. Demetrio, C. Menapace, Effect of the particle size on the thermal stability of nanostructured aluminum powder: dislocation density and second-phase particles controlling the grain growth, J Mater Sci, 45 (2010) 6739-6746.
[344] R.K. Rajgarhia, A. Saxena, D.E. Spearot, K.T. Hartwig, K.L. More, E.A. Kenik, H. Meyer, Microstructural stability of copper with antimony dopants at grain boundaries: experiments and molecular dynamics simulations, J Mater Sci, 45 (2010) 6707-6718.
[345] D.I. Shin, F. Gitzhofer, C. Moreau, Thermal property evolution of metal based thermal barrier coatings with heat treatments, J Mater Sci, 42 (2007) 5915-5923.
[346] G. Wilde, H. Rosner, Stability aspects of bulk nanostructured metals and composites, J Mater Sci, 42 (2007) 1772-1781.
[347] Y. Zhou, U. Erb, K.T. Aust, G. Palumbo, Magnetic and interface microstructure contribution to bulk specific heat of nanocrystalline Ni-P alloy, J Mater Sci, 48 (2013) 6141-6149.
[348] M. Zhu, Z.F. Wu, M.Q. Zeng, L.Z. Ouyang, Y. Gao, Bimodal growth of the nanophases in the dual-phase composites produced by mechanical alloying in immiscible Cu-Ag system, J Mater Sci, 43 (2008) 3259-3266.
[349] H.M. Tawancy, Synthesis of Bulk Nanostructured DO22 Superlattice of Ni-3(Mo, Nb) with High Strength, High Ductility, and High Thermal Stability, J Nanomater, (2012).
[350] K. Wawer, M. Lewandowska, K.J. Kurzydlowski, Precipitate Strengthening of Nanostructured Aluminium Alloy, J Nanosci Nanotechno, 12 (2012) 8783-8786.
[351] T. Danielson, C. Hin, Structural and electronic effects of helium interstitials in Y2Ti2O7: A first-principles study, Journal of Nuclear Materials, 452 (2014) 189-196.

[352] K.P. Tai, R.S. Averback, P. Bellon, Y. Ashkenazy, B. Stumphy, Temperature dependence of irradiation-induced creep in dilute nanostructured Cu-W alloys, Journal of Nuclear Materials, 422 (2012) 8-13.
[353] I. Roman, C. Fratila, E. Vasile, A. Petre, M.L. Soare, Electrochemical evaluation of the stability of ceramic nanostructured titanium oxide layers in Ringer solution, J Optoelectron Adv M, 12 (2010) 1597-1603.
[354] A. Sarkar, A.V. Murugan, A. Manthiram, Synthesis and characterization of nanostructured Pd-Mo electrocatalysts for oxygen reduction reaction in fuel cells, J Phys Chem C, 112 (2008) 12037-12043.
[355] T. Danielson, E. Tea, C. Hin, First-principles investigation of helium in Y2O3, J Phys D Appl Phys, 49 (2016).
[356] G.D. Samolyuk, Y.N. Osetsky, Thermodynamic approach to the stability of multi-phase systems: application to the Y2O3-Fe system, J Phys-Condens Mat, 27 (2015).
[357] M. Rajagopalan, K. Darling, S. Turnage, R.K. Koju, B. Hornbuckle, Y. Mishin, K.N. Solanki, Microstructural evolution in a nanocrystalline Cu-Ta alloy: A combined in-situ TEM and atomistic study, Mater Design, 113 (2017) 178-185.
[358] K.A. Darling, E.L. Huskins, B.E. Schuster, Q. Wei, L.J. Kecskes, Mechanical properties of a high strength Cu-Ta composite at elevated temperature, Mat Sci Eng a-Struct, 638 (2015) 322-328.
[359] G.D. Hibbard, V. Radmilovic, K.T. Aust, U. Erb, Grain boundary migration during abnormal grain growth in nanocrystalline Ni, Mat Sci Eng a-Struct, 494 (2008) 232-238.
[360] F. Khodabakhshi, M. Kazeminezhad, The annealing phenomena and thermal stability of severely deformed steel sheet, Mat Sci Eng a-Struct, 528 (2011) 5212-5218.
[361] K.T. Park, D.H. Shin, Annealing behavior of submicrometer grained ferrite in a low carbon steel fabricated by severe plastic deformation, Mat Sci Eng a-Struct, 334 (2002) 79-86.
[362] Y.L. Sun, S.Q. Xu, A.D. Shan, Effects of annealing on microstructure and mechanical properties of nano-grained Ni-based alloy produced by severe cold rolling, Mat Sci Eng a-Struct, 641 (2015) 181-188.
[363] J.M. Tao, G.M. Chen, W.W. Jian, J. Wang, Y.T. Zhu, X.K. Zhu, T.G. Langdon, Anneal hardening of a nanostructured Cu-Al alloy processed by high-pressure torsion and rolling, Mat Sci Eng a-Struct, 628 (2015) 207-215.
[364] H. Asgharzadeh, H.J. McQueen, Grain growth and stabilisation of nanostructured aluminium at high temperatures: review, Mater Sci Tech-Lond, 31 (2015) 1016-1034.
[365] W.J. Deng, Q. Li, B.L. Li, Z.C. Xie, Y.T. He, Y. Tang, W. Xia, Thermal stability of ultrafine grained aluminium alloy prepared by large strain extrusion machining, Mater Sci Tech-Lond, 30 (2014) 850-859.
[366] F.S. Sun, A. Zuniga, P. Rojas, E.J. Lavernia, Thermal stability and recrystallization of nanocrystalline Ti produced by cryogenic milling, Metall Mater Trans A, 37a (2006) 2069-2078.
[367] W.Z. Xu, L.L. Li, M. Saber, C.C. Koch, Y.T. Zhu, R.O. Scattergood, Microstructures and Stabilization Mechanisms of Nanocrystalline Iron-Chromium Alloys with Hafnium Addition, Metall Mater Trans A, 46a (2015) 4394-4404.
[368] G. Hibbard, U. Erb, K.T. Aust, U. Klement, G. Palumbo, Thermal stability of nanostructured electrodeposits, Mater Sci Forum, 386-3 (2002) 387-396.

[369] H.W. Zhang, K. Lu, R. Pippan, X. Huang, N. Hansen, Strong and Stable Nanostructured Ni by Light Alloying, Riso Mat Sci, (2012) 399-406.
[370] K. Lu, Stabilizing nanostructures in metals using grain and twin boundary architectures, Nat Rev Mater, 1 (2016).
[371] M. Huller, J. Vlcek, M. Dinkel, H.W. Hoppel, M. Goken, Hardening and thermal stability of nanocrystalline AlMg4.8 powder, Philosophical Magazine, 88 (2008) 1209-1226.
[372] W. Zhang, K. Du, X.Q. Chen, L.Y. Sheng, H.Q. Ye, Thermally stable coherent domain boundaries in complex-structured Cr2Nb intermetallics, Philosophical Magazine, 96 (2016) 58-70.
[373] C.C. Koch, R.O. Scattergood, B.K. VanLeeuwen, K.A. Darling, Thermodynamic Stabilization of Grain Size in Nanocrystalline Metals, Recrystallization and Grain Growth Iv, 715-716 (2012) 323-+.
[374] C.C. Koch, R.O. Scattergood, H. Kotan, M. Saber, Thermal Stability of Nanocrystalline Grain Size in Ternary Fe-base Alloys, Recrystallization and Grain Growth V, 753 (2013) 341-344.
[375] Y.R. Kolobov, A.G. Lipnitskii, M.B. Ivanov, I.V. Nelasov, S.S. Manokhin, Investigations of the Thermal Stability of the Microstructure of Titanium Produced by Intense Plastic Deformation, Russ Phys J+, 54 (2012) 918-936.
[376] K.J. Dusoe, S. Vijayan, T.R. Bissell, J. Chen, J.E. Morley, L. Valencia, A.M. Dongare, M. Aindow, S.W. Lee, Strong, ductile, and thermally stable Cu-based metal-intermetallic nanostructured composites, Scientific Reports, 7 (2017).
[377] L. Jiang, J.K. Li, P.M. Cheng, G. Liu, R.H. Wang, B.A. Chen, J.Y. Zhang, J. Sun, M.X. Yang, G. Yang, Microalloying Ultrafine Grained Al Alloys with Enhanced Ductility, Scientific Reports, 4 (2014).
[378] S.J. Zheng, J.S. Carpenter, R.J. McCabe, I.J. Beyerlein, N.A. Mara, Engineering Interface Structures and Thermal Stabilities via SPD Processing in Bulk Nanostructured Metals, Scientific Reports, 4 (2014).
[379] H. Asgharzadeh, A. Simchi, H.S. Kim, High-temperature deformation and structural restoration of a nanostructured Al alloy, Scripta Materialia, 66 (2012) 911-914.
[380] M.R. Shankar, B.C. Rao, S. Chandrasekar, W.D. Compton, A.H. King, Thermally stable nanostructured materials from severe plastic deformation of precipitation-treatable Ni-based alloys, Scripta Materialia, 58 (2008) 675-678.
[381] Y.M. Wang, A.F. Jankowski, A.V. Hamza, Strength and thermal stability of nanocrystalline gold alloys, Scripta Materialia, 57 (2007) 301-304.
[382] B.B. Zhang, N.R. Tao, K. Lu, A high strength and high electrical conductivity bulk Cu-Ag alloy strengthened with nanotwins, Scripta Materialia, 129 (2017) 39-43.
[383] H.J. Fecht, Nanostructure formation and thermal stability of nanophase materials prepared by mechanical means, Z Metallkd, 94 (2003) 1134-1142.
[384] K. Zhou, H. Li, J.B. Pang, Z. Wang, Effects of oxide distributed in grain boundaries on microstructure stability of nanocrystalline metals, in: Journal of Physics: Conference Series, IOP Publishing, 2013, pp. 012020.
[385] G.S. Was, Ion-Beam Modification of Metals - Compositional and Microstructural Changes, Prog Surf Sci, 32 (1989) 211-332.
[386] C. Chisholm, K. Hattar, A.M. Minor, In Situ TEM Concurrent and Successive Au Self-Ion Irradiation and He Implantation, Mater Trans, 55 (2014) 418-422.

[387] C.A. Schuh, Replacing chrome coatings with safer metal alloys, Advanced Manufacturing Technology, 30 (2009) 1-3.
[388] R.Z. Valiev, T.G. Langdon, Principles of equal-channel angular pressing as a processing tool for grain refinement, Prog Mater Sci, 51 (2006) 881-981.
[389] R.Z. Valiev, R.K. Islamgaliev, I.V. Alexandrov, Bulk nanostructured materials from severe plastic deformation, Prog Mater Sci, 45 (2000) 103-189.
[390] A. Misra, J. Hirth, R. Hoagland, Length-scale-dependent deformation mechanisms in incoherent metallic multilayered composites, Acta Materialia, 53 (2005) 4817-4824.
[391] S.I. Rao, P.M. Hazzledine, Atomistic simulations of dislocation–interface interactions in the Cu-Ni multilayer system, Philosophical Magazine A, 80 (2000) 2011-2040.
[392] S. Choudhury, D. Morgan, B.P. Uberuaga, Massive interfacial reconstruction at misfit dislocations in metal/oxide interfaces, Scientific reports, 4 (2014).
[393] J.S. Koehler, Attempt to Design a Strong Solid, Physical Review B, 2 (1970) 547-551.
[394] Y. Liu, D. Bufford, H. Wang, C. Sun, X. Zhang, Mechanical properties of highly textured Cu/Ni multilayers, Acta Materialia, 59 (2011) 1924-1933.
[395] R. Carpenter, C. Liu, Proceedings, Second International Conference on the Strength of Metals and Alloys, Pacific Grove, California, ASM, 2 (1970) 674.
[396] A. Brailsford, R. Bullough, The theory of sink strengths, Philosophical Transactions of the Royal Society of London A: Mathematical, Physical and Engineering Sciences, 302 (1981) 87-137.
[397] A.D. Brailsford, R. Bullough, M.R. Hayns, Point-Defect Sink Strengths and Void-Swelling, Journal of Nuclear Materials, 60 (1976) 246-256.
[398] R. Bullough, M. Hayns, C. Woo, The sink strength of dislocation loops and their growth in irradiated materials, Journal of Nuclear Materials, 84 (1979) 93-100.
[399] H. Rauht, M. Wood, R. Bullough, Void sink strength including bulk recombination, Philosophical Magazine A, 44 (1981) 1255-1276.
[400] N. Doan, G. Martin, Elimination of irradiation point defects in crystalline solids: Sink strengths, Physical Review B, 67 (2003) 134107.
[401] M. Demkowicz, R. Hoagland, B. Uberuaga, A. Misra, Influence of interface sink strength on the reduction of radiation-induced defect concentrations and fluxes in materials with large interface area per unit volume, Physical Review B, 84 (2011) 104102.
[402] A.P. Sutton, R.W. Balluffi, H. Lüth, J.M. Gibson, Interfaces in Crystalline Materials and Surfaces and Interfaces of Solid Materials, Physics Today, 49 (1996) 88.
[403] K. Yu, C. Sun, Y. Chen, Y. Liu, H. Wang, M. Kirk, M. Li, X. Zhang, Superior tolerance of Ag/Ni multilayers against Kr ion irradiation: an in situ study, Philosophical Magazine, 93 (2013) 3547-3562.
[404] S. Mao, S. Dillon, R.S. Averback, The influence of Cu–Nb interfaces on local vacancy concentrations in Cu, Scripta Materialia, 69 (2013) 21-24.
[405] Y. Chen, N. Li, D. Bufford, J. Li, K. Hattar, H. Wang, X. Zhang, In situ study of heavy ion irradiation response of immiscible Cu/Fe multilayers, Journal of nuclear materials, 475 (2016) 274-279.
[406] W. Han, M.J. Demkowicz, N.A. Mara, E. Fu, S. Sinha, A.D. Rollett, Y. Wang, J.S. Carpenter, I.J. Beyerlein, A. Misra, Design of radiation tolerant materials via interface engineering, Advanced materials, 25 (2013) 6975-6979.

[407] S. Zinkle, Microstructure of ion irradiated ceramic insulators, Nuclear Instruments and Methods in Physics Research Section B: Beam Interactions with Materials and Atoms, 91 (1994) 234-246.
[408] Q. Su, B. Cui, M.A. Kirk, M. Nastasi, Cascade effects on the irradiation stability of amorphous SiOC, Philosophical Magazine Letters, 96 (2016) 60-66.
[409] T. Höchbauer, A. Misra, K. Hattar, R. Hoagland, Influence of interfaces on the storage of ion-implanted He in multilayered metallic composites, Journal of applied physics, 98 (2005) 123516.
[410] X. Zhang, N. Li, O. Anderoglu, H. Wang, J. Swadener, T. Höchbauer, A. Misra, R. Hoagland, Nanostructured Cu/Nb multilayers subjected to helium ion-irradiation, Nuclear Instruments and Methods in Physics Research Section B: Beam Interactions with Materials and Atoms, 261 (2007) 1129-1132.
[411] I. Beyerlein, M. Demkowicz, A. Misra, B. Uberuaga, Defect-interface interactions, Prog Mater Sci, 74 (2015) 125-210.
[412] M. Demkowicz, Y. Wang, R. Hoagland, O. Anderoglu, Mechanisms of He escape during implantation in CuNb multilayer composites, Nuclear Instruments and Methods in Physics Research Section B: Beam Interactions with Materials and Atoms, 261 (2007) 524-528.
[413] K. Hattar, M. Demkowicz, A. Misra, I. Robertson, R. Hoagland, Arrest of He bubble growth in Cu–Nb multilayer nanocomposites, Scripta Materialia, 58 (2008) 541-544.
[414] N. Li, N. Mara, Y. Wang, M. Nastasi, A. Misra, Compressive flow behavior of Cu thin films and Cu/Nb multilayers containing nanometer-scale helium bubbles, Scripta Materialia, 64 (2011) 974-977.
[415] M. Zhernenkov, M.S. Jablin, A. Misra, M. Nastasi, Y. Wang, M.J. Demkowicz, J.K. Baldwin, J. Majewski, Trapping of implanted He at Cu/Nb interfaces measured by neutron reflectometry, Applied Physics Letters, 98 (2011).
[416] N. Li, M. Nastasi, A. Misra, Defect structures and hardening mechanisms in high dose helium ion implanted Cu and Cu/Nb multilayer thin films, International Journal of Plasticity, 32 (2012) 1-16.
[417] A. Kashinath, P. Wang, J. Majewski, J. Baldwin, Y. Wang, M. Demkowicz, Detection of helium bubble formation at fcc-bcc interfaces using neutron reflectometry, Journal of applied physics, 114 (2013) 043505.
[418] W. Han, N. Mara, Y. Wang, A. Misra, M. Demkowicz, He implantation of bulk Cu–Nb nanocomposites fabricated by accumulated roll bonding, Journal of nuclear materials, 452 (2014) 57-60.
[419] S. Mao, S. Özerinç, W.P. King, R.S. Averback, S.J. Dillon, Effect of irradiation damage on the shear strength of Cu–Nb interfaces, Scripta Materialia, 90 (2014) 29-32.
[420] T.G. Lach, E.H. Ekiz, R.S. Averback, N.A. Mara, P. Bellon, Role of interfaces on the trapping of He in 2D and 3D Cu–Nb nanocomposites, Journal of nuclear materials, 466 (2015) 36-42.
[421] N. Li, M. Demkowicz, N. Mara, Y. Wang, A. Misra, Hardening due to Interfacial He Bubbles in Nanolayered Composites, Mater Res Lett, 4 (2015) 75-82.
[422] S. Mao, S. Shu, J. Zhou, R.S. Averback, S.J. Dillon, Quantitative comparison of sink efficiency of Cu–Nb, Cu–V and Cu–Ni interfaces for point defects, Acta Materialia, 82 (2015) 328-335.
[423] W. Bollmann, O-Lattice calculation of an FCC–BCC interface, Physica status solidi (a), 21 (1974) 543-550.

[424] M.J. Demkowicz, R.G. Hoagland, J.P. Hirth, Interface structure and radiation damage resistance in Cu-Nb multilayer nanocomposites, Phys Rev Lett, 100 (2008) 136102.
[425] M.J. Demkowicz, J. Wang, R.G. Hoagland, Interfaces between dissimilar crystalline solids, Dislocations in solids, 14 (2008) 141-207.
[426] M. Demkowicz, D. Bhattacharyya, I. Usov, Y. Wang, M. Nastasi, A. Misra, The effect of excess atomic volume on He bubble formation at fcc-bcc interfaces, Applied Physics Letters, 97 (2010) 161903.
[427] K. Kolluri, M.J. Demkowicz, Dislocation mechanism of interface point defect migration, Physical Review B, 82 (2010) 193404.
[428] K. Kolluri, M.J. Demkowicz, Formation, migration, and clustering of delocalized vacancies and interstitials at a solid-state semicoherent interface, Physical Review B, 85 (2012) 205416.
[429] X.-Y. Liu, R. Hoagland, M. Demkowicz, M. Nastasi, A. Misra, The influence of lattice misfit on the atomic structures and defect energetics of face centered cubic–body centered cubic interfaces, Journal of Engineering Materials and Technology, 134 (2012) 021012.
[430] X.-Y. Liu, B.P. Uberuaga, M.J. Demkowicz, T.C. Germann, A. Misra, M. Nastasi, Mechanism for recombination of radiation-induced point defects at interphase boundaries, Physical Review B, 85 (2012) 012103.
[431] A. Kashinath, A. Misra, M. Demkowicz, Stable storage of helium in nanoscale platelets at semicoherent interfaces, Physical review letters, 110 (2013) 086101.
[432] K. Kolluri, M.J. Demkowicz, R.G. Hoagland, X.-Y. Liu, Behavior of vacancies and interstitials at semicoherent interfaces, Jom, 65 (2013) 374-381.
[433] M. McPhie, L. Capolungo, A. Dunn, M. Cherkaoui, Interfacial trapping mechanism of He in Cu–Nb multilayer materials, Journal of nuclear materials, 437 (2013) 222-228.
[434] L. Zhang, M.J. Demkowicz, Morphological stability of Cu-Nb nanocomposites under high-energy collision cascades, Applied Physics Letters, 103 (2013) 061604.
[435] A. Vattré, N. Abdolrahim, K. Kolluri, M. Demkowicz, Computational design of patterned interfaces using reduced order models, Scientific reports, 4 (2014).
[436] D. Yuryev, M. Demkowicz, Computational design of solid-state interfaces using O-lattice theory: An application to mitigating helium-induced damage, Applied Physics Letters, 105 (2014) 221601.
[437] L. Zhang, M. Demkowicz, Radiation-induced mixing between metals of low solid solubility, Acta Materialia, 76 (2014) 135-150.
[438] A. Vattré, T. Jourdan, H. Ding, M.-C. Marinica, M. Demkowicz, Non-random walk diffusion enhances the sink strength of semicoherent interfaces, Nature communications, 7 (2016).
[439] E. Fu, J. Carter, G. Swadener, A. Misra, L. Shao, H. Wang, X. Zhang, Size dependent enhancement of helium ion irradiation tolerance in sputtered Cu/V nanolaminates, Journal of nuclear materials, 385 (2009) 629-632.
[440] E. Fu, H. Wang, J. Carter, L. Shao, Y. Wang, X. Zhang, Fluence-dependent radiation damage in helium (He) ion-irradiated Cu/V multilayers, Philosophical Magazine, 93 (2013) 883-898.
[441] N. Li, J. Carter, A. Misra, L. Shao, H. Wang, X. Zhang, The influence of interfaces on the formation of bubbles in He-ion-irradiated Cu/Mo nanolayers, Philosophical Magazine Letters, 91 (2011) 18-28.

[442] J. Zhang, F. Zeng, K. Wu, Y. Wang, X. Liang, G. Liu, G. Zhang, J. Sun, Size-dependent plastic deformation characteristics in He-irradiated nanostructured Cu/Mo multilayers: Competition between dislocation-boundary and dislocation-bubble interactions, Materials Science and Engineering: A, 673 (2016) 530-540.
[443] Y. Gao, T. Yang, J. Xue, S. Yan, S. Zhou, Y. Wang, D.T. Kwok, P.K. Chu, Y. Zhang, Radiation tolerance of Cu/W multilayered nanocomposites, Journal of nuclear materials, 413 (2011) 11-15.
[444] M. Callisti, M. Karlik, T. Polcar, Bubbles formation in helium ion irradiated Cu/W multilayer nanocomposites: Effects on structure and mechanical properties, Journal of nuclear materials, 473 (2016) 18-27.
[445] C. González, R. Iglesias, Energetic analysis of He and monovacancies in Cu/W metallic interfaces, Mater Design, 91 (2016) 171-179.
[446] S. Chen, B. Liu, L. Lin, G. Jiao, Microstructural development and helium bubble formation in Cu/W (Re) nanometer multilayer films irradiated by He+ ion, Nuclear Instruments and Methods in Physics Research Section B: Beam Interactions with Materials and Atoms, 354 (2015) 244-248.
[447] Y. Chen, E. Fu, K. Yu, M. Song, Y. Liu, Y. Wang, H. Wang, X. Zhang, Enhanced radiation tolerance in immiscible Cu/Fe multilayers with coherent and incoherent layer interfaces, Journal of Materials Research, 30 (2015) 1300-1309.
[448] Q. Wei, N. Li, N. Mara, M. Nastasi, A. Misra, Suppression of irradiation hardening in nanoscale V/Ag multilayers, Acta Materialia, 59 (2011) 6331-6340.
[449] Q. Wei, Y. Wang, M. Nastasi, A. Misra, Nucleation and growth of bubbles in He ion-implanted V/Ag multilayers, Philosophical Magazine, 91 (2011) 553-573.
[450] F. Chen, X. Tang, Y. Yang, H. Huang, J. Liu, H. Li, D. Chen, Atomic simulations of Fe/Ni multilayer nanocomposites on the radiation damage resistance, Journal of nuclear materials, 468 (2016) 164-170.
[451] F. Chen, X. Tang, Y. Yang, H. Huang, D. Chen, Investigation of structural stability and magnetic properties of Fe/Ni multilayers irradiated by 300keV Fe 10+, Journal of nuclear materials, 452 (2014) 31-36.
[452] S. Shao, J. Wang, A. Misra, R.G. Hoagland, Spiral patterns of dislocations at nodes in (111) semi-coherent FCC interfaces, Scientific reports, 3 (2013).
[453] D. Reed, A review of recent theoretical developments in the understanding of the migration of helium in metals and its interaction with lattice defects, Radiation Effects, 31 (1977) 129-147.
[454] G. Thomas, Experimental studies of helium in metals, Radiation Effects, 78 (1983) 37-51.
[455] A.A. Lucas, Helium in metals, Physica B+C, 127 (1984) 225-239.
[456] D. Chen, N. Li, D. Yuryev, J. Wen, K. Baldwin, M.J. Demkowicz, Y. Wang, Imaging the in-plane distribution of helium precipitates at a Cu/V interface, Mater Res Lett, (2017) 1-8.
[457] M.J. Demkowicz, O. Anderoglu, X. Zhang, A. Misra, The influence of$\sum$ 3 twin boundaries on the formation of radiation-induced defect clusters in nanotwinned Cu, Journal of Materials Research, 26 (2011) 1666-1675.
[458] Y. Chen, Y. Liu, E. Fu, C. Sun, K. Yu, M. Song, J. Li, Y. Wang, H. Wang, X. Zhang, Unusual size-dependent strengthening mechanisms in helium ion-irradiated immiscible coherent Cu/Co nanolayers, Acta Materialia, 84 (2015) 393-404.

[459] H.L. Heinisch, F. Gao, R.J. Kurtz, The effects of interfaces on radiation damage production in layered metal composites, Journal of nuclear materials, 329 (2004) 924-928.
[460] N. Li, M. Martin, O. Anderoglu, A. Misra, L. Shao, H. Wang, X. Zhang, He ion irradiation damage in Al/Nb multilayers, Journal of applied physics, 105 (2009) 123522.
[461] M. Milosavljević, N. Stojanović, D. Peruško, B. Timotijević, D. Toprek, J. Kovač, G. Dražič, C. Jeynes, Ion irradiation induced Al–Ti interaction in nano-scaled Al/Ti multilayers, Applied Surface Science, 258 (2012) 2043-2046.
[462] D. Peruško, S. Petrović, M. Stojanović, M. Mitrić, M. Čizmović, M. Panjan, M. Milosavljević, Formation of intermetallics by ion implantation of multilatered Al/Ti nano-structures, Nuclear Instruments and Methods in Physics Research Section B: Beam Interactions with Materials and Atoms, 282 (2012) 4-7.
[463] N. Li, E. Fu, H. Wang, J. Carter, L. Shao, S. Maloy, A. Misra, X. Zhang, He ion irradiation damage in Fe/W nanolayer films, Journal of nuclear materials, 389 (2009) 233-238.
[464] M. Milosavljević, D. Toprek, M. Obradović, A. Grce, D. Peruško, G. Dražič, J. Kovač, K.P. Homewood, Ion irradiation induced solid-state amorphous reaction in Ni/Ti multilayers, Applied Surface Science, 268 (2013) 516-523.
[465] B. Liu, W. Lai, Q. Zhang, Irradiation induced amorphization in metallic multilayers and calculation of glass-forming ability from atomistic potential in the binary metal systems, Materials Science and Engineering: R: Reports, 29 (2000) 1-48.
[466] K.Y. Yu, Z. Fan, Y. Chen, M. Song, Y. Liu, H. Wang, M.A. Kirk, M. Li, X. Zhang, In situ Observation of Defect Annihilation in Kr Ion-Irradiated Bulk Fe/Amorphous-Fe2Zr Nanocomposite Alloy, Mater Res Lett, 3 (2015) 35-42.
[467] L.W. Hobbs, F.W. Clinard, S.J. Zinkle, R.C. Ewing, Radiation effects in ceramics, Journal of nuclear materials, 216 (1994) 291-321.
[468] M. Hong, F. Ren, H. Zhang, X. Xiao, B. Yang, C. Tian, D. Fu, Y. Wang, C. Jiang, Enhanced radiation tolerance in nitride multilayered nanofilms with small period-thicknesses, Applied Physics Letters, 101 (2012) 153117.
[469] M. Hong, F. Ren, Y. Wang, H. Zhang, X. Xiao, D. Fu, B. Yang, C. Jiang, Size-dependent radiation tolerance and corrosion resistance in ion irradiated CrN/AlTiN nanofilms, Nuclear Instruments and Methods in Physics Research Section B: Beam Interactions with Materials and Atoms, 342 (2015) 137-143.
[470] L. Jiao, A. Chen, M. Myers, M. General, L. Shao, X. Zhang, H. Wang, Enhanced ion irradiation tolerance properties in TiN/MgO nanolayer films, Journal of nuclear materials, 434 (2013) 217-222.
[471] I. Kim, L. Jiao, F. Khatkhatay, M. Martin, J. Lee, L. Shao, X. Zhang, J. Swadener, Y. Wang, J. Gan, Size-dependent radiation tolerance in ion irradiated TiN/AlN nanolayer films, Journal of nuclear materials, 441 (2013) 47-53.
[472] K.E. Sickafus, R.W. Grimes, J.A. Valdez, A. Cleave, M. Tang, M. Ishimaru, S.M. Corish, C.R. Stanek, B.P. Uberuaga, Radiation-induced amorphization resistance and radiation tolerance in structurally related oxides, Nature materials, 6 (2007) 217-223.
[473] Z. Bi, B. Uberuaga, L. Vernon, E. Fu, Y. Wang, N. Li, H. Wang, A. Misra, Q. Jia, Radiation damage in heteroepitaxial BaTiO3 thin films on SrTiO3 under Ne ion irradiation, Journal of applied physics, 113 (2013) 023513.
[474] P.P. Dholabhai, J.A. Aguiar, A. Misra, B.P. Uberuaga, Defect interactions with stepped CeO2/SrTiO3 interfaces: Implications for radiation damage evolution and fast ion conduction, The Journal of chemical physics, 140 (2014) 194701.

[475] S.J. Zinkle, V.A. Skuratov, D.T. Hoelzer, On the conflicting roles of ionizing radiation in ceramics, Nucl Instrum Meth B, 191 (2002) 758-766.
[476] M. Milosavljević, D. Peruško, V. Milinović, Z. Stojanović, A. Zalar, J. Kovač, C. Jeynes, Ion irradiation stability of multilayered AlN/TiN nanocomposites, Journal of Physics D: Applied Physics, 43 (2010) 065302.
[477] M. Milosavljević, M. Obradović, A. Grce, D. Peruško, D. Pjević, J. Kovač, G. Dražič, C. Jeynes, High dose ion irradiation effects on immiscible AlN/TiN nano-scaled multilayers, Thin Solid Films, 544 (2013) 562-566.
[478] M. Milosavljević, A. Grce, D. Peruško, M. Stojanović, J. Kovač, G. Dražič, A.Y. Didyk, V.A. Skuratov, A comparison of Ar ion implantation and swift heavy Xe ion irradiation effects on immiscible AlN/TiN multilayered nanostructures, Materials Chemistry and Physics, 133 (2012) 884-892.
[479] B. Pedro Uberuaga, E. Martinez, Z. Bi, M. Zhuo, Q. Jia, M. Nastasi, A. Misra, A. Caro, Defect distributions and transport in nanocomposites: A theoretical perspective, Mater Res Lett, 1 (2013) 193-199.
[480] M. Zhuo, E. Fu, L. Yan, Y. Wang, Y. Zhang, R. Dickerson, B. Uberuaga, A. Misra, M. Nastasi, Q. Jia, Interface-enhanced defect absorption between epitaxial anatase TiO 2 film and single crystal SrTiO 3, Scripta Materialia, 65 (2011) 807-810.
[481] M. Zhuo, B. Uberuaga, L. Yan, E. Fu, R. Dickerson, Y. Wang, A. Misra, M. Nastasi, Q. Jia, Radiation damage at the coherent anatase TiO2/SrTiO3 interface under Ne ion irradiation, Journal of nuclear materials, 429 (2012) 177-184.
[482] T.C. Kaspar, M.E. Bowden, C.M. Wang, V. Shutthanandan, N.R. Overman, R.M. Van Ginhoven, B.D. Wirth, R.J. Kurtz, Epitaxial Fe/Y 2 O 3 interfaces as a model system for oxide-dispersion-strengthened ferritic alloys, Journal of nuclear materials, 457 (2015) 352-361.
[483] Y. Chen, L. Jiao, C. Sun, M. Song, K.Y. Yu, Y. Liu, M. Kirk, M. Li, H. Wang, X. Zhang, In situ studies of radiation induced crystallization in Fe/a-Y2O3 nanolayers, Journal of Nuclear Materials, 452 (2014) 321-327.
[484] D. Porter, F. Garner, Irradiation creep and embrittlement behavior of AISI 316 stainless steel at very high neutron fluences, Journal of Nuclear Materials, 159 (1988) 114-121.
[485] K. Murty, I. Charit, Structural materials for Gen-IV nuclear reactors: Challenges and opportunities, Journal of Nuclear Materials, 383 (2008) 189-195.
[486] J. Zhang, Y. Liu, J. Chen, Y. Chen, G. Liu, X. Zhang, J. Sun, Mechanical properties of crystalline Cu/Zr and crystal–amorphous Cu/Cu–Zr multilayers, Materials Science and Engineering: A, 552 (2012) 392-398.
[487] J. Zhang, Y. Wang, X. Liang, F. Zeng, G. Liu, J. Sun, Size-dependent He-irradiated tolerance and plastic deformation of crystalline/amorphous Cu/Cu–Zr nanolaminates, Acta Materialia, 92 (2015) 140-151.
[488] J. Zhang, S. Lei, Y. Liu, J. Niu, Y. Chen, G. Liu, X. Zhang, J. Sun, Length scale-dependent deformation behavior of nanolayered Cu/Zr micropillars, Acta Materialia, 60 (2012) 1610-1622.
[489] M.D. Uchic, D.M. Dimiduk, J.N. Florando, W.D. Nix, Sample dimensions influence strength and crystal plasticity, Science, 305 (2004) 986-989.
[490] J.R. Greer, W.C. Oliver, W.D. Nix, Size dependence of mechanical properties of gold at the micron scale in the absence of strain gradients, Acta Materialia, 53 (2005) 1821-1830.

[491] M.D. Uchic, P.A. Shade, D.M. Dimiduk, Plasticity of micrometer-scale single crystals in compression, Annual Review of Materials Research, 39 (2009) 361-386.
[492] D. Kiener, P. Hosemann, S. Maloy, A. Minor, In situ nano-compression testing of irradiated copper, Nature materials, 10 (2011) 608.
[493] F. Kroupa, P. Hirsch, Elastic interaction between prismatic dislocation loops and straight dislocations, Discussions of the Faraday Society, 38 (1964) 49-55.
[494] J. Friedel, Dislocations, Pergamon, New York, 1964.
[495] S.J. Zinkle, Y. Matsukawa, Observation and analysis of defect cluster production and interactions with dislocations, Journal of nuclear materials, 329 (2004) 88-96.
[496] U. Kocks, The theory of an obstacle-controlled yield strength—report after an international workshop, Materials Science and Engineering, 27 (1977) 291-298.
[497] D.J. Bacon, U.F. Kocks, R.O. Scattergood, The effect of dislocation self-interaction on the orowan stress, Philosophical Magazine, 28 (1973) 1241-1263.
[498] N. Hashimoto, T. Byun, K. Farrell, S. Zinkle, Deformation microstructure of neutron-irradiated pure polycrystalline metals, Journal of nuclear materials, 329 (2004) 947-952.
[499] J. Wang, K. Kang, R. Zhang, S. Zheng, I. Beyerlein, N. Mara, Structure and property of interfaces in ARB Cu/Nb laminated composites, Jom, 64 (2012) 1208-1217.
[500] F. Chen, X. Tang, H. Huang, J. Liu, H. Li, Y. Qiu, D. Chen, Surface damage and mechanical properties degradation of Cr/W multilayer films irradiated by Xe 20+, Applied Surface Science, 357 (2015) 1225-1230.
[501] M. Callisti, S. Lozano-Perez, T. Polcar, Structural and mechanical properties of γ-irradiated Zr/Nb multilayer nanocomposites, Mater Lett, 163 (2016) 138-141.
[502] M. Milosavljević, V. Milinović, D. Peruško, A. Grce, M. Stojanović, D. Pjević, M. Mitrić, J. Kovač, K. Homewood, Stability of nano-scaled Ta/Ti multilayers upon argon ion irradiation, Nuclear Instruments and Methods in Physics Research Section B: Beam Interactions with Materials and Atoms, 269 (2011) 2090-2097.
[503] M. Gerboth, W. Setyawan, C.H. Henager, Displacement threshold energy and recovery in an Al–Ti nanolayered system with intrinsic point defect partitioning, Comp Mater Sci, 85 (2014) 269-279.
[504] W. Setyawan, M. Gerboth, B. Yao, C.H. Henager, A. Devaraj, V.R. Vemuri, S. Thevuthasan, V. Shutthanandan, Asymmetry of radiation damage properties in Al–Ti nanolayers, Journal of nuclear materials, 445 (2014) 261-271.
[505] Q. Su, L. Price, L. Shao, M. Nastasi, High temperature radiation responses of amorphous SiOC/crystalline Fe nanocomposite, Journal of Nuclear Materials, 479 (2016) 411-417.
[506] Q. Su, L. Price, L. Shao, M. Nastasi, Temperature-Dependent Helium Ion-Beam Mixing in an Amorphous SiOC/Crystalline Fe Composite, Metals, 6 (2016) 261.
[507] Q. Su, L. Price, L. Shao, M. Nastasi, Dose dependence of radiation damage in nano-structured amorphous SiOC/crystalline Fe composite, Mater Res Lett, 4 (2016) 48-54.
[508] Q. Su, F. Wang, B. Cui, M.A. Kirk, M. Nastasi, Temperature-dependent ion-beam mixing in amorphous SiOC/crystalline Fe composite, Mater Res Lett, (2016) 1-6.
[509] Q. Su, B. Cui, M.A. Kirk, M. Nastasi, In-situ observation of radiation damage in nano-structured amorphous SiOC/crystalline Fe composite, Scripta Materialia, 113 (2016) 79-83.
[510] X. Liang, J. Zhang, Y. Wang, S. Wu, F. Zeng, K. Wu, G. Liu, G. Zhang, J. Sun, Tuning the size-dependent He-irradiated tolerance and strengthening behavior of

crystalline/amorphous Cu/Ta nanostructured multilayers, Materials Science and Engineering: A, 672 (2016) 153-160.
[511] M.L. Lescoat, J. Ribis, Y. Chen, E.A. Marquis, E. Bordas, P. Trocellier, Y. Serruys, A. Gentils, O. Kaitasov, Y. de Carlan, A. Legris, Radiation-induced Ostwald ripening in oxide dispersion strengthened ferritic steels irradiated at high ion dose, Acta Materialia, 78 (2014) 328-340.
[512] O. Anderoglu, M. Zhou, J. Zhang, Y. Wang, S. Maloy, J. Baldwin, A. Misra, He+ ion irradiation response of Fe–TiO 2 multilayers, Journal of nuclear materials, 435 (2013) 96-101.
[513] Y. Xu, S.K. Yadav, J.A. Aguiar, O. Anderoglu, J.K. Baldwin, Y. Wang, A. Misra, H. Luo, B.P. Uberuaga, N. Li, Irradiation-induced formation of a spinel phase at the FeCr/MgO interface, Acta Materialia, 93 (2015) 87-94.
[514] Y. Xu, J. Aguiar, S.K. Yadav, O. Anderoglu, J. Baldwin, Y. Wang, J.A. Valdez, A. Misra, H. Luo, B.P. Uberuaga, Solute redistribution and phase stability at FeCr/TiO 2− x interfaces under ion irradiation, Acta Materialia, 89 (2015) 364-373.
[515] N. Li, S. Yadav, Y. Xu, J. Aguiar, J. Baldwin, Y. Wang, H. Luo, A. Misra, B. Uberuaga, Cr incorporated phase transformation in Y2O3 under ion irradiation, Scientific Reports, 7 (2017).
[516] H. Wang, Y. Gao, E. Fu, T. Yang, J. Xue, S. Yan, P.K. Chu, Y. Wang, Irradiation effects on multilayered W/ZrO 2 film under 4MeV Au ions, Journal of nuclear materials, 455 (2014) 86-90.
[517] E. Njoroge, C. Theron, J. Malherbe, N. van der Berg, T. Hlatshwayo, V. Skuratov, Surface and interface modification of Zr/SiC interface by swift heavy ion irradiation, Nuclear Instruments and Methods in Physics Research Section B: Beam Interactions with Materials and Atoms, 354 (2015) 249-254.
[518] M. Bugnet, T. Cabioc'h, V. Mauchamp, P. Guérin, M. Marteau, M. Jaouen, Stability of the nitrogen-deficient Ti2AlN x MAX phase in Ar2+-irradiated (Ti, Al) N/Ti2AlN x multilayers, J Mater Sci, 45 (2010) 5547-5552.
[519] L. Lu, Y. Shen, X. Chen, L. Qian, K. Lu, Ultrahigh strength and high electrical conductivity in copper, Science, 304 (2004) 422-426.
[520] X. Zhang, A. Misra, H. Wang, M. Nastasi, J.D. Embury, T.E. Mitchell, R.G. Hoagland, J.P. Hirth, Nanoscale-twinning-induced strengthening in austenitic stainless steel thin films, Applied Physics Letters, 84 (2004) 1096-1098.
[521] O. Anderoglu, A. Misra, H. Wang, F. Ronning, M.F. Hundley, X. Zhang, Epitaxial nanotwinned Cu films with high strength and high conductivity, Applied Physics Letters, 93 (2008) 083108.
[522] X. Zhang, H. Wang, X.H. Chen, L. Lu, K. Lu, R.G. Hoagland, A. Misra, High-strength sputter-deposited Cu foils with preferred orientation of nanoscale growth twins, Applied Physics Letters, 88 (2006) 173116-173116.
[523] S. Xue, Z. Fan, Y. Chen, J. Li, H. Wang, X. Zhang, The formation mechanisms of growth twins in polycrystalline Al with high stacking fault energy, Acta Materialia, 101 (2015) 62-70.
[524] X. Zhao, B. Xiao, A.J. Fletcher, K.M. Thomas, D. Bradshaw, M.J. Rosseinsky, Hysteretic adsorption and desorption of hydrogen by nanoporous metal-organic frameworks, Science, 306 (2004) 1012-1015.

[525] L. Lu, Z.S. You, K. Lu, Work hardening of polycrystalline Cu with nanoscale twins, Scripta Materialia, 66 (2012) 837-842.
[526] O. Anderoglu, A. Misra, J. Wang, R.G. Hoagland, J.P. Hirth, X. Zhang, Plastic flow stability of nanotwinned Cu foils, International Journal of Plasticity, 26 (2010) 875-886.
[527] D. Bufford, H. Wang, X. Zhang, High strength, epitaxial nanotwinned Ag films, Acta Materialia, 59 (2011) 93-101.
[528] R.T. Ott, J. Geng, M.F. Besser, M.J. Kramer, Y.M. Wang, E.S. Park, R. LeSar, A.H. King, Optimization of strength and ductility in nanotwinned ultra-fine grained Ag: Twin density and grain orientations, Acta Materialia, 96 (2015) 378-389.
[529] Z.X. Wu, Y.W. Zhang, D.J. Srolovitz, Dislocation-twin interaction mechanisms for ultrahigh strength and ductility in nanotwinned metals, Acta Materialia, 57 (2009) 4508-4518.
[530] L.L. Zhu, H.H. Ruan, X.Y. Li, M. Dao, H.J. Gao, J. Lu, Modeling grain size dependent optimal twin spacing for achieving ultimate high strength and related high ductility in nanotwinned metals, Acta Materialia, 59 (2011) 5544-5557.
[531] T.A. Furnish, A.M. Hodge, On the mechanical performance and deformation of nanotwinned Ag, Apl Mater, 2 (2014).
[532] J. Li, J.Y. Zhang, G. Liu, J. Sun, New insight into the stable grain size of nanotwinned Ni in steady-state creep: Effect of the ratio of effective-to-internal stress, International Journal of Plasticity, 85 (2016) 172-189.
[533] Y. Liu, N. Li, D. Bufford, J.H. Lee, J. Wang, H. Wang, X. Zhang, In Situ Nanoindentation Studies on Detwinning and Work Hardening in Nanotwinned Monolithic Metals, Jom, 68 (2016) 127-135.
[534] A.J. Cao, Y.G. Wei, Molecular dynamics simulation of plastic deformation of nanotwinned copper, Journal of Applied Physics, 102 (2007).
[535] T. Sinha, Y. Kulkarni, Alternating brittle and ductile response of coherent twin boundaries in nanotwinned metals, Journal of Applied Physics, 116 (2014).
[536] D. Bufford, Y. Liu, J. Wang, H. Wang, X. Zhang, In situ nanoindentation study on plasticity and work hardening in aluminium with incoherent twin boundaries, Nature Communications, 5 (2014).
[537] M.J. Makin, A.D. Whapham, F.J. Minter, Dislocation Loops and Hardening in Neutron Irradiated Copper, Philosophical Magazine, 6 (1961) 465-&.
[538] D. Norris, The growth of voids in nickel in a high-voltage electron microscope, Philosophical Magazine, 23 (1971) 135-152.
[539] R.J. Jahn, A.H. King, Vacancy Deposition during Diffusion-Induced Grain-Boundary Migration, Philos Mag A, 54 (1986) L3-L7.
[540] A. King, D. Smith, Stress-induced absorption and emission of point defects by grain boundaries, Metal Science, 14 (1980) 57-63.
[541] A.H. King, D.A. Smith, On the Mechanisms of Point-Defect Absorption by Grain and Twin Boundaries, Philos Mag A, 42 (1980) 495-512.
[542] R.L. Segall, Coherent Annealing Twin Boundaries as Vacancy Sinks, Acta Metallurgica, 12 (1964) 117-&.
[543] J. Gao, Z.J. Liu, F.R. Wan, Limited Effect of Twin Boundaries on Radiation Damage, Acta Metall Sin-Engl, 29 (2016) 72-78.
[544] X.Z. Xiao, D.K. Song, H.J. Chu, J.M. Xue, H.L. Duan, Mechanical behaviors of irradiated FCC polycrystals with nanotwins, International Journal of Plasticity, 74 (2015) 110-126.

[545] M. Niewczas, R. Hoagland, Molecular dynamic studies of the interaction of a/6⟨ 112⟩ Shockley dislocations with stacking fault tetrahedra in copper. Part II: Intersection of stacking fault tetrahedra by moving twin boundaries, Philosophical Magazine, 89 (2009) 727-746.
[546] J. Wang, H.C. Huang, Novel deformation mechanism of twinned nanowires, Applied Physics Letters, 88 (2006) 203112.
[547] Z.H. Jin, P. Gumbsch, K. Albe, E. Ma, K. Lu, H. Gleiter, H. Hahn, Interactions between non-screw lattice dislocations and coherent twin boundaries in face-centered cubic metals, Acta Materialia, 56 (2008) 1126-1135.
[548] T. Zhu, J. Li, A. Samanta, H.G. Kim, S. Suresh, Interfacial plasticity governs strain rate sensitivity and ductility in nanostructured metals, Proc Natl Acad Sci U S A, 104 (2007) 3031-3036.
[549] J. Wang, O. Anderoglu, J. Hirth, A. Misra, X. Zhang, Dislocation structures of S3 {112} twin boundaries in face centered cubic metals, Appl. Phys. Lett, 95 (2009) 021908.
[550] A.M. Hodge, T.A. Furnish, C.J. Shute, Y. Liao, X. Huang, C.S. Hong, Y.T. Zhu, T.W. Barbee, J.R. Weertman, Twin stability in highly nanotwinned Cu under compression, torsion and tension, Scripta Materialia, 66 (2012) 872-877.
[551] Y.M. Wang, F. Sansoz, T. LaGrange, R.T. Ott, J. Marian, T.W. Barbee Jr, A.V. Hamza, Defective twin boundaries in nanotwinned metals, Nat Mater, 12 (2013) 697-702.
[552] N. Li, J. Wang, A. Misra, X. Zhang, J.Y. Huang, J.P. Hirth, Twinning dislocation multiplication at a coherent twin boundary, Acta Materialia, 59 (2011) 5989-5996.
[553] D.K. Chen, Y. Kulkarni, Elucidating the kinetics of twin boundaries from thermal fluctuations, Mrs Commun, 3 (2013) 241-244.
[554] D.K. Chen, Y. Kulkarni, Entropic interaction between fluctuating twin boundaries, J Mech Phys Solids, 84 (2015) 59-71.
[555] S.Y. Jiao, Y. Kulkarni, Molecular dynamics study of creep mechanisms in nanotwinned metals, Comp Mater Sci, 110 (2015) 254-260.
[556] G.J. Tucker, S.M. Foiles, Quantifying the influence of twin boundaries on the deformation of nanocrystalline copper using atomistic simulations, International Journal of Plasticity, 65 (2015) 191-205.
[557] S.B. Zhang, Y. Wang, Molecular dynamics simulation of tension-compression asymmetry in plasticity of fivefold twinned Ag nanopillars, Phys Lett A, 379 (2015) 603-606.
[558] X. Zhao, C. Lu, A.K. Tieu, L.Q. Pei, L. Zhang, L.H. Su, L.H. Zhan, Deformation mechanisms in nanotwinned copper by molecular dynamics simulation, Mat Sci Eng a-Struct, 687 (2017) 343-351.
[559] X.L. Zhou, X.Y. Li, C.Q. Chen, Atomistic mechanisms of fatigue in nanotwinned metals, Acta Materialia, 99 (2015) 77-86.
[560] L.L. Zhu, C.S. Wen, C.Y. Gao, X. Guo, J. Lu, A study of dynamic plasticity in austenite stainless steels with a gradient distribution of nanoscale twins, Scripta Materialia, 133 (2017) 49-53.
[561] J. Wang, A. Misra, J.P. Hirth, Shear response of Sigma 3{112} twin boundaries in face-centered-cubic metals, Physical Review B, 83 (2011) 064106.
[562] Y. Chen, H. Wang, M.A. Kirk, M. Li, J. Wang, X. Zhang, Radiation induced detwinning in nanotwinned Cu, Scripta Materialia, 130 (2017) 37-41.

[563] J. Embury, R. Nicholson, The nucleation of precipitates: the system Al-Zn-Mg, Acta Metallurgica, 13 (1965) 403-417.
[564] J. Burke, D. Stuckey, Dislocation loop-free zones around grain boundaries in quenched aluminium and aluminium alloys, Philosophical Magazine, 31 (1975) 1063-1080.
[565] Y. Chen, X. Zhang, J. Wang, Radiation Enhanced Absorption of Frank Loops by Nanovoids in Cu, Jom, 68 (2016) 235-241.
[566] J. Li, K.Y. Yu, Y. Chen, M. Song, H. Wang, M.A. Kirk, M. Li, X. Zhang, In situ study of defect migration kinetics and self-healing of twin boundaries in heavy ion irradiated nanotwinned metals, Nano Lett, 15 (2015) 2922-2927.
[567] N. Li, J. Wang, J.Y. Huang, A. Misra, X. Zhang, Influence of slip transmission on the migration of incoherent twin boundaries in epitaxial nanotwinned Cu, Scripta Materialia, 64 (2011) 149-152.
[568] Y. Liu, J. Jian, Y. Chen, H. Wang, X. Zhang, Plasticity and ultra-low stress induced twin boundary migration in nanotwinned Cu by in situ nanoindentation studies, Applied Physics Letters, 104 (2014) 231910.
[569] N. Li, J. Wang, Y.Q. Wang, Y. Serruys, M. Nastasi, A. Misra, Incoherent twin boundary migration induced by ion irradiation in Cu, Journal of Applied Physics, 113 (2013) 023508.
[570] K.Y. Yu, D. Bufford, F. Khatkhatay, H. Wang, M.A. Kirk, X. Zhang, In situ studies of irradiation-induced twin boundary migration in nanotwinned Ag, Scripta Materialia, 69 (2013) 385-388.
[571] C. Fan, J. Li, Z. Fan, H. Wang, X. Zhang, In Situ Studies on the Irradiation-Induced Twin Boundary-Defect Interactions in Cu, Metallurgical and Materials Transactions A, (2017).
[572] L. Xu, D. Xu, K.N. Tu, Y. Cai, N. Wang, P. Dixit, J.H.L. Pang, J.M. Miao, Structure and migration of (112) step on (111) twin boundaries in nanocrystalline copper, Journal of Applied Physics, 104 (2008) 113717.
[573] B.N. Singh, A. Horsewell, P. Toft, D.J. Edwards, Temperature and Dose Dependencies of Microstructure and Hardness of Neutron-Irradiated Ofhc Copper, Journal of Nuclear Materials, 224 (1995) 131-140.
[574] M. Kiritani, Story of stacking fault tetrahedra, Materials Chemistry and Physics, 50 (1997) 133-138.
[575] S. Zinkle, L. Seitzman, W. Wolfer, I. Energy calculations for pure metals, Philosophical Magazine A, 55 (1987) 111-125.
[576] G.S. Was, Fundamentals of radiation materials science: metals and alloys, Springer Science & Business Media, 2007.
[577] H.J. Lee, J.H. Shim, B.D. Wirth, Molecular dynamics simulation of screw dislocation interaction with stacking fault tetrahedron in face-centered cubic Cu, Journal of Materials Research, 22 (2007) 2758-2769.
[578] H.J. Lee, B.D. Wirth, Molecular dynamics simulation of the interaction between a mixed dislocation and a stacking fault tetrahedron, Philosophical Magazine, 89 (2009) 821-841.
[579] J. Marian, E. Martinez, H.J. Lee, B.D. Wirth, Micro/meso-scale computational study of dislocation-stacking-fault tetrahedron interactions in copper, Journal of Materials Research, 24 (2009) 3628-3635.
[580] L. Saintoyant, H.J. Lee, B.D. Wirth, Molecular dynamics study of the interactions between dislocation and imperfect stacking fault tetrahedron in Cu, Journal of Nuclear Materials, 361 (2007) 206-217.

[581] D. Rodney, Molecular dynamics simulation of screw dislocations interacting with interstitial frank loops in a model FCC crystal, Acta Materialia, 52 (2004) 607-614.
[582] Y. Chen, J. Li, K.Y. Yu, H. Wang, M.A. Kirk, M. Li, X. Zhang, In situ studies on radiation tolerance of nanotwinned Cu, Acta Materialia, 111 (2016) 148-156.
[583] M.R. Sørensen, Y. Mishin, A.F. Voter, Diffusion mechanisms in Cu grain boundaries, Physical Review B, 62 (2000) 3658.
[584] J. Li, Y. Chen, H. Wang, X. Zhang, In Situ Studies on Twin-Thickness-Dependent Distribution of Defect Clusters in Heavy Ion-Irradiated Nanotwinned Ag, Metallurgical and Materials Transactions A, 48 (2017) 1466-1473.
[585] Y.C. C. Fan, Jin Li, Jie Ding, H. Wang, X. Zhang, Defect evolution in heavy ion irradiated nanotwinned Cu with nanovoids, Journal of Nuclear Materials, In press (2017).
[586] S.H. Joo, S.J. Choi, I. Oh, J. Kwak, Z. Liu, O. Terasaki, R. Ryoo, Ordered nanoporous arrays of carbon supporting high dispersions of platinum nanoparticles, Nature, 412 (2001) 169-172.
[587] M.E. Davis, Ordered porous materials for emerging applications, Nature, 417 (2002) 813-821.
[588] B.J. Scott, G. Wirnsberger, G.D. Stucky, Mesoporous and mesostructured materials for optical applications, Chem Mater, 13 (2001) 3140-3150.
[589] S. Jun, S.H. Joo, R. Ryoo, M. Kruk, M. Jaroniec, Z. Liu, T. Ohsuna, O. Terasaki, Synthesis of new, nanoporous carbon with hexagonally ordered mesostructure, J Am Chem Soc, 122 (2000) 10712-10713.
[590] R. Vogel, P. Hoyer, H. Weller, Quantum-Sized Pbs, Cds, Ag2s, Sb2s3, and Bi2s3 Particles as Sensitizers for Various Nanoporous Wide-Bandgap Semiconductors, J Phys Chem-Us, 98 (1994) 3183-3188.
[591] X. Lang, A. Hirata, T. Fujita, M. Chen, Nanoporous metal/oxide hybrid electrodes for electrochemical supercapacitors, Nat Nanotechnol, 6 (2011) 232-236.
[592] R.E. Morris, P.S. Wheatley, Gas storage in nanoporous materials, Angew Chem Int Ed Engl, 47 (2008) 4966-4981.
[593] S. Jeon, J.U. Park, R. Cirelli, S. Yang, C.E. Heitzman, P.V. Braun, P.J. Kenis, J.A. Rogers, Fabricating complex three-dimensional nanostructures with high-resolution conformable phase masks, Proc Natl Acad Sci U S A, 101 (2004) 12428-12433.
[594] T. Fujita, P. Guan, K. McKenna, X. Lang, A. Hirata, L. Zhang, T. Tokunaga, S. Arai, Y. Yamamoto, N. Tanaka, Y. Ishikawa, N. Asao, Y. Yamamoto, J. Erlebacher, M. Chen, Atomic origins of the high catalytic activity of nanoporous gold, Nat Mater, 11 (2012) 775-780.
[595] J. Biener, A.M. Hodge, J.R. Hayes, C.A. Volkert, L.A. Zepeda-Ruiz, A.V. Hamza, F.F. Abraham, Size effects on the mechanical behavior of nanoporous Au, Nano Lett, 6 (2006) 2379-2382.
[596] A. Asthana, K. Momeni, A. Prasad, Y.K. Yap, R.S. Yassar, In situ observation of size-scale effects on the mechanical properties of ZnO nanowires, Nanotechnology, 22 (2011) 265712.
[597] C. Sun, B.P. Uberuaga, L. Yin, J. Li, Y. Chen, M.A. Kirk, M. Li, S.A. Maloy, H. Wang, C. Yu, X. Zhang, Resilient ZnO nanowires in an irradiation environment: An in situ study, Acta Materialia, 95 (2015) 156-163.
[598] D.C. Bufford, K. Hattar, Physical response of gold nanoparticles to single self-ion bombardment, Journal of Materials Research, 29 (2014) 2387-2397.

[599] C. Sun, D. Bufford, Y. Chen, M.A. Kirk, Y.Q. Wang, M. Li, H. Wang, S.A. Maloy, X. Zhang, In situ study of defect migration kinetics in nanoporous Ag with enhanced radiation tolerance, Sci Rep, 4 (2014) 3737.
[600] J. Li, C. Fan, Q. Li, H. Wang, X. Zhang, In situ studies on irradiation resistance of nanoporous Au through temperature-jump tests, Acta Materialia, In press (2017).
[601] X.F. Zhu, J.S. Williams, M.J. Conway, M.C. Ridgway, F. Fortuna, M.O. Ruault, H. Bernas, Direct observation of irradiation-induced nanocavity shrinkage in Si, Applied Physics Letters, 79 (2001) 3416-3418.
[602] S.J. Wu, F. Cao, H. Zheng, H.P. Sheng, C. Liu, Y. Liu, D.S. Zhao, J.B. Wang, Fabrication of faceted nanopores in magnesium, Applied Physics Letters, 103 (2013) 243101.
[603] W. Xu, Y. Zhang, G. Cheng, W. Jian, P.C. Millett, C.C. Koch, S.N. Mathaudhu, Y. Zhu, In-situ atomic-scale observation of irradiation-induced void formation, Nat Commun, 4 (2013) 2288.
[604] E.M. Bringa, J.D. Monk, A. Caro, A. Misra, L. Zepeda-Ruiz, M. Duchaineau, F. Abraham, M. Nastasi, S.T. Picraux, Y.Q. Wang, D. Farkas, Are nanoporous materials radiation resistant?, Nano Lett, 12 (2012) 3351-3355.
[605] Y.C. Jin Li, H. Wang, X. Zhang, In situ study on enhanced heavy ion irradiation tolerance of porous Mg, Scripta Materialia, In press (2017).
[606] C.G. Zhang, Y.G. Li, W.H. Zhou, L. Hu, Z. Zeng, Anti-radiation mechanisms in nanoporous gold studied via molecular dynamics simulations, Journal of Nuclear Materials, 466 (2015) 328-333.
[607] A. Misra, M.J. Demkowicz, X. Zhang, R.G. Hoagland, The radiation damage tolerance of ultra-high strength nanolayered composites, Jom, 59 (2007) 62-65.
[608] W.Q. Liu, P.H. Chen, R.Z. Qiu, M. Khan, J. Liu, M.D. Hou, J.L. Duan, A molecular dynamics simulation study of irradiation induced defects in gold nanowire, Nucl Instrum Meth B, 405 (2017) 22-30.
[609] T.T. Jarvi, K. Nordlund, Sputtering of freestanding metal nanocrystals, Nucl Instrum Meth B, 272 (2012) 66-69.
[610] R.C. Birtcher, S.E. Donnelly, S. Schlutig, Nanoparticle ejection from gold during ion irradiation, Nucl Instrum Meth B, 215 (2004) 69-75.
[611] R.C. Birtcher, S.E. Donnelly, Plastic Flow Induced by Single Ion Impacts on Gold, Phys Rev Lett, 77 (1996) 4374-4377.
[612] M. Ghaly, R.S. Averback, Effect of viscous flow on ion damage near solid surfaces, Phys Rev Lett, 72 (1994) 364-367.
[613] R. Kissel, H.M. Urbassek, Sputtering from spherical Au clusters by energetic atom bombardment, Nucl Instrum Meth B, 180 (2001) 293-298.
[614] A. Berthelot, S. Hemon, F. Gourbilleau, C. Dufour, E. Dooryhee, E. Paumier, Nanometric size effects on irradiation of tin oxide powder, Nucl Instrum Meth B, 146 (1998) 437-442.
[615] D. Bufford, S.H. Pratt, T.J. Boyle, K. Hattar, In situ TEM ion irradiation and implantation effects on Au nanoparticle morphologies, Chem Commun (Camb), 50 (2014) 7593-7596.
[616] G. Greaves, J.A. Hinks, P. Busby, N.J. Mellors, A. Ilinov, A. Kuronen, K. Nordlund, S.E. Donnelly, Enhanced sputtering yields from single-ion impacts on gold nanorods, Phys Rev Lett, 111 (2013) 065504.

[617] A. Ilinov, A. Kuronen, K. Nordlund, G. Greaves, J. Hinks, P. Busby, N. Mellors, S. Donnelly, Sputtering yields exceeding 1000 by 80keV Xe irradiation of Au nanorods, Nuclear Instruments and Methods in Physics Research Section B: Beam Interactions with Materials and Atoms, 341 (2014) 17-21.
[618] I. Baranov, S. Kirillov, A. Novikov, V. Obnorskii, M. Toulemonde, K. Wien, S. Yarmiychuk, V. Borodin, A. Volkov, Desorption of gold nanoclusters (2–150nm) by 1GeV Pb ions, Nuclear Instruments and Methods in Physics Research Section B: Beam Interactions with Materials and Atoms, 230 (2005) 495-501.
[619] T.T. Jarvi, A. Kuronen, K. Nordlund, K. Albe, Damage production in nanoparticles under light ion irradiation, Physical Review B, 80 (2009).
[620] R. Kissel, H.M. Urbassek, Sputtering of a Au surface covered with large spherical clusters, Int J Mass Spectrom, 208 (2001) 29-35.
[621] V.V. Uglov, G.E. Remnev, N.T. Kvasov, I.V. Safronov, V.I. Shymanski, Radiation stability of iron nanoparticles irradiated with accelerated iron ions, Nucl Instrum Meth B, 354 (2015) 259-263.
[622] O. Dmitrieva, B. Rellinghaus, J. Kastner, M.O. Liedke, J. Fassbender, Ion beam induced destabilization of icosahedral structures in gas phase prepared FePt nanoparticles, Journal of Applied Physics, 97 (2005).
[623] U. Wiedwald, A. Klimmer, B. Kern, L. Han, H.-G. Boyen, P. Ziemann, K. Fauth, Lowering of the L10 ordering temperature of FePt nanoparticles by He+ ion irradiation, Applied Physics Letters, 90 (2007) 62508-62508.
[624] T.T. Jarvi, A. Kuronen, K. Nordlund, K. Albe, Structural modification of a multiply twinned nanoparticle by ion irradiation: A molecular dynamics study, Journal of Applied Physics, 102 (2007) 124304.
[625] T.T. Jarvi, D. Pohl, K. Albe, B. Rellinghaus, L. Schultz, J. Fassbender, A. Kuronen, K. Nordlund, From multiply twinned to fcc nanoparticles via irradiation-induced transient amorphization, Epl-Europhys Lett, 85 (2009) 26001.
[626] N.N. Ledentsov, V.M. Ustinov, V.A. Shchukin, P.S. Kop'ev, Z.I. Alferov, D. Bimberg, Quantum dot heterostructures: fabrication, properties, lasers (Review), Semiconductors+, 32 (1998) 343-365.
[627] Y.K. Mishra, F. Singh, D.K. Avasthi, J.C. Pivin, D. Malinovska, E. Pippel, Synthesis of elongated Au nanoparticles in silica matrix by ion irradiation, Applied Physics Letters, 91 (2007) 063103.
[628] A. Meldrum, R.F. Haglund, L.A. Boatner, C.W. White, Nanocomposite materials formed by ion implantation, Adv Mater, 13 (2001) 1431-+.
[629] T.R. Allen, J. Gan, J.I. Cole, M.K. Miller, J.T. Busby, S. Shutthanandan, S. Thevuthasan, Radiation response of a 9 chromium oxide dispersion strengthened steel to heavy ion irradiation, Journal of Nuclear Materials, 375 (2008) 26-37.
[630] N.A. Bailey, E. Stergar, M. Toloczko, P. Hosemann, Atom probe tomography analysis of high dose MA957 at selected irradiation temperatures, Journal of Nuclear Materials, 459 (2015) 225-234.
[631] B.W. Baker, L.N. Brewer, Joining of Oxide Dispersion Strengthened Steels for Advanced Reactors, Jom, 66 (2014) 2442-2457.
[632] D. Bhattacharyya, P. Dickerson, G.R. Odette, S.A. Maloy, A. Misra, M.A. Nastasi, On the structure and chemistry of complex oxide nanofeatures in nanostructured ferritic alloy U14YWT, Philosophical Magazine, 92 (2012) 2089-2107.

[633] D. Brimbal, L. Beck, O. Troeber, E. Gaganidze, P. Trocellier, J. Aktaa, R. Lindau, Microstructural characterization of Eurofer-97 and Eurofer-ODS steels before and after multi-beam ion irradiations at JANNUS Saclay facility, Journal of Nuclear Materials, 465 (2015) 236-244.
[634] T.Y. Chen, J.G. Gigax, L. Price, D. Chen, S. Ukai, E. Aydogan, S.A. Maloy, F.A. Garner, L. Shao, Temperature dependent dispersoid stability in ion-irradiated ferritic-martensitic dual-phase oxide-dispersion-strengthened alloy: Coherent interfaces vs. incoherent interfaces, Acta Materialia, 116 (2016) 29-42.
[635] P. Dou, A. Kimura, R. Kasada, T. Okuda, M. Inoue, S. Ukai, S. Ohnuki, T. Fujisawa, F. Abe, TEM and HRTEM study of oxide particles in an Al-alloyed high-Cr oxide dispersion strengthened steel with Zr addition, Journal of Nuclear Materials, 444 (2014) 441-453.
[636] J.C. He, F.R. Wan, K. Sridharan, T.R. Allen, A. Certain, Y.Q. Wu, Response of 9Cr-ODS steel to proton irradiation at 400 degrees C, Journal of Nuclear Materials, 452 (2014) 87-94.
[637] C. Heintze, F. Bergner, M. Hernandez-Mayoral, R. Kogler, G. Muller, A. Ulbricht, Irradiation hardening of Fe-9Cr-based alloys and ODS Eurofer: Effect of helium implantation and iron-ion irradiation at 300 degrees C including sequence effects, Journal of Nuclear Materials, 470 (2016) 258-267.
[638] P. Hosemann, E. Stergar, L. Peng, Y. Dai, S.A. Maloy, M.A. Pouchon, K. Shiba, D. Hamaguchi, H. Leitner, Macro and microscale mechanical testing and local electrode atom probe measurements of STIP irradiated F82H, Fe-8Cr ODS and Fe-8Cr-2W ODS, Journal of Nuclear Materials, 417 (2011) 274-278.
[639] L. Hsiung, M. Fluss, S. Tumey, J. Kuntz, B. El-Dasher, M. Wall, B. Choi, A. Kimura, F. Willaime, Y. Serruys, HRTEM study of oxide nanoparticles in K3-ODS ferritic steel developed for radiation tolerance, Journal of Nuclear Materials, 409 (2011) 72-79.
[640] Z.J. Huang, A. Harris, S.A. Maloy, P. Hosemann, Nanoindentation creep study on an ion beam irradiated oxide dispersion strengthened alloy, Journal of Nuclear Materials, 451 (2014) 162-167.
[641] J.A. Jung, S.H. Kim, S.H. Shin, I.C. Bang, J.H. Kim, Feasibility study of fuel cladding performance for application in ultra-long cycle fast reactor, Journal of Nuclear Materials, 440 (2013) 596-605.
[642] S. Kim, S. Ohtsuka, T. Kaito, S. Yamashita, M. Inoue, T. Asayama, T. Shobu, Formation of nano-size oxide particles and delta-ferrite at elevated temperature in 9Cr-ODS steel, Journal of Nuclear Materials, 417 (2011) 209-212.
[643] M. Klimenkov, A. Moslang, R. Lindau, EELS analysis of complex precipitates in PM 2000 steel, Eur Phys J-Appl Phys, 42 (2008) 293-303.
[644] A.V. Krajnikov, F. Morito, M.I. Danylenko, Embrittlement of molybdenum-rhenium welds under low and high temperature neutron irradiation, Journal of Nuclear Materials, 444 (2014) 404-415.
[645] S. Liu, G.R. Odette, C.U. Segre, Evidence for core-shell nanoclusters in oxygen dispersion strengthened. steels measured using X-ray absorption spectroscopy, Journal of Nuclear Materials, 445 (2014) 50-56.
[646] A.J. London, S. Lozano-Perez, M.P. Moody, S. Amirthapandian, B.K. Panigrahi, C.S. Sundar, C.R. Grovenor, Quantification of oxide particle composition in model oxide dispersion strengthened steel alloys, Ultramicroscopy, 159 Pt 2 (2015) 360-367.

[647] C.Y. Lu, Z. Lu, R. Xie, C.M. Liu, L.M. Wang, Microstructure of HIPed and SPSed 9Cr-ODS steel and its effect on helium bubble formation, Journal of Nuclear Materials, 474 (2016) 65-75.
[648] M.H. Mathon, M. Perrot, L. Poirier, M. Ratti, N. Herve, Y. de Carlanc, Development of new ferritic alloys reinforced by nano titanium nitrides, Journal of Nuclear Materials, 456 (2015) 449-454.
[649] B. Mazumder, C.M. Parish, H. Bei, M.K. Miller, The role of processing route on the microstructure of 14YWT nanostructured ferritic alloy, Journal of Nuclear Materials, 465 (2015) 204-211.
[650] P. Miao, G.R. Odette, T. Yamamoto, M. Alinger, D. Klingensmith, Thermal stability of nano-structured ferritic alloy, Journal of Nuclear Materials, 377 (2008) 59-64.
[651] K. Mo, D. Yun, Y. Miao, X. Liu, M. Pellin, J. Almer, J.S. Park, J.F. Stubbins, S. Zhu, A.M. Yacout, Investigation of High-Energy Ion-Irradiated MA957 Using Synchrotron Radiation under In-Situ Tension, Materials, 9 (2016).
[652] K. Nakajima, T. Shibayama, H. Kayano, Development of Ods Vanadium Alloy and Irradiation Effects on Its Properties, J Atom Energ Soc Jpn, 37 (1995) 338-345.
[653] C. Robertson, B.K. Panigrahi, S. Balaji, S. Kataria, Y. Serruys, M.H. Mathon, C.S. Sundar, Particle stability in model ODS steel irradiated up to 100 dpa at 600 degrees C: TEM and nano-indentation investigation, Journal of Nuclear Materials, 426 (2012) 240-246.
[654] S.V. Rogozhkin, A.A. Aleev, A.G. Zaluzhnyi, N.A. Iskanderov, A.A. Nikitin, P. Vladimirov, R. Lindau, A. Moslang, Atom probe tomography of nanoscaled features of oxide-dispersion-strengthened ODS Eurofer steel in the initial state and after neutron irradiation, Phys Met Metallogr+, 113 (2012) 98-105.
[655] M. Roldan, P. Fernandez, R. Vila, A. Gomez-Herrero, F.J. Sanchez, The effect of triple ion beam irradiation on cavity formation on pure EFDA iron, Journal of Nuclear Materials, 479 (2016) 100-111.
[656] A.F. Rowcliffe, L.K. Mansur, D.T. Hoelzer, R.K. Nanstad, Perspectives on radiation effects in nickel-base alloys for applications in advanced reactors, Journal of Nuclear Materials, 392 (2009) 341-352.
[657] M.B. Toloczko, F.A. Garner, V.N. Voyevodin, V.V. Bryk, O.V. Borodin, V.V. Mel'nychenko, A.S. Kalchenko, Ion-induced swelling of ODS ferritic alloy MA957 tubing to 500 dpa, Journal of Nuclear Materials, 453 (2014) 323-333.
[658] J.S. Veternikova, V. Slugen, S. Sojak, M. Skarba, E. Korhonen, S. Stancek, J. Degmova, V. Sabelova, I. Bartosova, Application of slow positron beam for study of commercial oxide-dispersion-strengthened steels, Journal of Nuclear Materials, 450 (2014) 99-103.
[659] W.Z. Xu, L.L. Li, M. Saber, C.C. Koch, Y.T. Zhu, R.O. Scattergood, Nano ZrO2 particles in nanocrystalline Fe-14Cr-1.5Zr alloy powders, Journal of Nuclear Materials, 452 (2014) 434-439.
[660] H.Q. Zhang, C.H. Zhang, Y.T. Yang, Y.C. Meng, J. Jang, A. Kimura, Irradiation hardening of ODS ferritic steels under helium implantation and heavy-ion irradiation, Journal of Nuclear Materials, 455 (2014) 349-353.
[661] S.Y. Zhong, J. Ribis, N. Lochet, Y. de Carlan, V. Klosek, M.H. Mathon, Influence of nano-particle coherency degree on the coarsening resistivity of the nano-oxide particles of Fe-14Cr-1W ODS alloys, Journal of Nuclear Materials, 455 (2014) 618-623.

[662] T. Lazauskas, S.D. Kenny, R. Smith, G. Nagra, M. Dholakia, M.C. Valsakumar, Simulating radiation damage in a bcc Fe system with embedded yttria nanoparticles, Journal of Nuclear Materials, 437 (2013) 317-325.
[663] Y. Ramjauny, G. Rizza, S. Perruchas, T. Gacoin, R. Botha, Controlling the size distribution of embedded Au nanoparticles using ion irradiation, Journal of Applied Physics, 107 (2010).
[664] G. Rizza, H. Cheverry, T. Gacoin, A. Lamasson, S. Henry, Ion beam irradiation of embedded nanoparticles: Toward an in situ control of size and spatial distribution, Journal of Applied Physics, 101 (2007) 014321.
[665] M.C. Ridgway, R. Giulian, D.J. Sprouster, P. Kluth, L.L. Araujo, D.J. Llewellyn, A.P. Byrne, F. Kremer, P.F. Fichtner, G. Rizza, H. Amekura, M. Toulemonde, Role of thermodynamics in the shape transformation of embedded metal nanoparticles induced by swift heavy-ion irradiation, Phys Rev Lett, 106 (2011) 095505.
[666] A. Oliver, J.A. Reyes-Esqueda, J.C. Cheang-Wong, C.E. Roman-Velazquez, A. Crespo-Sosa, L. Rodriguez-Fernandez, J.A. Seman, C. Noguez, Controlled anisotropic deformation of Ag nanoparticles by Si ion irradiation, Physical Review B, 74 (2006) 245425.
[667] R. Giulian, P. Kluth, L.L. Araujo, D.J. Sprouster, A.P. Byrne, D.J. Cookson, M.C. Ridgway, Shape transformation of Pt nanoparticles induced by swift heavy-ion irradiation, Physical Review B, 78 (2008) 125413.
[668] D.J. Sprouster, R. Giulian, L.L. Araujo, P. Kluth, B. Johannessen, D.J. Cookson, M.C. Ridgway, Swift heavy-ion irradiation-induced shape and structural transformation in cobalt nanoparticles, Journal of Applied Physics, 109 (2011) 113504.
[669] H. Amekura, B. Johannessen, D.J. Sprouster, M.C. Ridgway, Amorphization of Cu nanoparticles: Effects on surface plasmon resonance, Applied Physics Letters, 99 (2011) 043102.
[670] H. Amekura, N. Okubo, N. Ishikawa, D. Tsuya, K. Mitsuishi, Y. Nakayama, U.B. Singh, S.A. Khan, S. Mohapatra, D.K. Avasthi, Swift heavy ion irradiation of ZnO nanoparticles embedded in silica: Radiation-induced deoxidation and shape elongation, Applied Physics Letters, 103 (2013) 203106.
[671] M. Song, K. Mitsuishi, H. Yasuda, K. Furuya, Dynamic process of nano-structured inert gas precipitates introduced with ion implantation in aluminium, J Electron Microsc, 51 (2002) S211-S214.
[672] W. Jiang, W.J. Weber, J.S. Young, L.A. Boatner, Irradiation-induced formation of nanoparticles in cadmium niobate pyrochlore, Applied Physics Letters, 80 (2002) 670-672.
[673] V.K. Tiwari, P.K. Kulriya, D.K. Avasthi, P. Maiti, Radiation-resistant behavior of poly (vinylidene fluoride)/layered silicate nanocomposites, ACS applied materials & interfaces, 1 (2008) 311-318.
[674] J. Thomas, M. Myara, L. Troussellier, E. Burov, A. Pastouret, D. Boivin, G. Melin, O. Gilard, M. Sotom, P. Signoret, Radiation-resistant erbium-doped-nanoparticles optical fiber for space applications, Opt Express, 20 (2012) 2435-2444.
[675] M.C. Ridgway, P. Kluth, R. Giulian, D.J. Sprouster, L.L. Araujo, C.S. Schnohr, D.J. Llewellyn, A.P. Byrne, G.J. Foran, D.J. Cookson, Changes in metal nanoparticle shape and size induced by swift heavy-ion irradiation, Nucl Instrum Meth B, 267 (2009) 931-935.
[676] R.S. Nelson, J.A. Hudson, D.J. Mazey, The stability of precipitates in an irradiation environment, Journal of Nuclear Materials, 44 (1972) 318-330.

[677] P.B. Wells, T. Yamamoto, B. Miller, T. Milot, J. Cole, Y. Wu, G.R. Odette, Evolution of manganese-nickel-silicon-dominated phases in highly irradiated reactor pressure vessel steels, Acta Materialia, 80 (2014) 205-219.
[678] Y.Q. Wu, K.N. Allahar, J. Burns, B. Jaques, I. Charit, D.P. Butt, J.I. Cole, Fe-Cr-Mo based ODS alloys via spark plasma sintering: A combinational characterization study by TEM and APT, Cryst Res Technol, 49 (2014) 645-652.
[679] C.A. Yablinsky, K.E. Tippey, S. Vaynman, O. Anderoglu, M.E. Fine, Y.W. Chung, J.G. Speer, K.O. Findley, O.N. Dogan, P.D. Jablonski, S.A. Maloy, R.E. Hackenberg, A.J. Clarke, K.D. Clarke, Concepts for the Development of Nanoscale Stable Precipitation-Strengthened Steels Manufactured by Conventional Methods, Jom, 66 (2014) 2467-2475.
[680] M.J. Alinger, G.R. Odette, D.T. Hoelzer, The development and stability of Y-Ti-O nanoclusters in mechanically alloyed Fe-Cr based ferritic alloys, Journal of Nuclear Materials, 329 (2004) 382-386.
[681] P.P. Liu, R. Yu, Y.M. Zhu, M.Z. Zhao, J.W. Bai, F.R. Wan, Q. Zhan, Deuterium ion irradiation induced precipitation in Fe-Cr alloy: Characterization and effects on irradiation behavior, Journal of Nuclear Materials, 459 (2015) 81-89.
[682] K. Kaneko, T. Kato, M. Kitayama, Y. Tomokiyo, Precipitation of MgO-nAl(2)O(3) in Mg-doped alpha-Al2O3 under electron irradiation, J Am Ceram Soc, 86 (2003) 161-168.
[683] C. Zheng, M.A. Auger, M.P. Moody, D. Kaoumi, Radiation induced segregation and precipitation behavior in self-ion irradiated Ferritic/Martensitic HT9 steel, Journal of Nuclear Materials, 491 (2017) 162-176.
[684] E. Getto, G. Vancoevering, G.S. Was, The co-evolution of microstructure features in self-ion irradiated HT9 at very high damage levels, Journal of Nuclear Materials, 484 (2017) 193-208.
[685] X. Zhang, S.P. Shu, P. Bellon, R.S. Averback, Precipitate stability in Cu-Ag-W system under high-temperature irradiation, Acta Materialia, 97 (2015) 348-356.
[686] M.Z. Zhao, P.P. Liu, J.W. Bai, Y.M. Zhu, F.R. Wan, S. Ohnuki, Q. Zhan, In-situ observation of the effect of the precipitate/matrix interface on the evolution of dislocation structures in CLAM steel during irradiation, Fusion Eng Des, 89 (2014) 2759-2765.
[687] G. Martin, C. Sabathier, G. Carlot, P. Desgardin, C. Raepsaet, T. Sauvage, H. Khodja, P. Garcia, Irradiation damage effects on helium migration in sintered uranium dioxide, Nucl Instrum Meth B, 273 (2012) 122-126.
[688] P. Ahmedabadi, V. Kain, M. Gupta, I. Samajdar, S.C. Sharma, P. Bhagwat, R. Chowdhury, The role of niobium carbide in radiation induced segregation behaviour of type 347 austenitic stainless steel, Journal of Nuclear Materials, 415 (2011) 123-131.
[689] R.E. Stoller, The impact of mobile point defect clusters in a kinetic model of pressure vessel embrittlement, Am Soc Test Mater, 1325 (1999) 14-29.
[690] E.H. Lee, L.K. Mansur, Relationships between Phase-Stability and Void Swelling in Fe-Cr-Ni Alloys during Irradiation, Metall Trans A, 23 (1992) 1977-1986.
[691] A. Sipahigil, R.E. Evans, D.D. Sukachev, M.J. Burek, J. Borregaard, M.K. Bhaskar, C.T. Nguyen, J.L. Pacheco, H.A. Atikian, C. Meuwly, R.M. Camacho, F. Jelezko, E. Bielejec, H. Park, M. Loncar, M.D. Lukin, An integrated diamond nanophotonics platform for quantum-optical networks, Science, 354 (2016) 847-850.
[692] I. Freestone, N. Meeks, M. Sax, C. Higgitt, The Lycurgus Cup - A Roman nanotechnology, Gold Bull, 40 (2007) 270-277.